Molecular responses of cell adhesion upon cell-cell contact initiation in a 2-D ultrasound standing wave trap

A thesis submitted
for the degree of Doctor of Philosophy

by
Despina Bazou

Cardiff School of Biosciences
University of Wales
Cardiff

Examination committee:

Head of examination:	Prof. David Lloyd, Cardiff University
Internal Examiner:	Prof. Charles. W. Archer, Cardiff University
External Examiner:	Prof. Kevin. M. Shakesheff, University of Nottingham

Date of examination: 13 March 2006

Cardiff 2006

ProQuest LLC
789 East Eisenhower Parkway
P.O. Box 1346
Ann Arbor, MI 48106-1346

Declaration

This work has not previously been accepted in substance for any degree and is not being concurrently submitted in candidature for any degree.

Signed..... (Candidate)

Date.....05/05/06.....

Statement I

This thesis is the result of my own investigations, except where otherwise stated. Other sources are acknowledges by footnotes giving explicit references. A bibliography is appended.

Signed..... (Candidate)

Date.....05/05/06.....

Signed..... (Supervisor)

Date.....

Statement II

I hereby give my consent for my thesis, if accepted, to be available for photocopying and for interlibrary loan, and for the title and summary to be made available to outside organisations.

Signed..... (Candidate)

Date.....05/05/06.....

Acknowledgements

First of all, I would like to thank my supervisor, Prof. W. Terence Coakley for the opportunity to work under his guidance towards this doctoral thesis. He introduced me to the fascinating world of ultrasonics and has given me lots of support as well as freedom during my three-year journey of scientific and personal development.

I would also like to thank:

My advisor, Prof. Charlie W. Archer, for his help and support and for always having an open ear for problems. His group is characterised by an open mind and great hospitality. Thank you all!

Dr. George A. Foster for providing the neural cell system, for support and productive discussions.

Dr. Jim R. Ralphs for his help with microscopy and for showing understanding towards my constant worries about my fluorescent micrographs!

Prof. Wen G. Jiang and Dr. Gaynor Davies for a fruitful and fun collaboration that will eventually become a paper.

Many colleagues and workmates past and present, especially Kathryn A. J. Borthwick, who never stopped supporting me even when progress seemed impossible.

I would also like to express my deepest gratitude to my friends for taking part of all of the rest not mentioned here, particularly Theodora Vatopoulou, Efthimia Melista and Albert Alexander Krug. Thanks for always being there! Your constant encouragement, belief and true friendship mean a lot to me! This thesis is actually half your work.

Above all, I am thankful to my family for love, comfort, encouragement and understanding for all that I strive to achieve!

'Εμείς τη ζωή τη πιάνουμε απ'τα χέρια
Κοιτάζουμε τα μάτια της που μας ξανακοιτάζουν

Κι'αν είναι αυτό που μας μεθάει μαγνήτης,
το γνωρίζουμε
Κι'αν είναι αυτό που μας πονάει κακό,
το 'χουμε νοιώσει

Εμείς τη λέμε τη ζωή, πηγαίνουμε μπροστά
Και χαιρετούμε τα πουλιά της που μισεύουνε
Είμαστε από καλή γενιά'

'Οδυσσέας Ελύτης'

Contents

Abstract

This thesis explores the interactions of cells and particles brought into contact in suspension in an ultrasound standing wave trap as aggregates or monolayers. The influence of [$CaCl_2$], and hence modulation of electrostatic particle interaction force, on the growth and morphology of aggregates of 25 μm latex spheres was initially characterised by techniques including fractal dimension, and void analysis. At low [$CaCl_2$] additions highly hexagonally ordered structures were formed while with increasing [$CaCl_2$] additions the aggregate morphology gradually 'crossed over' from being essentially closely packed to a dendritic, highly disordered one.

The physical environment of cells aggregating in the trap was then examined to assess the extent to which ultrasound might influence cell viability and function. The temperature rise was < 0.5 K. The drag due to acoustic streaming was smaller than the stress imposed by gentle preparative cell centrifugation. The attractive acoustic force between cells was small compared to the force required to reverse a single receptor-receptor bond and to the attractive van der Waals force. Acoustic spectrum analysis detected no cavitation activity in the suspensions. Fluorescent indicators showed that the number of viable cells (99 %) did not change during 1 h in the trap.

The progression of cell-cell interactions *i.e.* length of membrane-membrane contact, and the integral intensities of stained cadherin/catenin complex molecules, the actin cytoskeleton and (for chondrocytes) gap junctions were examined over 60 min in primary chondrocytes, and in neural, prostate epithelial and prostate cancer cell lines. The aggregate form changed concurrently from hexagonally ordered cells to a continuous sheet of mostly quadrilateral and pentagonal cells. Rapid molecular responses to cell contact in other systems are reviewed.

The cells in this work progressed from physical aggregation, through molecular adhesion, to displaying the intracellular consequences of receptor interactions. The ability to form mechanically strong confluent cell monolayers that can be monitored *in situ* or harvested from the trap provides a technique with general potential for monitoring the synchronous development of cell responses to receptor-triggered adhesion.

Chapter 1

Introduction

1.1 General

Many of a cell's responses to its environment are triggered by its interaction with other cells or the extracellular matrix. It is therefore not surprising that cell-cell and cell-matrix adhesion have a central place in virtually all major phenomena of multicellular organisms from embryo development, organisation of organs and their substructures, through diverse functions of the mature organism, including angiogenesis, wound repair and defence against pathogens. In view of the broad array of cell functions associated with cell adhesion, it is no wonder that this field is rapidly diversifying; each new investigation emphasises the complexity of cell-cell and cell-matrix adhesion events.

One clear general theme is that cells do not simply 'stick' together to form tissues, but rather are organised into very diverse and highly distinctive patterns. A variety of cell adhesion mechanisms are responsible for assembling cells together and in association with their connections to the cytoskeleton, determine the overall architecture of the tissue. Thus, cell adhesion systems should be regarded as mechanisms that help translate basic genetic information into complex patterns of cells in tissues (Gumbiner, 1996).

A number of specialised junctional complexes are at the heart of the cell-cell and cell-matrix adhesion events. Focal contacts (or focal adhesions) are junctions

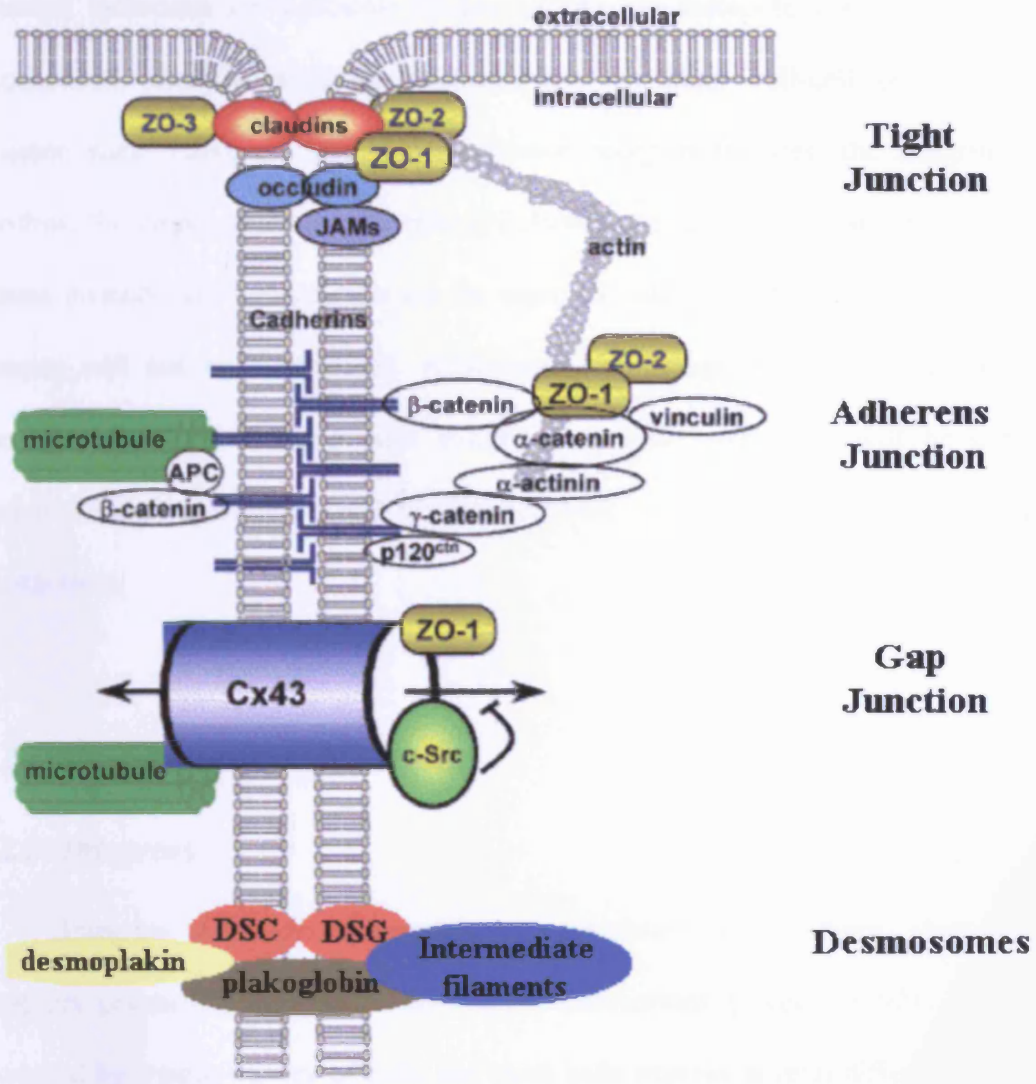

Figure 1.1: Molecular and cellular organisation of cell-cell junctions. The adhesion (adherens, tight and desmosomes) and gap junction receptors, together with their associated proteins, including cytoskeletal elements are identified (Giepmans, 2004).

observed at cell-matrix interactions, while intercellular adhesion complexes are composed of i) tight junctions, ii) adherens junctions, iii) desmosomes and iv) gap junctions (Fig. 1.1). These junctions are not 'static' but dynamic, determining the adhesive status of cells. The functional units of these junctions are the cell

adhesion molecules (or adhesion receptors) that are linked to components of the cytoskeleton, thereby establishing connections to other cell-cell or cell-matrix adhesion sites. There are four major adhesion receptor families; the integrins, the selectins, the immunoglobulin superfamily (IgSF) and the cadherin superfamily. The present contribution concentrates on the topic of cell-cell adhesion, therefore focal contacts will not be emphasised. Additionally, as integrins and selectins are not directly involved in the processes examined in this work, they will be initially discussed briefly. Attention will be directed here on IgSF and cadherins adhesion mechanisms.

1.2 Cell adhesion molecules

1.2.1 Integrins

Integrins are calcium-dependent transmembrane heterodimeric glycoprotein receptors primarily involved in cell-matrix interactions (Hynes, 1992). They are produced by a wide variety of cells and most cells express several different types of integrins (Hynes, 1992). Integrins are composed of α and β subunits non-covalently bound to each other (Fig. 1.2); they have extracellular domains which bind to the extracellular matrix (ECM) and cytoplasmic domains which associate with the actin cytoskeleton and affiliated proteins, including vinculin, talin, paxillin and α-actinin (this protein binds directly to the actin filaments) (Fig. 1.2) to lead to the formation of stress fibers (described in Sec.1.4.1.2) (Fath *et al.*, 1989; Bourdeau and Jones, 1999; Critchley, 2004). The interaction of integrins with the ECM, together with the association of the cytoskeleton leads to the formation of focal contacts, junctions that

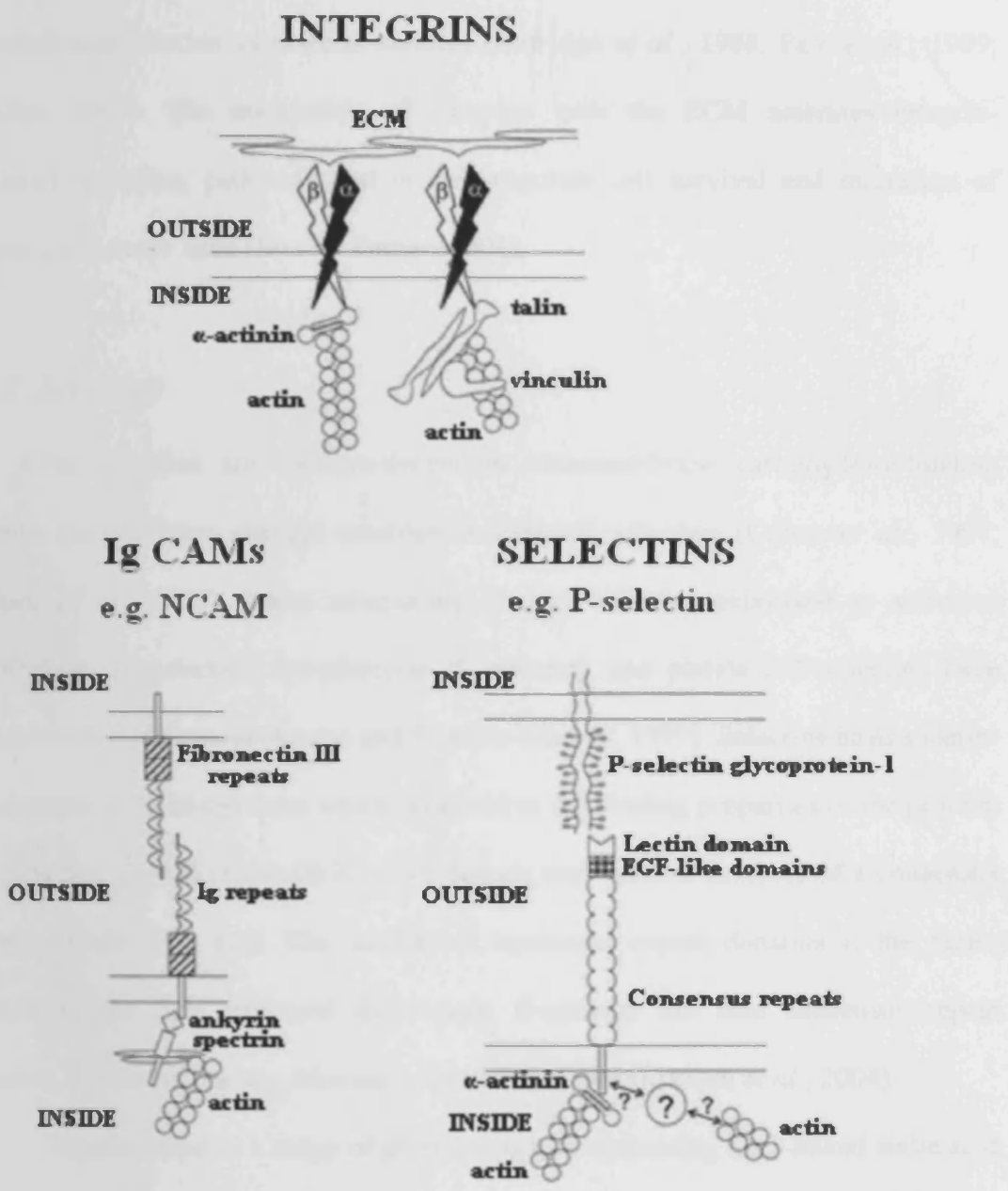

Figure 1.2: Schematic representation of integrins and specific examples of IgCAMs and Selectins together with their typical extracellular ligands and associated cytoskeletal components are shown (Adapted from Juliano, 2002).

are clearly resolved when cells are cultured on an artificial substratum (it is noted that structurally similar adhesions have been observed in smooth muscle cells and in the

myotendinous junction of skeletal muscle) (Burridge *et al.*, 1988; Fath *et al.*, 1989; Schaller, 2001). The association of integrins with the ECM activates integrin-regulated signalling pathways that in turn regulate cell survival and migration of normal and tumour cells (Jin and Varner, 2004).

1.2.2 Selectins

The selectins are calcium-dependent transmembrane carbohydrate-binding proteins (lectins) that mediate heterophilic cell-cell adhesion (Cohen *et al.*, 1997; Ehrhadt *et al.*, 2004). Three structurally distinct selectins expressed at activated endothelium (E-selectin), lymphocytes (L-selectin) and platelets (P-selectin) have been identified (Gonzalez-Amaro and Sanchez-Madrid, 1999). Selectins have a lectin-like domain at the N-terminus which is central to the binding properties of the protein, an epidermal growth factor (EGF-) like domain and various numbers of a consensus repeat domain (Fig. 1.2). The number of consensus repeat domains is the factor accounting for their structural differences; P-selectin has nine consensus repeat domains, E-selectin has six, whereas L-selectin has two (Ehrhadt *et al.*, 2004).

Selectins bind to a range of glycoconjugates containing α2,3-linked sialic acid as well as to sialic acid deficient glycans such as sulphate glycans (heparin) (McEver, 2002). However, the best documented receptor for a selectin is the P-selectin glycoprotein-1 (PSGL-1) (Fig. 1.2), a mucin-like transmembrane glycoprotein found on leukocytes and lymphoid cells (Juliano, 2002). Anchorage in the plasma membrane occurs through a single transmembrane domain. PSGL-1 also contains a small cytoplasmic tail (McEver, 2002). Little has been reported on selectin association with the cytoskeleton; however an interaction between the cytoplasmic domain of P-selectin and α-actinin has been reported (Dwir *et al.*, 2001) (Fig. 1.2). The role of

selectins is to promote tethering and rolling (by rapid formation and breakage of the selectin adhesive bonds) of circulating leukocytes on endothelial cells, platelets and other leukocytes during inflammation (McEver, 1997). Inhibition of the interaction between leukocytes and endothelial cells may result in a number of autoimmune diseases, such as allergy, psoriasis, multiple sclerosis and rheumatoid arthritis.

1.2.3 The immunoglobulin superfamily (IgSF)

The IgSF is the largest protein superfamily, including more than 100 polypeptides (Williams and Barclay, 1988). Members of this family include: a) the Igs themselves, b) Major Histocompatibility Complex (MHC) class I and II molecules, c) proteins of the T-cell receptor (TCR) complex, d) virus receptors and other lymphocyte surface glycoproteins (Brummendorf and Rathjen, 1995). This functional diversity of Ig-like proteins has arisen through variation of amino acid residues of the Ig repeats (Fig. 1.2) and their combination within one immunoglobulin polypeptide (Brummendorf and Rathjen, 1995). Here, the focus is on the Ig molecules and in particular on the neural cell adhesion molecule (NCAM).

1.2.3.1 Structure of NCAM

NCAM, originally described by Jørgensen and Bock (1974) as a synaptic membrane glycoprotein termed D2, was the first vertebrate molecule to be identified and characterised as a cell adhesion molecule (Thiery *et al.*, 1977). NCAM is a calcium-independent cell membrane glycoprotein, the extracellular part of which contains five Ig-homology modules, followed by fibronectin type III, F3, -homology modules, proximal to the membrane (Fig. 1.3). Individual Ig- and F3-homology modules are typically composed of ~100 amino acid residues, which form a sandwich

structure composed of two anti-parallel β-sheets; in addition, Ig-homology modules contain an intramodule disulfide bond connecting the two β-sheets, whereas such a bond is absent in F3-homology modules (Fig. 1.3) (Walmod *et al.*, 2004).

As a result of alternative splicing of the gene encoding NCAM, three main isoforms known as NCAM-180, NCAM-140 and NCAM-120 (the numbers referring to the relative molecular weight, M_r, on a sodium dodecyl sulphate-polyacrylamide gel electrophoresis (SDS-PAGE)) are generated (Walmod *et al.*, 2004). Figure 1.3 schematically represents the different NCAM isoforms. NCAM-180 and NCAM-140 both attach to the plasma membrane through a transmembrane domain, whereas they differ in the length of their cytoplasmic domain (NCAM-180 has a longer cytoplasmic domain). NCAM-120 on the other hand, is attached to the plasma membrane through a glucosylphosphatidylinositol (GPI) anchor (Kiselyov *et al.*, 2005). There is relatively little known about the interactions of NCAM with cytoskeletal proteins. A proposed interaction is linkage of NCAM to the actin cytoskeleton via ankyrin and spectrin (Fig. 1.2). Association of NCAM with α-actinin as well as α- and β-tubulin has also been reported (Büttner *et al.*, 2003). NCAM is the only mammalian protein that carries the negatively charged sugar polysialic acid (PSA), which is post-translationally attached to the fifth Ig domain (Povlsen *et al.*, 2003). PSA is a long, linear α-2,8-linked carbohydrate composed of N-acetylneuraminic acid (Neu5Ac) residues (Johnson *et al.*, 2001). Expression of the polysialiated form of NCAM (PSA-NCAM) peaks early in development and decreases with age (Johnson *et al.*, 2005).

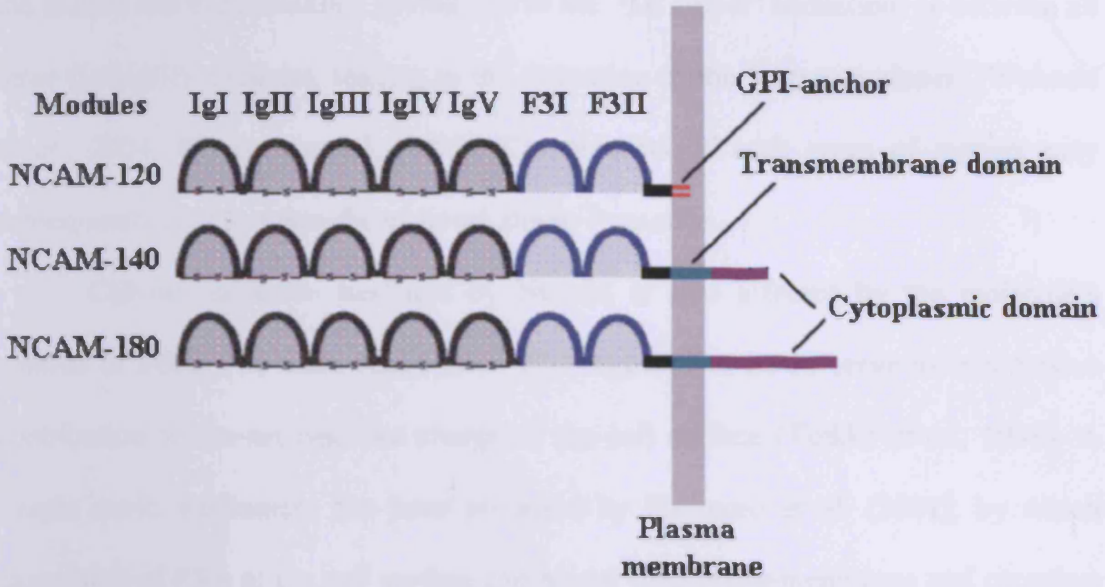

Figure 1.3: Schematic representation of NCAM isoforms, showing the immunoglobulin homology modules (black) IgI-V, and the fibronectin type III homology modules (blue) F3I and F3II. The disulphide bonds are indicated with S. NCAM-120 is attached to the plasma membrane via a GPI anchor (red), while both NCAM-140 and NCAM-180 attach to the plasma membrane through a transmembrane domain (green); NCAM-140 and NCAM-180 differ in the length of their cytoplasmic domain (purple) (Adapted from Walmod *et al.*, 2004).

1.2.3.2 NCAM and cell-cell adhesion

Intensive research on the mechanism of NCAM homophilic binding has led to the development of a number of different models. The currently accepted idea involves primarily the presence of NCAM on the cell surface in a *cis*-dimeric form, *i.e.* NCAM molecules form dimers on the surface of the same cells. This *cis*-dimerisation process is mediated by the first two Ig modules (Fig.1.3). The *trans*-homophilic interaction (*i.e.* interaction of NCAM dimers present on apposing cell membranes) of the *cis*-dimers is probably mediated by an interaction either between

the second and third modules, giving rise to the 'flat zipper' formation, or between all three (IgI-IgIII) modules, leading to the formation of the 'compact zipper' (Walmod *et al.*, 2004; Kiselyov *et al.*, 2005). Combination of both types of zippers may subsequently lead to a two-dimensional zipper formation.

Cell-cell adhesion mediated by NCAM is also affected by the molecule's content of PSA. The main function of PSA appears to be to serve as a repulsive contribution to the net negative charge of the cell surface (Toikka *et al.*, 1998). A simple steric mechanism has been proposed by Fujimoto et al. (2001), by which expression of PSA at the cell surface can hinder membrane-membrane and receptor-receptor apposition, as the intercellular spacing has been shown in electron microscopy images to be increased by 10-15 nm, keeping NCAM receptor molecules on apposing membranes at a separation greater than that required for two NCAM molecules to bridge with each other (Johnson *et al.*, 2005).

1.2.4 The cadherin superfamily

The evolutionarily diverse cadherin protein superfamily in humans consists of approximately 80 members (Yagi and Takeichi, 2000). Cadherins are calcium-dependent proteins and are made up of an extracellular domain responsible for cell-cell interactions, a transmembrane domain and a cytoplasmic domain that is usually linked to the cytoskeleton (Wu and Maniatis, 1999). Based on domain composition, genomic organisation and overall structure, the superfamily is divided into six subgroups: (a) classical or Type I cadherins, (b) Type II cadherins (closely related to type I), (c) desmosomal cadherins, (d) protocadherins, (e) FAT-like cadherins and (f) Flamingo cadherins (Gooding *et al.*, 2004). The structural diversity of the cadherin superfamily is represented in Fig. 1.4.

1.2.4.1 Structural diversity of cadherins

Members of the Type I classical cadherins include the: epithelial (E-), neural (N-), placental (P-), retinal (R-), heart (H-) and EP- (a cadherin discovered in *Xenopus laevis* having comparable homology to both E- and P- cadherins) cadherins. Type I cadherins are composed of five tandem extracellular cadherin domains (EC1-EC5) (comprising an approximately 110 amino acid peptide), that are connected by short linker regions, each containing two to three calcium-binding sites (Häussinger *et al.*, 2002), a single segment transmembrane domain and a distinct, highly conserved cytoplasmic tail (Fig. 1.5) that specifically binds to catenins (Sec. 1.3.2; Fig. 1.5). EC1 to EC4 are homologous cadherin repeats and include the His-Ala-Val (HAV)-sequence, while EC5 is a less-related membrane-proximal domain.

Type II cadherins (vascular-endothelial (VE-), kidney (K-), 7-12, 18, 19, and 20) differ in their structure to Type I cadherins in that the first of the EC domains lacks the HAV sequence believed to play a role in Type I adhesion. These proteins are expressed in loosely associated cells and are responsible for comparatively weaker intercellular adhesion.

The third cadherin subgroup, the desmosomal cadherins, is further divided into two subfamilies: the desmocollin (DSC) (90-100 kDa) and desmoglein (DSG, 130-165 kDa) proteins. Both DSC and DSG consist of five cadherin domains in the extracellular portion of the molecule (EC1-EC5), a transmembrane domain and a cytoplasmic domain that associates with plakoglobin, plakophillins and desmoplakin (Fig. 1.3), which in turn link the cadherins to the intermediate filament cytoskeleton (Green and Gaudry, 2000). Desmosomal cadherins interact in a heterotypic manner

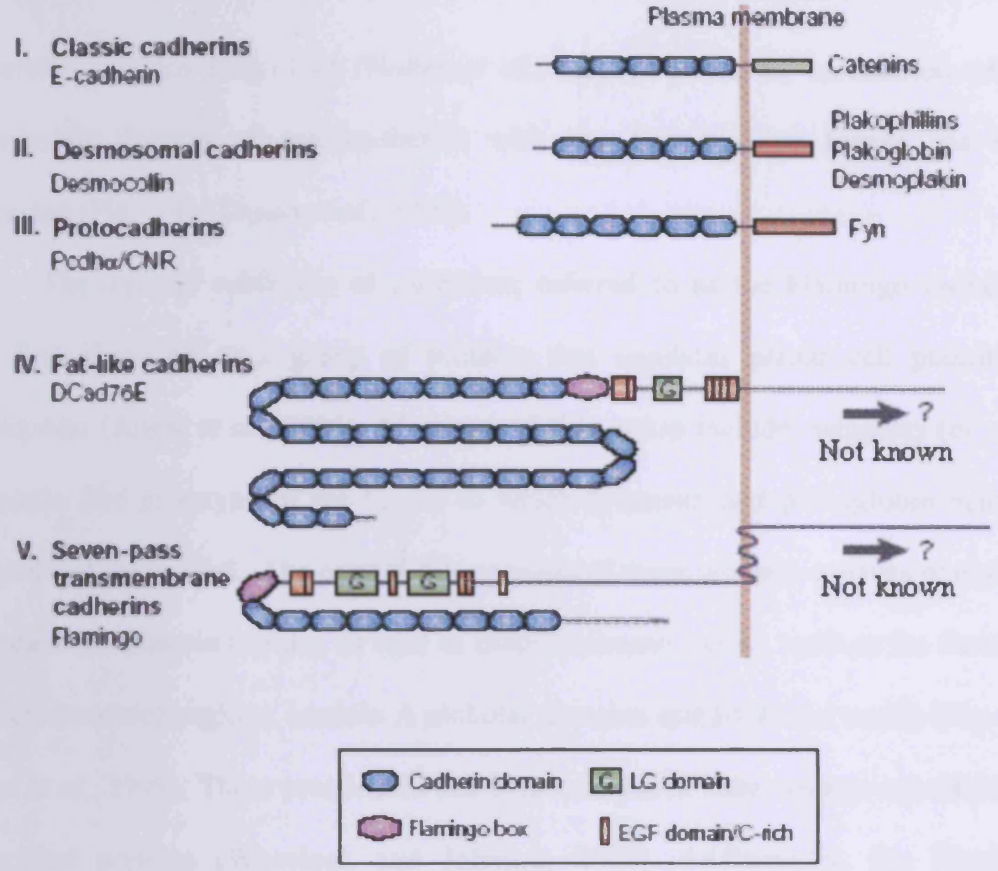

Figure 1.4: Schematic representation of the structure of 5 of the 6 cadherin subfamilies. A schematic for Type II classical cadherins is not shown, as the only difference from Type I cadherins is that the first of the EC domains lacks the HAV sequence. Representative protein members of each of the remaining five cadherin subfamilies are shown (Adapted from Tepass *et al.*, 2000).

(Garrod *et al.*, 2002); *i.e.* desmoglein interacts with desmocollin, and cells must express at least one desmoglein isoform and one desmocollin isoform to assemble a desmosome (Wheelock and Johnson, 2003).

Protocadherins were identified by Sano et al. (1993). They consist of a large subfamily of cadherin-like adhesion proteins highly expressed in the synapses of the central nervous system (Gooding *et al.*, 2004) and have up to seven extracellular domains (Fig. 1.4). Moreover, there is little evidence that they bind to cytoskeleton-

associated proteins (Fig. 1.4) (Nollet *et al.*, 2000). However, association of the cytoplasmic domain of protocadherins with the Fyn tyrosine kinase has been suggested (Fig. 1.4) (Tepass *et al.*, 2000).

The unusual subfamily of cadherins, referred to as the Flamingo cadherins, was first identified as a group of proteins that regulates planar cell polarity in *Drosophila* (Angst *et al.*, 2001). Members of this group include: wingless (or wnt), armadillo (the prototype of the family to which β-catenin and plakoglobin belong), frizzled and disheveled. The extracellular portion of these proteins consists of eight or nine cadherin domain repeats, as well as other structural motifs, such as the flamingo box, cysteine-rich regions, laminin A globular domains and EGF-like motifs (Fig. 1.4) (Usui *et al.*, 1999). These proteins do not bind catenins or other known cytoskeleton-associated proteins (Wheelock and Johnson, 2003). Additionally, the Flamingo cadherins have a unique seven transmembrane segment, unlike the single transmembrane segment observed in classical cadherins (Fig. 1.4).

FAT-like cadherins were first identified as tumour suppressor proteins in *Drosophila* and they contain 34 extracellular repeats (Fig. 1.4) (Angst *et al.*, 2001). Taking into account the large size of the extracellular portion, it has been suggested that FAT cadherin plays a role outside of adhesion, and is possibly involved in cell repulsion, acting as a sensor of cell to cell proximity and a brake on cell proliferation (Cox *et al.*, 2000).

Finally, in addition to the cadherins that fall within the defined subgroups discussed earlier, numerous atypical cadherin proteins occupy unique, isolated positions within the cadherin superfamily. The Truncated (T-) cadherin (or cadherin-13) is such a member. T-cadherin shares its ectodomain organisation with classical cadherins, but lacks both the transmembrane and cytoplasmic regions. T-cadherin is

instead modified with a glycosyl-phosphatidylinositol (GPI) moiety that anchors it to the plasma membrane (Angst *et al.*, 2001).

Since Type I cadherins were the only class of cadherins investigated in the present study, the term 'cadherin' refers in this work, unless otherwise stated, to Type I cadherin.

1.3 Mechanisms of cadherin-based adhesion

A fundamental challenge in the research area of cadherin-based adhesion is to understand how cells utilise the components of the cadherin adhesive system to generate and regulate a dynamic range of adhesive strengths. For this reason, the following discussion will distinguish between the cadherin interactions in the extracellular and cytoplasmic domain.

1.3.1 Extracellular domain interactions

It is now realized that two types of cadherin interactions are distinguishable in the cellular adhesion process: a) The occurrence of parallel binding to a neighbouring cadherin on the same cell (a *cis*-interaction, also referred to as a 'strand dimer' interaction; and b) the interaction between two antiparallel oriented cadherin molecules protruding from opposing cells (*trans*-interaction, also termed 'adhesion dimer' interaction) (Shapiro *et al.*, 1995).

An early model (Shapiro *et al.*, 1995) of the organisation of *cis*-dimers proposed that two cadherin molecules extending from the same cell surface interact laterally through hydrophobic interactions. The most prominent feature of this interaction is the reciprocal intercalation of a conserved tryptophan (Trp2) sidechain, localised at the second domain in classic cadherins, into the hydrophobic cavity

formed by the paired molecules. Another early model (Nagar *et al.*, 1996; Pertz *et al.*, 1999) proposed that lateral (or *cis*-interactions) cadherin dimers are stabilised by mutually coordinating calcium ions. *Trans*-interactions have been shown by electron microscopy studies to occur only after formation of *cis* contacts, thus demonstrating the cooperativity of the two processes (Tomschy *et al.*, 1996; Koch *et al.*, 1997; Häussinger *et al.*, 2002).

Identification of which of the five EC domains are involved in cadherin-cadherin binding (or *trans*-interactions) and specificity sites has been attempted by several investigators using experimental approaches such as mutational (Blaschuk *et al.*, 1990) or cell aggregation inhibition (Nose *et al.*, 1990) assays. N- and E-cadherin transfectants sorted to form separate tissue-like cell-aggregates, but swapping domains between N- and E-cadherin sometimes swapped the specificity of cell aggregation. Notably, it was the EC1 domain that carried this property, providing strong evidence in support of the idea that the adhesive binding site of cadherins is localised primarily within the EC1 domain (Patel *et al.*, 2003). Additionally, a predomain (usually less than 80 amino acids) between the signal sequence and the start of the EC1 domain exists at the N-terminus. Correct cleavage of this predomain is absolutely essential for cadherin function (Patel *et al.*, 2003). Finally, Tomschy and co-workers (1996) and Pertz et al. (1999) have reported a variety of electron microscopy studies of cadherin fusion proteins, which have uniformly shown interaction between cadherins at or near the EC1.

Several models of homophilic cadherin *trans*-binding, which suggest multiple adhesive interactions, have been proposed more recently. Sivasankar et al. (1999; 2001) demonstrated that the strongest interaction was detected when the antiparallel proteins fully overlapped, leading to an extensive overlay of multiple EC domains.

More specifically, by measuring the absolute distance at which opposed cadherin fragments bind and by numerically calculating the changes in the interaction potentials resulting from deletions of individual domains, it was shown that at least two domains per molecule are required for homophilic cadherin binding. In another model based on bead aggregation and laminar flow cell adhesion assays, Chappuis-Flament and colleagues (2001) proposed that the homophilic interactions formed between cadherins may arise from multiple interactions or different combinations of interactions between EC domains.

Nevertheless, it is now well accepted that many, if not all, EC domains contribute to the formation of the cadherin homophilic interaction, contrasting early studies (Shapiro *et al.*, 1995) where only EC1-EC1 interactions were identified. However, it is still unclear whether the interactions involving the EC1 domain or multiple EC domains occur under physiological conditions or are possible only in some crystalline states (Gooding *et al.*, 2004).

1.3.2 Cytoplasmic domain interactions

The cytoplasmic domain of cadherins plays a crucial role in cell adhesion through cytoskeleton interaction and during extracellular lateral cadherin clustering (Gooding *et al.*, 2004). The highly conserved, serine-rich, cytoplasmic region of cadherins consists of approximately 70 amino acids and is divided into two domains, a conserved membrane proximal domain and a distal one. Key to adhesive activity is the interaction between the cytoplasmic region of cadherins and proteins β-catenin or plakoglobin (γ-catenin), which form the link to the actin cytoskeleton via α-catenin (Pokutta and Weiss, 2002) (Fig. 1.5).

1.3.2.1 α-catenin

α-catenin has a molecular weight of 102 kDa and is homologous to the actin-binding protein vinculin, a cytoplasmic protein located in focal contacts (Sec. 1.2.1) (Rüdiger, 1998). a-catenin is the protein that connects the E-cadherin/β- (or γ-) catenin complex and the actin cytoskeleton (Kobeliak and Fuchs, 2004) either through direct interaction with filamentous (F-) actin or indirectly through association with the actin binding proteins vinculin, α-actinin, zona occludens 1 and 2 (ZO-1, ZO-2) (Figs 1.1 and 1.5) (Pokutta and Weis, 2002; Wheelock and Johnson, 2003). Cells lacking α-catenin or with mutations in α-catenin do not form the tight cell-cell contacts typical of adherens junctions (Wheelock and Johnson, 2003). Additionally, loss or impairment of the function of α-catenin is a marker for cancer development (Davies *et al.*, 2000; Nakopoulou *et al.*, 2002; Buda and Pignatelli, 2004). Finally, it has been suggested that overexpression of α-catenin binds to cytoplasmic β-catenin disturbing in this way the β-catenin mediated wnt signals (Nagafuchi, 2001) described in Section 1.5.1.

1.3.2.2 β-catenin

β-catenin is a 92 kDa protein that interacts directly with the cadherin cytoplasmic domain (Figs. 1.1 and 1.5) (Dalseg *et al.*, 1994) and shares about 68% identity with γ-catenin (Wheelock and Johnson, 2003). It has been suggested that β- and γ-catenins can directly substitute for one another as structural components of the adherens junction (Wheelock and Johnson, 2003). Dysfunction or loss of β-catenin may result in cell-cell disengagement which contributes to subsequent cancer cell invasiveness (Kawanishi *et al.*, 1995; Winjhoven *et al.*, 2004). β-catenin as well as being a component of adherens junctions, also serves as a transcriptional activator of the wnt signalling pathway described in Section 1.5.1.

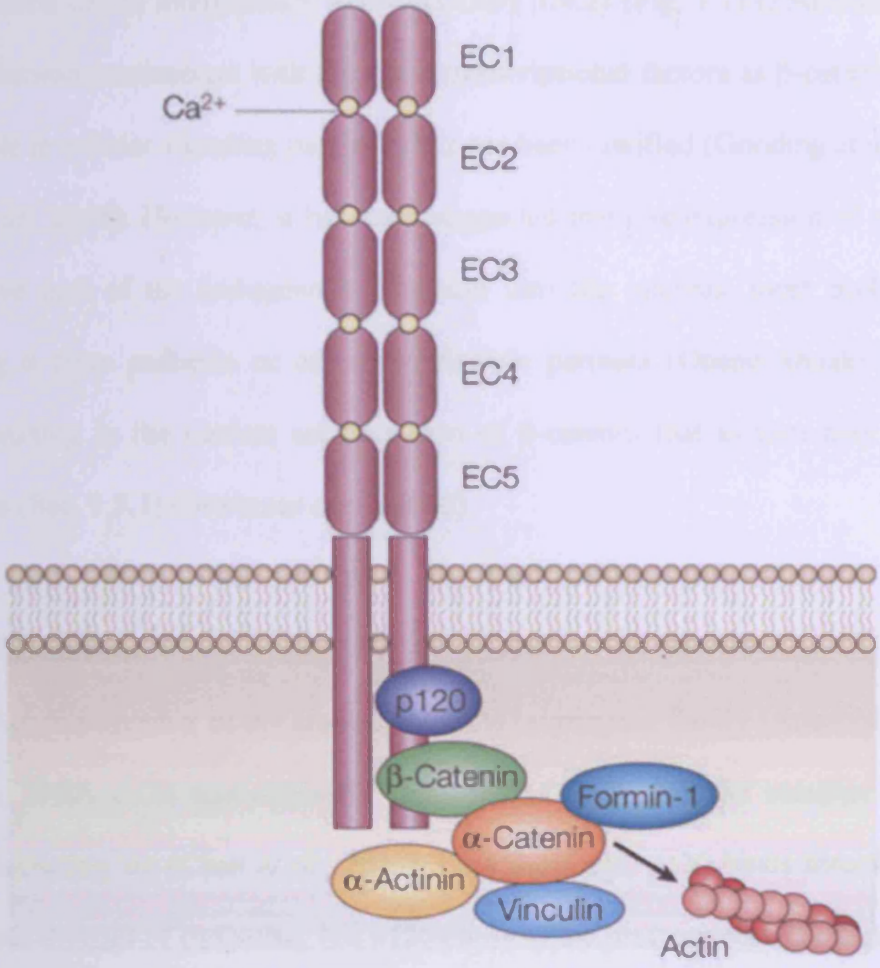

Figure 1.5: The cadherin-catenin protein complex. The core universal-catenin complex consists of p120 catenin bound to the juxtamembrane region, β-catenin bound to the distal region, which also binds to α-catenin. α-catenin then binds to actin filaments and actin-binding proteins such as vinculin, α-actinin or formin-1. γ-catenin is not shown in the Figure, but it directly substitutes β-catenin in the adherens junction complex (Gumbiner, 2005).

1.3.2.3 γ-catenin

γ-catenin, an 83 kDa protein, is also known as plakoglobin (Dalseg *et al.*, 1994). α-catenin binds to γ-catenin in adherens junctions (Fig. 1.1) but in desmosomes, γ-catenin binds to DSG and DSC and to desmoplakin that provide a link

to the keratins of the intermediate filaments (Sec. 1.4.2) (Fig. 1.1) (Zhurinsky *et al.*, 2000). γ-catenin can interact with the same transcriptional factors as β-catenin but its precise role in cellular signaling pathways has not been clarified (Gooding *et al.*, 2004; Shiina *et al.*, 2005). However, it has been suggested that overexpression of γ-catenin could drive part of the endogenous β-catenin into the nucleus, most probably by displacing it from cadherin or other cytoplasmic partners (Ohene-Abuakwa *et al.*, 2000), resulting in the nuclear accumulation of β-catenin that in turn may activate oncogenes (Sec. 1.5.1) (Bremmes *et al.*, 2002).

1.3.2.4 p120 catenin

p120 is a member of the armadillo (ARM) supergene family (Anastasiadis and Reynolds, 2000). p120 was originally identified as a substrate for receptor tyrosine kinases, including src (Chen *et al.*, 2003). Like β-catenin, p120 binds directly to the cytoplasmic domain of cadherins, but p120 binds to the juxtamembrane (or proximal) rather than the distal region (Figs. 1.1 and 1.5) (Peiper and Yap, 2003). The function of p120 in cell-cell adhesion has not been resolved. It has been proposed that p120 might be required for clustering of cadherins and for strong cell-cell adhesion (Yap *et al.*, 1998; Thoreson *et al.*, 2000). Davis et al. (2003), alternatively, have suggested that p120 might modulate cell adhesion through modulation of the Rho family of small GTPases (actin cytoskeleton modulators described in Sec. 1.4.1.3). p120 may then promote the local assembly and organisation of the actin cytoskeleton, supporting cadherin-bound p120 involvement in actin driven cadherin clustering (Gooding *et al.*, 2004). It has been suggested that this positive adhesion regulation is the principal function of p120 (Ireton *et al.*, 2002). The armadillo family also includes δ-catenin

and ARVCF (armadillo repeat deleted in velocardiofacial syndrome), two proteins that are less well studied but have similar functions to p120 (Gumbiner, 2005).

1.4 The cytoskeleton

The cytoskeleton of eukaryotic cells is a dynamic intracellular system composed primarily of three different types of fibrous structures: a) actin microfilaments, b) intermediate filaments and c) microtubules, which built a network throughout the cell's cytoplasm (Kürner *et al.*, 2004). These elements, while composed of different proteins, are in constant interaction with each other.

1.4.1 Actin microfilaments

1.4.1.1 Actin dynamics

Actin is one of the most abundant and highly conserved proteins in all eukaryotes and typically makes up 5% of all intracellular protein (Egelman and Orvala, 1995; Pantaloni *et al.*, 2001). Actin serves not only in the maintenance of cell shape and structure (Cramer *et al.*, 1994), but also has roles in other fundamental cellular functions including cell motility and spreading (Carlier and Pantaloni, 1997), particle movement (*i.e.* transport of particles and receptors over the cell surface) (Cramer *et al.*, 1994) and phagocytosis (Pollard *et al.*, 2003).

Actin occurs as globular (G-actin) monomer or as polymerised filaments (F-actin) that are particularly concentrated just beneath the plasma membrane (cortical actin) (Orlova *et al.*, 2004). The polymerisation process of actin is briefly described here. Actin filaments are structurally and kinetically polarised, *i.e.* the rapidly growing end of a filament is called the barbed end, while the slowly growing end is called the pointed end (Pollard *et al.*, 2000). G-actin monomers assemble rapidly at

the barbed end, leading to the formation of helical double stranded actin filaments (F-actin). This process is accompanied by hydrolysis of ATP to ADP. As filaments are formed, the concentration of monomers falls until it reaches the critical concentration at which monomers and filaments are at equilibrium (Revenu *et al.*, 2004). At the equilibrium state, the filament adds monomers at the barbed end and simultaneously loses monomers from the pointed end, leading to the property of filament 'treadmilling' (Carlier, 1998).

1.4.1.2 Actin organisation

Alberts et al. (2003) has found it useful to characterise three different 3-D arrays of filamentous actin, all formed by interaction of actin with different binding proteins: i) gel-like network, ii) contractile bundles (or stress fibers) and iii) tight parallel bundles (the latter two being referred to as fibrous arrays). Gel-like networks are formed by interactions of actin filaments with the flexible actin binding protein molecule *filamin*; the latter promotes the formation of a highly viscous gel by linking together two actin filaments roughly at right angles (Alberts *et al.*, 2003). Tight parallel bundles on the other hand, are formed by interaction of actin with binding proteins such as *villin*, *fibrin* and *fascin*. Finally, contractile bundles or stress fibers are arranged in an anti-parallel fashion, but are more widely spaced than actin bundles (Furukawa and Fechheimer, 1997). The proteins associated with actin in stress fibers are predominantly *α-actinin* and *myosin II* (Alberts *et al.*, 2003).

1.4.1.3 Cell-cell adhesion and the cytoskeleton

The actin cytoskeleton is closely associated with cadherin-mediated adhesion, especially at the adherens junction, similar to the linkage of integrins to actin at focal

adhesions (Perez-Moreno *et al.*, 2003). Gumbiner (2005) has suggested that the actin cytoskeleton might be coupled to sites of adhesion at the adherens junctions so as to generate changes in cell shape (for example flattening) and/or cell movements, to help in the organisation of cell structure and to establish cell polarity.

A number of insights into the molecular mechanisms that couple cytoskeletal and adhesive dynamics have been gained through *in vitro* studies that exploited the ability to modulate intercellular junction formation through calcium stimulation or inhibition and through cadherin-inactivating antibodies (Jamora and Fuchs, 2002). Insights into actin dynamics and intercellular adhesion have also come from the use of green fluorescent protein (GFP)-tagged E-cadherin and real time microscopy to study the mechanism of adhesion in Madin Darby Canine Kidney (MDCK) epithelial cells (Adams *et al.*, 1998). At the initial stages of intercellular adhesion, E-cadherin, β- and α-catenin organise into distinct aggregates, referred to as 'puncta' (Yonemura *et al.*, 1995; Adams *et al.*, 1998). These cadherin-catenin complexes are linked to the cytoskeleton through thin bundles of actin that forms a bridge between the puncta and cortical F-actin belt. In the second 'maturation' step of intercellular adhesion, cortical actin disappears and is replaced by a continuous line of actin fibres at the interface of adhering cells, arranged in parallel with the plasma membrane (Jamora and Fuchs, 2002).

The actin rearrangements seen in cadherin-mediated cell-cell adhesion are regulated by the Rho family of small GTPases (Braga 2000, Braga, 2002; Wheeler and Ridley, 2004, Chu *et al.*, 2004). These signalling proteins cycle between an activated GTP-bound state and an inactive GDP-bound state (Kaibuchi *et al.*, 1999). This cycle is regulated *in vivo* by GTPase activating proteins (GAPs) and guanine nucleotide exchange (GDP for GTP) factors (GEFs) (Lambrechts *et al.*, 2004). The Rho family

of small GTPases includes the Rho subfamily members that promote stress fiber formation, Rac, that initiates lamellipodia (periphery of the cells) or ruffle (top of the cell) formation and Cdc42 that can generate filopodia (Braga 2002).

However, while the above molecules have been found to localize at adherens junctions in various studies (Braga *et al.*, 1997; Takaishi *et al.*, 1997; Braga *et al.*, 1999), it has not been clearly established whether Rho family GTPases activation is a direct consequence of cadherin *trans*-interactions or involves cell membrane-dependent signals that require cadherin adhesion of apposing cells, but are not themselves directly activated by cadherins (Yap and Kovacs, 2003). In other words, although cadherin inhibition activity, by cadherin-blocking antibodies, identifies some necessity for cadherin adhesion, it cannot distinguish between primary and secondary signaling events (Yap and Kovas, 2003). The current idea is that activation of Rho GTPases plays a role, through interactions with p120 catenin, in the clustering of cadherins, which is an early event in the formation of a junction (Wheelock and Johnson, 2003).

1.4.2 Intermediate filaments

The name 'intermediate filaments' comes from their diameter, 10-12 nm, being intermediate between that of microtubules (25 nm) and microfilaments (7-10 nm) (Strelkov *et al.*, 2003). Intermediate filaments exhibit unique structural features clearly differentiating them from actin microfilaments and microtubules. Firstly, in contrast to microtubules and microfilaments, which are assembled from highly conserved globular proteins, the elementary unit of an intermediate filament is a very elongated (~45 nm) and thin (~2-3 nm) rod-like dimer (a so called 'coiled-coil' structure) (Chang and Goldman, 2004), formed by alignment of two intermediate filament

monomers alongside one another in the same orientation (DePianto and Coulombe, 2004). Subsequently, two dimers are assembled into an anti-parallel tetramer, which in turn associates with an intermediate filament growing laterally and longitudinally, resulting in the formation of a 10-12 nm filament (DePianto and Coulombe, 2004). Secondly, both actin microfilaments and microtubules are polarized, a feature that allows them to actively transport along them associated motor proteins such as myosins and kinesins. Intermediate filaments on the other hand, have no polarity, as individual dimers are oriented both 'up' and 'down' along the filament (Strelkov *et al.*, 2003). Thirdly, *in vivo* intermediate filaments appear to be the most dynamic of the three filament types. In particular, association of intermediate filaments dimers can occur along the entire filament length and not just at both ends as in microfilaments and microtubules (Strelkov *et al.*, 2003).

Intermediate-filament proteins have been divided in terms of their subcellular localisation (cytoplasmic or nuclear) and assembly properties into three groups (Hermann and Aebi, 2004). Assembly group 1 consists of the keratins, proteins that form filaments composed of heterodimers and are the cytoplasmic intermediate filaments. Assembly group 2 consists of vimentin, desmin, glial fibrillary associated protein (GFAP) and peripherin, as well as neurofilament proteins. Assembly group 2 proteins are able to form heterodimer complexes with other proteins within their class and are, like keratins, cytoplasmic intermediate filaments. Finally, assembly group 3 is composed of the nuclear intermediate-filament proteins, the lamins (Hermann and Aebi, 2004; Chang and Goldman, 2004).

Intermediate filaments are the cytoskeletal anchoring site for desmosomal cadherins involved in the formation of desmosomes (Sec. 1.2.4.1; Fig. 1.1). The resulting junction plays a key role in providing mechanical integrity to tissues such as

the epidermis and heart which experience mechanical stress (Yin and Green, 2004; DePianto and Coulombe, 2004). Furthermore, the importance of intermediate filaments in the process of cell-substrate adhesion comes from reports where mutated fibroblasts lacking the protein vimentin are considerably less adherent to a substratum than normal fibroblasts (Chang and Goldman, 2004). Finally, upregulation of vimentin and downregulation of keratins results in increased cell motility, an attribute that is a characteristic of tumour progression and metastasis (Anguelow, 2000; DePianto and Coulombe, 2004).

1.4.3 Microtubules

Microtubules are the largest structures of the cytoskeleton and consist of linear tubular polymers of a globular protein called tubulin. There are three tubulin isomers: α-, β- and γ-. Microtubules are hollow tubes composed of α- and β-tubulin dimers organized in a head to tail fashion, leading to the formation of heterodimers. Heterodimers associate with other dimers to form oligomers, which then elongate and produce the protofilaments (Amos and Baker, 1979). Similarly to actin microfilaments, microtubules are polarised having a 'plus' and a 'minus' end (Watanabe *et al.*, 2005). Microtubules are nucleated from their minus ends that localize predominantly at the microtubule-organising centre (MTOC) that is usually a centrosome of which γ-tubulin is a part (Job *et al.*, 2003). The plus ends of microtubules alternate between phases of growth and shrinkage (a state termed 'dynamic instability') similar to the 'treadmilling' dynamics shown for actin microfilaments. During cell migration, stabilisation of the plus ends of microtubules at target destinations, such as kinetochores on the mitotic spindle and cell cortex, enables the microtubule-organising centre (MTOC) to reorient towards the leading edge,

which results in a polarised microtubule array that facilitates cell migration (Watanabe *et al.*, 2005).

Microtubules function to provide intracellular tracks for the cell and transport vesicles, granules and organelles around the cytoplasm (Gross, 2004; Dohner *et al.*, 2005). They play major role in the mitotic spindle in the separation of chromosomes during anaphase in mitosis (Nasmyth, 2005). It has also been suggested that microtubules and actin do not have distinct functions but participate together in most cellular functions and in particular, cooperate to modify cell shape, cell motility and cell polarity (Etienne-Manneville, 2004).

1.5 The cadherin-catenin complex in cell signalling

Cells obtain and process information from their environments to modulate their behaviour during normal embryonic development and during abnormal processes such as tumourigenesis. Such signals are activated by growth factors (Yap *et al.*, 1997), by interactions of cells with the extracellular matrix (Juliano, 2002) or by cell-cell interactions (Juliano, 2002). Cadherin signalling through cell-cell interactions involves: a) the wnt pathway, b) signalling through the Rho family of small GTPases described in Section 1.4.1.3, and c) signalling through receptor tyrosine kinases.

1.5.1 The wnt pathway

The β-catenin/wnt pathway is probably the best studied signalling pathway that involves cadherins (Wheelock and Johnson, 2003).

In the absence of a wnt signal, β-catenin is sequestered in a complex with the adenomatous polyposis coli (APC) gene product, a serine threonine glycogen synthetase kinase (GSK-3β), protein phosphatase 2A and the scaffolding protein axin,

enabling phosphorylation and degradation of free β-catenin (Aplin and Juliano, 2001; Ebert *et al.*, 2003). This complex formation ensures low levels of free cytoplasmic β-catenin. Residual catenins help maintain intercellular adhesion by binding to cadherins. Stimulation of the wnt pathway, by association of the wnt family of secreted glycoproteins and their membrane receptor 'frizzled', leads to activation of the cytoplasmic dishevelled (Dsh) protein, which is recruited to the cell membrane (Bremmes *et al.*, 2002). The activated Dsh downregulates the APC, GSK-3β, axin complex, so that it no longer can phosphorylate β-catenin. This results in an increase of free cytosolic β-catenin, which translocates to the nucleus, where it forms complexes with transcriptional factors of the LEF/TCF (lymphocyte enhancing factor/T cell factor) family, which in turn activate other genes that may act as oncogenes (Chesire and Isaacs, 2003; Buda and Pignatelli, 2004). The wnt pathway, in which β-catenin acts as a transcription coactivator, plays a key role in the control of cell differentiation and development as well as tumourigenesis (Bremmes *et al.*, 2002).

1.5.2 Signalling through receptor tyrosine kinases

Receptor tyrosine kinases can also interact with proteins of the adherens junction. Receptor tyrosine kinases are situated in close proximity to, and can physically interact with, E-cadherin (Brady-Kalnay *et al.*, 1995). In general, tyrosine kinases induce the phosphorylation of cell-cell adhesion proteins such as β-catenin, thus ensuring low levels of free cytoplasmic β-catenin (Mauro and Surmacz, 2004). Abnormal stimulation of tyrosine kinase signalling pathways leads to the development of tumours (Mauro *et al.*, 2003).

1.6 Gap junctions

1.6.1 Architecture of gap junctions

Gap junctions (Fig. 1.1) are specialised intercellular junctions at locations characterised by a narrow 2-3 nm gap between the plasma membranes of apposing cells (Wei *et al.*, 2004). Gap junctions contain hydrophilic membrane channels that allow diffusion of molecules of less than ~1000 Da (Giepmans, 2004). One gap junction consists of a connexon tightly packed in a hexagonal array and each connexon has a hemichannel made up of six protein subunits known as the connexins (Kumar and Gilula, 1996) (Fig. 1.6). A connexin has two extracellular domains, four hydrophobic membrane-spanning domains and three cytoplasmic domains including an intracellular loop and amino and carboxyl termini (Wei *et al.*, 2004). A gap junction is thus formed when a connexon of one cell docks with a connexon of a neighbouring cell (Wei *et al.*, 2004).

To date, around 20 connexin genes have been identified in humans (Willecke, 2002) and the respective proteins have been described using either their sequence homology or their molecular mass, with the latter classification being the most widely used (Evans and Martin, 2002). Hence, the 43 kDa connexin protein is referred to as connexin 43 (Cx43). Most tissues express more than one connexin isotype. Connexons may be composed of six identical connexin subunits (homomeric) or more than one connexin isotype (heteromeric). Accordingly, two identical connexons can form a homotypic channel whereas a heterotypic channel is generated by two connexons having different connexin isotypes (Wei *et al.*, 2004).

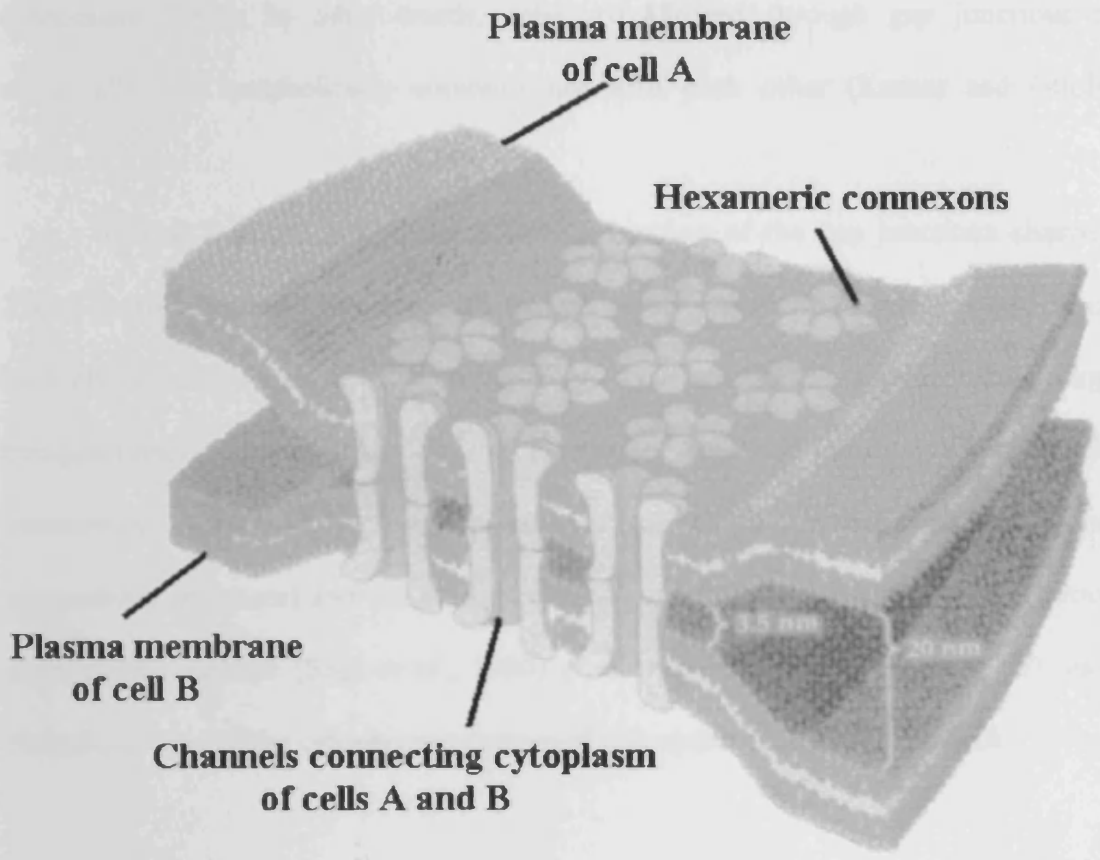

Figure 1.6: Model of a gap junction. The hexameric connexin subunits in each of the plasma membranes dock to generate the gap junction channel connecting the two cytoplasmic compartments (Evans and Martin, 2002).

1.6.2 Physiological functions of gap junctions

The physiological importance of gap junctions is seen in: i) the rapid transmission of action potentials in heart and in neuronal tissue via so-called electric synapses (Simon *et al.*, 1998), ii) the diffusion of metabolites and nutrients such as nucleotides and glucose, which depend on the channel type (*i.e.* Cx32 channels are more permeable to adenosine than Cx43 channels, while ATP passes more readily through Cx43 channels (Goldberg *et al.*, 2002)), iii) the diffusion of second messengers, such as Ca^{2+}, inositol tris phosphate (IP3) and cyclin nucleotides

(Giepmans, 2004). In other words, cells are allowed through gap junctions to electrically and metabolically communicate with each other (Kumar and Gilula, 1996).

Several factors regulate the differential gating of the gap junctions channel. These factors include the intracellular pH (gap junction channels close upon intracellular acidification), the voltage of the membrane of the cells (large transjunctional voltages result in the closure of the gap junction channel), the intracellular levels of Ca^{2+} (upon intracellular Ca^{2+} decrease, gap junctional permeability increases) and the phosphorylation state of the connexins (gap junction permeability increase (Saez *et al.*, 1990) or decrease (Berthoud *et al.*, 1997) upon phosphorylation of the cytoplasmic domain of connexins have been reported).

1.6.3 Functional roles of gap junctions

Gap junction communication between cells plays a role in embryogenesis and development as well as in disease (Levin, 2001; Evans and Martin, 2002; Vine and Bertram, 2003; Wei *et al.*, 2004).

The patterning of the heart during development (Mercola, 1999) is an example. Several members of the connexin family are expressed in the mammalian heart, including Cx37, Cx43 and Cx45 (Levin, 2001). Cx45 mutant mice exhibit an endocardial cushion defect due to an impairment of the epithelial-mesenchymal transformation of the cardiac endothelium (Kumai *et al.*, 2000), while Cx43 mutant mice exhibit a blockage of the right ventricular outflow tract (Ewart *et al.*, 1997). The patterning of the vertebrate limb is another example; gap junction communication serves an important role in the early events of the precartilaginous mesenchymal

condensation process that determine the morphology of the limb (Hall and Miyake, 2000), as it will be in detail discussed in Chapter 5.

Connexin mutations account for a wide spectrum of human diseases. Mutations in Cx32 are associated with Charcot Marie-Tooth-X disease, a disease resulting in progressive degeneration of peripheral nerves caused by a defect in Schwann cells (Bergoffen *et al.*, 1993). Mutations in Cx26 account for about half of the cases of inherited deafness (Steel and Kros, 2001) as well as for many skin disorders (Richard, 2003), while mutations in Cx46 and Cx50 are linked with cataract abnormalities (Pal *et al.*, 2000). Finally, low expression of connexins has been postulated as an independent marker for breast cancer tumours (Laird *et al.*, 1999), lung and renal carcinomas (Vine and Bertram, 2002), skin carcinoma (Stuhlmann *et al.*, 2003) and prostate cancer tumours (Vidulescu *et al.*, 2004).

1.6.4 Gap junctions and cell-cell adhesion

Strong association between members of the cadherin-catenin complex and gap junctions has been reported, as cadherin-mediated cell-cell adhesion has been reported to be a prerequisite for formation of gap junctions (Zuppinger *et al.*, 2000; Giepmans, 2004). Hernandez-Blasquez et al. (2001) reported that gap junctional communication in murine skin papilloma cells is dependent on E-cadherin that is in turn closely associated with actin fibers. Similarly, blockage of N-cadherin with A-CAM antibodies prevented adherens and gap junctions' formation on Novikoff cells (Meyer *et al.*, 1992). E-cadherin and α-catenin are co-localised with newly formed junctions, which might reflect an adherens junction focus that primes gap junction formation (Fujimoto *et al.*, 1997). Another study also suggests that α-catenin is important for Cx43 trafficking and assembly (Govindarajan *et al.*, 2002). Given than N-cadherin and

catenins are co-assembled in the endoplasmic reticulum/Golgi compartments (Wahl *et al.*, 2003), this raises the possibility that Cx43 is assembled as part of a multi-protein complex that may coordinately regulate adherens and gap junction assembly in the form of a dynamic cross talk (Wei *et al.*, 2004).

1.7 Tight Junctions

Tight junctions (Sec. 1.1; Fig. 1.1) function to fuse the lateral margins of contiguous epithelial and endothelial cell together and thereby form a continuous selective permeability barrier between these cells and the extracellular space (Denker and Nigam, 1998). In addition, tight junctions maintain the strict organisation of the plasma membrane in an apical and basolateral compartment (Giepmans, 2004). The major proteins of the tight junctions are occludin, zona occludens 1 and 2 (ZO-1, ZO-2) and the claudin family of proteins (Schneeberger and Lynch, 2004) (Fig. 1.1). However, tight junctions have not been examined in the present study, therefore further reference will be omitted.

1.8 Methods for studying cell-cell interactions

A variety of methods reported in the literature have been used to study cell-cell interactions. Biological methods have been more widely and traditionally used, whereas recently, physical approaches have been developed. In the following, a distinction between the biological methods and assays, and the physical techniques will be made.

1.8.1 Biological methods

The most widely used method for assaying cell-cell interactions involves the 2-dimensional monolayer culture system. Cells plated in a tissue culture dish adhere to the substratum, proliferate and finally cover the entire area of the dish. Each cell is then in contact with adjacent cells and in many cases forms adhesive and communicating junctions. A variation of the monolayer culture system is the 'calcium-switch' approach, first presented by Hennings and Holbrook (1983), and subsequently used by various investigators (Mary *et al.*, 2002; Braga, 2002). This approach has contributed significantly to the extraction of temporal information on cell-cell adhesion, as cells are rapidly and synchronously stimulated to initiate cell-cell contact upon transfer to complete growth medium; however, the cells are on coverslips when undergoing the switch process (Freshney, 2000; Dihne *et al.*, 2003) so that cell-cell interactions are not free of the influence of the solid substratum.

The effect of the solid substratum on cell interactions is overcome, for one of the partner cells, by the donor-acceptor (Ko *et al.*, 2000) or cell settlement (Becker and Green, 2002) methods. In this approach, a cell population (donor) is overlaid on another one (acceptor) already grown as a monolayer on a substratum.

Micromass and pellet cultures, developed around 1977 (Ahrens *et al.*, 1977) provide a scaffold-free 3-dimensional cell culture environment, a situation particularly useful for the growth of cells whose differentiation status is lost when plated as 2-dimensional monolayers, as for example, for chondrocytes, or for the mimicking of developmental processes, such as chondrogenesis. Cells in micromass and pellet cultures may not be disturbed for analysis within an hour of seeding, in the sense that 60 min is the period 'allowed for adhesion to occur' prior to initiating studies of micromass properties (Coelho and Kosher, 1991).

Other approaches to overcome the effects of rigid substrata include growth of cells in agar, agarose or Methocell (agar and agarose are gels, while Methocell is a high-viscocity sol) (Freshney, 2000). Growth of cells in microcarriers, such as polystyrene, Sephadex, collagen, gelatine or alginate beads has also been used for the propagation of cells in suspension. Difficulties associated with temporal monitoring of cell-cell adhesion free in suspension include identifying cells that are about to interact and maintaining those cells in focus for a significant period of time.

This work explores a technique that allows cells to interact freely in suspension while remaining accessible to continuous microscopic monitoring.

1.8.2 Physical techniques

Physical methods of manipulating suspended cells (or microparticles) at single-particle microscopic resolution include optical (Grier, 2003), dielectrophoretic (Heida *et al.* 2002) and ultrasonic (Miller 1976; Wu 1991; Spengler and Coakley 2003; Coakley *et al.*, 2004) traps.

Optical traps, with their unavoidably small focal-volumes, have contributed significantly to single cell, subcellular organelle and molecular studies. A multiple optical trap that increases the number of cells that can be manipulated at once has been created by forming light intensity patterns in a sample (Grier, 2003). One such approach, where optical tweezers trap a number of particles by dwelling briefly on each one before moving on to the next (Mio *et al.*, 2001) is limited (Grier, 2003) by the time required to reposition each of the multiple wandering objects. Holographic optical tweezers can transfer arrays of particles along computer-controlled trajectories (Grier, 2003). However, these optical fields do not act as sinks towards which many

cells migrate and aggregate, nor can they simultaneously arrange a collection of cells in close (*ca.* 50 nm proximity) for non-intrusive study of cell interactions.

In contrast, cells can move spontaneously into a microscope-focused concentration region in acoustic or dielectrophoretic traps. Dielectrophoresis is the phenomenon whereby neutral particles in a non-uniform electric field experience net force directed towards (positive dielectrophoresis) or away (negative dielectrophoresis) from locations of high field intensity according to the (frequency dependent) physical properties of particles and medium. Neuronal cell clusters have been formed on electrode surfaces by positive dielectrophoresis to provide an interface between the cell network and an external electric circuit for sensing or for stimulation (Heida *et al.*, 2002). Single cells have been levitated and observed in a 3-D negative dielectrophoresis trap of electrode separation of the order of 100 μm (Muller *et al.*, 1999). This small-scale constraint avoids undesirable temperature rises that accompany electrolytic physiological cell suspending-phase exposure to alternating current (a.c.) fields (Muller *et al.*, 1999). Difficulties can also arise in aligning electrodes in such small 3-D negative dielectrophoretic traps (Manaresi *et al.*, 2003). An 8×8 mm^2 chip has recently been described that offers over 10^4 individual traps as part of an approach to the "essential manipulation requirement for the investigation of complex interactions among cells" (Manaresi *et al.*, 2003). Single 50 μm diameter latex particles were trapped in non-contacting arrays in this system while discrete aggregates of the smaller (5 μm) yeast, *Saccharomyces cerevisiae*, were formed in adjacent traps (Manaresi *et al.*, 2003). It may be significant (in the context of heating effect) that the exemplar cells were suspended in low-conductivity sugar solution rather than in the physiological media that are more appropriate for animal cell studies.

An ultrasound trap on the other hand, can form and levitate aggregates of cells as 2-D or 3-D structures in suspension, free of the substratum effects that are known to influence cell properties (Redey *et al.*, 2000) and in the focal plane of a light microscope (Spengler and Coakley, 2003; Coakley *et al.*, 2004).

In the following, the experimental phenomena observed in an ultrasound trap will be described followed by an overview of the state of research on ultrasound.

1.9 Phenomena and theoretical background

1.9.1 Principle phenomenon of particle aggregation in USW

The particle aggregation process in a USW is illustrated diagrammatically in Fig. 1.7a (elevation view), b (plan view). A particle suspension is placed in a container that has an ultrasound transducer at one end and a reflector at the opposite end to produce a standing wave. Only one half wavelength is shown in Fig. 1.7a for reasons of clarity. However, the following description also applies to each half wavelength of multi-wavelength systems. Homogeneously distributed particles (Fig. 1.7a, i) are first driven into the pressure nodes within a time of the order of ~1s (Fig. 1.7a, ii), depending on the particle properties and the operating conditions. Over a longer time (of the order of a few seconds to minutes) the particles move within the nodal plane to finally concentrate into aggregates (Fig. 1.7a, iii; b).

Multi-wavelength systems form aggregates at essentially the same lateral position in each node plane so that the concentrated particle clumps appear as columns of clumps punctuated at each half wavelength. In megahertz frequency systems multiple columns are formed in the standing wave fields because of the local pressure maxima that arise across the face of a transducer when its diameter is many times the acoustic wavelength (Whitworth and Coakley, 1992).

1.9.2 Theory of the direct acoustic radiation force

A discontinuity in the propagating phase, for example a particle, cell, droplet or bubble, acquires a position-dependent acoustic potential energy by virtue of being in the sound field (Whitworth and Coakley, 1992). Suspended particles tend therefore to move towards and concentrate at positions of minimum acoustic potential energy. Gor'kov (1962) formulated an expression for the acoustic potential energy of a particle suspended in a sound field. The acoustic radiation force on the particle is derived from this potential by determining its negative gradient. The approach is valid for arbitrary acoustical fields, a non-viscous fluid and compressible spherical particles, which are much smaller than the wavelength.

For a plane harmonic standing wave the axial radiation force DRF_a that drives spheres of volume V, density ρ_p and compressibility β_p in an axial direction, *i.e.* to a node or antinode plane, in a liquid of density ρ_o and compressibility β_o, is given by

$$DRF_a = -\frac{\pi P_o^2 V \beta_o}{2\lambda} \cdot \phi(\beta,\rho) \cdot \sin\left(\frac{4\pi z}{\lambda}\right) \qquad (1.1)$$

where P_o is the sound pressure amplitude, z is distance from a pressure node, and λ is the wavelength at the driving frequency in the suspending phase. The contrast factor $\varphi(\beta,\rho)$ in Equation 1.1 is

$$\phi(\beta,\rho) = \frac{(5\rho_p - 2\rho_o)}{(2\rho_p + \rho_o)} - \frac{\beta_p}{\beta_o} \qquad (1.2)$$

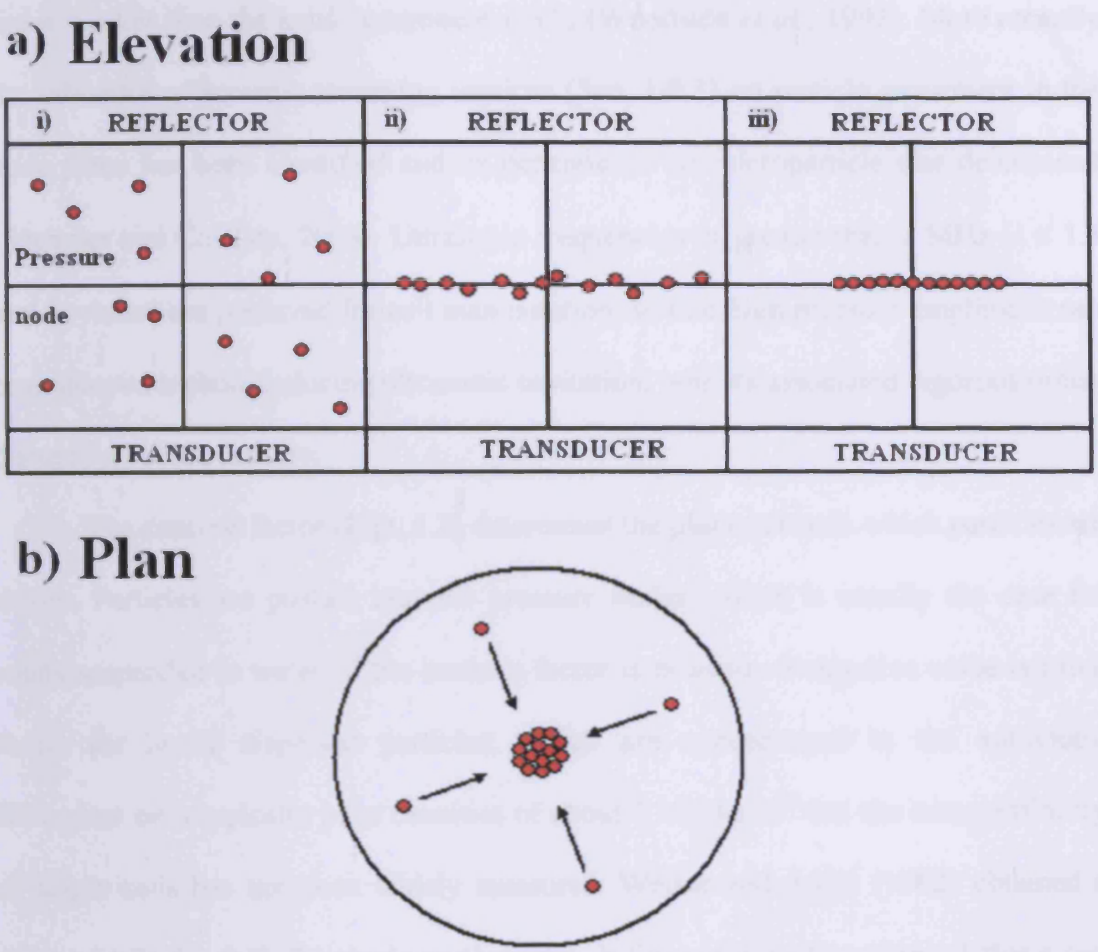

Figure 1.7: Schematic diagram of the temporal progression a) elevation and b) plan (from time zero (a, i) to less than 1s (a, ii) to 10s (a, iii) of seconds) of aggregation of suspended particles in a single pressure node half-wavelength ultrasound trap.

DRF_a is dependent on both the properties of the sound field (P_0, and λ), which are established by the experimenter, and the properties of the particle, *i.e.* its volume and its density and compressibility relative to those of the suspending medium. The lateral component of the radiation force (DRF_l) arising, in most practical non-ideal 'plane' wave situations, from inhomogeneities in the pressure distribution in the nominally 'nodal' pressure plane, is responsible for the concentration of particles and cells into aggregates. The lateral component of the total radiation force on a particle is about 100

times weaker than the axial component DRF_a (Woodside *et al.*, 1997). More recently the influence of acoustic streaming vortices (Sec. 1.9.3) on particle movement in the node plane has been identified and its dependence on microparticle size determined (Spengler and Coakley, 2003). Ultrasonic frequencies of greater than 1 MHz (λ < 1.5 mm in water) are preferred for cell manipulation, so that high pressure amplitudes can be employed without inducing ultrasonic cavitation, with its associated vigorous order-disrupting bubble activity.

The contrast factor (Eqn. 1.2) determines the plane towards which particles are driven. Particles are pushed into the pressure nodes, which is usually the case for solids suspended in water, if the contrast factor is positive. A negative value is often found for liquid dispersed particles, which are concentrated in the antinodes. Biological cells typically have densities of about 1,100 kg m^{-3} but the compressibility of single cells has not been widely measured. Weiser and Apfel (1982) obtained a value of 0.76 for $\beta_p \beta_o$ for single erythrocytes. It follows from Equation 1.1 that a cell in a 3 MHz standing wave of peak pressure amplitude 0.5 MPa will experience a maximum force 40 times that of gravity as it travels the short distance ($<\lambda/4$ = 0.12 mm) towards the nearest pressure node.

1.9.3 Acoustic and convective streaming

Flows that are either environmental or acoustic in origin will exert a drag on particles suspended in a resonator. Grundy (1994) showed that background flow due to environmental temperature gradients increases from about 5 to 250 μm/s when container dimensions are increased from millimetre to centimetre scales. Acoustically generated temperature gradients, due to transducer heating, can drive large scale streaming in systems where the transducer and suspension are physically close

(Hawkes *et al.*, 1998b). Because of the above considerations, particular attention is paid to minimising acoustic streaming and temperature-gradient flows in ultrasonic particle/cell separation systems through attention to the quality of the acoustic resonance (Spengler and Jekel, 2000; Gaida *et al.*, 1996; Lee and Peng, 2005).

Acoustic streaming can manifest itself as container scale Eckart, wavelength scale Rayleigh and boundary layer scale Schlichting streaming (Zarembo, 1971; Spengler *et al.*, 2003). An overview of the different types of streaming is given in Table 1.1. Real, as distinct from ideal, standing wave systems consist, because of acoustic absorption in the sample, of travelling and standing wave components. Energy deposition in the sample through attenuation of the travelling wave component generates container scale flows that are known as Eckart or 'quartz wind' streaming. The induction of order in a suspension (as in Fig. 1.6iii) requires that DRF_a (Eqn. 1.1) be capable of holding particle/cells against such background streaming. Where the drag is large it can influence particle aggregation by sweeping single particles away or limiting the size of a growing aggregate by drawing particles off its perimeter. However, at the operational conditions of a short pathlength acoustic trap employed in the present study, large-scale streaming can be ruled out and will not be considered further.

Rayleigh streaming occurs generally due to energy dissipation in the viscous boundary layer of the waveguide and other solid surfaces present. Rayleigh (1945) showed that where a plane standing wave is situated between parallel walls a distribution of vortices of thickness $\lambda/4$ in the direction normal to the nodal planes results. Schlichting microstreaming is essentially a vortex flow inside the viscous boundary. It has the same origin as outside-boundary Rayleigh streaming discussed above and can be seen as a near-wall counter rotating flow to the Rayleigh vortices.

The vortices extend about twice the boundary layer thickness, defined as $\delta = [\nu/(\pi f)]^{0.5}$ where ν is kinematic viscosity and f is frequency, from a wall. The value of δ, for typical particle manipulation studies, *e.g.* 2 MHz in water, is about 0.27 μm. Control of the inhibitory influence of acoustically induced streaming on particle aggregate formation in large sample volumes has been addressed by Spengler and Jekel (2000), while the more complex roles of Rayleigh streaming on particle movement and aggregation have been established for short, sub-wavelength, acoustic pathlength chambers (Spengler *et al.*, 2003; Kuznetsova and Coakley, 2004).

Table 1.1: Types, wavelength scales, origins and effects on USW particle and cell manipulation of the different streaming types (Spengler, 2002).

Streaming type	***Scale***	***Origin***	***Effect***
Eckart/ Quartz wind	$>>\lambda$	Bulk energy absorption	Fluid circulation on container size scale throughout a poly-wavelength system
Thermal convection	$>>\lambda$		
Rayleigh	$\approx \lambda$	Losses in viscous boundary layers, inhomogeneous	Circulations between nodal planes
Schlichting	$<<\lambda$	acoustic velocity distribution	High shear rate streaming in narrow boundary layer

1.9.4 Particle-particle interaction forces

Particles present in the sound wave act as wave scattering obstacles, which cause additional radiation force fields in their proximity. These density- and

compressibility-dependent secondary acoustic interaction forces, known as Bjerknes forces influence the attraction between particles that have been concentrated by the radiation force and thus are of importance only when the particles are already close together (usually less than one particle diameter separation) (Nyborg, 1978). Particles, which are aligned perpendicular to the sound axis, are attracted to each other. Those aligned on an axis parallel to the sound propagation direction experience a repulsive force (Nyborg, 1978). The Bjerknes interaction forces increase with particle diameter.

The density-dependent interactive force between two rigid spheres of equal size may be described (Thomas *et al.*, 1999) by radial-coordinate components $F_{\rho r}$ and $F_{\rho\varphi}$, in the direction of the line connecting the particle centre and in the direction of the angle φ between the lines connecting the particle centre and the direction of fluid movement in the absence of particles, respectively. The forces are given by (Nyborg, 1978) as:

$$F_{\rho r} = \frac{2\pi(\rho_p - \rho_o)^2\left(\frac{P_o}{\rho_o c_o}\right)^2 r^6(3\cos^2\varphi - 1)}{[3\rho_o(2r+h)^4]} \tag{1.3}$$

$$F_{\rho\varphi} = \frac{2\pi(\rho_p - \rho_o)^2\left(\frac{P_o}{\rho_o c_o}\right)^2 r^6(\sin 2\phi)}{[3\rho_o(2r+h)^4]} \tag{1.4}$$

For two adjacent particles in the pressure node plane ($\varphi = \pi/2$), $F_{\rho r}$ is zero while $F_{\rho\varphi}$ is attractive and equal to $-2\pi\ (\rho_p - \rho_0)^2\ (P_0/\rho_0 c_0)\ 2r^6 / [3\rho_0\ (2r + h)^4]$. For an exemplar particle of diameter of 25 μm, r is of the order of 10 μm and h, for typical surface separations, is taken to be of the order of 10 nm. $F_{\rho r}$ may then be approximated by:

$$F_{\rho_r} = \frac{2\pi(\rho_p - \rho_o)^2 \left(\frac{P_o}{\rho_o c_o} \right)^2 r^6}{3\rho_o (2r)^4} \qquad (1.5)$$

$F_{\rho r}$ is equal to 7.2 pN when $2r$ = 25 μm, P_0 = 1 MPa, ρ_p = 1056 kg m^{-3} and c_0 = 1480 m s^{-1}. The attractive compressibility-dependent interparticle force F_β on spherical particles suspended in a standing wave decreases to zero as particles reach the pressure node (Doinikov and Zavtrak, 1997).

The extent to which ultrasonic interaction forces might modify the probability that particles and cells will stick on contact is investigated in Chapter 2. The ultrasonic interaction forces will be then compared with the influence of factors such as the van der Waals interaction and electrostatic repulsion (Chap. 2; Sec. 2.1.1.1) normally governing microparticle interactions.

1.10 An overview of the research on ultrasonic standing waves (USW)

1.10.1 Fundamental studies on acoustic standing waves

Acoustic standing waves have been investigated since about 1868 (Kundt, 1868; Kundt and Lehmann, 1874). These authors exploited the principal effect of acoustic standing waves in aerosols and aqueous suspensions; they first reported a structuring effect on dispersions in an acoustic standing wave, established by the interference of an emitted and a reflected wave. The same authors also observed that particles could be brought into contact, when pushed into the pressure nodal planes

(periodically located half a wavelength apart from each other) of the standing wave (Kundt and Lehmann, 1874).

Early work on ultrasonic manipulation of particles in suspension was carried out by Söllner and Bondy (1936). The authors reported sonication experiments with an emulsion of toluene and a suspension of quartz. They observed that the quartz particles (higher density than the dispersion medium) were driven into planes separated by half a wavelength, whereas the toluene globules (lower density than the suspending phase) were accumulated into planes separated by a quarter wavelength from the bands formed by the quartz particles. This investigation also introduced the influence of the particle diameter on the aggregation phenomenon (larger particles moved considerably faster into the nodal planes than smaller ones), in line with the theory of the axial acoustic radiation force (DRF_a) presented by King (1935). Fundamental studies on acoustic streaming (the major effect disturbing particle and cell aggregation) were proceeding in parallel (Rayleigh, 1945; Schlichting, 1932; Eckart, 1948).

However, it was in 1971 (Dyson *et al.*, 1971) that the ultrasonic manipulation of cells was first reported. The authors were investigating the effects of low intensity ultrasound on blood circulation in living tissues of chick embryos, as they were primary concerned with safety issues of diagnostic and therapeutic ultrasound. Aggregation and blood flow cessation was observed under a 3 MHz sonication.

Fundamental studies on aggregation and particle behaviour in USW, stimulated by the work of Dyson et al. (1971), were carried out by a number of authors (Gould and Coakley, 1974; ter Haar and Wyard, 1978; Coakley *et al.*, 1993), who demonstrated the banding phenomenon of particles and cells in megahertz frequency ultrasonic standing wave fields. Theoretical contributions investigated the

influence of the DRF_a on suspended particles and considered the influence of Brownian motion (Higashitani *et al.*, 1981) and the DRF_a distribution in USW fields of different geometries (Barmatz and Collas, 1985). The ultrasonically induced particle-particle interaction mechanisms, which contribute to particle aggregation, have also been investigated (ter Haar and Wyard, 1978; Weiser *et al.*, 1984; Coakley *et al.*, 1989). The role of acoustically induced streaming on particle manipulation in USW was also addressed (Coakley *et al.*, 1989; Whitworth and Coakley, 1992). Many recent contributions have brought further insights into the complex field of USSW manipulation of disperse systems. Particle transportation and concentration in a stationary field was reported by Whitworth and Coakley (1992), who were in particular interested in the existence and position of particle columns, employing a radiation force in the direction perpendicular to the sound beam axis. A theory for the transport of particles in a pseudo-standing wave field was developed by Petersson (1986) and Whitworth et al. (1991). Measurements of the DRF_a (Yasuda, 1999) and DRF_l (Tuziuti *et al.*, 1999, Woodside *et al.*, 1997) have also been reported, while Doinikov (1994) calculated the DRF_a exerted by a spherical sound field.

1.10.2 USW in phase separation application

Suspensions have been acoustically clarified in batch (Cousins *et al.*, 2000) and flow (Gröschl *et al.*, 1998; Hwang and Koo, 2003) systems by sedimentation and by electronic modulation of the sound field (Whitworth *et al.*, 1991). In sedimentation-separation resonators the transducer, reflector planes, as well as the resulting pressure nodal planes are usually vertical. The aggregates formed settle considerably faster than would single cells or particles. In flow ultrasonic sedimentation filters the suspension enters the filter below the standing wave field and the particles are trapped in the nodal

planes as the suspension flows upwards between the transducer and reflector. Acoustic aggregation proceeds until the clumps become too heavy and sediment within the nodal planes, remaining essentially intact as they drop below the inlet level (Gaida *et al.*, 1996; Groschl *et al.*, 1998; Benes *et al.*, 2001).

Suspensions of interest have been a variety of particle model systems such as latex particles (Hawkes *et al.*, 1998a, b), microorganisms (Limaye and Coakley, 1998) and blood (Cousins et al., 2000). Ultrasonic phase separations have found interest in the area of water treatment and environmental protection (~150 l/h of particle containing suspensions are treated) (Spengler *et al.*, 2001), as well as in small scale analytical separations, where small volume samples from *e.g.* ecological, clinical or biotechnological environments are usually analysed. Approaches such as the use of small standing wave filters (Mandralis and Feke, 1993), microfabricated microfluidic systems (Harris *et al.*, 2004) and microchannels in conjunction with laminar flow (Hawkes *et al.*, 2004) have been developed.

Other applications of USSW for phase separation processes include the development of an immunosensor for the detection of pathogenic bacteria such as *Bacillus anthracis* (Hawkes *et al.*, 2004; Martin *et al.*, 2005) and large pore filters for the retention of mammalian cells in an acoustically driven polymer mesh without compromising cell viability (Gupta and Feke, 1998; Wang *et al.*, 2004).

Calculations of the overall costs of standing wave processes in comparison to established separation technologies have yet to be carried out. However, the cost issue is of minor importance in biotechnology where sedimentation ultrasonic filters for recovery of the high value molecular biology and pharmaceutical products from perfusion cell cultures are now in commercial use (Durrschmid *et al.*, 2003; Shirgaonkar *et al.*, 2004) and can operate at flow through rates of 200 l/day (Gorenflo

et al., 2002). Cost is also not a central issue when small samples are processed for assay and 'information' about a larger system is the high-value 'product'.

1.10.3 USW in molecular and cell diagnostics

The principal of destabilisation of particle suspensions by introducing an attractive interparticle force (arising from macromolecular cross-linking) has long been exploited in immuno-diagnostic assays. The general approach employs commercially available stable suspensions of antibody-coated micron-scale latex particles. Batches of the coating antibody (a molecule that interacts specifically with the test molecule; the antigen) are initially isolated from the plasma of an animal that had been injected with the antigen. The antigen can be in solution or can be a surface molecule acting as a marker for the presence of a virus or bacterium in a clinical, industrial or environmental sample. The basic latex agglutination test (LAT) is carried out by mixing droplets of a test sample and the latex suspension on a solid surface, the coated beads rapidly crosslink to give latex aggregates of a size visible to the unaided eye in the presence of appropriate concentrations of test antigen. Latex beads from samples free of or low in antigen content sediment without forming visible aggregates. The LAT test is simple and rapid but is often limited in sensitivity. Grundy et al. (1993) improved the rate (and therefore the sensitivity in a fixed time) of the agglutination process by rapidly concentrating antibody-coated latex beads in a 30 µl sample of test protein in a capillary on the axis of a cylindrical ultrasonic standing wave system. Following sonication the sample was ejected onto a standard LAT test card. The ultrasound had increased the sensitivity ×256 compared to the test card control. Ultrasound aggregation of test particles as above decreased the conventional LAT technique concentration limit for antigen detection by factors ranging from 500-

fold for fungal antigen, 64-fold for bacterial polysaccharide, 16-fold for viral antigen (Ellis and Sobanski, 2000; Jenkins *et al.*, 1997).

For the case where a bacterial cell is the test analyte, Bhaskar et al. (2002) reported an increase from 94% to 97% in ultrasound-assisted detection of *Mycobacterium tuberculosis*. Particular attention has been given to ultrasound enhancement of the LAT detection of meningitis causative bacteria. It was shown that the 10% positive identification of pathogens in clinically confirmed patient blood samples was increased to 50% in the cylindrical transducer system described, for molecular antigen detection, above (Gray *et al.*, 1999). A study of samples from clinically-confirmed patients showed that the detected antigen level correlated with the severity of the clinical outcome of infection (Gray *et al.*, 1999). The technique has been developed to a stage, where it is seen as a reliable, cheap and rapid test complementing the timely and cost effective polymerase chain reaction (PCR) technique (Gray *et al.*, 1999). However, more recent work confirmed the high detection rate of USELAT device but found that its positive identification was lower than with PCR and did not give complementary support for samples that were in doubt from PCR analysis (Porritt *et al.*, 2003). The authors concluded that, in the context of meningococcal detection, the technique had application in environments without PCR facilities and noted that a degree of technical expertise and familiarity was required to apply the USELAT technique independently.

Ultrasound standing waves have also been combined with fluorescence measurement in a bacterial detection format (Zhou *et al.*, 1998). In this case, a 10-fold increase in the detection level of *Salmonella typhimurium* was reported. More recently, Wiklund et al. (2004) exploited the standing wave concentration of hormone-

trapping coated latex with the contrast enhancement of confocal laser scanning microscopy to increase the sensitivity of the hormone assay by 100 fold.

1.11 Aims of this study

The overall aim of the work described in this thesis is to determine the temporal progression of cell-cell interactions from the early stages of receptor engagement to cytoskeletal organisation in a range of cell systems using a 2-D ultrasound standing wave trap. The specific objectives of the individual Chapters are presented below.

Chapter 2 aims to characterise the morphology of 2-D polystyrene latex particle aggregates formed out of suspensions with different stability in the ultrasound trap. The objective is to set the framework for the establishment of the particle-particle interaction parameters defining aggregate morphology. Additionally, the suitability of various image analysis techniques for the characterisation of mammalian cell aggregates described in the following chapters is determined.

Chapter 3 aims to examine how the ultrasound trap restrains a cell and how the physical forces might influence the cell directly or through changing its environment. The objective is to establish the suitability of the ultrasound trap as a non-invasive technique for the study of cell-cell interactions.

Chapters 4 and 5 aim to determine the timing of appearance of the molecular consequences following cell-cell interactions with particular reference to cell adhesion and communication events, while the final experimental chapter (Chap. 6) seeks to establish the potential of the ultrasound trap in the area of cancer biology.

Further promising applications of the ultrasound trap as well as aspects of the cell-cell adhesion processes that could be further clarified by means of ultrasound facilitated cell adhesion are described in Chapter 7 and will end this report.

Chapter 2

Characterisation of the morphology of 2-D particle aggregates in different electrolyte concentrations in an ultrasound trap

2.1 Introduction

Particle aggregation in colloidal suspensions is an important component of many chemical, environmental, biotechnological, pharmaceutical and food industry processes. The growth of 3-dimensional (3-D) aggregates is usually characterised by population light scattering parameters (Gregory, 2004). The insights on coagulation kinetics, internal dynamics and annealing processes, to be obtained from 2-dimensional (2-D) systems have been recognised for many years. Hurd and Schaefer (1985) developed an optical microscopy approach for the aggregation of microparticles trapped by surface tension at an air-water interface. The authors also pointed out that the interpretation of image processing data from 2-D images was free of the ambiguities, such as projection of a 3-D object onto a 2-D surface, inherent in many other experiments. This optical microscopy interfacial layer approach has since been applied extensively (Hidalgo-Alvarez *et al.*, 1996; Ghezzi *et al.*, 2001). It is known that full description of 2-D aggregate formation at interfaces requires modification of expressions for the inter-particle van der Waals, electrostatic and structural forces compared to those for particles in bulk suspension (Hidalgo-Alvarez *et al.*, 1996).

Spengler and Coakley (2003) introduced a new approach that produces 2-D aggregates in the bulk phase rather than at an air-water interface. This technique avoids any requirement for modification of interaction terms or consideration of meniscus or capillary effects. The approach also opens up a method for study of biological cell aggregation (Coakley *et al.*, 2004). The technique (Spengler and Coakley, 2003) employs an ultrasound standing wave trap that has a single half wavelength acoustic pathlength at the transducer driving frequency and an epi-fluorescence microscope to optically investigate aggregate formation. Spengler et al. (2003) showed that aggregates of 25, 10 and 5 μm diameter latex in distilled water formed closely packed aggregates that reformed to give an orderly internal structure when joined by new clusters, whereas 25 and 5 μm latex particles in 10 mM $CaCl_2$ formed open dendritic aggregates.

The present Chapter considers the fundamental properties of aggregate development and aggregate morphology characterisation in an ultrasound trap from a particle perspective to subsequently explore in the following Chapters (Chaps. 3-6) the biological consequences of USW-facilitated cell-cell interactions. More specifically, the effect of a wide range of $CaCl_2$ concentrations on the growth of aggregates of 25 μm latex particles is principally investigated with the purpose to identify the transition phase from a highly ordered system to a disordered one. Macroscopic observation of the aggregation of 25 μm latex particles suspensions at various ionic strengths has been compared with established theoretical models for aggregate growth. It was seen that both aggregate structure and the behaviour of the aggregates during sedimentation was significantly different. The findings were qualitatively in agreement with various theoretical approaches to suspension stability, aggregation kinetics and aggregate strength.

The chapter also explored a range of microscope image analysis techniques to quantify differences in aggregate structure with change in suspension stability (microscopic analysis). A standard perimeter fractal dimension analysis characterised the aggregates well. Fast Fourier Transform (Issa *et al.*, 2003) and void analysis (Ashmawi and Zirky, 2003) have been employed previously to characterise 2-D surfaces. The sensitivities of these techniques to morphology change at different stages of the range of electrolyte concentration are compared here with that of the perimeter fractal dimension approach. Attention was paid both to detecting early transitions from the orderly pattern of the closely packed aggregates at low [$CaCl_2$] and the extent of 'openness' of the aggregates at high [$CaCl_2$].

The effect of a number of physical mechanisms on aggregation, like the *DRF* (axial and lateral) and acoustic micro-streaming, as well as the effect of inter-particle (also called colloidal) forces like electrostatic repulsion and van der Waals interaction will be introduced here to the degree necessary for discussion of the results presented in this chapter.

2.1.1 Theory on suspension stability and particle aggregation

2.1.1.1 The DLVO theory of colloidal stability

The classic Derjaguin-Landau-Verwey-Overbeek (DLVO) theory (initials corresponding to its originators) states that the inter-particle potential contains two contributions: i) the electro-static repulsion due to the negatively charged particle surfaces and ii) the van der Waals attraction caused by dipole interaction of the electron clouds surrounding the particle surface (Jones, 1975). The unequal concentration of the positive and negative ions at the charged surface, is responsible for the existence of a diffuse electrical double layer. This layer becomes thinner the

higher the concentration of the counter ions in the suspension is. As a measure of the thickness of the electrical double layer the factor κ^{-1} (Debye length) is considered, which according to the Goüy-Chapman theory (Jones, 1975) is dependent on the ion concentration in the solution (n) and the valence of the ions (u). The smaller n and u are, the larger the electrical potential is and the greater the thickness of the electrical double layer will be. It is the interaction between the double layers that prevents particles from approaching each other; as a result the van der Waals can not counterbalance the electric repulsion and particles keep apart.

Particle aggregation though, can be facilitated by means of double layer compression (reduction of the double layer thickness). Increasing the concentration (or the valence) of the counter ions will result in a reduction of the magnitude of the electrical potential and the particles will be allowed to adhere.

The Schulze-Hardy rule of thumb is thus introduced; it is an extension of the DLVO theory and states that the critical coagulation concentration (ccc) of particles depends only on the concentration and valence of the ion with charge opposite that of the surface charge (Caplan *et al.*, 2000). The relation between the effectiveness of mono-, di- and tri-valent ions is 1: 50: 10,000. This simply means that one Ca^{+2} ion is as affective as 50 Na^{+}, whereas one Fe^{+3} ion is as effective as 200 Ca^{+2} ions.

The interaction of particles is also affected by short-range effects (non-DLVO forces). These comprise hydration forces, hydrophobic interactions, steric repulsion and polymer bridging. However, because electrostatic repulsion and van der Waals attraction are the controlling parameters here, the above forces shall not be considered further.

Particles or cells in order to be considered as colloidal should, by definition, have at least one dimension in the size of 1 μm or less. This condition is not met for

the particles and cells investigated in this thesis; however, the principles underlying the DLVO give good insight for the non-colloidal systems of interest here.

2.1.1.2Aggregation kinetics

The kinetics of the aggregation phenomenon and the evolution of the particle distribution over time were introduced by von Smoluchowski (1918). The Smoluchowski equation describes kinetics of irreversible aggregation in terms of the reaction probability between clusters. The time evolution of the number concentration n_k of a particle of mass k can be expressed as:

$$\frac{dn_k}{d_t} = \frac{1}{2}\alpha \sum_{i+j=k} \beta(i,j) n_i n_k - \alpha \sum_i \beta(i,k) n_i n_k \qquad (2.1)$$

The term dn_k/dt represents the rate of formation of mass k aggregates; α is the collision efficiency, simply referring to the strength of 'stickiness' of the particles. The terms β (i, j) and β (i, k) are called collision efficiency frequency kernels or collision probability factors. The three principal collision mechanisms related to the collision frequencies are the Brownian diffusion, shear-induced collisions and differential settling (Thill *et al.*, 2001). DLVO aspects of aggregation (suspension stability) are usually incorporated into Equation 2.1 with a collision efficiency ($0 \leq \alpha \leq 1$), representing the fraction of collisions that result in the attachment of the particles. The Smoluchowski approach has been successfully used for computer prediction of the time development of particle size distributions (Elimelech *et al.*, 1995). In the context of this study aggregation kinetics are of interest only at the collision efficiency level and further reference will be omitted.

However, the von Smoluchowski theory does not provide information on the actual aggregate form or structure obtained, factors that are particularly important for subsequent processing of the aggregates. A number of techniques for aggregate structure characterisation have been used in the literature. Computer simulations have played a significant role in understanding aggregate structure, simply because it is difficult to devise real experiments that can isolate an aggregation mechanism as precisely as do computer simulations. These computer simulations based on a number of different principles have attempted to predict not only particle size distributions but also aggregate structures (Meakin, 1988; Elimelech *et al.*, 1995). The two fundamental models underlying these simulations and describing the aggregation process have been extensively studied by Meakin (1988). These can be distinguished as: i) the so-called particle-cluster versus cluster-cluster aggregation model shown in Figure 2.1a, b and ii) the Diffusion Limited Colloidal Aggregation (DLCA) versus Reaction Limited Colloidal Aggregation (RLCA) model depicted in Figure 2.1c, d.

The particle-cluster and cluster-cluster regime simply predicts the different aggregate structures that are obtained when single particles or small aggregates respectively, are added to a growing aggregate. In particular, this type of simulation allows particles or aggregates to move into close proximity with each other according to specified trajectories (usually Brownian or linear) and stick irreversibly with no reconstructuring at their point of contact.

Single particles, due to their size, are more capable of penetrating the formed aggregate and thus fill gaps, than small aggregates (clusters). The particle-cluster and cluster-cluster regimes assume a collision efficiency factor of 1.

The DLCA model describes the aggregation process when every contact between two surfaces leads to a permanent attachment. As a result DLCA aggregates

exhibit an open structure (so-called 'dendritic'). This model also assumes a collision efficiency factor of 1. On the other hand, the RLCA model predicts than in the aggregation process the particles do not permanently attach at first contact, but they are able to detach again. As a result the RLCA aggregates undergo structural modifications (rearrangements) that finally lead to a closer packing of the particles in the aggregate. The RLCA regime assumes a collision efficiency factor of 0.

It is therefore obvious that in the case of an unstable suspension (*i.e.* collision efficiency factor of 1) DLCA will occur together with both particle-cluster and cluster-cluster aggregation at the beginning of the aggregate growth. Single particles will attach on first contact with each other, taking their final position in the aggregate from the initial steps of the aggregate growth. With time, however, more and more pre-formed clusters will be present so that cluster-cluster aggregation will govern. The result will be an open, dendritic structure according to both theories, DLCA and particle-cluster and cluster-cluster aggregation, respectively, due to the more likely occurrence of cluster-cluster aggregation with time.

In the case of RLCA, particle-cluster and cluster-cluster aggregation will also be present, but in this case all clusters joining the aggregate, single particles added and significant parts of the growing aggregate itself will be able to rearrange.

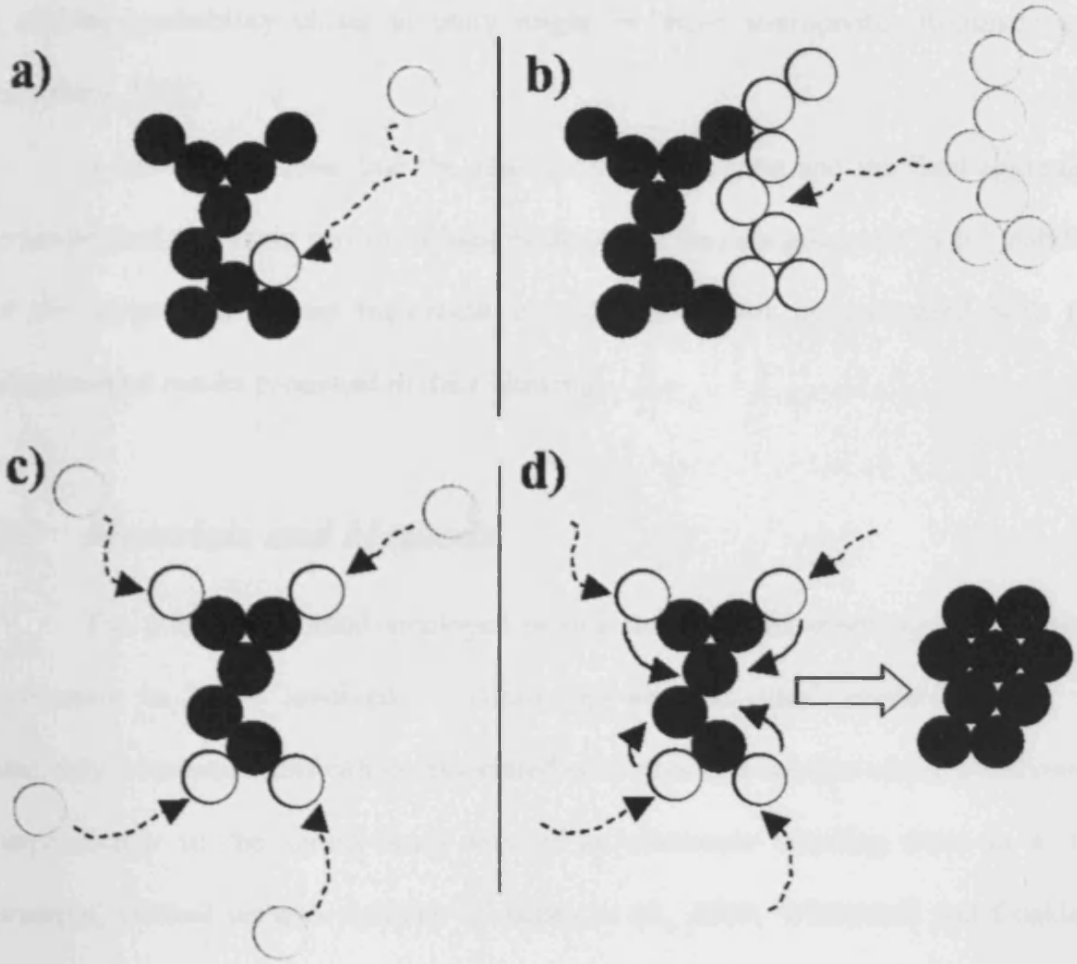

Figure 2.1: Model picture of (a) particle-cluster vs. (b) cluster-cluster aggregation and (c) Diffusion Limited Colloidal Aggregation (DLCA) vs. (d) Reaction Limited Colloidal Aggregation (RLCA) (Spengler, 2002).

The final aggregate will rearrange itself to accommodate incoming particles and clusters, delivering a closely-packed aggregate structure.

In other words, in the absence of an electrolyte in the suspension, the dipole-dipole repulsion is strong, so a sticking probability close to zero is expected; in contrast, by adding electrolyte to the suspension the Debye screening length can be reduced to such small magnitudes that the van der Waals attraction will dominate and

a sticking probability closer to unity might be more appropriate (Robinson and Earnshaw, 1992).

It has become clear that the aggregation mechanism and the final aggregate structure (and so a main part of the aggregate properties) are governed by the stability of the suspension. These theoretical considerations will be compared with the experimental results presented in the following.

2.2 Materials and Methods

The principle method employed in this study for the observation of particle movement in USW involved a 'microscopy-acoustic trap' assembly. Such an assembly overcomes difficulties associated with previous set-ups where observation perpendicular to the sound beam axis of an ultrasonic standing wave in a, for example, vertical perspex cylinder (Coakley *et al.*, 1989; Whitworth and Coakley, 1992) or through a transparent container side wall (Tuziuti *et al.*, 1999) is usually restricted to multi-wavelength traps. Long pathlengths in multi- wavelength systems on the other hand, increase the likelihood of the development of large scale streaming, making this way the tracing of individual particles particularly difficult (Spengler *et al.*, 2001). A laser light sheet to illuminate only a 'plane of interest' for observation has been applied (Spengler and Jekel, 2000) to overcome part of these problems. Conditions for particle concentration into a single or multiple bands were identified by Hawkes et al. (1998a, b) by downstream observations of the suspension in a laminar flow expansion chamber; yet this approach does not allow monitoring of particle behaviour in the USW field itself.

However, the 'microscopy-acoustic trap' assembly, proposed by the same authors (Hawkes *et al.*, 1998 a, b), allows direct focusing on a banding plane through

However, the 'microscopy-acoustic trap' assembly, proposed by the same authors (Hawkes *et al.*, 1998 a, b), allows direct focusing on a banding plane through a transparent glass reflector. A similar approach had been employed long before by Harvey and Loomis (1928) and Miller (1976) to examine the biophysical effects of ultrasound. The short acoustic pathlength (half wavelength) of the trap used in the present study limits the number of the banding planes of suspended particles to one and reduces the likelihood of large-scale streaming. Additionally, good optical viewing conditions are achieved (Spengler *et al.*, 2001). Figure 2.2 illustrates the principal assembly of such an 'acoustic trap'.

2.2.1 Acoustic trap

The three main components of the trap employed in this work were: the transducer, the spacer and the reflector. Four screws, positioned at each corner of the trap secured these three components, holding in place the top and the bottom part of the trap. Two rubber gaskets ensured the water-tightness of the trap (Fig. 2.2). A lead zirconate piezoelectric transducer is a ceramic of a defined shape and size, which has both electrical and mechanical properties (Hueter and Bolt, 1955). When a voltage alternating at a specific frequency is applied to the transducer, an alternating electric field is produced across the transducer. The ceramic piezoelectric material expands and contracts periodically in response to this alternating electric field. It is this mechanical movement that generates the sound wave. Each individual transducer has its own fundamental thickness resonance frequency. At this frequency the thickness of the transducer is equal to half wavelength of sound in the ceramic. The mechanical movement of the ceramic is at a maximum at this frequency.

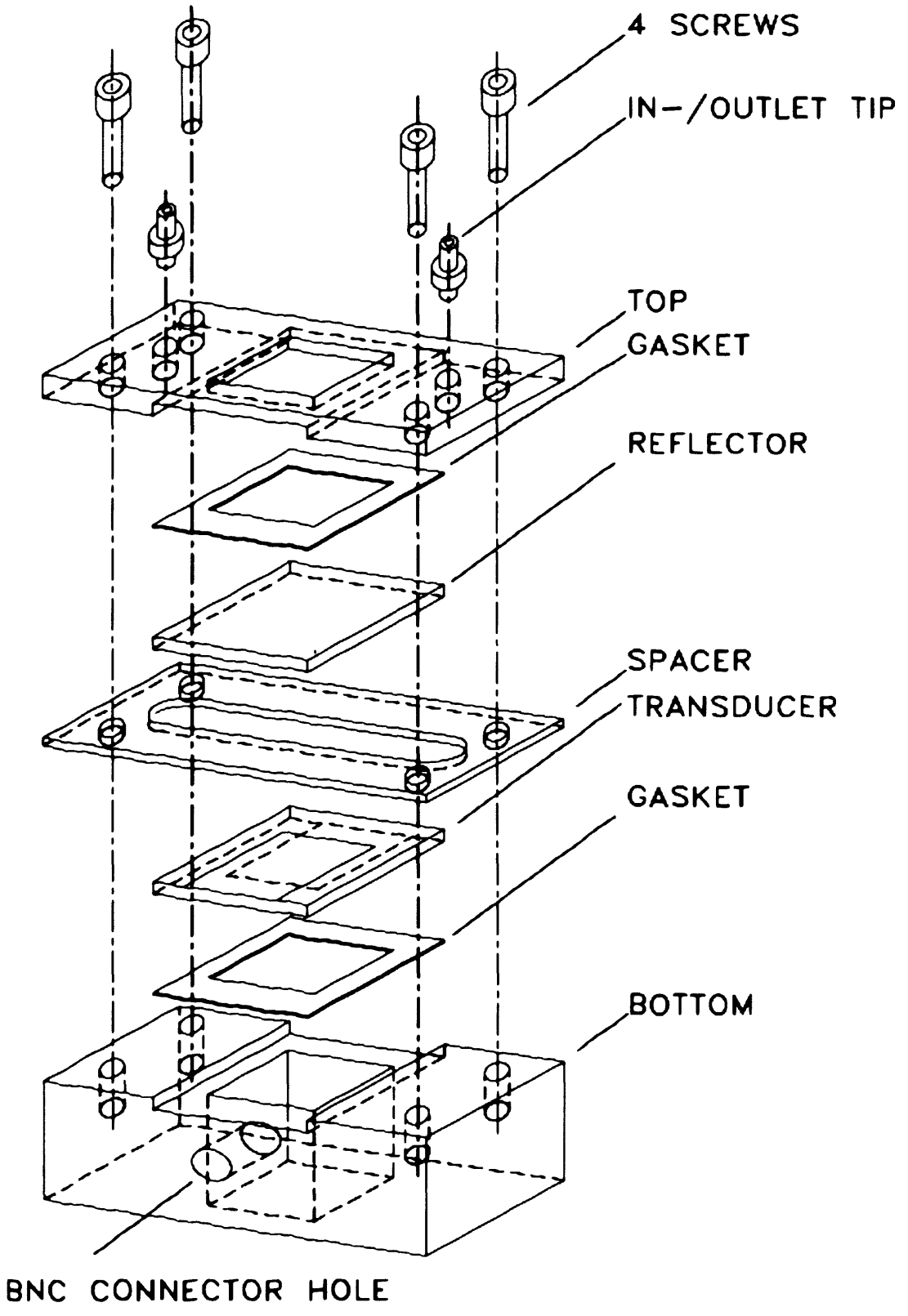

Figure 2.2: Schematic representation of the acoustic trap used for short pathlength observation of particle aggregation (Adapted from Spengler *et al.*, 2001).

The transducer described in this Chapter had a resonance frequency of 3 MHz. The active radiation area of the transducer was generated by electrode etching (Hawkes and Coakley, 2001). The quartz glass reflector allowed the direct focusing on a 'banding' plane. Optimum reflection properties were achieved by manufacturing its thickness on the basis of odd integer multiples of a quarter wavelength (Spengler *et al.*, 2001). A 10-mm-wide channel was formed by a fixed thickness spacer made of PTFE material.

The distance between transducer and reflector resulted in the formation of a single pressure node plane in the trap when driven at an appropriate frequency. This operation is called 'trap resonance' in order to distinguish it from the nominal transducer thickness resonance. The trap resonance was usually close to the transducer thickness resonance. The characteristics of the acoustic trap used in this Chapter are listed in Table 2.1.

The special feature of the acoustic trap was a circular back electrode with a diameter of 6 mm. A similar electrode layout was successfully employed by Whitworth and Coakley (1992) in an axial column in a multi-wavelength set-up. The spacer's thickness (0.25 mm) was one half wavelength in water (at the trap's resonant frequency). It was therefore expected to contain only one particle aggregation plane.

It is clear from the above that an ideal set-up should have radiation characteristics which maintain only one potential well into which particles are drawn, a characteristic that requires the excitation of the transducer in the lowest axially symmetric mode. The acoustic trap presented fulfils these requirements: a single clump in the centre of the trap was formed when the trap was driven at a frequency of about (day to day variations in system resonance frequency were in the range of ±100 kHz) 3.17 MHz.

Table 2.1: Characteristics of the rectangular acoustic trap used in the present study

Geometry	½λ
Ceramic nominal thickness resonance frequency	3 MHz
Acoustic trap resonance	3.17 MHz
Top electrode area	10×10 mm^2
Back electrode diameter	6 mm
Active radiation area	28.3 mm^2
Spacer thickness	0.25 mm
Reflector thickness	1.482 mm

2.2.2 Ultrasonic standing wave (USW) control unit

The basic experimental arrangement for ultrasound generation and amplification has been previously described by Spengler (2002). The transducer was driven by an ENI 2100 L (ENI, Rochester, NY) amplifier, with a sine wave generated by a Hewlett Packard 33120A function synthesiser. An oscilloscope (WAVETEK 9020) monitored the voltage across the transducer. A computer, directly connected to the control unit, provided a constant USW control. The software 'STAND', developed at Cardiff University, programmed the computer to initially locate the resonance frequency (through voltage-frequency spectra), and then maintain resonance for the required time period (Hawkes and Coakley, 1996). This method ensured reproducible and stable sonication conditions in the trap. The typical voltage scan of the acoustic trap used here is shown in Figure 2.3. Three pairs of pronounced maxima and minima can be seen. As already described a single clump at the centre of

the trap is formed when the trap is driven at the second voltage maximum (drive frequency of 3.17 MHz).

2.2.3 Optical system and video recording

A TV zoom lens (U-CMAD-2) and an Olympus BX40 epi-fluorescence microscope (Appendix B) allowed observation in the direction of the sound propagation (z-) axis. The former allowed observation of almost the whole active trap area, while the latter achieved resolution of single cells. The light source was an URFL-T Olympus mercury burner. A standard PAL CCD Fujitsu camera was fitted with the macroscopic TV zoom lens via a 0.5× Video Attachment Adaptor (U-TV0.5×), that gave a field of view of about 1.3×1.0 mm^2. Microscope objectives with ×5, ×10, ×20 and ×50 magnification were available. Their optical characteristics are listed in Appendix B. The vernier scale of the microscope stage enabled reproducible spatial positioning of the trap.

The video sequences at 25 Hz were recorded onto a Panasonic VCR system. The individual video clips were saved with the .avi extension on the miroVIDEO Capture DC30+ hardware (Advanced Mode). The data were compressed (Compression Factor 3:50:1, Data Rate: 6169 Kb/s) into a MJPEG format, in order to be imported (and exported) into the Adobe Premiere 5.1 (DC30 Editing Mode) hardware, and further image analysis to be possible. The frame resolution chosen for most of the individual video clips was 768 × 576 $pixels^2$. However, in some of the video clips, the TV Cropping application was enabled, bringing the frame resolution down to 720 × 540 $pixels^2$ (TV Cropping 48 × 36 $pixels^2$).

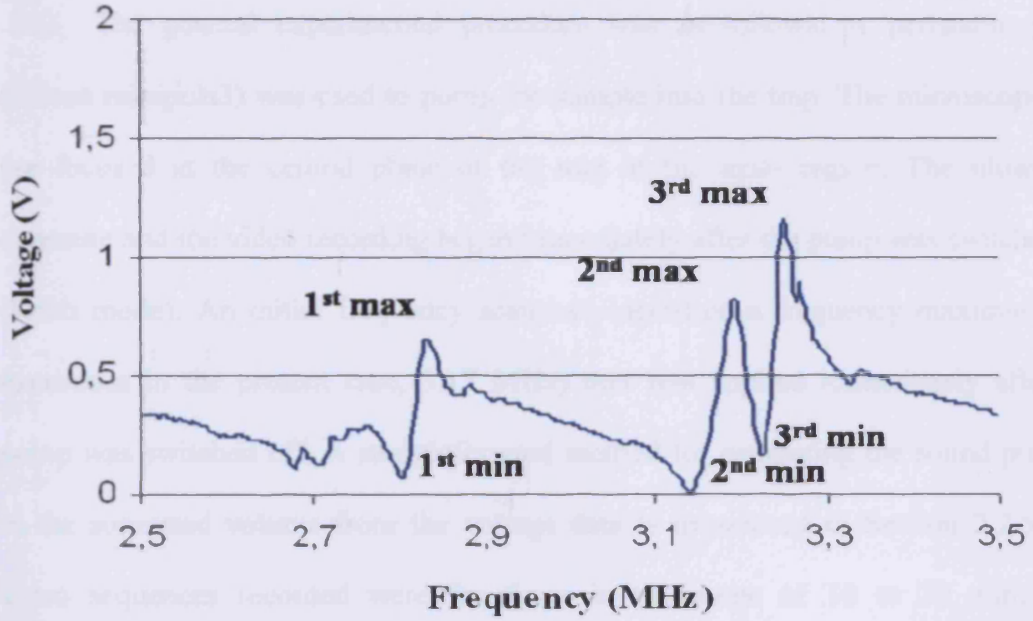

Figure 2.3: Voltage scan of the acoustic trap; 3 MHz transducer, 0.075 Voltage, deionised water, 0.5 MPa calculated sound pressure (P_0). The trap was driven at the 2nd max (3.17 MHz).

2.2.4 Suspensions and experimental procedure

25 μm diameter polystyrene latex particles (density 1,056 kg/m^3) were supplied as a 10 % suspension of solids by Polymer Laboratories (Church Stretton, UK). Aliquots were diluted here to 20 ml to give 0.15 % solids in deionised water and in 2, 4, 8, 10 and 20 mM $CaCl_2$ solutions. A Bright–Line haemocytometer (Sigma, Dorset, UK) was used for particle concentration counts. These suspensions were prepared in small concentrations (0.10 - 0.015 % suspension of solids) in order that a single 2-D aggregate, occupying a reasonable area in the acoustic trap, be formed, ensuring the accuracy of the image analysis techniques described in the following, as high particle concentrations have been shown experimentally (data not shown) to result in a multi-layering of particles predominantly at the centre of the aggregate.

The general experimental procedure was as follows: A peristaltic pump (Gilson minipuls3) was used to pump the sample into the trap. The microscope was pre–focused at the central plane of the trap at the axial region. The ultrasound exposure and the video recording began immediately after the pump was switched off (batch mode). An initial frequency scan had identified a frequency maximum (2^{nd} maximum in the present case, 3.17 MHz) that was applied immediately after the pump was switched off. A straightforward method for estimating the sound pressure in the sonicated volume from the voltage data is introduced in Section 2.2.5. The video sequences recorded were for times in the range of 10 to 30 min. Each experiment was repeated twice under the same experimental conditions. No difference in results, which might be attributed to a drifting sonication system, between these repetitions was identified during the study.

2.2.5 Acoustic pressure (P_0) estimation

A single polystyrene latex particle (25 or 45 μm in diameter) was introduced into the trap, held in suspension when the sound was on and observed with the microscope. Large particles were used as they are considerably more influenced by the DRF_a rather than the acoustic streaming drag (Spengler, 2002). The voltage across the transducer was lowered to a threshold voltage, where the buoyancy-corrected gravitational force (Eqn. 2.2) was just counterbalanced by the axial DRF_a (Eqn. 1.1).

$$F_g = (\rho_p - \rho_o) \cdot g \cdot V_p \qquad (2.2)$$

Exploitation of this relationship allows the calculation of the acoustic pressure when the latex particle is just held in suspension. With the material constants for water (c_0 =

1500 m s $^{-1}$, ρ_p = 1000 kg m $^{-3}$) and latex (c_p = 2350 m s $^{-1}$ and ρ_p = 1050 kg m $^{-3}$) (Whitworth and Coakley, 1992) this approach delivered for the acoustic trap used here a P_0 of about 50 kPa for the 0.27 V threshold transducer voltage. The values for the sound pressure in the trap have been linearly extrapolated to operational voltage levels employed in the experiments described in the following.

2.2.6 2-D image analysis of aggregates

Three different 2-D image analysis techniques were employed. However, the following principal steps were carried out in all cases: a) *Image Capturing* refers to the conversion of the image into a computer file suitable for image processing. Captures images were imported as 32-bit RGB .tif files into Adobe Photoshop 5.5. b) *Greyscale establishment* whereby any colour information was discarded in all captured images so as to simplify image processing (conversion to 16-bit grey .tif files). c) *Object detection* involving the identification of the surface texture. This was achieved by i) manual post–processing to whiten the areas very close to the object, as well as the areas that were not part of it so as to reduce background noise and ii) applying a black perimeter around the object and around the voids.

2.2.6.1 Perimeter fractal dimension analysis

Fractal geometry came to the fore in the mid 1970's from work presented by Mandelbrot (Mandelbrot, 1977). It refers to the geometry of roughness and is a powerful tool for the characterisation of the structure of aggregates. Fractals are characterized by a non-integer power law dependence of a measurable quantity upon the length of the object. The fractals quantified in this study are called length fractals

(2-D) because the volume of the aggregate is not taken into account. The Koch curve illustrated by Russ (1998) is such an example.

The equation which fully describes the concept of the fractal structure of aggregates can be expressed by the following proportionality

$$F \alpha L^{D} \tag{2.3}$$

where F denotes a certain feature of the aggregate or property of the aggregate and L is the linear measure of size (length or diameter of the aggregate). The most widely used feature embodied in the above equation is the mass of an aggregate (Lin *et al.*, 1989; Kim and Berg, 1999; Bushell *et al.*, 2002). A comprehensive summary about the most common fractal dimensions used in the literature has been given by Jiang and Logan (1996).

It is though more straightforward in the interest pursued here to employ the perimeter fractal dimension whose values will increase from 1 towards 2 as the aggregate perimeter moves from a closely-packed form to an open, dendritic structure (Skeljtrop, 1987). This direction of perimeter fractal dimension change is in contrast to the decrease in mass fractal dimension (Bushell *et al.*, 2002).

2.2.6.2 Void analysis

Captured images were processed with the analySIS 3.1 software (Soft Imaging System GmbH, Germany). The contrast was adjusted to enhance the quality of the images, which were then converted into binary format. The total void area (A_v) was determined for the final images. The total area within the perimeter (including the

void area) (A_p) was also determined. A void index (A_v/A_p) was then calculated for each aggregate. The area of the entire image was determined after filling all the voids.

2.2.6.3 Fast Fourier Transformation

Pattern Recognition analysis of the images was performed with the Fast Fourier Transformation (FFT) method. The analySIS 3.1 software allowed the computation of the FFT method using a standard approach. All the Fourier images were chosen to have 128 pixels per line and an information depth of 32 bit (128×128 ×32).

2.3 Results

2.3.1 Macroscopic observation of the aggregation process of 25 μm particles

The 25 μm particles were driven almost instantaneously (within two video frames) into the pre-focused nodal plane as single particles on initiation of the ultrasound exposure, under the action of the axial DRF_a. Following this banding of the particles, the lateral component of the DRF_l moved the particles in-plane towards the central area of the trap. Single particles and small clusters approached the central aggregate that had developed by 10 s. Generally larger clusters (usually formed outside the field of view and then moving into the central trap area) and a few single particles were approaching the growing aggregate. The aggregation process was almost complete after 40 s as no free particles were left in the field of view. This behaviour was consistent across the range of the $CaCl_2$ solutions studied.

2.3.2 Microscopic analysis of the 25μm particle aggregates

2.3.2.1 Influence of ionic strength

Typical images of 25 μm latex aggregates, reflecting the influence of ionic strength upon aggregate shape are shown in Figure 2.4. The experiments were conducted in an identical way for all ionic strengths.

Aggregation in the stable suspension (Fig. 2.4a; deionised water) was associated with considerable rearrangement of the central aggregate. Video observations showed that the single particles and clusters rolled, within the nodal plane, about each other before taking up their final position in a closely-packed aggregate. The aggregate therefore underwent structural modifications that led to a highly ordered structure with only a few holes in the aggregate structure. However, particle-cluster and cluster-cluster aggregation was also observed. With time the likelihood of cluster-cluster collision increased, which is in agreement with the theory presented in Section 2.1.2. The stable suspension used in this study, produced closely-packed, highly ordered but mechanically weak aggregates, an observation supported by their sedimentation behaviour. The sound was switched off minutes after the aggregate growth has reached an end point (as estimated by the absence of free particles in the field of view) and the aggregate was allowed to settle. The aggregate literally felt apart, resulting in its complete disintegration, indicating that few if any permanent particle contacts were established.

Aggregation in an unstable suspension (Fig. 2.4f; 20 mM $CaCl_2$) is significantly different. Every contact between two particles led to permanent attachment. There was virtually no sign of rearrangement. The aggregates exhibited a striking dendritic structure. Particle-cluster and cluster-cluster aggregation was observed as well, with the cluster-cluster aggregation dominating as the aggregate

growth time increased. It must be noted that as the 'backbone' of the dendritic structure grew, some folding took place, as also was the situation when long clusters joined the main aggregate. The unstable suspension yielded dendritic, highly disordered but mechanically strong aggregates. When the sound was switched off, the aggregate reached the bottom of the trap intact without disintegrating.

The aggregates formed with intermediate ionic strength suspensions (Fig. 2.4 (a) 2, (b) 4, (c) 8, (d) 10 mM $CaCl_2$) lie between the two extremes presented. The ability of particles to form permanent contacts increased with increasing calcium concentration, resulting in aggregates with more and more evident dendritic structures. Particle-particle and cluster-cluster aggregation was also observed. A decrease in the ability of the aggregate to rearrange itself was also apparent; however, the tendency for folding increased. As the stability of the suspensions increased, the sedimentation behaviour and the disruption degree altered.

2.3.2.2 Perimeter fractal dimension analysis

The perimeter fractal dimensions of duplicate series of 25 μm latex aggregates formed in increasing electrolyte concentrations are shown in Figure 2.5. The analysis was performed on the final aggregate images, as the perimeter-area of the aggregates was of interest. The perimeter fractal dimension data are plotted against the square root of $[CaCl_2]$, since the square root of the suspending phase ionic strength is proportional to the reciprocal of the Debye length κ^{-1} (Jones, 1975).

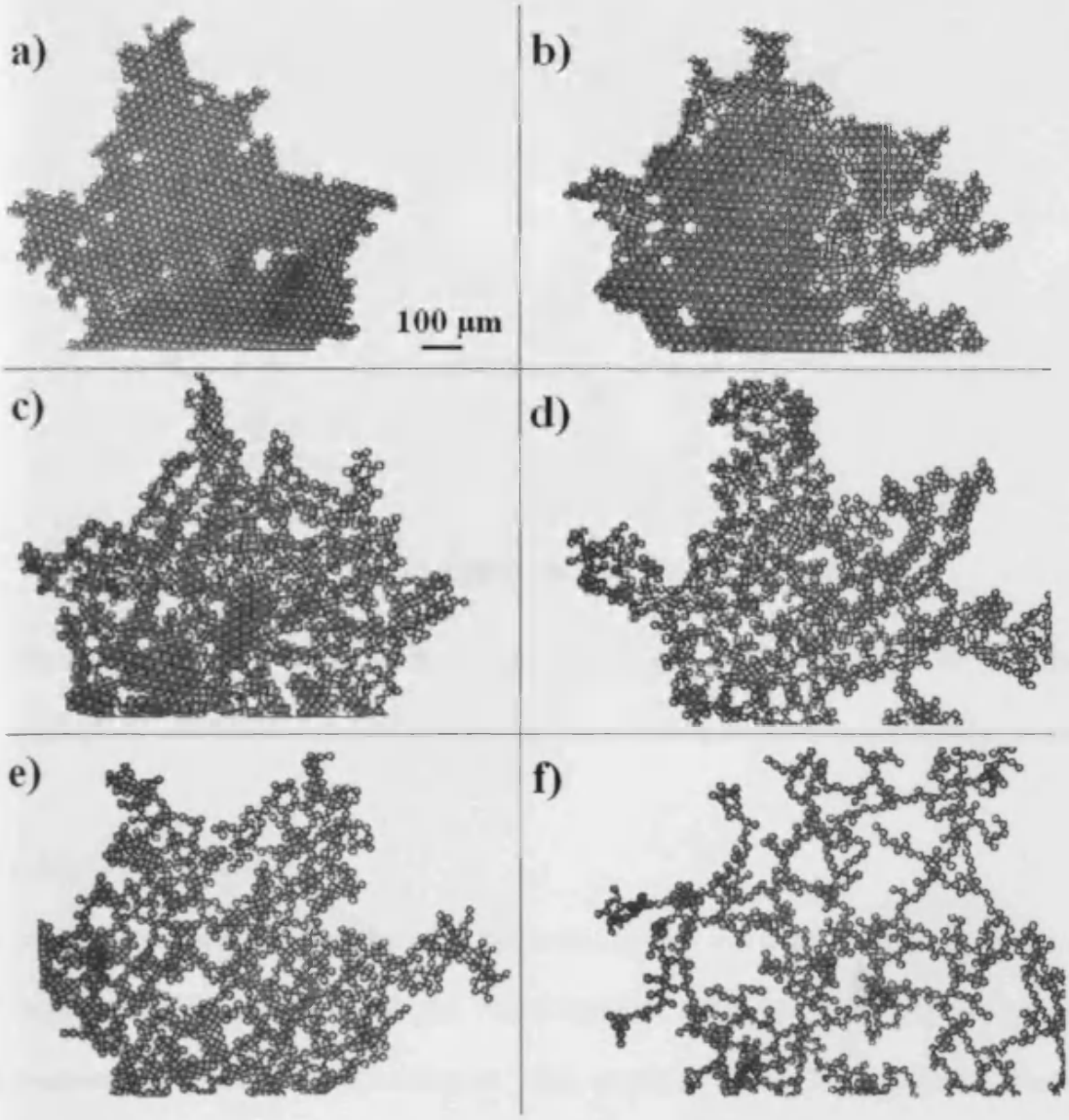

Figure 2.4: 25 µm latex aggregates suspended in 0 (a), 2 (b), 4 (c), 8 (d), 10 (e) and 20 (f) mM $CaCl_2$. These final aggregate forms were taken at the end of the aggregate growth phase that is characterised by the absence of free particles in the field of view. The details presented, that are representative of the aggregate structure (duplicate experiments), include about 60% of the particles in each final aggregate.

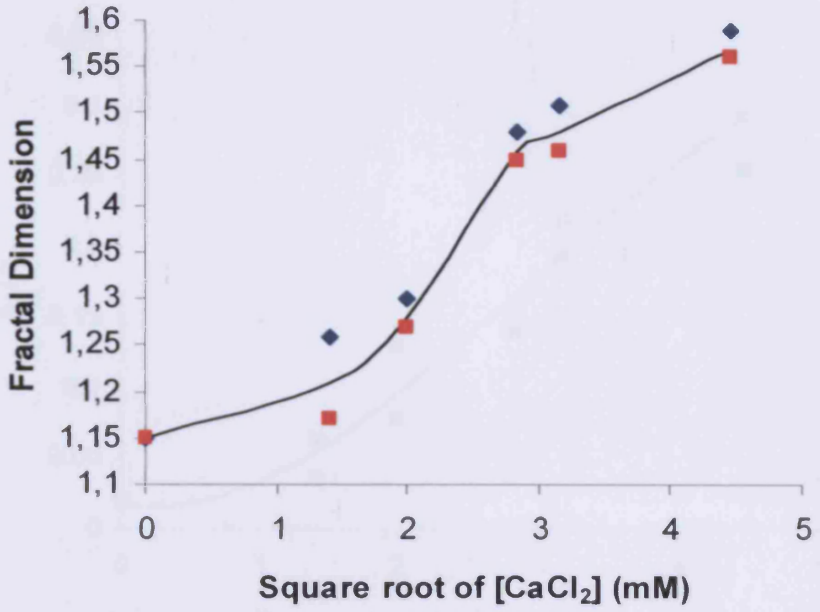

Figure 2.5: [$CaCl_2$] dependence of the fractal index of duplicates of 25 μm latex aggregates. The trend is drawn through the mean values for each concentration of salt.

2.3.2.3 Void analysis

The dependence of the void index (A_v/A_p) on salt concentration is shown in Figure 2.6. The pattern of the void indices obtained with increasing salt concentrations shows similarities to that obtained from the perimeter fractal dimension analysis at low and intermediate salt concentrations.

However, the void index continues to increase from 10 to 20 mM salt concentration while the perimeter fractal dimension is beginning to plateau. The result is consistent with the video records of the aggregate growth where the shape of clusters joining the aggregate changes from a grouped pattern (low calcium concentration) to a short string array as the salt concentration increased.

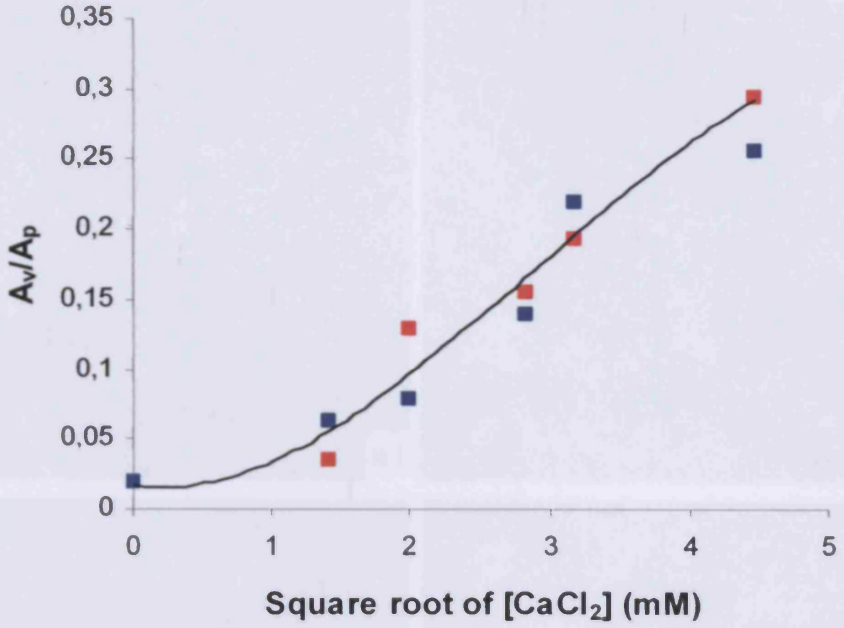

Figure 2.6: [$CaCl_2$] dependence of the void index (total void area/total image area) for duplicates of 25 μm latex aggregates. The trend is a third order polynomial best fit to the data.

2.3.2.4 Fast Fourier Transformation method

The images of 25 μm latex aggregates formed in deionised water (Fig. 2.7a) show a high degree of hexagonal order. This order continues to be dominant at 2 and 4 mM but is essentially lost at 8, 10 and 20 mM $CaCl_2$. The degree of order of the 25 μm latex aggregate suspended in deionised water as reflected in the FFT pattern is shown in Figure 2.7a.

The sensitivity of the FFT method allowed, through loss of the punctate pattern (Fig. 2.7a), the detection of differences between 2 and 4 mM $CaCl_2$ (Fig. 2.7b, c). Little change was detectable using this index at higher (8-20 mM $CaCl_2$) salt concentrations. Significant differences from the control are apparent at 8 mM (Fig. 2.7d).

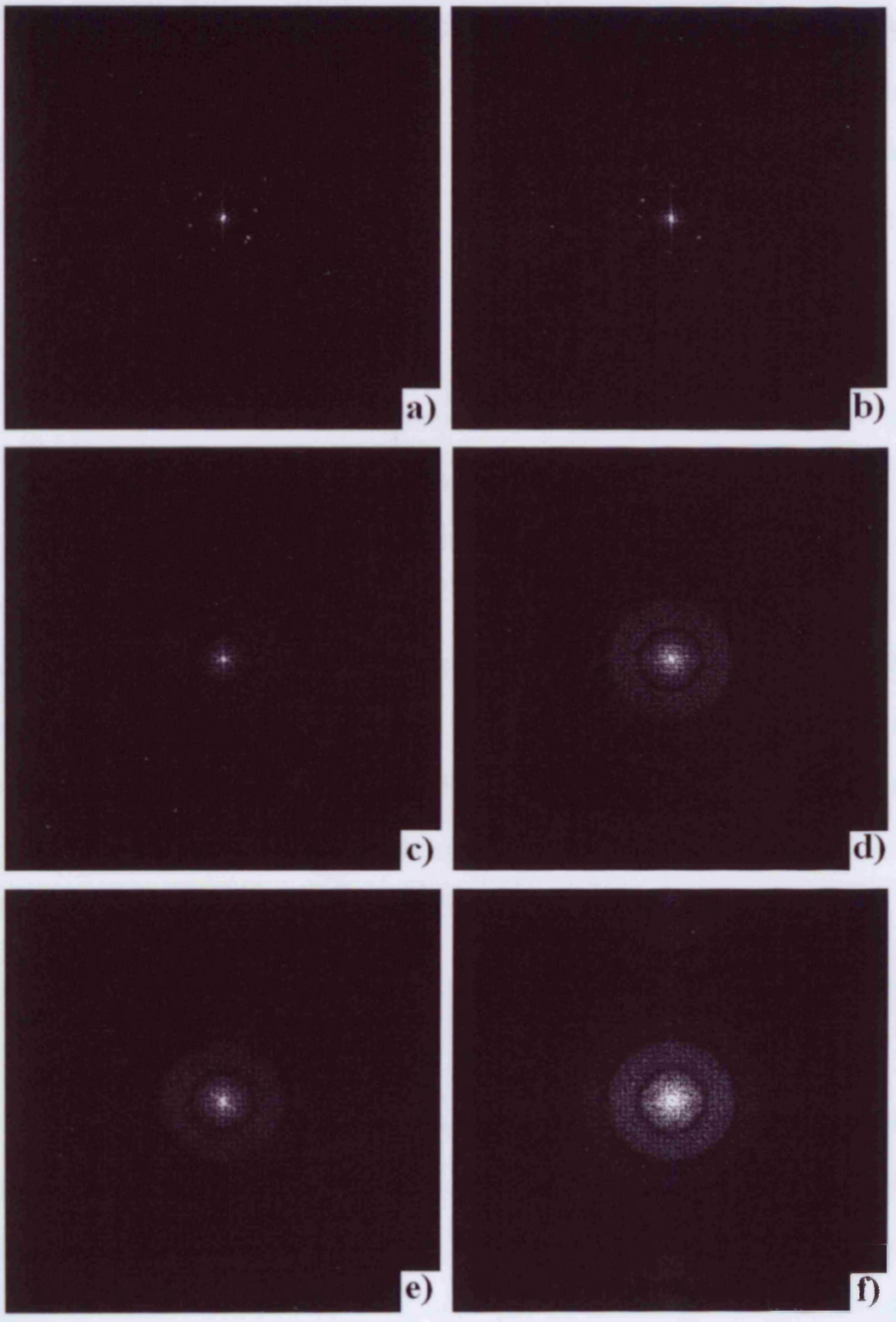

Figure 2.7: Fourier images of 25 μm latex aggregates formed in (a) 0, (b) 2, (c) 4, (d) 8, (e) 10 and (f) 20 mM $CaCl_2$. The punctate pattern is evident in (a-b), while it is lost in (c). (d-f) show the progressive broadening of the intensity distribution.

Less difference is observed between 10 and 20 mM $CaCl_2$ suspended aggregates (Fig. 2.7e-f). The images presented in these Figures are typical FFT images of these specific series of experiments. Similar Fourier images were produced for the replicate series.

2.4 Discussion

The results obtained from the macroscopic and microscopic analysis of the particle aggregation were presented in Section 2.3. However, the contribution of a number of different physical mechanisms on aggregation, as the direct acoustic force and micro-streaming will be discussed here. The influence of $CaCl_2$ on the aggregation behaviour of particles in the trap will be also discussed; this involves the investigation of the inter-particle forces, like electrostatic repulsion and van der Waals attraction, as described by the DLVO theory (Jones, 1975). The potentials and pitfalls of the different image analysis techniques are also addressed.

2.4.1 Macroscopic observation of the aggregate growth of 25 μm particles

Video observations of the aggregation process showed that the 25 μm particles were driven almost instantly into the nodal plane as single particles under the influence of the axial DRF_a. Spengler and Coakley (2003) used an analytical expression (Limaye and Coakley, 1998) to predict the time t required for all particles of initial distance z_1 ($z_1 < \lambda/4$) or less from the nodal plane to be moved, under the influence of the DRF_a only, within a distance z_2 from the nodal plane. The time t is given by:

$$t = \frac{(3\lambda^2 \eta r / \pi)[\ln(\tan(2\pi z / \lambda)]_{z_1}^{z_2}}{P_0^2 V \beta_w \phi(\beta, \rho)} \qquad (2.4)$$

where, η is the viscosity of the water and r is the radius of the particle. The distance from the pressure node to the reflector or transducer ($\lambda/4$) is approximately 0.125 μm. Taking into account the fact that the centre of mass of a 25 μm particle at the transducer wall is 12.5 μm from that wall, an estimate of the time for some part of all particles to lie in the node plane can be obtained. For that condition, since 12.5 μm equals 0.1 ($\lambda/4$), the values of limits z_1 and z_2 for Equation 2.4 are 0.9 ($\lambda/4$) and 0.1 ($\lambda/4$), respectively. The resulting time estimate is 19 ms. The time is consistent with the experimental observation of all 25 μm particles being clearly in the pre-focused nodal plane within two video frames (< 80 ms).

Following this banding of the particles, the lateral component of the acoustic radiation force (DRF_l) concentrated the particles into aggregates. This is a much slower process than the banding, because DRF_l is expected to be much weaker than the axial roughly by two orders of magnitude (Woodside *et al.*, 1997; Tuziuti *et al.*, 1999).

The only knowledge to be exploited here is, as presented by Spengler et al. (2001) that *DRF* (axial and lateral) and acoustic microstreaming drag on particles are two opposing but simultaneously acting forces. *DRF* (axial and lateral) increases linearly with particle volume, whereas the streaming Stokes drag shows a linear dependence on diameter. Therefore, the *DRF* becomes more important the larger the particles are, while acoustic microstreaming becomes dominant the smaller the particles are. The 25 μm particles' behaviour, consistently with the ideas reported

above, is dominated by the *DRF*, whereas they seem to be hardly affected by the micro-streaming,. This pattern formation was reproducible and consistent with the reference stable and unstable suspensions used in this study.

Acoustically induced particle-particle forces (Chap. 1; Sec. 1.9.4) do not influence the general tendency to form an aggregate. It has been shown by Nyborg (1978) that inter-particle interactions can be essentially neglected above particle separations larger than a particle diameter.

2.4.2 Microscopic analysis of the 25 μm particle aggregates

Particles with weak or zero net attractive interactions roll about each other before taking up their final position in a 'closely packed' aggregate. These aggregates therefore undergo structural modifications that lead to highly ordered structures. This description applies to the mechanically weak aggregates formed at low calcium additions (Fig. 2.4 (a) 0, (b) 2, (c) 4 mM $CaCl_2$), that were also observed to disintegrate when they reached the bottom of the trap when the sound was off. The aggregation pattern just presented, in agreement with the theoretical discussion in Section 2.1.2, is largely, a RLCA condition with a low collision efficiency factor (tending to zero).

Aggregation processes where every contact between two surfaces leads to a permanent attachment exhibit an open structure. Such aggregates formed here at 8, 10 and 20 mM [$CaCl_2$]. (Fig. 2.4d-f). These aggregates were highly disordered but mechanically strong. The DLCA model (of a high collision efficiency tending to 1) lying behind the present description, theoretically supports the experimental observations.

However, the models just described, have to be considered simultaneously, as a single approach cannot describe the real aggregation phenomenon extensively. The difference in the suspension stability in relation to the collision efficiency factor, is of great importance, as the reference samples lie in the collision efficiency range of almost 0 (stable suspension-0 mM $CaCl_2$, Fig. 2.4a) to almost 1 (unstable suspension-20 mM $CaCl_2$, Fig. 2.4f) (Meakin, 1988).

It is therefore evident that the most crucial mechanism which determines the final structure of an aggregate is obviously its ability to rearrange itself in the USW. The morphologies arising from isolated particle-cluster and cluster-cluster aggregation processes observed during the initial aggregate growth steps are predictive of the different aggregate structures that characterise fully grown aggregates. Single particles were more capable, than were small aggregates (clusters), of penetrating the formed aggregate and thus filling gaps, in line with the more general conclusion of Meakin (1988).

Collision efficiencies intermediate between 0 and 1 need to be considered to describe the real aggregation phenomenon extensively and more importantly describe the gradual crossover (Di Biasio *et al.*, 1994; Asnaghi *et al.*, 1995; Puertas *et al.*, 2001; Moncho-Jordá *et al.*, 2002) from an ordered to an open structure that occurs in our experiments between 4 and 8 mM $CaCl_2$.

Here, the perimeter fractal dimension increased from 1.15 (deionised water) with increasing salt concentration to reach 1.58 in 20 mM $CaCl_2$.

The $CaCl_2$ concentration range (2- 20 mM) here includes part of the range (13 mM – 30 mM) of $MgCl_2$ previously employed to monitor the dependence of 3-D aggregation of 0.13 μm latex on salt concentration (Asnaghi *et al.*, 1992). Closely-packed aggregates were formed at the lower range of salt concentration studied

whereas open, dendritic aggregates at the upper limit. The long (> 48 h) time for an aggregate to develop in salt concentrations less than 13 mM precluded their study. (This temporal limitation does not apply to the present work.) The authors proposed that the fractal dimensions they measured at intermediate concentration represented a type of cross-over from packed to open structured aggregates and represented 'effective' rather than ideal fractal parameters. Figures 2.5 and 2.6 show similar transition regions here. The transitions are centred around a $CaCl_2$ concentration of 6 mM (ionic strength = 0.018).

While fractal analysis clearly identified the limiting aggregate formation states and the parameter reflects fundamental properties of aggregating systems, it can be limited (Robinson and Earnshaw, 1992; Gardner *et al.*, 1998) in its ability to detect fine changes in an aggregation. This need might arise where one wishes to establish the initial stage at which some clusters do not reorganise fully to give a well-ordered system (compare Fig. 2.4a and Fig. 2.4c) or where the extent of 'openness' of an aggregate might have implications for the mechanical strength and sedimentation rate of that aggregate (Fig. 2.4e and Fig. 2.4f). Two operational indices of order have been explored above. The first, void analysis, was investigated as a sensitive detector of 'openness' while the second, FFT, was chosen to detect early signs of loss of order.

The pattern of the void indices obtained with increasing salt concentrations shows similarities to that obtained from the perimeter fractal dimension analysis at low and intermediate salt concentrations. However, the void index continues to increase from 10 to 20 mM salt concentration while the perimeter fractal dimension is beginning to plateau. The result is consistent with the video records of the aggregate growth where the shape of clusters joining the aggregate changes from a grouped

pattern (low calcium concentration) to a short string array as the salt concentration increased.

In two dimensions, the Fourier transform from a lattice of identical circular particles is the product of the Fourier transform of a single particle (this is known as an Airy pattern) and the Fourier transform of the lattice (a series of well defined spots). The Fourier transform of such an assembly of particles normally consists of a series of spots whose relative positions are related to those of the lattice points and whose intensity is modulated by sampling the Airy pattern (Gagnet *et al.*, 1962; Harburn *et al.*, 1983). Aggregation of the latex particles in stable suspensions (deionised water) resulted in 'close-packed' aggregates exhibiting hexagonal structural order. In the FFT (Fig. 2.7a) this leads to a series of bright spots with 6-fold rotational symmetry (in Fig. 2.7a note that the pattern of spots repeats itself every 60 degrees around each ring); the appearance of more than six spots around the rings results from the presence of hexagonal domains with different orientations within the sample). The presence of spots in the FFT is a direct indication that a high degree of order exists in the packing of the particles.

Unstable suspensions resulted in 'dendritic' aggregates with little or no lattice structure. This can be seen in the Fourier transforms by the broadening and reduced intensity of the lattice-derived spots, and by the increased intensity of the central Airy disc. The concept governing this approach is that, as the packing of the aggregates gets poorer (due to the increased ionic strength), the interference effects due to the regular packing diminish and we head towards the FFT of a disordered array of particles, characterised by a broad Airy disc at the centre of the pattern (Fig. 2.7f). The method is sensitive to small changes in the order in the particle packing and this is demonstrated by the transition from the case where the lattice structure dominates the

FFT to that where the Airy pattern dominates the FFT. Early signs of loss of order are evident abruptly between Figure 2.7b and Figure 2.7c, *i.e.* between 2 and 4 mM $CaCl_2$.

2.5 *Quantification of the forces acting on particles*

The extent to which ultrasonic interaction forces might modify the probability that particles will stick on contact is quantified in the following. The ultrasonic interaction forces (Chap. 1. Sec. 1.9.4) are quantified and compared with the influence of the van der Waals interaction and electrostatic repulsion normally governing microparticle interactions (Sec. 2.1.1.1). The calculations will be performed for an exemplar latex particle of diameter 25 μm.

The van der Waals interaction potential between two equal-sized spheres of radius r and nearest centre to centre approach $2r + h$ may be approximated, for $r \gg h$, by $Ar/(12h)$ where A is the Hamaker constant (Heimenz, 1986). The resulting attractive interaction force is:

$$F_w = \frac{-Aa}{12h} \tag{2.5}$$

The Hamaker constant for polystyrene is 2.2×10^{-20} J. The attractive acoustic force (Chap. 1; Sec. 1.9.4; Eqn. 1.5) can be placed in the context of the van der Waals attraction by noting that they are equal in magnitude, for $2r$ = 25 μm, when h = 57 nm. The van der Waals force then becomes increasingly more important than the acoustic force for smaller values of h.

An expression for the electrostatic repulsive force between identical particles with surface potential ψ_s in a symmetrical monovalent electrolyte of counterion concentration n_0 ions m^{-3} is given by Heimenz (1986) as

$$F_c = (64\pi\eta_o kT\gamma_o^2)\cdot(\alpha\kappa^{-1})\cdot\exp(-\kappa h) \qquad (2.6)$$

where k is the Boltzmann's constant, γ_0 is given by Equation 2.8 and T the absolute temperature. At a temperature of 25°C and an electrolyte ionic strength I, κ^{-1} and γ_0 are given (Heimenz, 1986) by equations (2.7) and (2.8):

$$\kappa^{-1} = 4.31\cdot10^{-10}(2I)^{-0.5} \qquad (2.7)$$

and

$$\gamma_0 = \frac{\left[\exp\left(\frac{e\psi_s}{2\kappa T}\right)-1\right]}{\left[\exp\left(\frac{e\psi_s}{2\kappa T}\right)+1\right]} \qquad (2.8)$$

The attractive acoustic force is placed in the context of the van der Waals force for different experimental situations.

For the suspending phases considered later in this work, *i.e.* $CaCl_2$ solutions (I = 0.06 at 20 mM) and physiological media (I = 0.15; Chaps. 3-6) κ^{-1} equals 1.24 and 0.79 nm respectively. These distances are very small compared to the separation of 57 nm above at which acoustic attraction becomes smaller than the van der Waals force. It follows that, for the particles and cells considered in this thesis, acoustic interaction does not make a significant contribution to the forces that determine the surface-surface interactions controlling aggregate morphology and collision efficiency.

2.6 Preliminary conclusions

Investigation of the effect of ionic strength on particle interactions in USW showed that the concentration of electrolyte ($CaCl_2$) influences the aggregation process (free rearrangements or direct attachment of the particles) and consequently the final 2-D aggregate morphologies (orderly packed or 'dendritic' aggregates). Particles with weak or zero net attractive interactions (collision efficiency tending to zero) deliver 'closely-packed' hexagonally ordered aggregates with a low perimeter fractal dimension. Mechanically weak aggregates (that dispersed during sedimentation following sound termination) were formed at low calcium additions (0, 2, 4 mM [$CaCl_2$]).

In contrast, aggregation processes where every contact between two surfaces leads to a permanent attachment (collision efficiency factor of 1) exhibit an open structure with higher fractal dimensions as it is the case for aggregates formed at 8, 10 and 20 mM [$CaCl_2$]. These aggregates were mechanically strong, as when the sound was switched off they reached the bottom of the trap intact.

'Cross-over' behaviours from packed to open structures, as clearly identified by the fractal analysis, occurred here at a [$CaCl_2$] of about 6 mM. FFT was a sensitive indicator of loss of hexagonal order in the 2-D structures at low salt concentrations, while void analysis was sensitive to the identification of the transition zone and may be a useful index as the collision efficiency increases towards 1, a situation where fractal index is rather insensitive to change.

The observations and results presented in this Chapter were also in agreement with the DLVO theory of colloidal stability, providing in this way experimental evidence of the applicability of different model ideas on aggregate growth and final aggregate structure. However, the observations showed that a sole treatment of

aggregation kinetics with either the particle-cluster/cluster-cluster or DLCA/RLCA models cannot fully describe the real aggregation process; rather a combination of the above approaches is essential for a complete description.

Chapter 3

Physical environment and biological wellbeing of 2-D cell aggregates formed in a short pathlength ultrasound standing wave trap

3.1 Introduction

Physical methods of manipulating suspended cells or microparticles at single-particle microscopic resolution include optical (Grier, 2003), dielectrophoretic (Heida *et al.* 2002) and ultrasonic (Miller 1976; Wu 1991; Spengler and Coakley 2003; Coakley *et al.* 2004) traps (Chap. 1; Sec. 1.8.2). Optical and dielectrophoretic manipulations of cells have been extensively exploited, whereas less attention has been paid to ultrasound traps. Particle (Spengler *et al.* 2003; Chap. 2) and cell (Khanna *et al.* 2003; Coakley *et al.* 2004) aggregates of diameter of the order of a millimetre and a depth of one particle or cell ('2-D aggregates') have been formed in appropriately designed single half wavelength ultrasound traps. Formation of 2-D cell aggregates in a trap deep in the bulk phase rather than at an air-water interface (Hidalgo-Alvarez *et al.* 1996), an environment that is unsuitable for animal cells, offers an advanced approach for the study of animal cell interactions. An ultrasound trap that can facilitate the study *in vitro* of interactions of cell consortia in a manner that is, at least in part, tissue-mimetic and allows interactions away from glass or plastic substrata that can influence cell behaviour (Cukierman *et al.*, 2002) and even phenotype has some potential as a tool in cell biology.

It is therefore important to examine how the ultrasound trap restrains a cell and how the physical forces might influence the cell directly or through changing its environment. It is noted that an equivalent discussion has not been reported for dielectrophoretic or optical traps. Nyborg (2001) reviewed the eighty year history of studies of biological effects of ultrasound that were undertaken because of interest in applications of ultrasound to medical diagnostics, therapy and biotechnology particularly to assess the safety of the widespread medical applications of ultrasound. He treated thermal effects that can arise because of sound absorption, effects due to cavitation and phenomena attributed to acoustic radiation force or torque or acoustic streaming. Measurements of all these variables (except torque) are performed in this Chapter and their significance is set in the context of the cell environment in an ultrasound standing wave trap.

A small sensing bead was developed to measure temperature *in situ* in the trap while cell aggregation was taking place. Acoustic microstreaming analysis around the aggregate has been carried out with the experimental set-up presented in Chapter 2 (Sec. 2.2.3), and particle image velocimetry (PIV) has been used to quantify the velocities of moving particles. The results from the PIV plots have been set in the context of hydrodynamic stress imposed on cells by routinely used general preparation procedures, such as centrifugation. Acoustic spectrum analysis has been carried out with a hydrophone in direct contact with the trap. In addition, the attractive acoustic force between ultrasonically agglomerated cells (Sec. 1.9.4) has been theoretically compared to the normal attractive van der Waals force that operates at close cell surface separations using the approach described in Chapter 2 (Sec. 2.5). Finally, different viability assays have been performed to search for any direct impact of the

trap's environment on the viability of cell aggregates over the time scaling of the current experiments.

3.2 Materials and Methods

The acoustic trap used for the work conducted with model polystyrene latex particles has been described in Chapter 2 (Sec. 2.2.1). The design of the 'rectangular' acoustic trap used there was fairly complex; its many individual components had to be carefully designed, selected and optimised so as the most advantageous sound transmission into the sonicated volume to be ensured. Nevertheless, the circular 6 mm back electrode of the square transducer provided the essential symmetry for a single central potential well into which particles were drawn; a feature particularly desirable for cell aggregation and adhesion studies performed in the following Chapters (Chaps. 4-6).

Difficulties related with the 'rectangular' acoustic trap included:

(i) High manufacturing demands; the trap consisted of many different parts that had to be precisely manufactured and their acoustic properties had to match for optimum operational performance.

(ii) As far as the sound field itself is concerned, it was observed that the paths of a number of particles led them not directly to the centre, but along bent trajectories. This created two distinctly preferred directions of the particles' approach towards the centre of the trap: from the upper and the lower edge of the field of view (Spengler *et al.*, 2003). The movement of particles towards the centre of the trap was therefore to a degree undesirably biased.

A fairly straightforward set-up of a so-called 'circular' acoustic trap is introduced here; it overcomes these difficulties and accommodates some of the needs for use in the biological/medical area. The steel circular acoustic trap body is simple and less time consuming to machine. Formation of a resonant system can be easily carried out by adding only a transducer and a reflector. Furthermore, removal and replacement of the reflector for thorough washing of the steel coupling layer can be performed without detectable change of the trap's acoustic properties. Finally, its circular design predisposed towards a radially symmetric sound field, allowing particles and cells to approach the single central potential well from around the active area rather than from preferred directions. Figure 3.1 illustrates, through PIV maps (described in Sec. 3.2.2.1), the paths towards the central aggregation area that particles follow in the sound field of the rectangular (Fig. 3.1a) and circular (Fig. 3.1b) acoustic trap respectively. It is noted that the map corresponding to the circular trap is a qualitative, descriptive one based on observation of radial cell movement towards the axis in a way that did not show preferred pathways as in Figure 3.1a. The principal assembly of a 'circular' acoustic trap is shown in Figure 3.2.

3.2.1 'Circular' acoustic trap

An acoustic trap has three essential features: a transducer in a housing of radial symmetry attached to a steel coupling layer, an aqueous phase and a reflector that provided optical access from above. The main body of the trap was made of steel. The characteristics of this trap are listed in Table 3.1.

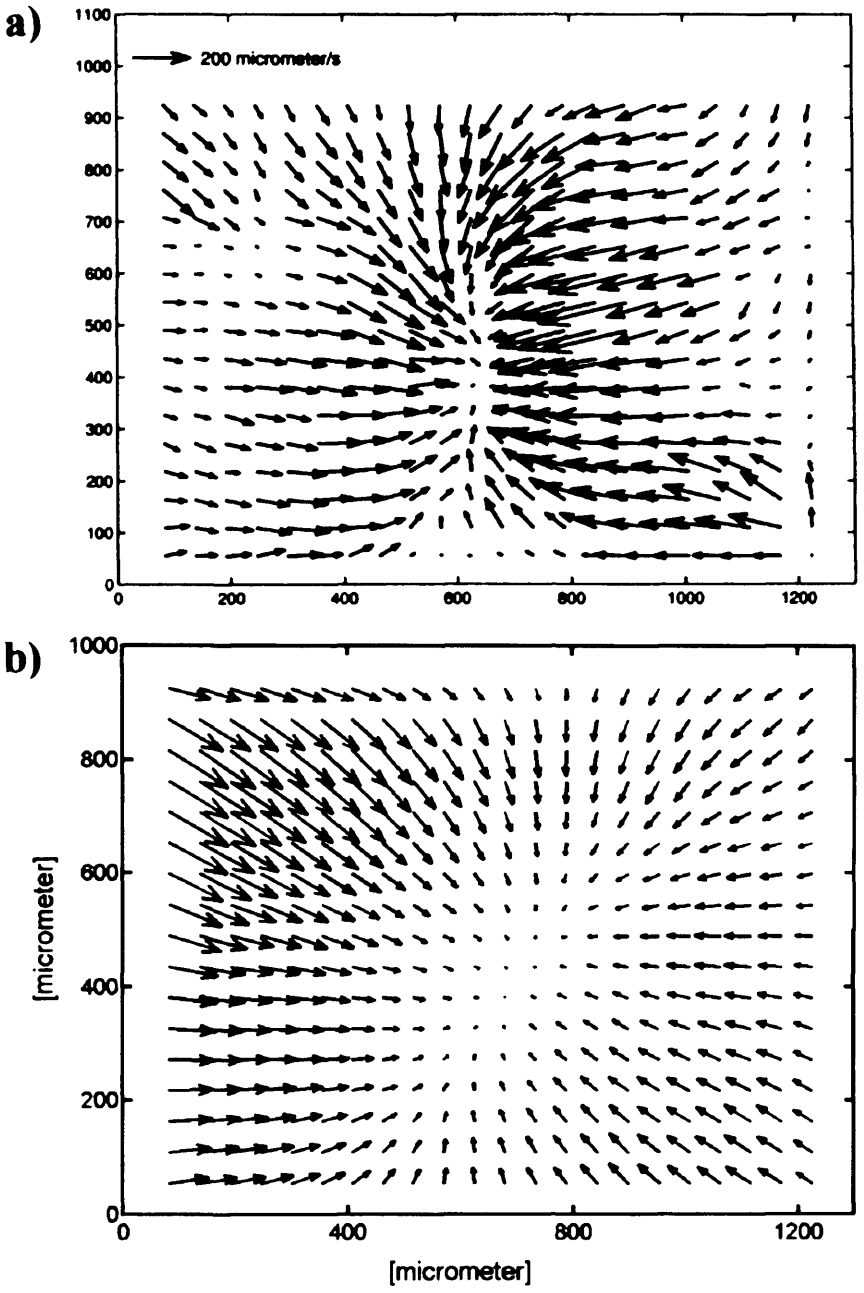

Figure 3.1: PIV maps showing the trajectories followed by 25 μm diameter latex particles towards the central aggregation area in the rectangular ((a); Spengler, 2002) and circular (b) acoustic trap. It is noted that (b) is a qualitative, descriptive map based on observation of radial cell movement towards the axis in a way that did not show preferred pathways as in Figure 3.1a

The transducer was disc-shaped, 12 mm in diameter, with a nominal thickness resonance frequency of 1.5 MHz. Its electrodes were etched (Hawkes and Coakley,

2001) to give an overlapping circular active area of 6 mm in diameter on its back, with the objective, as with the 'rectangular' acoustic trap, to produce a single central potential well in a half wavelength trap (Spengler *et al.*, 2003). The steel coupling layer on which the transducer was mounted had a thickness of $3\lambda_{steel}/4$.

Table 3.1: Characteristics of the 'circular' acoustic trap used in the present study

Geometry	½λ
Ceramic nominal thickness resonance frequency	1.5 MHz
Acoustic trap resonance	1.57 MHz
Transducer diameter	12 mm
Back electrode diameter	6 mm
Active radiation area	14 mm*
Reflector diameter	25 mm
Reflector thickness	1.0 mm

*Based on the fact that particles in Figure 3.1b move towards the central aggregation area from all directions, the entire sample volume is the active radiation area of the trap.

The quartz glass reflector was also disc-shaped, 25 mm in diameter, with a thickness of 1 mm ($\lambda_{glass}/4$), so that the single pressure node plane in the sample volume would be located half way through that volume (Hawkes *et al.*, 2002).

The trap, driven at 1.57 MHz, had an acoustic pathlength of one half wavelength in water (0.5 mm) at the driving frequency. The experimental set-up was as described in Chapter 2 (Sec. 2.2.2). The trap could be driven either through computer control or manually with a linearly connected layout consisting of (i) a function generator (HM 3138, Hameg, Germany) and (ii) an oscilloscope

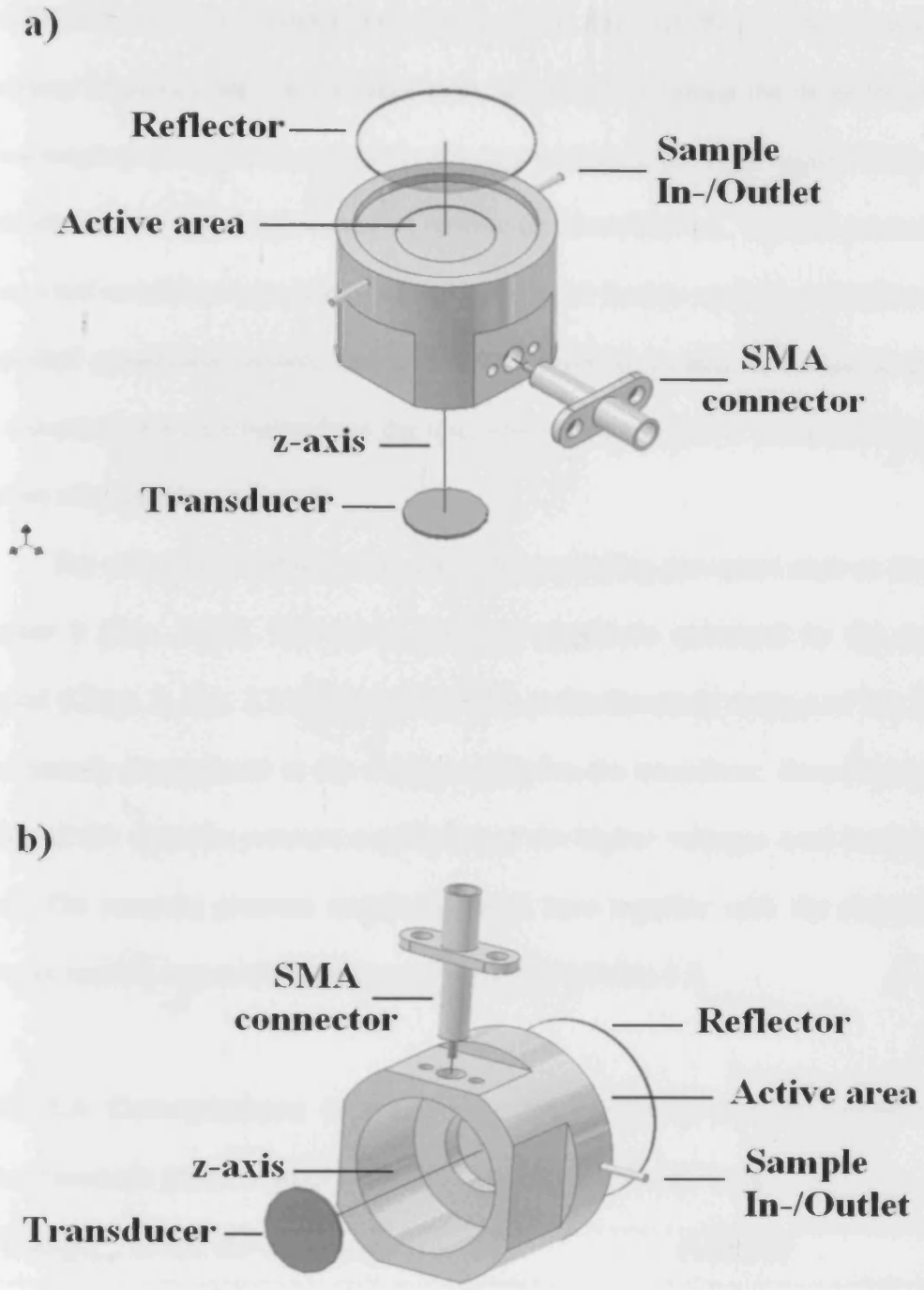

Figure 3.2: 3-D schematic representation of the front (a) and back (b) of a circular ultrasound trap used for investigation of cell-cell interactions. The resonator outer diameter is 32 mm. The thicknesses of the different layers were selected to give a highly resonant system. The individual components of the trap are also indicated.

(WAVETEK 9020) to monitor the voltage across the transducer. The acoustic trap's operating frequency was, in the latter case, identified by tuning the drive frequency to give a single potential well, at which cells aggregated, in the axial region. Both control methods showed good agreement in resonance identification. Manual control of the operational conditions was preferred and used in all further studies, as it offers a more controlled operational system and it is further possible to alter (increase or decrease) the acoustic pressure amplitude in the trap while the aggregation process is in progress or even after aggregate growth.

The microscopic observation and video recording processes were as detailed in Chapter 2 (Sec. 2.2.3). The sound pressure amplitude estimated by the described method (Chap. 2; Sec. 2.2.5) gives 0.06 MPa at the threshold voltage of 2.2 V. Since P_0 is linearly proportional to the voltage applied to the transducer, linear extrapolation delivered the acoustic pressure amplitudes at the higher voltages used in the present work. The acoustic pressure amplitudes used here together with the corresponding voltages applied across the transducer are shown in Table 3.2.

Table 3.2: Correspondence of the voltage applied across the transducer and the derived acoustic pressure amplitudes (P_0) used in the present work

Voltage$_{p\text{-}p}$ across the transducer (V)	***P_0 (MPa)***
72.5	1.96
20	0.54
10	0.27
2.2	0.06

Data on the acoustic pressure amplitude in the trap carry more information than the individual voltage values, as they can be 'transferred' to other systems and

resonators of different electromechanical efficiencies, and they can also be directly used for the numerical calculation of the DRF_a and acoustic interparticle forces (Chap. 1; Eqns. 1.1, 1.3 and 1.4); therefore reference to the voltage values will now be discontinued.

3.2.2 Suspensions

The suspensions employed here were neural cells (approximately 14 μm in diameter) and 1 μm diameter polystyrene fluorescent latex particles (Polymer Laboratories, Church Stretton, UK), both suspended in Neuronal Supplemented Medium (NSM). The individual components of NSM can be found in Appendix A. The neural cell culture procedure will be given in detail later in Chapter 4 (Sec. 4.2.2). For the viability assays articular cartilage cells were also employed; their isolation and culture procedure will be described in Chapter 5 (Sec. 5.2.2). The properties of the latex particles used here are shown in Table 3.3. The experimental procedure details, together with the suspension details, are given in the individual Materials and Methods sections described below.

3.2.3 Measurement of the temperature in the acoustic trap

An alumel/chromel thermocouple was fabricated from a 75 μm diameter alumel and a 50 μm diameter chromel wires (Omega Engineering, Inc, USA) using a spark welding technique. The spherical thermocouple junction had a diameter 200 μm. The thermocouple voltage was measured with a pen recorder (Labdata Instrument Services Ltd, Surrey, UK). Calibration of the thermocouple was performed at the following temperatures: 0°C (the junction was immersed in iced water), 25°C (the

junction was kept at room temperature) and 40°C (the junction was placed in a 40°C temperature-controlled room).

Table 3.3: Properties of the fluorescent polystyrene latex particles together with their concentration and average number

Manufacturer	*[Solids]*	*Size (μm)*	*Std.Dev of Size (%)*	*Average number of particles (no.ml^{-1})*	*Colour*	*Excitation (nm)*	*Emission (nm)*
Polysciences, Inc	2.5 %	1.00	≤ 3	4.55×10^{10}	Bright Blue	365	435

A 1 K temperature change resulted in a 2 mm pen recorder deflection, and a 1 mm pen recorder deflection resulted in a 20 μV change, thus giving a thermocouple sensitivity of 40 μV/K.

The thermocouple was then placed at the centre of the trap where temperature measurements were conducted *in situ* in a water-loaded trap at the driving frequency of 1.57 MHz and at a pressure of 0.54 MPa. The thermocouple response was continuously recorded for a sonication time of 30 min.

Further temperature measurements *in situ* in the trap where conducted in the presence of a neural cell aggregate. A single neural cell suspension was introduced into the trap with the peristaltic pump. Ultrasound exposure was immediately initiated. Temperature measurements were conducted at the driving frequency of 1.57 MHz and at an acoustic pressure amplitude of 0.54 MPa. The thermocouple response was again monitored for an overall time of 30 min. It must be noted that temperature measurements at 1.96 MPa were conducted with a non-intrusive portable infrared thermometer (Raytek Ltd. UK) rather than with the thermocouple bead, so as to protect the bead itself from any possibility of cavitation onset. Also, measurements

were, in the latter case, conducted only for 30 s, so as to protect the trap from the higher power input that might mechanically stress the glue or other components of the resonator.

3.2.4 Acoustic microstreaming analysis

3.2.4.1 Experimental procedure

Acoustic microstreaming in the ultrasound field was measured in both the presence and absence of a cell aggregate. These experiments were carried out with the following suspensions: a) 1 μm polystyrene fluorescent latex particles diluted in NSM to a concentration of 6.25×10^{-4} % solids and b) a mixture of 1 μm particles at the concentration mentioned above, and neural cells suspended in NSM at a concentration of 5×10^{4}/ml. 1 μm fluorescent latex particles were chosen for the measurement of the acoustic microstreaming of the sound field, as according to the considerations in Chapter 2 (Sec. 2.4.1), they are literally unaffected by the axial and lateral radiation force and act as pure microstreaming tracers. They were also employed to give high particle-image contrast against a black background as required for the particle image velocimetry (PIV) software described in the following (Sec. 3.2.4.2). The size of the cells (~14 μm) suggests that they are affected more by *DRF* (axial and lateral) rather than by the microstreaming drag (Spengler *et al.*, 2003), therefore an aggregate would be expected to be formed in the trap within the first seconds of ultrasound initiation.

The samples (1 μm latex particles alone and a mixture of 1 μm particles and neural cells) were introduced into the trap with the peristaltic pump. The microscope (×10 objective) had been focused on the central plane of the trap at the axial region. The field of view was approximately 1.3 × 0.95 mm^2. The pump was switched off and video recording and sonication were initiated. Exposure times were in the range of 1 to

5 min at pressure amplitudes of 0.54, 0.27 and 0.06 MPa. The process was video recorded and the video sequences were converted into computer files as described earlier (Chap. 2; Sec. 2.2.2 and 2.2.3). Acoustically induced particle interactions were minimised by the appropriate choice of particle concentration (*i.e.* 6.25×10^{-4} % solids) and by analysing the first 0.5 s of each experiment, where most particles and cells were still single unaggregated entities (Spengler *et al.*, 2003).

3.2.4.2 PIV analysis of particle and cell movement

Particle Image Velocimetry (PIV) is a direct measurement technique for obtaining instantaneous whole field velocities based on the two fundamental dimensions of the velocity: length and time (Raffel *et al.*, 1998). The property actually measured in PIV is the distance traveled by particles in the flow within a known time interval. These particles are added to the flow and known as seeding (Dantec Dynamics Software User's guide).

PIV analysis was performed here off-line with the FlowManager software developed by Dantec Dynamics (Denmark). Successive single frames (n~10) were extracted as 8-bit greyscale images from the recorded video sequences. The time points selected were 1 and 3 s after ultrasound initiation. The interlaced images were split into odd and even half images by interpolation. Two-frame cross correlation analysis was then employed. The image interval for every pair of odd and even half-images analysed was set to be 4 μs. The interrogation area was 64 × 64 pixels^2. Interrogation areas were then overlapped by 50% to trace particle positions between two successive frames. This resulted in a 23 × 17 velocity map over the image area for an image size of 768 × 576 pixels^2, *i.e.* 391 vectors in total.

Validation algorithms were then applied so that outliers (*i.e.* erroneous vectors) caused by a low signal-to-noise ration, could be detected and removed. A low signal-to-noise ratio is caused by poor image contrast or when the number of seeding particles within each interrogation area is low. With a large number of seeding particles, there will be many true correlations ensuring a high signal-to-noise ratio and so that a valid displacement measurement will be produced. It is recommended that generally a minimum of 5 particles per interrogation area be monitored for reasonable results using the cross correlation technique (Dantec Dynamics Software User's guide). In the present case ~8 particles per area were analysed fulfilling the above requirement. Additionally, an upper limit of the standard error of the mean of 10% was defined as the maximum tolerable uncertainty of the measured velocity (Spengler *et al.*, 2003). PIV analysis is also sensitive to 'out of focus' particle motion, a feature that could lead to invalid vector maps, particularly in the present case for the data analysed after 1 s of ultrasound initiation. However, as described in Chapter 2 (Sec. 2.4.1) all particles in the ultrasound field were almost instantaneously pushed into the pressure nodal plane and were held in that plane (relocation time into the pressure nodal plane of less than 80 ms has been observed).

The particle velocity field was finally calculated by averaging the data for each individual vector point over the validated maps.

3.2.5 Cavitation monitoring

Analyses of the acoustic emissions were performed as follows: a 5 mm diameter PZ 26 piezoceramic disc was mounted in a cylindrical steel holder. The assembly was coupled to the side of the trap housing by ultrasonic transmission gel (Henleys Medical, Herts, UK). The signals from the microphone went to an Agilent

spectrum analyser (E4401 B, UK). The data were saved as .csv files and further processed in Microsoft Excel.

Neural cells were suspended in NSM at a concentration of 10^6/ml. They were then introduced into the trap with the peristaltic pump. The pump was switched off and the ultrasound exposure (of 1 min duration) was immediately initiated. Experiments were conducted at pressure amplitudes ranging from 0.06 MPa to 1.96 MPa at the driving frequency of 1.57 MHz.

3.2.6 Cell viability tests

3.2.6.1 Non-sonicated samples

Cell suspensions (neural and chondrocyte cells) were placed in a centrifuge tube at room temperature at a concentration of 3×10^6/ml. Cell viability was measured over the following 12 h using 0.4% trypan blue dye (Sigma, UK) or over 2 h using 1 μM ethidium homodimer-1 (EthD-1; Molecular Probes, Inc. Eugene, OR, USA) exclusion. Samples were examined hourly with a bright–line heamocytometer (Reichert, USA) under a Leica DMLS microscope. A positive control for both dyes was obtained by killing the cells with 70% ethanol; all cells were stained in those samples.

3.2.6.2 Cells in the ultrasound trap

Viability assays were performed *in situ* on cells suspended for 1 h in the trap in NSM (neural cells) or serum-free DMEM/Ham's F-12 (chondrocytes) containing the viability markers outlined below. The number of cells that had taken up the dye after 1 min of ultrasound exposure was compared to that after 1 h of ultrasound exposure.

Calcein AM. A stock solution of 1 mM solution (Molecular Probes, Inc. Eugene, OR, USA) in anhydrous dimethylsulfoxide (DMSO) (Sigma, UK) was diluted in culture media to a final concentration of 1 μM. Calcein AM is membrane permeable and is cleaved by esterases in live cells to yield cytoplasmic green fluorescence (calcein); therefore, green fluorescence is an indicator that cells have esterase activity as well as an intact membrane to retain the esterase products (Ikeguchi *et al.*, 2003).

Ethidium homodimer-1 (EthD-1). A stock solution of 1 mM solution of EthD-1 (Molecular Probes, Inc. Eugene, OR, USA) in anhydrous dimethylsulfoxide (DMSO) (Sigma, UK) was diluted in culture media to a final concentration of 1 μM. EthD-1 passes across the compromised membranes of dead or dying cells, binds to nucleic acids and produces a red fluorescence (Ikeguchi *et al.*, 2003).

Mito Tracker Green FM. MitoTracker Green FM (Molecular Probes, Inc. Eugene, OR, USA) is non-fluorescent in aqueous solution but it exhibits a bright green fluorescence once it accumulates in the lipid environment of mitochondria of live cells (Garner *et al.*, 1997). A stock solution of 50 μg of lyophilized solid was dissolved with DMSO to a concentration of 100 μM. For cell labelling, this solution was diluted to 100 nM in culture media. The cells were incubated with the dye for 45 min at room temperature prior to ultrasound exposure.

3.3 Results

The results presented in the following have been derived from experiments with model suspensions (1 μm latex particles) as well as neural and chondrocyte cell (~14 μm in diameter) suspensions of biological interest. The results presented apply to all ultrasound traps and biological systems used in the course of this study. Formation of cell aggregates in the trap was achieved by applying the procedure described in the

following (Sec. 3.3.1). This procedure represents the general protocol followed for all cell suspensions in the course of this study. All experiments were repeated at least twice under the same experimental conditions.

3.3.1 Formation of cell aggregates

Neural cells suspended in neuronal supplemented medium (NSM) and exposed to ultrasound at a pressure amplitude of 0.54 MPa moved into the microscope-focused nodal plane within 1 s under the action of the axial DRF. A small aggregate had formed 3 s later at the central region of the trap as a result of the effect of the lateral DRF_l (Chap. 1; Sec. 1.9.2). Single cells and dendritic small clusters were approaching the main aggregate from all directions in the nodal plane. After a 30 s ultrasound exposure the pressure amplitude was decreased to 0.27 MPa for 5 min. Aggregation continued but at a slower rate. The aggregation process had completed within 5 min of ultrasound initiation, as characterised by the absence of individual cells in the field of view (Fig. 3.3). The pressure amplitude was then further decreased to 0.06 MPa for 1 h, the level at which the acoustic radiation force just balanced the gravitational force on the aggregate and thus maintained the aggregate in suspension.

3.3.2 Temperature measurements

Temperature measurements were conducted *in situ* in a water-loaded trap or in the presence of a neural cell aggregate at a pressure amplitude of 0.54 MPa at the driving frequency of 1.57 MHz.

The thermocouple bead was located at the centre of the trap without effectively disturbing the sound field (in the sense that cell aggregation proceeded in the same manner with or without the thermocouple in place). There was no

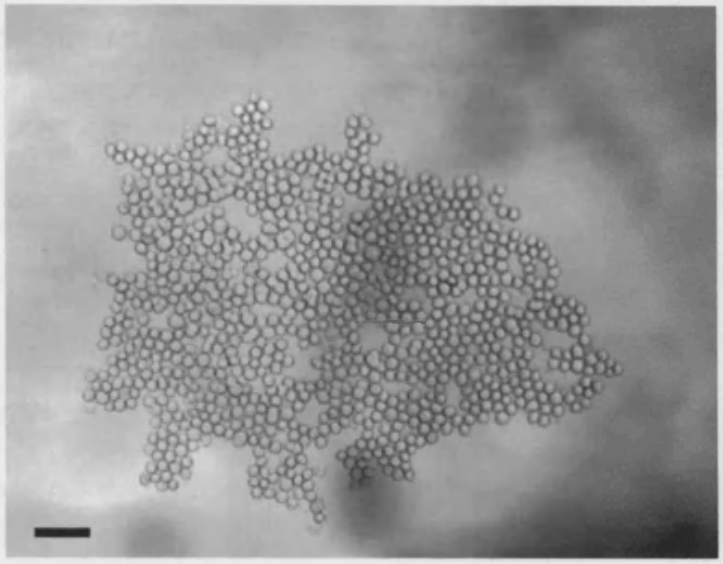

Figure 3.3: Neural cells suspended in the ultrasound trap 30 min after initiation of ultrasound; pressure, 0.06 MPa. Scale bar is 70 μm. Image capture has been performed as in Chapter 4 (Sec. 4.2.1).

measurable movement of the recorder pen over a 30 min ultrasound exposure, chosen to ensure total equilibration. Since a 1 mm pen deflection would have been detectable with confidence, and the sensitivity of the recorder was 2 mm/K, it was shown that the temperature rise in the trap was less than 0.5 K in both cases (*i.e.* trap loaded with water or in the presence of a neural cell aggregate). ΔT was calculated for the different pressure amplitudes P_0 as being $< 0.5\ (P_0 / 0.54)^2$ K, where $P_0 = 0.54$ was the pressure amplitude at which ΔT was estimated. The resulting calculations show that the ΔT was < 0.125 K at a pressure amplitude of 0.27 MPa, whereas at the levitation threshold pressure amplitude of 0.06 MPa ΔT was < 0.006 K. On the other hand, when the pressure amplitude was increased to 1.96 MPa only for 30 s, ΔT was 4 K, as measured with the IR thermometer. These results are summarised later in Table 3.4 (end of Sec. 3.3.6).

3.3.3 Acoustic streaming measurements

The hypothesis underlying the following set of experiments is that the particle and cell behaviour in small pathlength ultrasonic traps is dominated by DRF_I and acoustic microstreaming drag once particles and cells are driven into the nodal plane.

The approach is to observe and characterise how acoustic microstreaming might affect cell aggregate growth and viability, by measuring particle movement velocities in the ultrasound field with or without the presence of a cell aggregate.

3.3.3.1 Analysis of the behaviour of 1 μm latex particles

During all experiments the microscope (×10 objective) was pre-focused at the centre of the trap on the area in the pressure node plane where the cell aggregate was usually formed, *i.e.* the x, y plane half way along the vertical axial height of the sample layer. The first 6 to 8 frames after sound was switched on were not analysed, as the particles had not all yet reached the pre-focused nodal plane. At 0.54 MPa, 1 μm particles in the pressure node plane moved across the field of view. The velocity of streaming in the centre of the area where a cell aggregate was usually formed was on average 250 μm/s at the beginning of sonication (*i.e.* 1 s after ultrasound initiation) (Fig. 3.4a). The streaming changed direction over the next 2 s of sonication and the particles started leaving the area of cell aggregate formation at a velocity of 450 μm/s (Fig. 3.4b). In particular, 1 μm particles followed an 'arc-type' trajectory (Fig. 3.4b) eventually resulting in the formation of a ring. A second ring of particles was also formed close to the central aggregation area. These two counter-rotating vortices were each about 2 mm in diameter and circulated in the node plane (their planes of circulation were parallel to the transducer) (Fig. 3.5). The cell aggregation region was

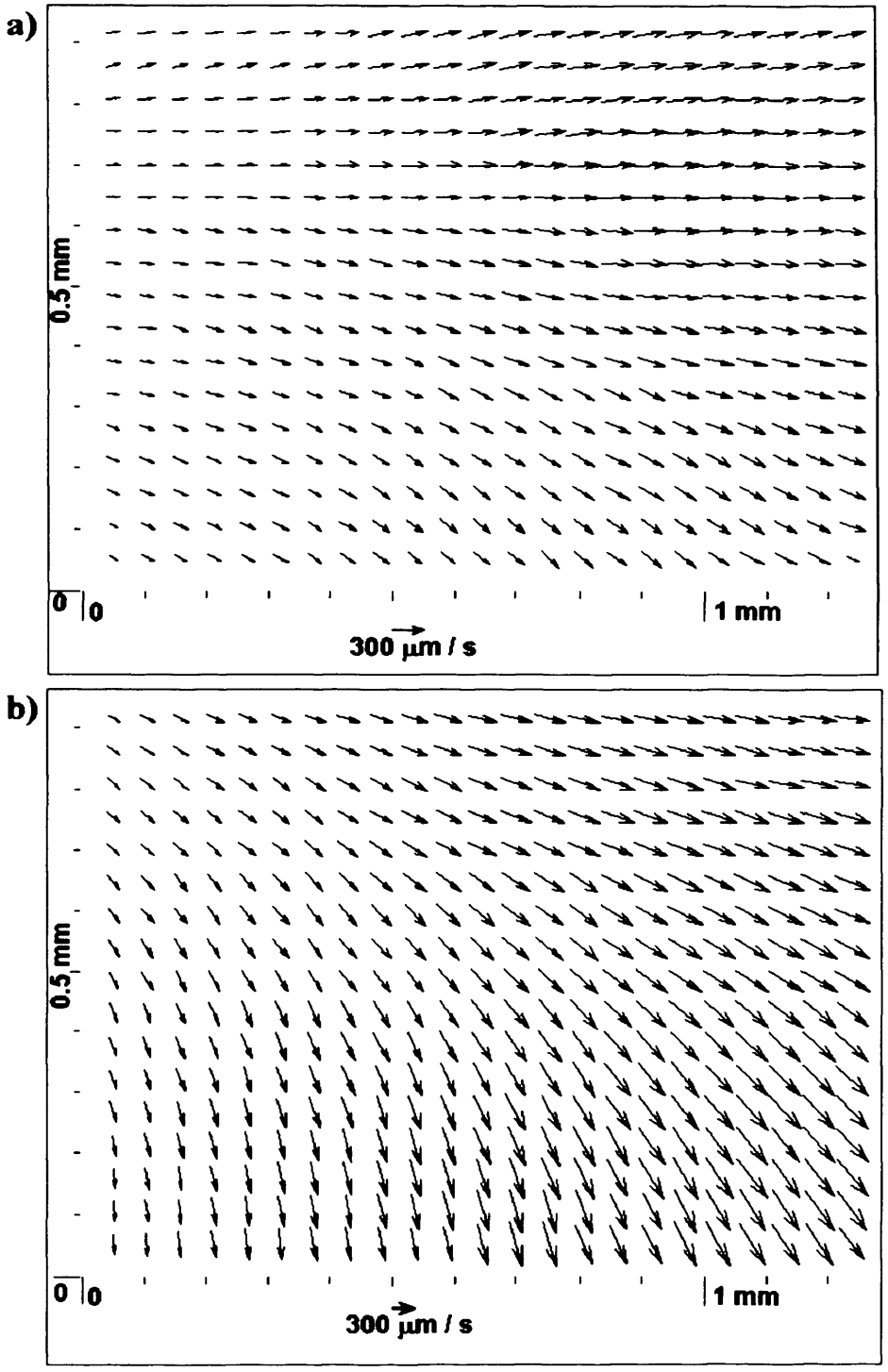

Figure 3.4: PIV analysis of 1 µm diameter latex particles behaviour at the centre of the trap (where an aggregate is usually formed) (a) 1 s after ultrasound initiation and (b) 3 s after ultrasound initiation. The development of the ultimate circulation is already clear at 3 s. P_0: 0.54 MPa.

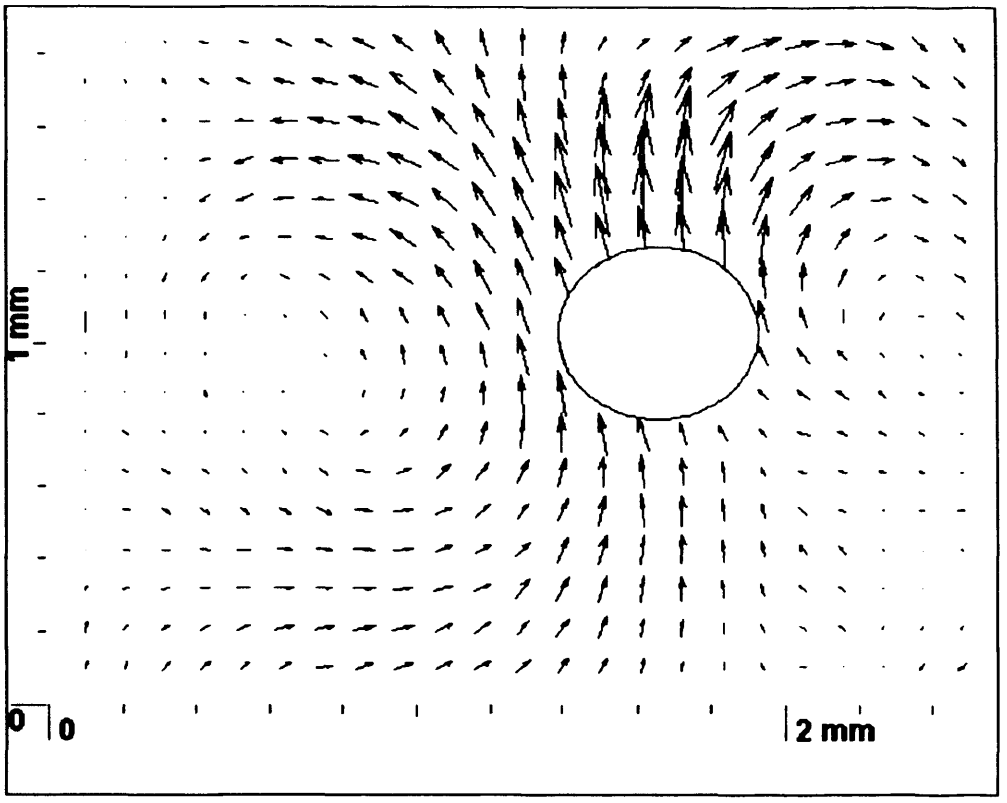

Figure 3.5: Schematic showing the position and direction of the two vortices present in the trap. The aggregation area, located at the overlap of the two vortices, is marked with a circle.

located at the overlap of these rotating vortices, shown schematically in Figure 3.5 with a circle.

A similar pattern was observed at 0.27 MPa although the velocities of streaming were lower, about 70–80 μm/s and 60-65 μm/s after 1 and 3 s of ultrasound exposure respectively. Finally, at 0.06 MPa, streaming could not be visually detected. PIV analysis established very slow movement (3–5 μm/s) of particles across the observed area; however the low velocity of the streaming and superimposed Brownian motion of the particles led to a significant uncertainty in these measurements.

3.3.3.2 Analysis of the behaviour of 1 μm particles in the presence of a neural cell aggregate

The microscope was again focused at the centre of the trap *i.e.* at the aggregate formation area. The first 6 to 8 frames after sound was switched on were not analysed, as particles and cells had not all yet reached the pre-focused nodal plane. At 0.54 MPa, after 1 s of ultrasound application, streaming-convected 1 μm particles moved across the field of view unidirectionally. The direction of particle movement was different to that without cells in the system and the average streaming velocity was 120 μm/s (Fig. 3.6a).

At 3 s after ultrasound initiation, the cell aggregate started forming in the centre of the trap and at the same time the streaming changed its direction: 1 μm particles moved from the aggregate area towards its periphery. At this point the average streaming velocity of the particles was $\leq$ 70 μm/s (Fig. 3.6b; Table 3.4). The cell clusters moving towards the aggregation site changed the local streaming pattern in their close vicinity owing to their size (50-55 μm) and velocity (80–150 μm/s) of their movement: smaller tracer particles were entrapped in vortex-like streaming around the moving cell clusters (Fig. 3.7). Few, if any, particles were left in the microscope field of view after 10 s. At 0.27 MPa the pattern of streaming was similar with average velocities of 80–100 μm/s and 30–35 μm/s after 1 and 3 s of ultrasound initiation respectively (Table 3.4). At 0.06 MPa, the behaviour of 1 μm particles was similar to the one described above in the absence of cells: no streaming was observed in the pressure node plane.

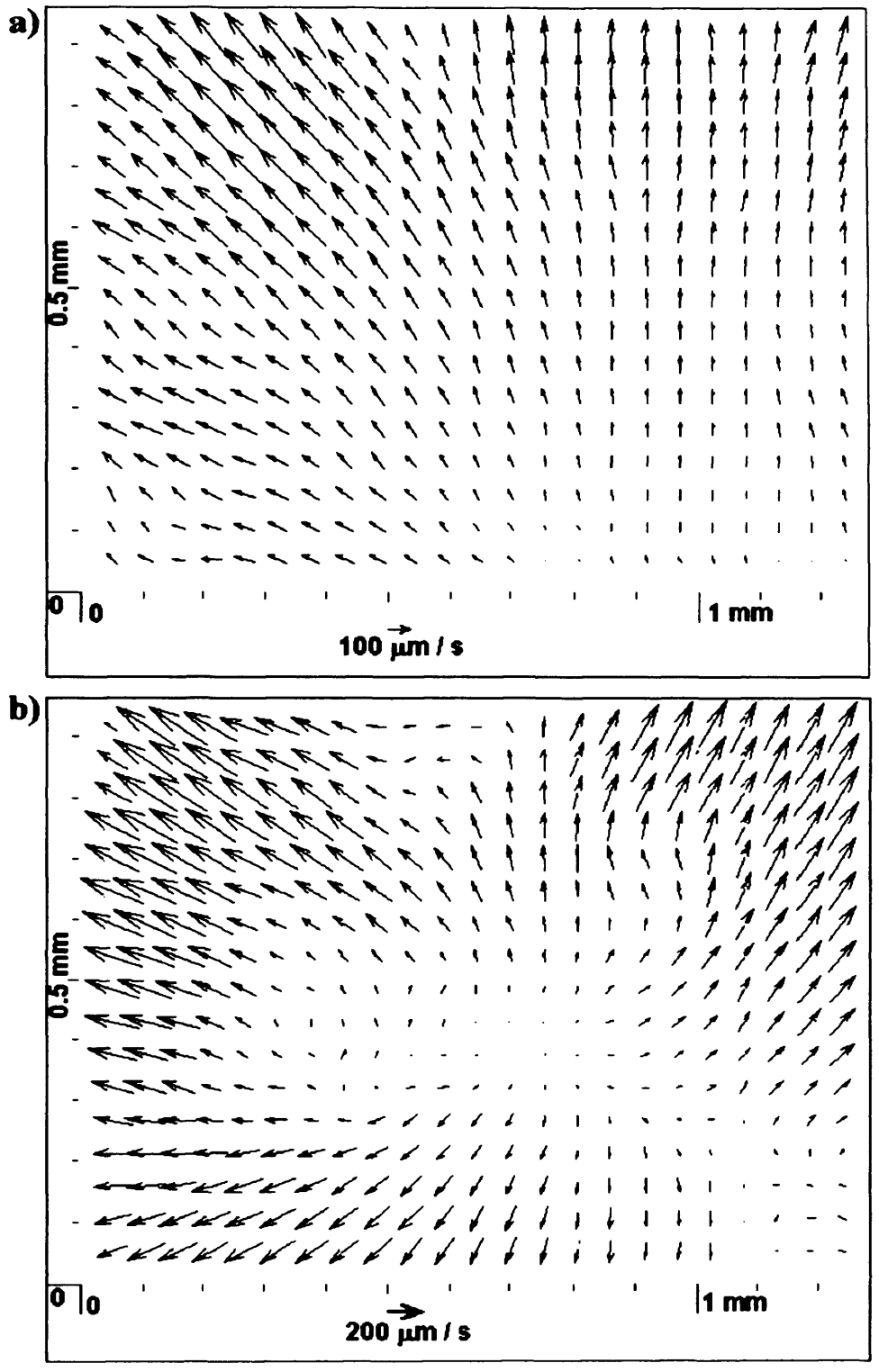

Figure 3.6: PIV analysis of 1 µm diameter latex particles behaviour in the presence of a neural cell suspension at the centre of the trap (a) 1 s after ultrasound initiation and (b) 3 s after ultrasound initiation, when an aggregate has been formed. The presence of the aggregate causes the streaming in the nodal plane to emanate from the centre. The acoustic pressure amplitude was 0.54 MPa.

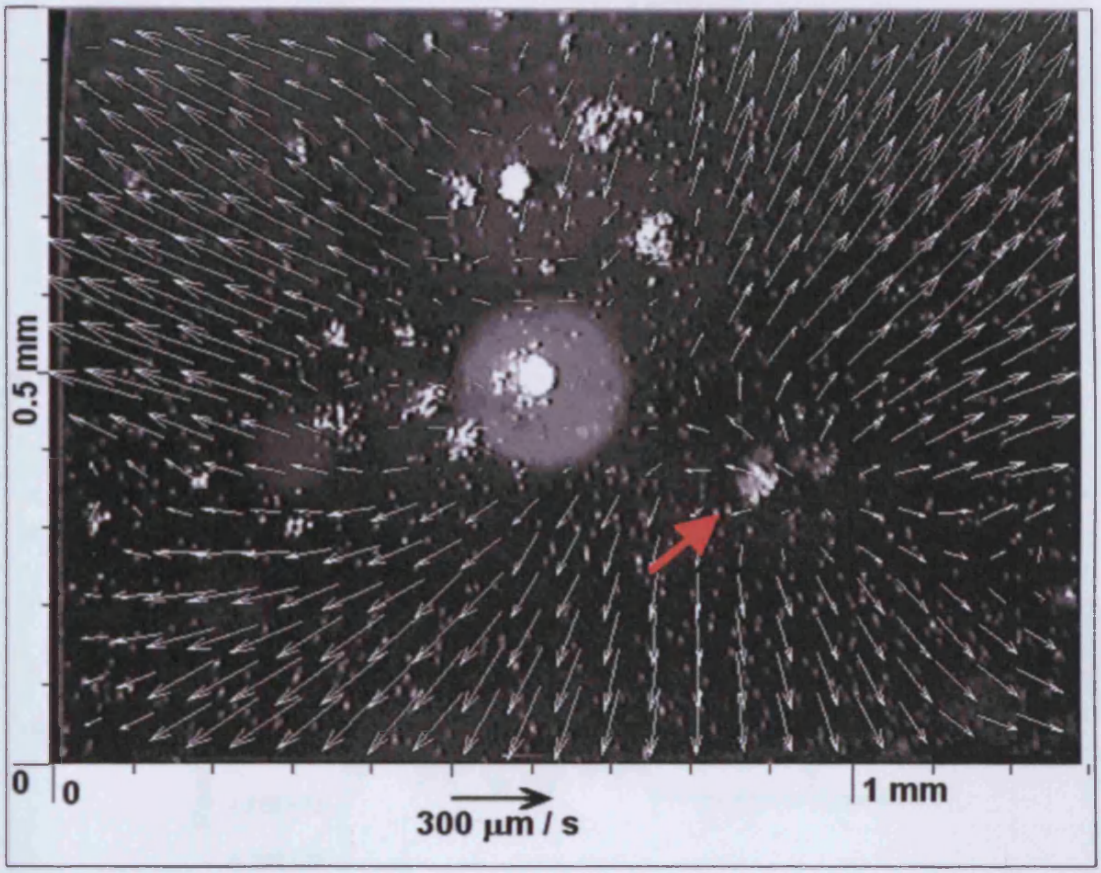

Figure 3.7: PIV field of the velocity distribution of fluorescent latex tracer particles superimposed on a fluorescence micrograph of cells and cell clusters that have captured fluorescent particles as they approach the central aggregation region located at the centre of the trap. Attention is drawn (red arrow) to the disturbance of the flow pattern about the incoming clusters.

3.3.4 Acoustic spectrum analysis

Emission spectra from neural cell samples exposed to ultrasound at the driving frequency of 1.57 MHz at 0.54, 0.27 and 0.06 MPa are shown in Table 3.4. Figure 3.8a shows the acoustic spectrum analysis for the highest operational pressure amplitude of 0.54 MPa. The driving frequency (1.57 MHz) and the first harmonic (3.2 MHz) are clearly seen. No growth of subharmonic (Table 3.4; Fig. 3.8a) was

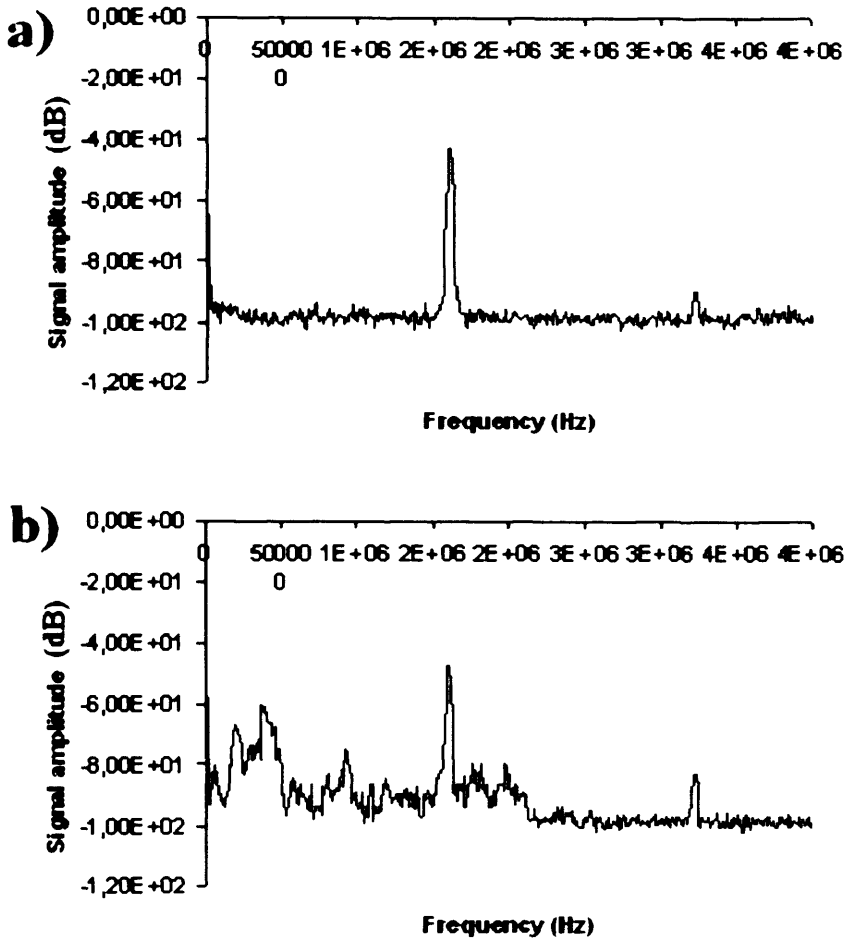

Figure 3.8: Acoustic spectrum analysis (a) for 0.54 MPa, where only the driving frequency (at 1.58 MHz) and the first harmonic (at 3.2 MHz) are detected and (b) appearance of broadband emission at 1.96 MPa.

detected even after 1 h of ultrasound exposure at 0.54 MPa. Similarly, at 0.27 and 0.06 MPa only the driving frequency and the first harmonic could be detected.

Broadband emission, often associated with the occurrence of transient cavitation, was detected only when the pressure amplitude was increased to 1.96 MPa (Table 3.4, Fig. 3.8b). Cells were exposed at 1.96 MPa for only 30 s, so as to protect the trap. However, at the pressure amplitudes employed in the cell suspensions sonicated in the present work, cavitation activity does not occur.

3.3.5 Cell viability

X^2-tests for trypan blue assays at a number of times between 0 and 12 h and EthD-1 assays at times between 0 and 2 h showed that there was no significant association between percentage of dead cells in non-sonicated samples and time. The percentages of dead cell in non-sonicated samples determined from the trypan blue and EthD-1 assays were 2% and 2.4% respectively.

Duplicate viability assays of cells in levitated monolayers were performed *in situ*. The low magnification micrograph of neural cells in EthD-1 (Fig. 3.9a) shows an entire aggregate while the low incidence of stained dead cells in that aggregate is emphasised in Figure 3.9b. Similarly, Figure 3.9c shows the high incidence of live cells in an aggregate of chondrocyte cells, whereas Figure 3.9d shows that the individual organelles, *i.e.* mitochondria, of single cells remain functional. These assays showed that cell viability in the ultrasound trap was >99 % and had no detectable dependence on exposure time over the 1 h period.

3.3.6 Monolayer development independence of acoustic pressures and cell concentrations

The viability assays described in Section 3.3.5 were performed in aggregates suspended in the trap at P_0 equal to 0.54 MPa for 1 h. Experiments were also performed where P_0 was maintained at 0.54 MPa for only 30 s, *i.e.* until the aggregate was formed. P_0 was then decreased to 0.27 MPa for 5 min and then to 0.06 MPa, the level at which the acoustic radiation force just balanced the gravitational force on the aggregate and thus levitated the monolayer in suspension, according to the protocol described in Section 3.3.1. Cell viability over time was again >99 %.

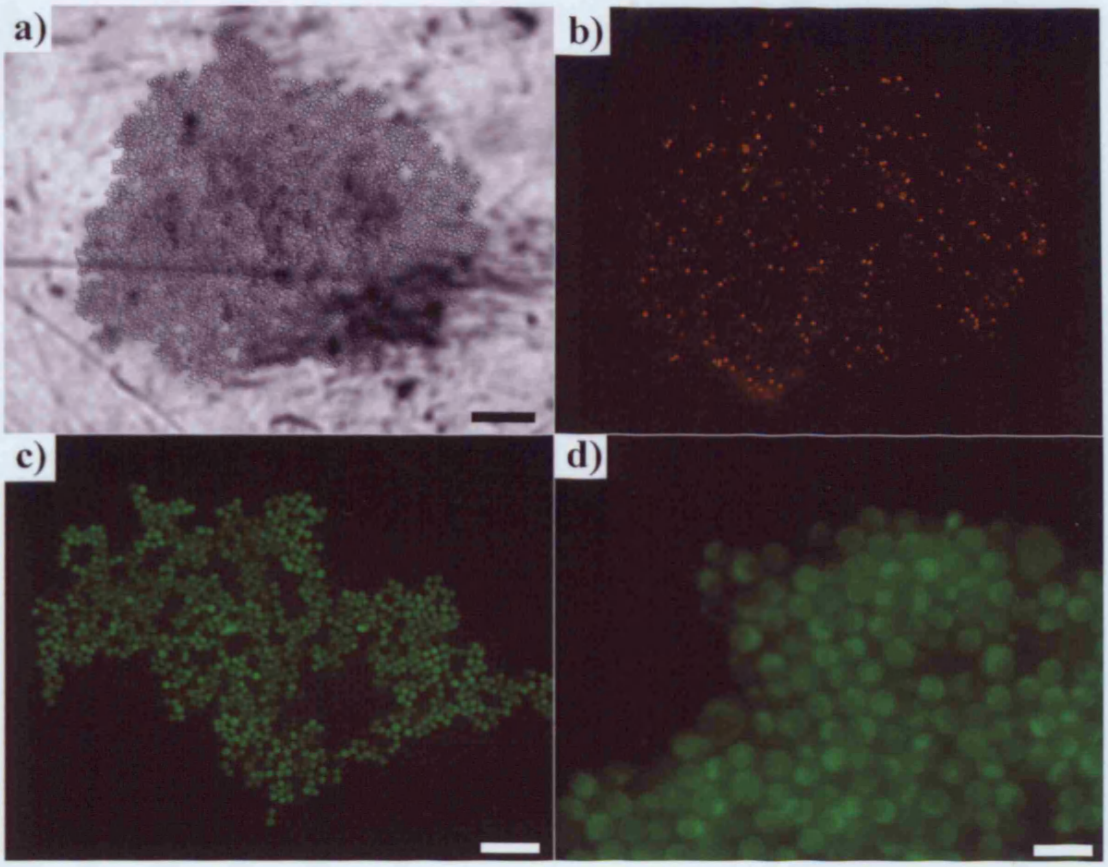

Figure 3.9: Viability assays. (a, b) Staining of dead neural cells (prepared as in Chap. 4; Sec. 4.2.2) with EthD-1, bright field and fluorescence microscopy respectively at time (t) = 60 min after ultrasound initiation (Scale bar is 250 μm); (c) Staining of live chondrocytes (prepared as in Chap. 5; Sec. 5.2.2) with Calcein AM at (t) = 15 min (Scale bar is 100 μm); (d) Staining of mitochondria of live chondrocytes with MiToTracker green FM at (t) = 60 min (Scale bar is 20 μm).

Nutrient availability in the trap was tested by reducing the cell concentration to 10^4/ml (*i.e.* the aggregate consisted of approximately 550 cells) and pumping medium through the trap at intervals. The viability of cells remained at >99% and showed no dependence on cell concentration (ranging from 10^4 to 3×10^6) or medium flow.

Table 3.4: Tabular summary of the physical conditions in the trap at various pressure amplitudes. (Note that the exposure protocol during aggregate development and levitation was 30 s exposure at 0.54 MPa, 2 min exposure at 0.27 MPa and 1 h exposure at 0.06 MPa).

Sound Pressure Amplitude (MPa)	***Temperature Measurements***		***Acoustic Microstreaming Analysis***		***Acoustic Spectrum Analysis***	
	Ultrasound Exposure Time (min)	Temperature rise ΔT (K)	Ultrasound Exposure Time (s)	Streaming Velocity (μm/s)***	Ultrasound Exposure Time (min)	Cavitation Emissions
1.96	0.5	4**	N.A	N.A	0.5	White noise
0.54	30	< 0.5*	3	≥70	60	None
0.27	30	< 0.25*	3	30-35	2	None
0.06	30	< 0.01*	3	3-5	2	None

*ΔT was calculated for different pressure amplitudes P_0 as being $<0.5\ (P_o/0.54)^2$ K, where P_o =0.54 was the pressure amplitude at which ΔT was estimated and 0.5 K was the smallest temperature rise clearly detectable by the recorder.

** ΔT at 1.96 MPa was measured using a portable infrared thermometer (Raytek Ltd. UK) rather than with the thermocouple bead.

***The streaming velocities refer to the condition where an aggregate has been formed at the centre of the trap, *i.e.* after 3 s of ultrasound exposure.

3.4 Discussion

3.4.1 Temperature measurements

The principal sources of heat generation in ultrasonic systems would arise from sound absorption in the aqueous phase and from heat generated by losses in the transducer itself. For a particular system operating at a particular frequency both of these effects would be expected to generate heat at a rate proportional to the square of the sound pressure amplitude. Table 3.4 shows the temperatures estimated for the lower pressure amplitudes employed during the levitation of the aggregate. The response of the pre-calibrated thermocouple (Sec. 3.2.3) to temperature change while in the trap was checked by placing iced water on the reflector surface in the absence of ultrasound. The thermocouple output responded accordingly. An independent estimate of temperature increase in the resonator was obtained when the pressure amplitude was increased to the transient cavitation threshold of 1.96 MPa, as reported in Section 3.3.3. The thermocouple was not in the system for this experiment. The temperature increase, estimated with an IR surface thermometer after 30 s exposure to ultrasound was 4 K. Assuming that the steady state temperature rise is approximately proportional to the heat input rate, an estimation of temperature increase at the highest continuous operating pressure of the trap was then $4 / [(1.96 / 0.54)^2]$ K or 0.3 K which is less than the upper limit of 0.5 K (Table 3.4) from the thermocouple experiment. Accordingly, the estimated temperature increase at the threshold pressure amplitude was 3.7×10^{-3} K. Temperature increases in the trap are therefore smaller even than those that might be expected from fluctuations in the control of a laboratory incubator. The resulting temperatures are also very much smaller than those (41-44°C) applied for times of 30 min or longer to synchronise the cell cycles of tissue cultured cells without affecting cell viability (Kühl *et al.*, 2000; Roigas *et al.*, 2002). It is therefore

concluded that the temperature increases in the trap do not reach values that might modify or compromise normal cell function.

3.4.2 Microstreaming

Investigation of the streaming pattern was made possible with the use of 1 μm latex particles, which, following the rationale already described in Chapter 2 (Sec. 2.4.1), were hardly affected by the DRF and therefore acted as tracers for the streaming. This was consistent with the different dependence of microstreaming (linear dependence) and radiation force (third power dependence) on the particle diameter (Spengler *et al.*, 2003).

Microscopic observation of the movement of 1 μm latex spheres at the highest operational pressure amplitude (drive frequency 1.57 MHz) showed that particles moved across the field of view (Fig. 3.4a, b) and did not form any aggregates. Thus, microstreaming prevented the aggregation of small particles. However, Limaye and Coakley (1998) have previously reported that aggregation of *E. coli* bacteria (approximately 1 μm in size) can occur at considerably high bacterial concentrations (16% v/v). It is therefore reasonable to assume that some aggregation of 1 μm particles might also take place in the ultrasound trap at higher particle concentrations.

The corresponding PIV maps indicating the movement pattern and the particle velocities of each image are shown in Figure 3.4a, b. Comparing the velocity-proportional length of the vectors in Figure 3.4a, b, a significant increase from about 250 μm/s (1 s) (Fig. 3.4a) to about 450 μm/s (3 s) (Fig. 3.4b) is seen at the area where the aggregate is formed.

The velocity of 1 μm diameter latex particles in an ultrasound trap consisting of a rectangular transducer with a circular back electrode has earlier been reported by

Spengler et al. (2003). Streaming velocities of the same order of magnitude as those presented in this study (*i.e.* 150 μm/s) were reported at a pressure amplitude of 0.5 MPa in a 3 MHz field. These authors considered their streaming pattern as a classic form of Rayleigh streaming between parallel walls, *i.e.* the streaming flowed laterally from a central source point towards the periphery of the sonicated volume (Spengler *et al.*, 2003). Rayleigh streaming of 1 μm particles with a velocity of 166 μm/s was also reported for similar ultrasound traps at pressure amplitudes of 0.52 MPa (Kuznetsova and Coakley, 2004). However, in the present case the classical from of Rayleigh streaming was not observed. 1 μm particles did not leave the central 'aggregation' area but followed an 'arc-type' trajectory (Fig. 3.5) eventually resulting in the formation of two rings, each about 2 mm in diameter, with the cell aggregation region located at the overlap of these rotating vortices (Fig. 3.5). These two counter-rotating vortices circulated in the node plane (their planes of circulation were parallel to the transducer). This kind of streaming has been reported earlier for similar standing wave resonators and for the same range of frequencies and acoustic pressures (Kuznetsova and Coakley, 2004). These authors ruled out the possibility that these vortices are hydrodynamically linked to the walls of the trap and therefore are not Rayleigh or Schlicting streaming connected. They also reported that these vortices are not of a centrifugal origin or cavitation induced, but possibly they originate from spatial variations in the later radiation pressure distribution.

At a pressure amplitude of 0.27 MPa the same movement pattern was observed although the velocities of streaming were lower, about 70–80 μm/s and 60-65 μm/s after 1 and 3 s of ultrasound exposure respectively. As the acoustic particle velocity is linearly proportional to the acoustic pressure amplitude in the trap, significantly lower particle velocities measured at 0.27 MPa were expected.

On the other hand, 1 μm latex spheres in the presence of a neural cell suspension moved unidirectionally after 1 s of ultrasound exposure at a velocity of 120 μm/s (Fig. 3.6a). 2 s later, as the neural cell aggregate started forming at the centre of the trap, particles moved from the central aggregate area towards its periphery at a velocity of 70 μm/s (Fig. 3.6b). The streaming field shown in Figure 3.6b, is not perfectly symmetrical to the aggregate formation area. However, the streaming pattern seems to be close enough to Rayleigh's streaming in the way this has been described in a cylindrical ultrasound field by Spengler et al. (2003) and Kuznetsova and Coakley (2004), even though assumptions (for example a perfect plane standing wave was not present in the volume due to inhomogeneous radiation and sound reflection (Spengler *et al.*, 2003)) for Rayleigh's model were not met in the experiments described here.

Cell clusters that were moving towards the aggregation area changed the local streaming pattern and the sound field properties (*e.g.* acoustic pressure) in their close vicinity owing to their size (50-55 μm) and velocity (80–150 μm/s) of their movement. It was observed that smaller tracer particles were entrapped in vortex-like streaming around the moving cell clusters (Fig. 3.7).

The effect of a streaming velocity of 70 μm/s (Table 3.4) on cells at the initial period of aggregate formation (P_0 = 0.54 MPa) can be set in the context of hydrodynamic stresses to which cultured cells are routinely exposed in general preparation procedures *e.g.* during centrifugation, as follows: the question to be asked is 'what centrifugal force would need to operate on a cell of radius a to drive it through a fluid of viscosity η at a velocity v = 70 μm/s?' The centrifugal force is given by Equation 3.1

$$F_c = V(\rho_P - \rho_O)\omega^2 r_\alpha \qquad (3.1)$$

where ω is the angular frequency of the centrifuge and r_a is the radius of the centrifuge arm. The Stokes drag is given by Equation 3.2

$$F_{St} = 6\pi\eta\alpha v \tag{3.2}$$

That force can be determined by setting the centrifugal force (F_c) equal to the Stokes drag (F_{St}) on a cell when fluid flows past at 70 μm /s, *i.e.*

$$V(\rho_P - \rho_O)\omega^2 r_a = 6\pi\eta\alpha v \tag{3.3}$$

When the viscosity is taken as 10^{-3} kg $s^{-1}m^{-1}$, and a and ρ_p are measured as 7 μm and 1,058 kg/m^3 respectively, then $\omega^2 r_a$ = 111 m/s^2 = 111/9.81 g = 11.3 g. The cells in these experiments were prepared by centrifugation at 28 g for 5 min. The related hydrodynamic stress is therefore greater than that experienced by cells in an acoustic streaming flow of 70 μm/s for 30 s. The stress falls by the square of the pressure amplitude so that it is reduced 81 fold when the pressure amplitude is reduced from 0.54 to 0.06 MPa for most of the sonication exposure.

3.4.3 Acoustic spectrum analysis

The emission spectra from neural cell samples exposed to ultrasound at 0.54, 0.27 and 0.06 MPa (Table 3.4, Fig. 3.8a, b) showed no growth of subharmonic (Table 3.4) even when the sample at 0.54 MPa was exposed for 1 h. Broadband emission, often associated with the occurrence of transient cavitation (Tezel *et al.*, 2002), was detected only when the pressure amplitude was increased to 1.96 MPa (Table 3.4, Fig. 3.8b). This high cavitation threshold for a standing wave system is consistent with the

high value of 3.5 MPa at a frequency of 1.25 MHz reported for filtered water samples in the classical standing wave work of Barger (1964).

The detection system employed in the present work was sensitive enough to detect subharmonic emission when cavitation was induced at 0.98 MPa by seeding the samples with acoustic contrast microbubbles that helped reduce the cavitation threshold pressure (Khanna *et al.* 2003).

In the present work cavitation activity does not occur in the cell suspensions sonicated at 0.54, 0.27 and 0.06 MPa. Additionally, microscopic observation of cells at a higher magnification level (×50 objective and 0.5×TV adaptor) showed no apparent stress-related shape changes even when cells were exposed to ultrasound at the highest operational acoustic pressure amplitude (0.54 MPa).

3.4.4 Acoustic interparticle attraction

It has been shown in Chapters 1 and 2 (Secs. 1.9.4 and 2.5) that it is possible to quantify the extent to which ultrasonic interaction forces might modify the probability that particles will stick on contact; the ultrasonic interaction forces were quantified and compared with the influence of factors such as the van der Waals interaction and electrostatic repulsion normally governing colloidal interactions. This approach has also been used to calculate the attractive acoustic force between ultrasonically agglomerated cells of 10 μm diameter and compare it to the van der Waals force (Coakley *et al.* 2004). Coakley et al. (2004) showed that the attractive acoustic force equals the van der Waals force at surface separations of 34 nm when the pressure amplitude is 0.25 MPa in a 1.5 MHz trap.

For the 14 μm diameter cells examined in the present study the acoustic force initially (*i.e.* when the pressure amplitude is 0.54 MPa, 30 s of ultrasound exposure)

equals the van der Waals force at a surface separation of 25 nm. The van der Waals force dominates the essentially constant acoustic force at smaller separations. When the pressure amplitude is reduced to 0.27 MPa the acoustic force decreases and is less than the van der Waals attraction when the separation is less than 50 nm. Finally, when the pressure amplitude is reduced to 0.06 MPa during aggregate levitation, the acoustic interaction is less than the van der Waals force at separations less than 225 nm and is negligible at the surface separation at which receptors operate. The van der Waals force even at a separation distance of 24 nm is only 5.8 pN. This force is much smaller that the 60 pN required to disrupt even a single cadherin-cadherin bond (Perret *et al.*, 2004) and negligible compared to the 20 nN required to separate two sarcoma S180 cells that has been in contact for just 30 s (Chu *et al.*, 2004). It is concluded that the standing wave trap operates only to concentrate cells locally, as in tissue, and does not modify the *in vitro* expression of surface receptor interactions.

3.4.5 Viability assays

Fluorescence assays showed that cell viability in the ultrasound trap was >99% and had no detectable dependence on exposure time over the 1 h period examined, *i.e.* 1% cell death arises as a result of the cell preparation procedures. The conclusion that the ultrasound trap did not compromise the viability of cells during exposure is consistent with the general experience of investigators of biological effects of ultrasound on cells *in vitro* when cavitation or excessive heating does not occur (Doblhoffdier *et al.*, 1994; Wang *et al.*, 2004).

3.5 Preliminary conclusions

In this Chapter the ultrasound trap has been employed to form and levitate a neural cell aggregate in suspension. Several physical parameters including, temperature increase and acoustic streaming, cavitation and intercellular forces that might influence the function of cells in the trap were quantified. It was shown that the temperature increase was <0.5 K at the highest pressure employed for 2 min at the beginning of cell aggregation and was estimated to be of the order of 0.005 K during the longer low pressure exposures maintaining the aggregate in suspension.

Acoustic streaming velocities about the aggregate exposed the cells to less stress than the gentle centrifugation processes employed during cell suspension preparation. No acoustic emissions, that are the signature of cavitation activity, were detected during the exposures.

The attractive intercellular acoustic forces were initially (30 s) equal to the normal attractive van der Waals interaction between cells at a cell surface separation of 25 nm a distance greater than the range of surface receptor molecules. Acoustic interaction equalled the van der Waals force at a separation of 225 nm when the pressure amplitude was reduced to 0.06 MPa during aggregate levitation. Consequently, the van der Waals force dominated any ultrasonic contribution at the low separations at which homophilic surface receptors engage.

Additionally, a range of viability assays performed with neural cells and chondrocytes showed that the wellbeing of the cells is not compromised when held in suspension in the ultrasound trap. Values of >99% for the cell viability were measured and had no detectable dependence on exposure time over the 1 h period examined.

In general, the structure of the aggregate, the outcome of cell-cell interactions in a suspended aggregate and their consequences for cell behaviour are not

compromised by or dependent on the physical environment of the 2-D trap described here. The next Chapter will introduce neural cell-cell interactions with particular emphasis on the molecular consequences following receptor engagement in apposing cells.

Chapter 4

Molecular adhesion development in a neural cell monolayer forming in an ultrasound trap

4.1 Introduction

Intercellular adhesion is a fundamental biological property in multicellular organisms and plays a key role in processes such as tissue construction (Takeichi, 1991), embryonic development (Hynes, 1996), differentiation (Klimkovsky and Parr, 1995) and wound healing (Yamada and Kemler, 2002) as well as in the field of tissue engineering (Pearson *et al.*, 2003). The cadherin superfamily (Chap. 1; Sec. 1.2.4) of homophilic adhesive membrane glycoproteins has been implicated in many processes such as cell segregation, proliferation (Takeichi, 1991) and invasive behaviour (Mareel and Leroy, 2003). Functional cadherin receptors can influence the reorganisation of the actin cytoskeleton (Chap. 1; Sec. 1.4) as well as the formation of adhesive structures such as adherens junctions (Tepass, 2002; Perego *et al.*, 2002). Cadherin association with the actin cytoskeleton is mediated (Braga, 2002; Gooding *et al.*, 2004) by the intracellular proteins α-catenin, β-catenin, plakoglobin and p120 (Chap. 1; Sec.1.3.2; Fig. 1.5). The actin cytoskeleton brings about cell movements and morphological interactions that underlie normal cell shape (Zicha *et al.*, 2003).

This chapter will present an evaluation of the neural cell line (*i.e.* a homogeneous group of cells derived from a single conditionally immortalised primary cell) 921203-6 as a model cell system to study cell-cell adhesion in an ultrasound trap.

The advantages of this system are given below. The 921203-6 cell line is clonal (C6) and able to replicate as a homogeneous population of progenitor cells. No crisis has yet been reached, even after 120 doublings. A second advantage is its conditional immortalisation. Regulatable oncogenes for immortalisation can and have been used to allow the *in vitro* and *in vivo* differentiation of the resulting cell lines (Stringer *et al.*, 1994). As previously described by Stringer and colleagues (1994), immortalisation was achieved by transduction with retroviral particles containing a construct (tsA58) incorporating a retroviral long-terminal repeat (LTR) region (promoter/enhancer region), (ts) SV40-T and a resistance marker to geneticin ($G418^r$) (Noble *et al.*, 1992). The (ts) SV40-T construct is a regulatable oncogene; at 33°C (permissive temperature) the large T antigen is expressed. Upon temperature increase (39°C, non-permissive temperature), the gene product degrades to an inactive form, the mitogenic drive is removed and the immortalised cells differentiate down one of at least 3 different neural routes. The resistance marker ($G418^r$) allowed the selection of transduced cells and so the elimination of all non-immortalised cells.

C6 neural cell 2-D aggregates (cell monolayers) were synchronously and rapidly (within 30 s) formed and levitated, away from any substratum, in suspension. The rate of membrane-membrane spreading and the distribution of NCAM, N-cadherin and F-actin were monitored over a 30 min period. The distribution of these molecules changed significantly with time. These differences were quantified by image analysis.

The chapter will also describe the different approaches followed to investigate the regulation of cell-cell adhesiveness. The findings provide insight into the roles of the different receptor molecules and how these interact to provide an organised outcome.

4.2 Materials and Methods

4.2.1 Acoustic trap, optical system and experimental procedure

The acoustic trap employed here for cell aggregation and molecular adhesion has already been described in Chapter 3 (Sec. 3.2.1). The trap was manually driven with a function generator and an oscilloscope as reported in Chapter 3 (Sec. 3.2.1). Microscopic observations were performed with a fast, high-resolution CCD F-view camera (12-bit depth) mounted on an Olympus BX41M reflection epi-fluorescent microscope (Appendix B) via a 0.3× TV adapter (U-PMTVC). Samples were introduced into the trap at room temperature with a 2 ml sterile syringe (Plastipak, Becton Dickinson, UK). Ultrasound exposure was then immediately initiated. Images were captured and processed using the analySIS 3.1 software.

4.2.2 Culture of 921202-6 (C6) neural cells

C6 neural cells were maintained as a replicative culture at 33°C (the permissive condition for the immortalising oncogene SV40-T), under an atmosphere of 95% air and 5% CO_2, in neuronal supplemented medium (NSM) (Appendix A) and supplemented with 5 ng/ml fibroblast growth factor (FGF-2) (Sigma, UK) (Stringer *et al.*, 1994). The cells were plated on gelatin-coated plastic culture flasks that had been dried and UV-irradiated overnight, followed by poly-L-lysine addition (1 mg/ml, Sigma, UK). 2.5 ng/ml of FGF-2 was added as daily maintenance of trophic support. Half the medium was changed every third day. At the confluence phase cells were rinsed with Dulbecco's Phosphate Buffered Saline (Sigma, UK) (DPBS) without Ca^{2+} or Mg^{2+}. Cells were then treated with 1 ml of ethylenediaminetetraacetic acid (EDTA) (200 μg/ml) for 30 s to release cells from the culture flask surface. 5 ml of NSM were then added. One sixth of the cells were plated

to a fresh gelatin/poly-L-lysine coated flask. The remaining cells were centrifuged at 28 g, resuspended in NSM, counted on a Bright-line haemocytometer (Reichert, USA) and finally diluted to the desired concentration.

4.2.3 Test of cell integrity

Assays that are more sophisticated than those described in Chapter 3 (Sec.3.2.6.2) were performed *in situ* on cells suspended for 1 h in the trap in NSM containing the markers outlined below.

ApoAlert Annexin V. Annexin V-FITC was used along with propidium iodide (PI) (BD ApoAlert Annexin V Apoptosis kit, BD Biosciences, UK) to identify very early and late apoptotic cells respectively. Annexin-FITC stains only early apoptotic cells as it is based on the observation that, approximately 1 h after initiating apoptosis, the membrane phospholipid phosphatidylserine (PS) translocates from the inner face of the plasma membrane to the cell surface (Martin *et al.*, 1995). Propidium iodide stains late apoptotic cells and necrotic cells when the plasma membrane has become significantly permeable.

Neural cells were subcultured as described above and diluted to a concentration of 2×10^5/ml. The sample was centrifuged at 28 g for 5 min. The supernatant was removed and 200 µl of 1× binding buffer (provided as part of the apoptosis kit) were added. 5 µl of annexin V-FITC (20 µg/ml in Tris-NaCl) and 10 µl of propidium iodide (50 µg/ml in 1X binding buffer) were added. The sample was incubated at room temperature in the dark for 15 min. Finally, NSM medium was added to achieve a cell concentration of 10^5/ml. The final dye concentrations were 0.25 µg/ml and 1.2 µg/ml respectively. A second non-sonicated cell sample was incubated for 48 h at 39°C to induce apoptosis (positive control).

Calcein AM and MitoTracker Green FM assays were also performed as described in Chapter 3 (Sec. 3.2.6.2).

4.2.4 Void analysis

Images of cell aggregates suspended in the trap (cell concentration of 5×10^5/ml) were captured and processed using the analySIS 3.1 software. The objective magnification used was ×50, therefore a single microscope field contained only part of an aggregate. The areas of the voids (cell-free regions within the aggregate periphery) were outlined manually using the free-hand tool. The percentage of the void area in a field of view was calculated as follows: the void area (Chap. 2; Sec. 2.2.6.2) after 8 and 30 min of ultrasound exposure was divided by the initial void area (*i.e.* after 1 min of initiation of ultrasound) of the part of the aggregate in the field of view.

4.2.5 Rate of membrane spreading

The extent of membrane spreading was assessed by measuring a) the 'outer edge' separation distance of two cells (indicated in Fig. 4.4a with range (1)) and b) the 'width' of the tangentially developing contact area of the cells (indicated in Fig. 4.4a with range (2)) over a time period of 1 h.

4.2.6 Immunolabelling

The concentration of C6 neural cells introduced to the trap was 3×10^6 cells/ml. An aggregate of significant size (*i.e. ca.* 1 mm diameter) was formed within 30 s of ultrasound exposure. Aggregates were held in the trap for 1, 8 and 30 min. They were then slowly removed using a 2 ml sterile syringe, placed on a HistoBond microscope

slide (RA Lamb, UK) and fixed with 90% ethanol. The slides were then rinsed with saline.

Filamentous actin (F-actin) was labelled by adding a few drops of Phalloidin-FITC conjugate (5 μg/ml; Sigma, UK) or Phalloidin-AlexaFluor 488 conjugate (2 U/ml; Molecular Probes, Inc. Eugene, OR, USA). The slides were incubated at room temperature in the dark for 1h, rinsed and mounted in Vectashield (Vector, UK) prior to examination. The integral intensity of the phalloidin labelling at the cell interface was quantified by placing a rectangle provided by the analySIS 3.1 software, to contain the interface of each of 50 randomly selected pairs of cells. The integral intensity of an image is defined for this purpose as the sum of all the intensities within the defined area multiplied by the pixel area (analySIS 3.1 User's guide), and it is used here as an indicator of change in the amount of the labeled molecule that might reasonably be expected to reflect the degree of adhesiveness of the neural cell system.

Samples prepared and fixed as described above were also assayed for N-cadherin and NCAM. The fixed samples were serum blocked at room temperature with 100 μl of goat serum (DAKO, UK) at 1:20 dilution in PBS for 20 min, and incubated with the primary antibody (monoclonal anti-A-CAM or anti-NCAM, 5 μg/ml, Sigma, UK) overnight at 4°C. After washing in PBS, samples were incubated with Alexa 488 conjugated anti-mouse IgG (5 μg/ml, Molecular Probes, Inc. Eugene, OR, USA) for 1 h. After further washing (×3), specimens were mounted in Vectashield (Vector, UK) prior to examination.

Immunolabelling of non-sonicated neural cells was performed on cells (10^6 cells/ml) retained for 1 h in suspension in NSM. A 100 μl cell suspension aliquot was placed on a Histobond slide, fixed and separately stained for NCAM, N-cadherin and F-actin.

4.2.7 Modulation of the extracellular [Ca^{2+}] and cell surface NCAM density

Neural cells were prepared (to a concentration of 3×10^6/ml) as described in Section 4.2.2, and then subjected to different treatments prior to introduction to the trap as it will be described in the following sections. In all cases, cells were suspended in the trap for an overall period of 30 min. The cell aggregates were then removed, placed on HistoBond slides and immunolabeled for F-actin as detailed in Section 4.2.6. These series of experiments were conducted in order to examine the influence of free extracellular [Ca^{2+}] (Sec. 4.2.7.1) and modulation of cell surface NCAM density (Sec. 4.2.7.2) on the development of the neural cell actin cytoskeleton.

4.2.7.1 Calculation of free [Ca^{2+}] in NSM

Free [Ca^{2+}] was calculated in NSM solutions containing 0, 1, 3 and 10 mmol/L of the chelator EDTA. Chelation is a special case of complex formation in which a compound (chelator or chelating agent) forms a complex compound with metal ions, the chelate (Hill and Holman, 1995). This is an equilibrium reaction and is shown for Ca^{2+} in the following:

$$Ca^{2+} + H_2EDTA^{2-} \rightleftharpoons CaEDTA^{2-} + 2\,H^{+} \qquad (4.1)$$

The dissociation constant Kd_{Ca} is $10^{-10.7}$ (Rauscher *et al.*, 1982). NSM (0 mM in EDTA) contains 1.05 mM of Ca^{2+} (NSM contains Dulbecco's Modified Eagles Medium (DMEM) and Ham's F-12 medium at a ratio of 1:1 (Appendix A).

The free [Ca^{2+}] contained in NSM that is 10 mM in EDTA is calculated as follows:

$$[Ca^{2+}] = \frac{[CaEDTA]}{[EDTA]} \times K_{dCa} \quad (4.2)$$

Where [CaEDTA] = 1.05 mM and free [EDTA] = 8.95 mM, the resulting free [Ca^{2+}] is 2.3 pM. The free [Ca^{2+}] contained in NSM solution that is 3 mM in EDTA is 10 pM. Finally, in NSM solution that is 1 mM in EDTA, the free [Ca^{2+}] is 50 μM (1 mM EDTA will chelate 1 mM Ca^{2+} (1:1 reaction), therefore the [Ca^{2+}] left in solution is 0.05 mM). The free [Ca^{2+}] contained in NSM solutions prepared with 0, 1, 3 and 10 mM in EDTA are summarised in Table 4.1.

Table 4.1: Concentrations of free [Ca^{2+}] contained in various NSM solutions

Solution	***NSM***	***NSM 1 mM EDTA***	***NSM 3 mM EDTA***	***NSM 10 mM EDTA***
Free [Ca^{2+}]	1.05 mM	50 μM	10 pM	2.3 pM

4.2.7.2 NCAM treatments

Two different assays were performed in order to explore the influence of NCAM on the extent of cytoskeletal reorganisation of neural cells. In the first assay, neural cells were suspended in NSM containing 0.5 mg/ml anti-NCAM (*antibody blockage*). In the second assay, cells were suspended in NSM containing 20 U/ml of Endo-neuraminidase (Endo-N, AbCys S. A., Paris, France) and incubated for 2 h at 33°C/5 % CO_2. These were then centrifuged for 5 min at 28 g and resuspended in phosphatidyl-inositol-specific phospholipase C (PI-PLC) (2 U/ml, Sigma, UK). Cells were incubated for an additional 1 h at 33°C/5% CO_2, centrifuged at 28 g and finally suspended in NSM (*sequential proteolytic digestion*).

4.3 Results

4.3.1 Formation and morphology of cell monolayers

Cells suspended in NSM moved into the optically focussed nodal plane of the USW within 1 s of initiation of sonication. A small aggregate had formed 20 s later at the central region of the nodal plane. Incoming single cells and dendritic small clusters formed strong contact instantly with the peripheral of the growing aggregate, *i.e.* they did not roll along the periphery. However, the short dendritic clusters rotated, without internal reorganisation, about their first contact point with the main aggregate so that it developed a more closely packed form, without widespread hexagonal order over an extended area (Chap. 3; Fig. 3.3) as observed in latex suspensions in distilled water (Chap. 2; Fig. 2.4a). An aggregate was fully formed within 5 min of ultrasound exposure, as characterised by the absence of free single cells from the field of view.

The void index ($A_v \backslash A_p$) of a typical neural cell aggregate was 0.21, resembling a particle aggregate suspended in 8-10 mM $CaCl_2$ (Chap. 2, Sec. 2.3.2.3). Compaction continued, *i.e.* the void area within the aggregate decreased, during the following 20 min. The void area of the part of a monolayer shown in Figure 4.1 decreased from 4.2×10^3 μm^2, after 1 min of ultrasound exposure, to 3.4×10^3 μm^2, after 8 min of ultrasound exposure (image not shown) to 1.3×10^3 μm^2, after an overall ultrasound exposure of 30 min, *i.e.* there was a 68% reduction in the void area (Table 4.2).

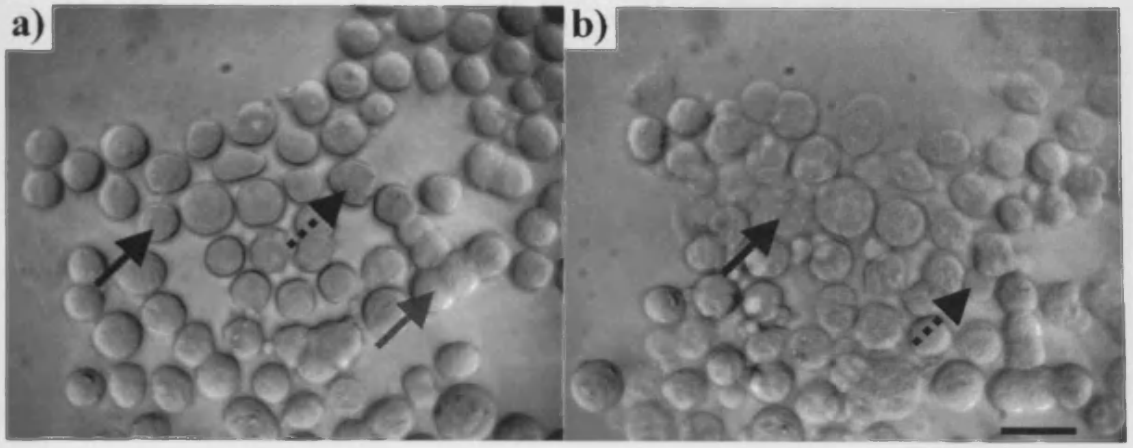

Figure 4.1: Neural cells suspended in the ultrasound trap a) 1 min and b) 30 min after initiation of ultrasound. Membrane spreading (grey arrow), blebbing (dotted arrow) and loss of refractility (black arrow) are shown. Scale bar is 25 μm.

4.3.2 Changes in the morphology of neural cells in a monolayer

Single cells suspended in NSM following detachment from the culture flask had gradually adopted a circular or nearly circular outline by the time of their introduction into the ultrasound trap. Cells were then observed for 60 min. Plasma membranes of neighbouring cells progressively spread over one another (indicated with grey arrow in Fig. 4.1a), occasionally resulting in a visual loss of the resolutions individual cell boundaries. As a result, initially circular neighbouring cells gradually developed a more ellipsoidal shape. A small percentage of both single cells and cells that had spread, underwent additional morphological changes such as blebbing (indicated with dotted arrow in Fig. 4.1a, b) or reduced refractility (indicated with black arrow in Fig. 4.1a, b).

Table 4.2: Decrease in void area and increase in actin filament intensity with time.

Time (min)	***1***	***8***	***30***
Void area (μm^2)	4.2×10^3	3.4×10^3	1.3×10^3
Intensity of F-actin (μm^2)	$14\times10^3 \pm 682$	$25\times10^3 \pm 1002$	$46\times10^3 \pm 1994$

4.3.3 Assays of cell integrity in sonicated samples

The marked changes in cell morphology taking place during 1 h levitation in the trap (Fig. 4.1) raised the question of whether these changes represented the first signs of apoptosis, which could not be identified by the viability markers presented in Chapter 3 (Sec. 3.2.6.2). Additionally, duplicate viability assays of cells in levitated monolayers were performed *in situ* to further characterise the status of the morphological changes of neural cells described in Section 4.3.2. Figure 4.2a-f shows details (×50 objective) that were selected at time points between 5 and 60 min to characterise the properties of spreading and blebbed cells, as well as cells with low refractility. Calcein AM (Fig. 4.2a, b), PI (Fig. 4.2c, d) and MiToTracker Green FM (Fig. 4.2e, f) results were concordant in reporting that spreading cells and the 'main bodies' of cells with blebs were viable, while cells of low refractility were dead (Table 4.3). In agreement with these results MiToTracker Green FM stained the mitochondria of cells that had spread. PI and Calcein AM confirmed that the membranes of blebs were intact, while MiToTracker Green FM showed that they were mitochondria-free (Table 4.3). Annexin V-FITC did not show any fluorescence over a 1 h period of ultrasound exposure (Table 4.3). The positive control cells (cells in which apoptosis has been induced by incubation at 39°C, the non-permissive condition for the immortalising oncogene) did stain with annexin V-FITC after 48 h incubation. Since blebs have been also reported on cells during spreading on solid substrata (Yamaji *et*

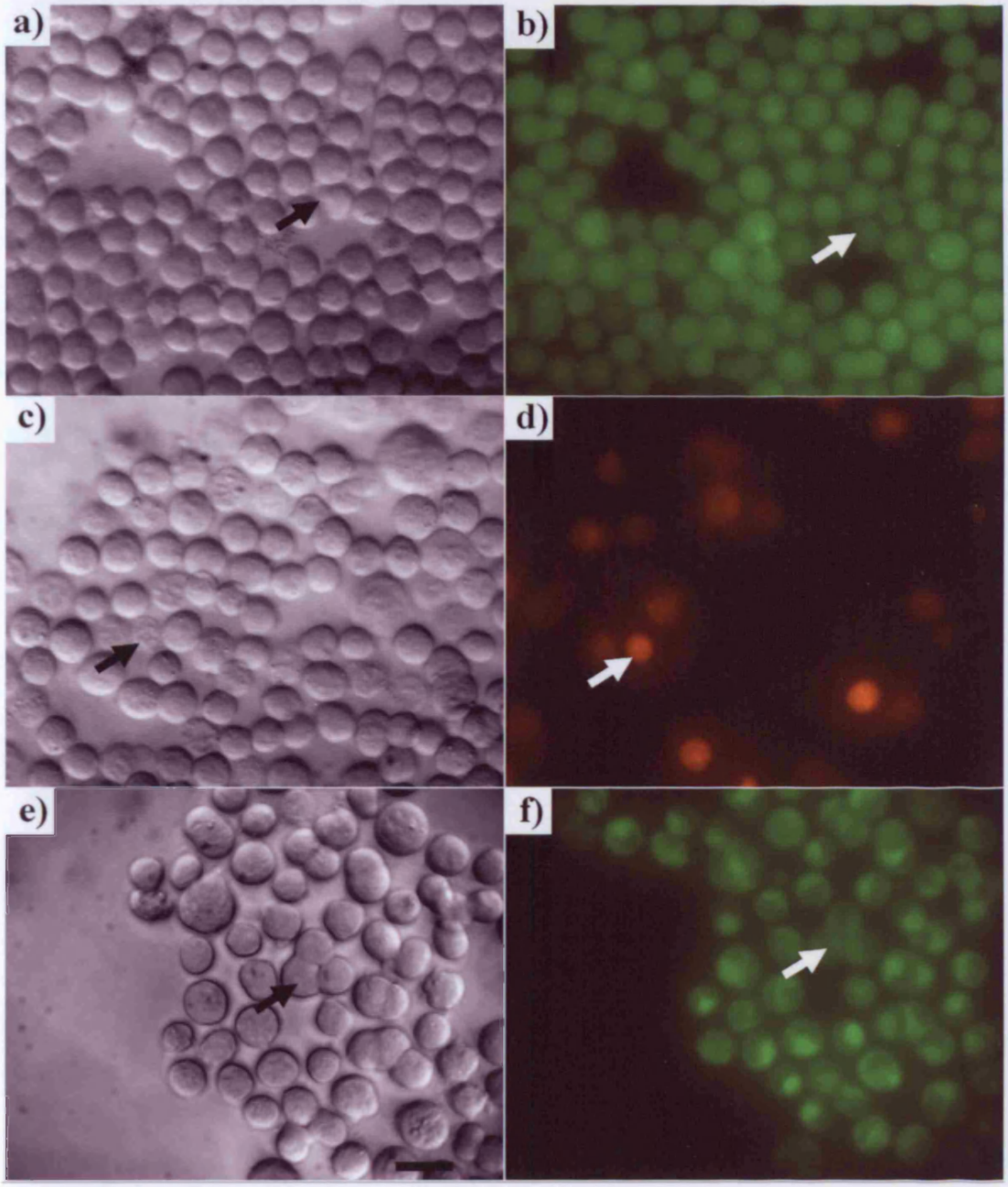

Figure 4.2: (a, b) Staining of live cells with Calcein AM, bright field and fluorescence microscopy respectively at time (t) = 15 min after ultrasound initiation; blebbed cells, but not the blebs, have been stained (arrows). (c, d) Dead cells staining with PI. Low refractility cells have been stained (arrows), (t = 60 min); (e, f) Staining of mitochondria of live cells with MiToTracker green FM. Spread cells have stained (arrows), (t = 5 min). Scale bar is 20 μm.

al., 2001; Fey *et al.*, 2002; Balto, 2004) and in Matrigel (Voura *et al.*, 1998) and since the Annexin V-FITC test for apoptosis (Delhon *et al.*, 2002) was negative here, it was concluded that the bleb formation was associated with cell spreading rather than cell distress in the trap.

Table 4.3: Responses of cells exposed *in situ* to different dyes for 1 h in a levitated monolayer

Fluorescent label	***Spread cells***	***Blebs***	***Blebbed cells***	***Cells with low refractility***	***Cell death***
Propidium Iodide	Unstained (V)	Unstained (IM)	Unstained (V)	Stained (NV)	< 1%
Calcein AM	Stained (V)	Stained (IM)	Stained (V)	Unstained (NV)	< 1%
MitoTracker Green FM	Stained (V)	Unstained (Mito-free)	Stained (V)	Weak signal (Mito-compromised)	< 1%
Annexin V-FITC	Unstained (apoptosis-ve)	Unstained (apoptosis-ve)	Unstained (apoptosis-ve)	Unstained (apoptosis-ve)	*NA*

Abbreviations: V (viable), NV (nonviable), IM (intact cell membrane), NA (not applicable), Mito (mitochondria), -ve (negative).

4.3.4 Rate of membrane spreading

Membrane spreading occurs progressively with some reduction in the resolution of the individual cell boundaries occurring between 30 min and 60 min. Figure 4.3 can be considered as representative of the phenomenon. Soon after ultrasound initiation (1 min), neighbouring neural cells come into close contact. At this point, the width of the advancing membrane front of the illustrated doublet was 3.7 μm (Fig. 4.3a). The width of the developing contact region increases to 6.98 and

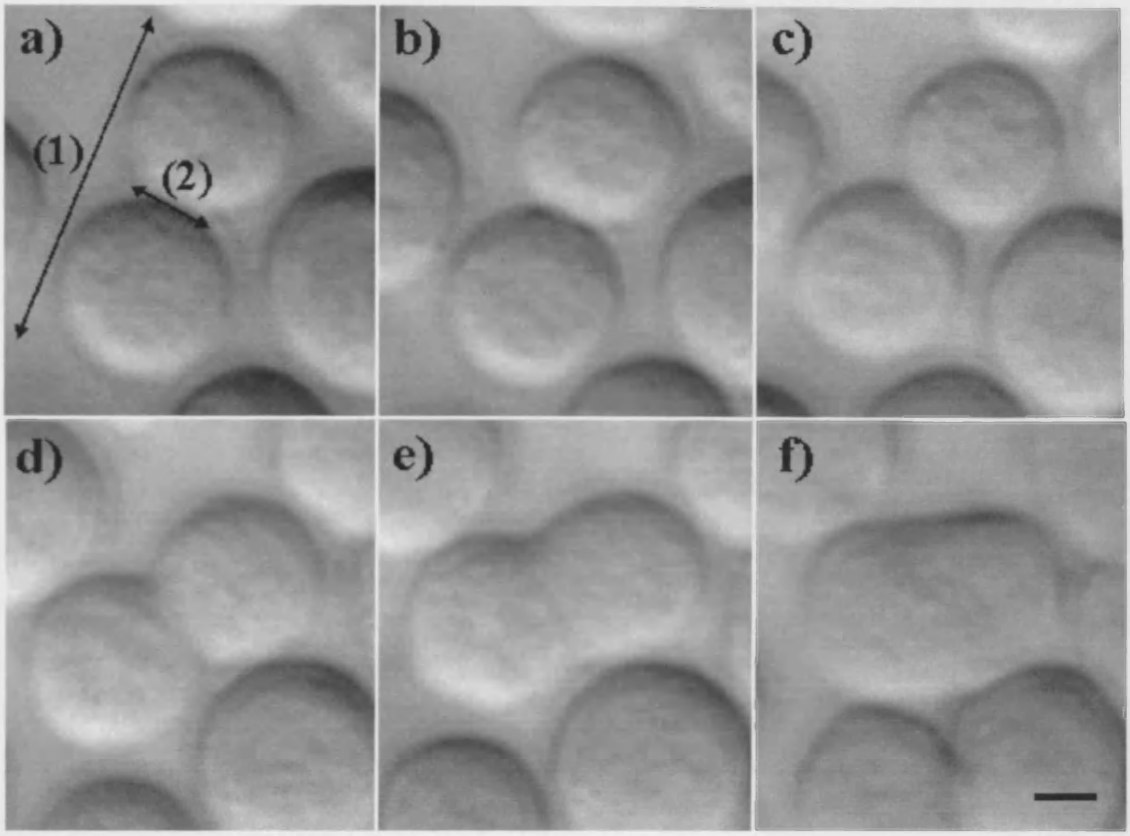

Figure 4.3: Development of membrane spreading in an example neural cell doublet a) 1 min, b) 10 min, c) 20 min, d) 30 min, e) 40 min and f) 60 min after ultrasound initiation. The 'outer edge' separation distance (range 1) and the measured 'width' of the tangentially developing contact area (range 2) are shown. Scale bar is 6 μm.

9.86 μm after 30 and 40 min respectively (Fig. 4.3d, e). Progression of cell contact to a stage where the image of the advancing front could no longer be resolved (Fig. 4.3f) was unusual. The outer edge separation distance between the two cells spreading in Figure 4.3, decreased from an initial (t = 0) value of 26 μm (Fig. 4.3a) to 18 μm at t = 60 min (Fig. 4.3f). Measures of neural membrane spreading described above are shown, as a function of time for 7 random pairs of cells in Figure 4.4a, b. The rate of the tangentially spreading between two cells was 0.19 μm/min (Fig. 4.4a), while the rate of change of edge to edge separation distance was − 0.3 μm/min (Fig. 4.4b).

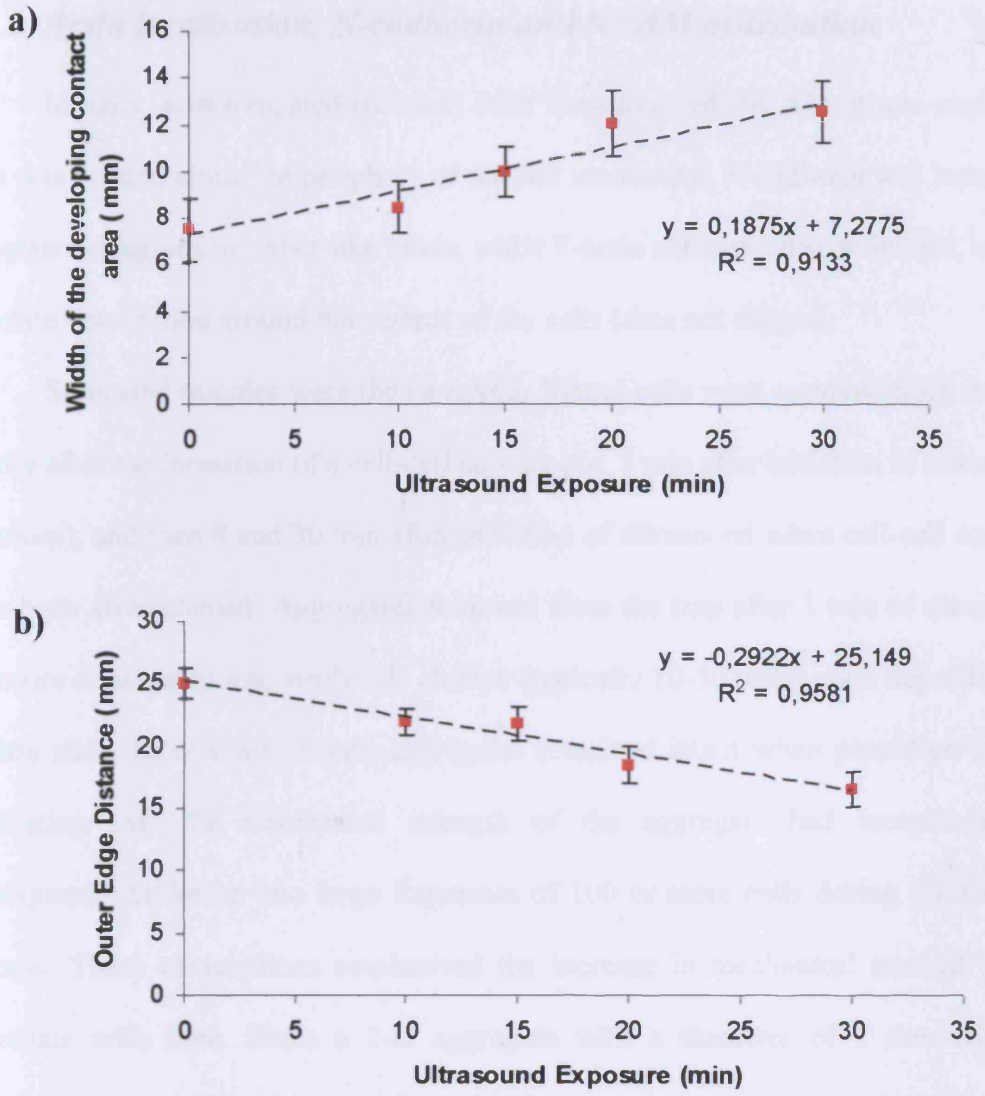

Figure 4.4: Temporal progression of: a) the 'width' of the developing contact area and b) the 'outer edge' separation distance of selected pairs of spreading cells (n = 7; error bars indicating the standard error of the mean).

4.3.5 Actin localisation, N-cadherin and NCAM distribution

Initially, non-sonicated (control) cells were assayed. NCAM in non-sonicated cells was located along the periphery of the cell membrane; N-cadherin was located at cytoplasmic regions in a spot-like mode, while F-actin showed a discontinuous, almost punctate distribution around the surface of the cells (data not shown).

Sonicated samples were then assayed. Neural cells were removed from the trap shortly after the formation of a cell-cell contact (*i.e.* 1 min after initiation of ultrasound exposure), and then 8 and 30 min after initiation of ultrasound when cell-cell contacts have been strengthened. Aggregates removed from the trap after 1 min of ultrasound exposure dissociated into small 2-D clumps (typically 10-50 cells) upon deposition on a glass slide. In contrast 30 min aggregates remained intact when placed on a slide (indicating that the mechanical strength of the aggregate had increased); but subsequently broke up into large fragments of 100 or more cells during the fixation process. These observations emphasised the increase in mechanical strength of an aggregate with time. Since a 2-D aggregate with a diameter of 1 mm contains approximately 10,000 cells, approximately 100 large fragments (each containing ~100 cells) were present on every slide. Images were captured from all the fragments of the aggregate (for all immunostaining experiments described in this thesis), providing guidance on the typical recurring patterns characteristic of a sample.

The distributions of filamentous actin, N-cadherin and NCAM were then analysed using immunofluorescence techniques (Fig. 4.5). It should be noted that samples were removed from the trap after 1, 8 and 30 min but the respective immunofluorescent images correspond to the 'real' times of 2.5, 9.5 and 31.5 min due to the time gap from termination of ultrasound (1, 8 and 30 min) to specimen fixation.

However, the time at which aggregates were removed from the trap will be from now and in the following Chapters used as the standard notation.

NCAM at 1 min was located at the cell membrane (as for control, non-sonicated cells) but the fluorescence signal at the cell-cell interface was quite weak and occasionally discontinuous (Fig. 4.5a, arrows). The signal at the interface was more continuous 7 min later (Fig. 4.5b, arrows), while after 30 min of ultrasound exposure NCAM was distributed evenly at the cell-cell contact area (Fig. 4.5c, arrows). The signal was then relatively strong.

N-cadherin, at 1 min of ultrasound exposure, was located mostly in the interior of the cells in a spot-like mode (Fig. 4.5d, arrows) as described for non-sonicated cells, while some staining at the cell-cell interface was also detectable. After 8 min N-cadherin was concentrated at the surface of the cells at interfaces (Fig. 4.5e, arrows) and 30 min after ultrasound initiation it exhibited a discontinuous, strong signal at the surface of the cells (Fig. 4.5f, arrows) possibly associated with the formation of adherens junctions.

Finally, F-actin in cells after 1 min in the trap was retained in a discontinuous, almost punctate distribution around the surface of the cells as observed for non-sonicated cells; however, some accumulation of F-actin at the cell-cell contact interface was also observed (Fig. 4.5g, arrows). After 8 min, the F-actin label at the interfaces of the cells had increased (Fig. 4.5h, arrows), and after 30 min strong labelling was shown at the cell-cell contact region (Fig. 4.5i, arrows). The intensity of F-actin was measured at the above times for 50 randomly selected pairs of cells from two slides of each of three replicate experiments. The average integral intensities of cells increased from $14\times10^3 \pm 682$ to $46\times10^3 \pm 1994$ μm^2, as time progressed from 1 to 30 min of neural cell aggregate levitation in the trap (Table 4.2).

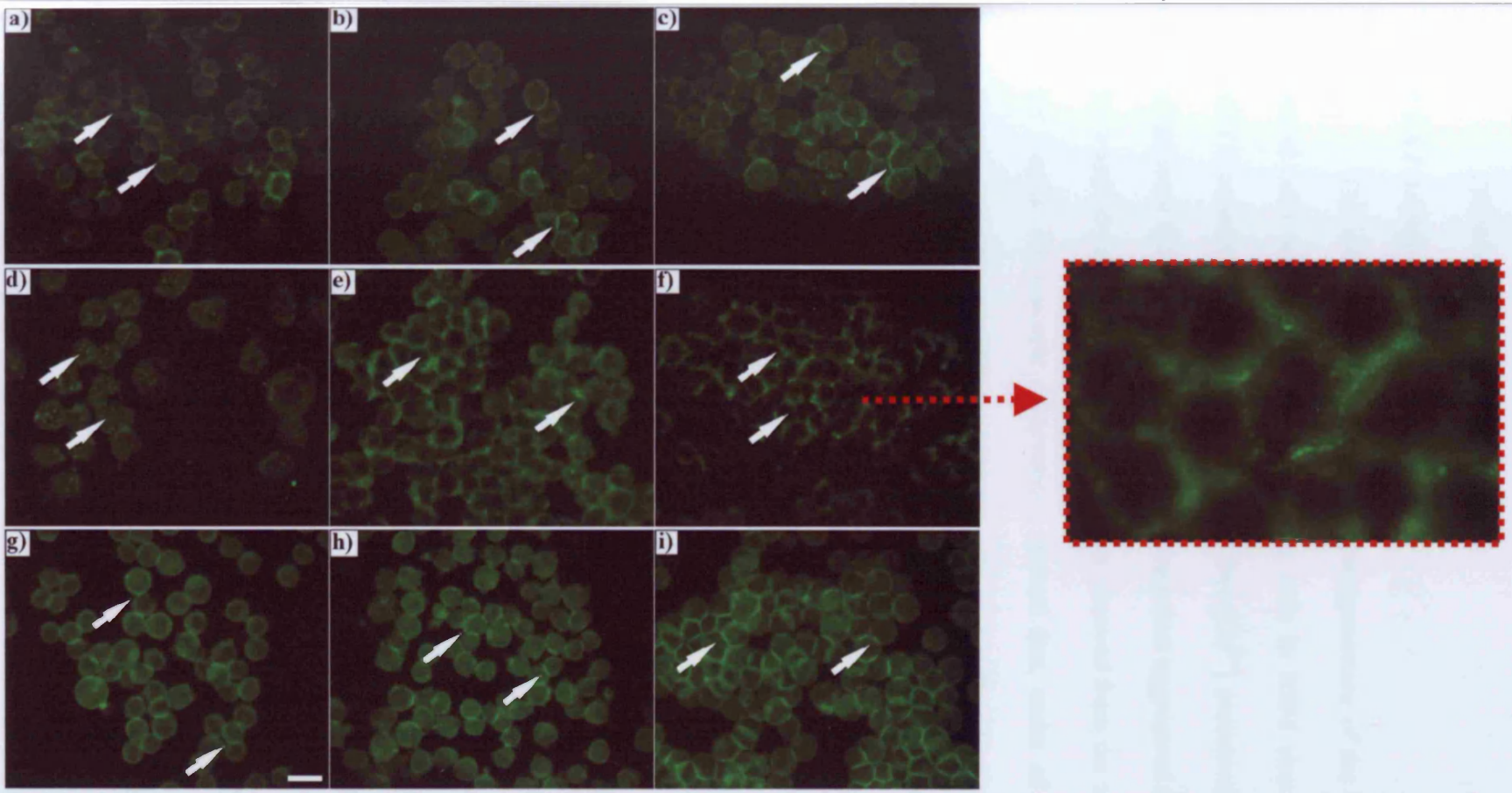

Figure 4.5: Representative fields of view from triplicate experiments showing distribution of (a-c) NCAM (a, weak membranous; b, weak interfacial; c, strong interfacial staining)(arrows), (d-f) N-cadherin (d, intracellular spots; e, interfacial; f, interfacial punctate staining)(arrows), and (g-i) F-actin (g, short interface; h, long interface; i, longer interfacial staining) (arrows) in aggregates isolated from the trap after 1min (a, d, g), 8 min (b, e, h) and 30 min (c, f, i) of ultrasound initiation. The punctate interfacial N-cadherin staining is highlighted in the zoom-in image in the red dotted rectangle. Scale bar is 25 μm.

4.3.6 Influence of $[Ca^{2+}]$ on the reorganization of the F-actin cytoskeleton

4.3.6.1 Addition of different [EDTA]

The influence of calcium on the reorganisation of the F-actin cytoskeleton of neural cells was assessed by suspending cells in NSM also containing a range of EDTA concentrations. Table 4.1 lists the free $[Ca^{2+}]$ contained in NSM after addition of different EDTA concentrations. Cells were then aggregated and levitated in the trap for 1 and 30 min; the aggregates were then removed from the trap and immunolabeled for F-actin. Microscopic observations showed that, under all conditions (*i.e.* in the presence of different EDTA additions), after 1 min F-actin displayed a discontinuous distribution around the unattached periphery of the cells, whereas after 30 min of exposure a clear accumulation of F-actin at the cell-cell interface was observed (Fig. 4.8b) consistent with the observations reported above (Section 4.3.5) for the EDTA-free cell suspension (Fig. 4.8a). The respective bright field images also showed clear evidence of membrane spreading. The intensity of F-actin (Fig. 4.6) was measured for the different times and conditions reported above for 20 randomly selected pairs of cells from two slides of each of duplicate experiments. Figure 4.6 shows that the integral intensity of F-actin for different EDTA concentrations at times 1 and 30 min. Tests of variance and means showed that there was no dependence of F-actin integral intensity on EDTA for either the 1 or 30 min samples. The 1 and 30 min sets of data were pooled for each time. A t-test confirmed the significant difference ($p < 0.001$) between the average integral intensity after 1 min (12×10^3 μm^2) and that after 30 min (28×10^3 μm^2).

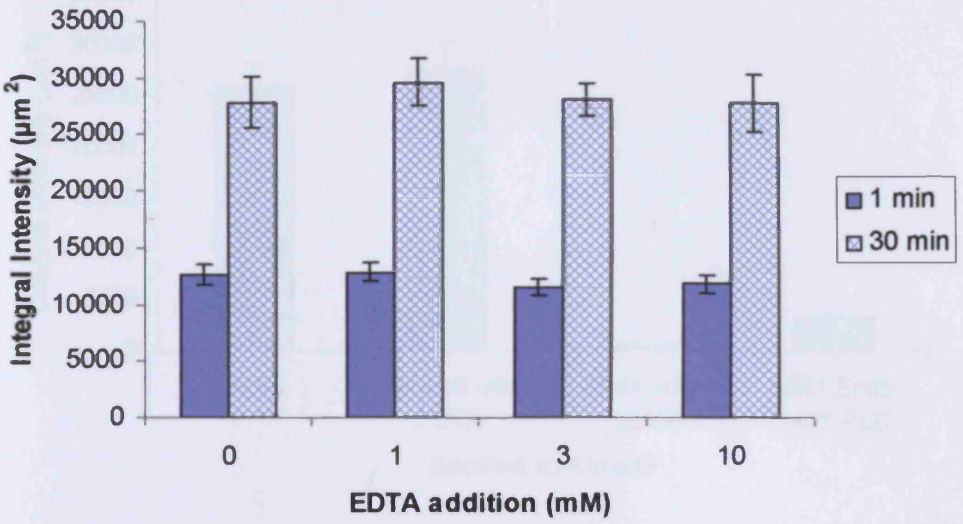

Figure 4.6: Measurements of the integral intensity of F-actin at the cell-cell contact interface of cells suspended in NSM containing various concentrations of EDTA, in relation to time (n = 20, duplicate experiments; error bars represent one standard error of the mean).

4.3.6.2 Addition of anti-NCAM

In order to investigate the role of NCAM on the organisation of the neural F-actin cytoskeleton, cells were suspended in NSM containing 0.5 mg/ml anti-NCAM alone. Cells were levitated in the trap for 30 min, removed from the trap and immunolabeled for F-actin. Figure 4.8c shows little, if any, accumulation of F-actin at the cell-cell contact interface. The respective bright field images showed no signs of membrane spreading; instead cells were perfect spheres (Fig. 4.9b). The intensity of F-actin (Fig. 4.7) was measured for 20 randomly selected pairs of cells from two slides of each of duplicate experiments. The average integral intensities of 20 random pairs of cells were 0.6×10^3 μm^2.

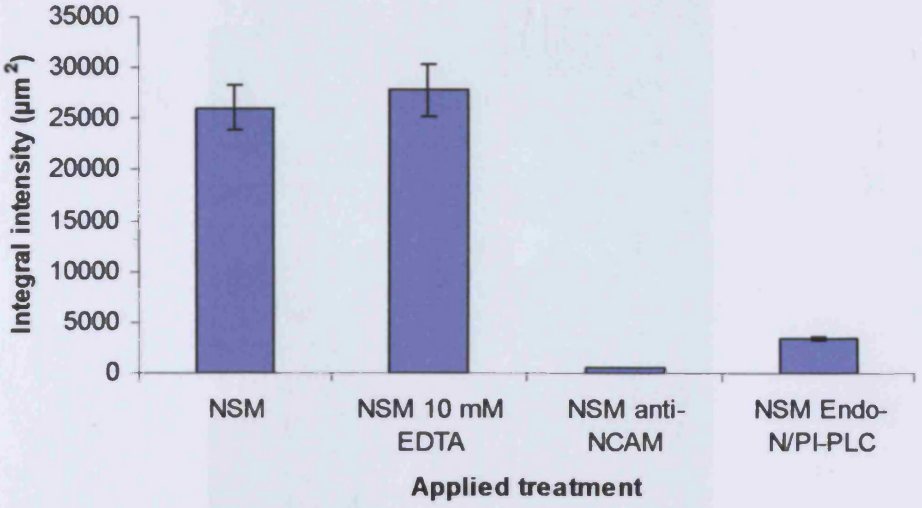

Figure 4.7: Measurements of the integral intensity of F-actin at the cell-cell contact interface of neural cells subjected to various treatments and suspended in the trap for 30 min (n = 20; error bars represent one standard error of the mean). The standard error of the mean for the NSM anti-NCAM sample is too small to be depicted on the graph (596 ± 35.8 µm^2). Experiments in the presence of 10 mM EDTA and anti-NCAM were performed twice, while the endo-N/PI-PLC treatment was performed once.

4.3.6.3 Enzymatic proteolysis of NCAM

Neural cells were subjected to sequential digestion in endo-neuraminidase and PI-PLC. Figure 4.8d shows little accumulation of F-actin at the cell-cell contact interface after 30 min of ultrasound exposure. Membrane spreading was not detectable in the bright field images. The intensity of F-actin (Fig. 4.7) was measured for 20 randomly selected pairs of cells from two slides of a single experiment. The average integral intensities of 20 random pairs of cells were 3.4×10^3 µm^2.

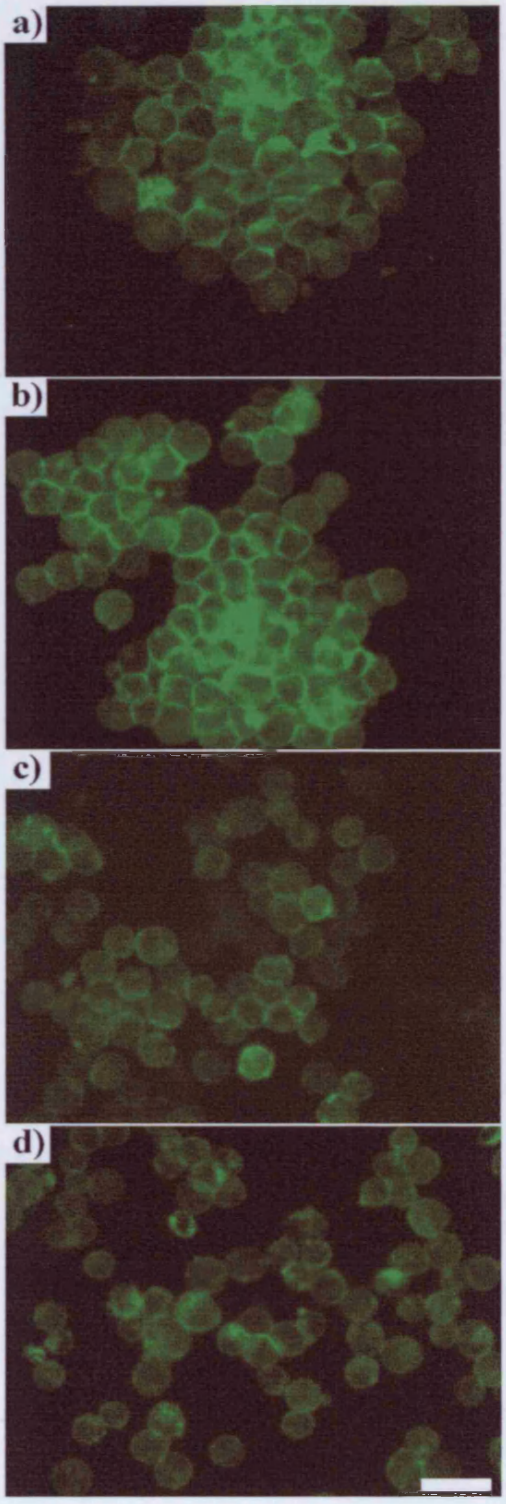

Figure 4.8: Distribution of F-actin in aggregates of cells subjected to different treatments: a) NSM, b) 10 mM EDTA, c) anti-NCAM and d) endo-N/PI-PLC. Little accumulation of F-actin at the cell-cell interface was observed for anti-NCAM (c) and endo-N/PI-PLC (d) treated cells. Scale bar is 20 μm.

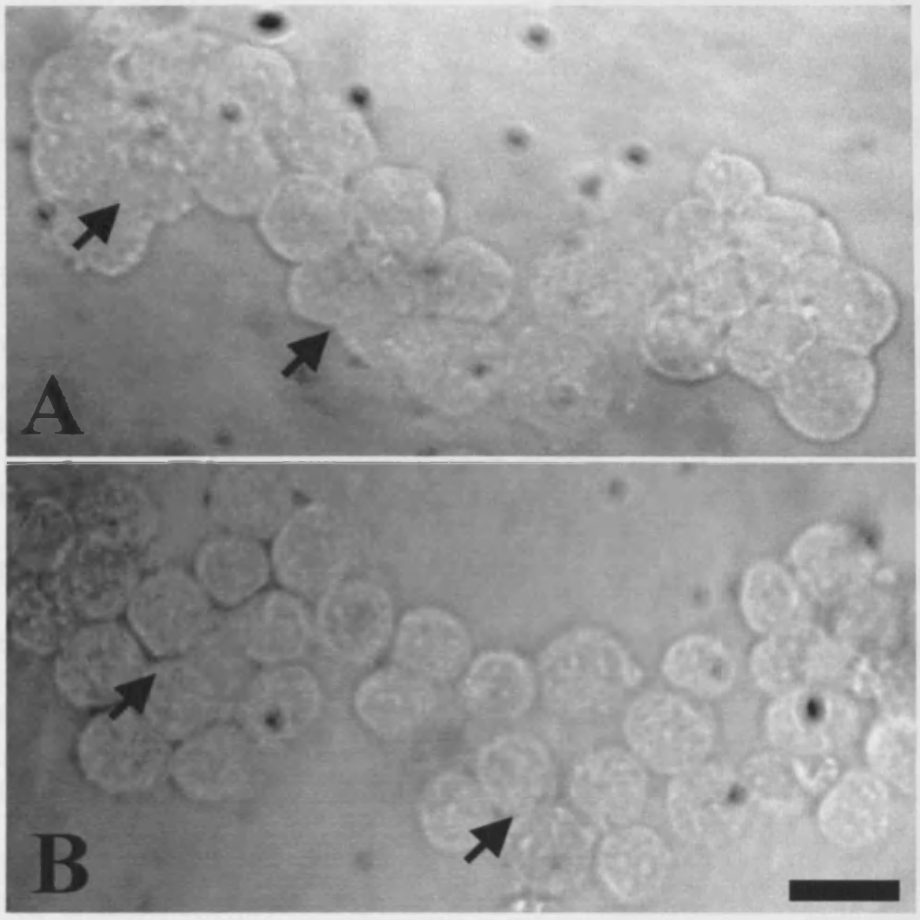

Figure 4.9: Effect of anti-NCAM on the spreading behaviour of neural cells: a) cells suspended in NSM show a high degree of membrane spreading (arrows) and b) cells suspended in NSM in the presence of anti-NCAM (cells remain as 'spheres' and no spreading is observed, arrows). Scale bar is 20 μm.

4.4 Discussion

4.4.1 Viability

Fluorescence assays showed that cells exhibiting membrane blebs in the developing monolayers were viable. Taken with the negative Annexin V-FITC results for apoptosis it was concluded that the membrane blebs observed during monolayer reorganisation were of similar origin to those associated elsewhere with cell spreading

on a substratum (Yamaji *et al.*, 2001; Balto, 2004), *i.e.* they were not indicators of necrosis or apoptosis.

The use of the conditionally-immortalised cell line C6 presented here (Stringer *et al.*, 1994) has relevance for the interpretation of the negative Annexin V-FITC results for apoptosis. Most cell lines in use today are derived from spontaneously-occurring tumours in which the genetic aberration commonly results in a defect in, *inter alia*, the ability of the cell to undergo apoptosis. As a result, cells that should die *via* apoptosis instead survive. In contrast, apoptosis was still elicited in clone 6 cells by switching off the oncogenic drive using NSM and a 39°C incubation temperature. The absence of expression of apoptotic cell death markers, such as Annexin V, after ultrasound exposure is therefore due not to a compromised cell death program but to a genuine lack of pathological abnormalities. The conclusion that the morphological changes presented here for neural cells are not related to the ultrasound trap is consistent with the general discussion presented in Chapter 3 (Sec. 3.3.5).

4.4.2 Cell aggregate morphology and molecular adhesion

The initially open form of the neural cell aggregates reflects strong binding of the neural cells on coming into contact in the sound field. The transition from hexagonally ordered cell clusters (typical of aggregates of non-interacting solid spheres (Spengler and Coakley, 2003)) to the continuous sheet of quadrilateral and pentagonal cells typical of confluent monolayers on glass (Braga *et al.*, 1997) has been shown here to occur in 30 min. The ability of cells to repack from circles in point contact to irregular pentagons in continuous contact reflects a freedom to reorganise form rapidly within the unconstrained suspended monolayer.

NCAM-NCAM interactions (Chap. 1; Sec. 1.2.3.2) between molecules on apposing cells (*trans*-interactions) lead directly to a strong cell-cell contact (Johnson *et al.*, 2004). Cadherins also mediate a homophilic binding on adjacent cells. Cadherin receptors bind to the same type of cadherin on adjacent cells (homophilic binding) (Takeichi, 1991) (Step1). Upon adhesive interaction, cadherins accumulate at sites of cell-cell contacts (Step 2) and are held together within each membrane via interaction with the cytoskeleton (Step 3) (Tepass, 2002). Clustering and association with the cytoskeleton are important for strengthening the forces provided by the cadherin homophilic binding (Gumbiner, 1996). In the present study, NCAM was present at the cell-cell interface from the initial aggregate formation stage with progressive accumulation of NCAM molecules at the cell-cell interface over 30 min of ultrasound exposure (Fig. 4.5a-c). The results on N-cadherin distribution are consistent with reports of cadherin trafficking obtained from cells on solid substrata (Adams *et al.*, 1996; Monier-Gavalle and Duband, 1997; Le *et al.*, 1999; Mary *et al.*, 2002; Braga, 2002; Chen *et al.*, 2003; Spinardi *et al.*, 2004). As is the case with other transmembrane proteins, the synthesis, recycling and degradation of cadherins are driven by a complex network of intracellular trafficking pathways (Peiper and Yap, 2003). The cytoplasmic pool of N-cadherin molecules shown in Figure 4.5d suggests that following detachment of cells from the flask using the chelator EDTA, cadherins were endocytosed as cell to cell contacts were perturbed. N-cadherin molecules were then rapidly (within 7 min) trafficked back to the cell surface (Fig. 4.5e) via a post-Golgi pathway (Le *et al.*, 1999). Upon formation of stable cell-cell contacts (Fig. 4.5f), N-cadherin remained at the cell surface (Le *et al.*, 1999; Mary *et al.*, 2002) for the remainder of the 30 min duration of the experiment. Finally, Figure 4.5g-i shows the associated temporal progression of actin localization. Filamentous actin after 1 min of

ultrasound exposure is distributed in a spot-like mode around the surface of the cells; 7 min later, actin is accumulating at the interfaces of the cells, whereas after a 30 min exposure strong junctional localisation is observed.

There are few reports of fluorescence microscopy studies of the time course of the molecular development of the cell cytoskeleton in a cell monolayer following receptor mediated cell-cell interaction. Hennings and Holbrook (1983) , in one of the earlier studies, examined adhesion in keratinocyte monolayers growing in standard (1.2-1.8 mM calcium) and low calcium concentrations (0.02-0.1 mM). In the first case cells were connected by 'desmosomes' (a term used in the 1980's to include both adherens junctions and desmosomes (Darnell *et al.*, 1986) and finally stratified to 4-6 cell layers, whereas in the latter case cells grew as a monolayer with no desmosomal connections. This 'calcium switch' approach has since been used in further keratinocyte studies (Watt *et al.*, 1984; Braga, 2002). These authors (Watt *et al.*, 1984; Braga, 2002) reported major cytoskeletal reorganisation and formation of desmosomes within 2 and 1 h respectively after addition of normal calcium concentrations to the cultures, in general agreement with our results for a neural cell monolayer in suspension. The 'calcium switch' approach has also been used by Mary et al. (2002) to investigate the distribution of N-cadherin using confluent monolayers of REF-52 fibroblasts attached to glass coverslips. In particular, confluent monolayers were treated with EGTA to disturb cell-cell contacts. Within 10-15 min N-cadherin accumulated at the perinuclear region and was excluded from the adherens junctions. Restoration of extracellular Ca^{2+} rapidly resumed N-cadherin at cell-cell contact sites. It was found that after 90 min of addition of extracellular Ca^{2+} the distribution of N-cadherin was comparable to that in untreated confluent cells. In a similar study performed by Chen et al. (2003), HEK293 confluent cells were again treated with

EGTA for 30 min, followed by incubation in complete growth medium (recovery). It was shown that 15 min after calcium recovery there was strong N-cadherin accumulation at cell-cell contacts. The rapid temporal progression of adherens junctions formation in cell on solid substrata has been qualitatively reported in a number of studies (Adams *et al.*, 1996; Monier-Gavale and Duband, 1997; Spinardi *et al.*, 2004; Chu *et al.*, 2004).

It is therefore shown that the ultrasound technique can simply, rapidly and with some precision produce data on molecular changes during development of adhesion free of the effects of solid substrata as is the case in the studies reported earlier (Adams *et al.*, 1996; Monier-Gavalle and Duband, 1997; Le *et al.*, 1999; Mary *et al.*, 2002; Braga, 2002; Chen *et al.*, 2003; Spinardi *et al.*, 2004).

4.4.3 Measurements of membrane spreading

In the present work membrane spreading and actin dynamics have been studied as the ability of cells to attach to and spread over each other rather than on a substratum. The rate of membrane contact spreading ('width' of the tangentially developing contact area) was 0.19 μm/min, while that of the edge to edge separation distance was −0.3 μm/min (Fig. 4.4a, b). Note that these measurements of spreading of contact lie in the range reported for cell migration, a process also involving actin filaments. CHOK1 (Manabe *et al.*, 2002) and neural progenitor cells (Scemes *et al.*, 2003) migrate at rates of about 0.4 μm/min, rat autonomic motor neurons at 0.06 μm/min (Wetts and Vaughn, 2000) while the more specialised T cells crawl across a surface at 2-6 μm/min (Friedl and Brocker, 2002).

4.4.4 The Ca^{2+} effect

The first approach for the analysis of the role of [Ca^{2+}] on the distribution of the F-actin cytoskeleton of neural cells involved its depletion from the culture medium using the chelator EDTA. It was shown that even at very low concentrations of free [Ca^{2+}] in the medium (*i.e.* in the presence of 10 mM EDTA, 2.3 pM free [Ca^{2+}]; Table 4.1), redistribution of the actin cytoskeleton from a weakly stained circular-type of distribution around the surface of the cells, towards an accumulation at the cell-cell contact interface occurred within 30 min of ultrasound exposure (Fig. 4.8b) in agreement with the observations for the control conditions where cells were suspended in NSM (Fig. 4.8a). Under all concentrations of EDTA used in the present study, the integral intensity at the cell-cell contact interface increased over a 30 min aggregate levitation in the trap, in agreement with the measurements obtained for the control suspension (Fig. 4.7). It was therefore shown that depleting Ca^{2+} from the culture medium does not affect (at least as assessed at the microscopy level) the ability of cells to redistribute their actin cytoskeleton upon stimulation of cell-cell contact in the trap.

The extent to which cadherins in low calcium conditions participate in the reorganisation of the cytoskeleton is now discussed.

Direct cell adhesion experiments on glass coverslips, as those presented in Section 4.4.2, have shown that at low calcium concentrations (0.02-0.1 mM) cells were unable to attach to each other or form adherens junctions/'desmosomes'. Upon restoration of extracellular [Ca^{2+}] to standard levels (1.2-1.8 mM), accumulation of cadherin molecules at sites of cell-cell contacts and formation of adherens junctions was observed (Hennings and Holbrook,1983; Watt *et al.*, 1984; Braga, 2002; Mary *et al.*, 2002; Chen *et al.*, 2003). These results clearly demonstrated the need for the

presence of calcium for cell adhesion and formation of adherens junctions in these particular *in vitro* systems.

As discussed in Chapter 1 (Sec. 1.3.1) two types of cadherin interactions are involved in the cellular adhesion process: *cis*- and *trans*-interactions (Shapiro *et al.*, 1995; Nagar *et al.*, 1996; Tomschy *et al.*, 1996; Koch *et al.*, 1997). Additionally, two models of organisation of *cis*-dimers have been suggested; an early model proposed cadherin dimerisation through hydrophobic interactions (Shapiro *et al.*, 1995), while the second model suggested cadherin dimerisation by mutual coordination of calcium ions (Nagar *et al.*, 1996).

Based on experiments using purified cadherin molecules, [Ca^{2+}] concentrations ranging from 0.05-3 mM are required for *cis*-interactions (Koch *et al.*, 1997; Takeda *et al.*, 1999; Baumgartner *et al.*, 2000; Häussinger *et al.*, 2002; Koch *et al.*, 2004) in favour of the second model, whereas Ca^{2+}-independence of *cis*-interactions has also been reported (Brieher *et al.*, 1996; Chitaev and Troyanovsky, 1998; Tamura *et al.*, 1998; Shan *et al.*, 2000), in favour of the first model. Consequently, the importance of calcium for the *cis*-interactions appears quite conflicting in the literature.

On the other hand, the published literature on *trans*-interactions, based on studies using purified cadherin molecules, is consistent in reporting the requirement for calcium for these to occur. Nevertheless, great variation, ranging from 1 mM (Koch *et al.*, 1999, 2004) to 5 mM (Häussinger *et al.*, 2002) has been reported for the 'essential' calcium concentration for *trans*-interactions. In contrast, in cell-based adhesion studies Wheelock and Johnson (2003) remarked that a concentration of 200 nM was sufficient for cadherin adhesion. A detailed account of the latter experiment has not been published, but the result has been confirmed to this author (Wheelock M, personal communication, 2005). Note though that it is not possible, in

cell-based adhesion studies due to the nature of the experiments, to identify whether *cis-* or *trans*-interactions were abolished at lower Ca^{2+} concentrations, as the cytoskeletal organisation was the end point measured.

However, in the present study F-actin reorganisation and membrane spreading of neural cells did not require extracellular Ca^{2+} concentrations above at least 2.3 pM, in agreement with the report presented by Wheelock and Johnson (2003). Suspending cells in NSM containing 10 mM EDTA, corresponding to an extracellular free Ca^{2+} concentration of 2.3 pM, had no effect on the organisation of the actin cytoskeleton at sites of cell-cell contact (Fig. 4.8b).

The role of NCAM interactions will now be considered. Figure 4.5a-c shows that NCAM was present at the cell-cell interface from the initial aggregate formation stage with progressive accumulation of NCAM molecules at the cell-cell interface over 30 min of ultrasound exposure. NCAM mediates homophilic binding via its Ig modules in a Ca^{+2}-independent manner (Johnson *et al.*, 2004) (Chap. 1; Sec. 1.2.3.2). Suspending neural cells in NSM containing 10 mM EDTA is expected to have no effect on the structure and function of NCAM molecules. It is therefore reasonable to consider that NCAM molecules on apposing cells provide the primary binding and thus the stabilisation of the cell-cell contacts upon their initiation in the trap. As cells are held in close and stable contact via NCAM interactions, cadherin *trans*-interactions might take place, hence resulting in the redistribution of the F-actin cytoskeleton over a 30 min levitation in the trap (Fig. 4.8b). It should be noted that, as described in Chapter 1 (Sec. 1.2.3.1) NCAM has been shown to interact with the actin cytoskeleton via ankyrin and spectrin (Juliano, 2002), as well as directly with α-actinin, α- and β-tubulin (Büttner *et al.*, 2003). The association of NCAM with the actin cytoskeleton in the neural cell system should not be precluded, however, these

are individual studies and a generally accepted view on the NCAM-cytoskeleton interactions is not resolved in the published literature.

Inactivation of NCAM by suspending cells in NSM containing anti-NCAM antibody provides further evidence for the role of NCAM interactions. Figure 4.8c shows little, if any, accumulation of F-actin at the cell-cell interface. Intensity measurements (Fig. 4.7) showed a drastic decrease, *i.e.* 48-fold, of F-actin labelling at the cell-cell interface of cells held in the trap for 30 min, in relation to cells suspended in NSM alone. Inactivation of NCAM by anti-NCAM antibody had also a pronounced effect on membrane spreading (Fig. 4.9). Cells in the absence of anti-NCAM spread over one another with visual loss of the individual cell boundaries (Fig. 4.9a), whereas in the presence of the antibody cells presented as perfect spheres with clear resolution of the individual cell boundaries (Fig. 4.9b).

Nevertheless, such a drastic decrease could well be due to repulsive steric effects, caused by the antibody increasing the effective separation distance between homophilic receptors on adjacent cells, thus overwhelming both homophilic NCAM and cadherin attraction (Johnson *et al.*, 2005). For this reason, NCAM was subjected to sequential glycolytic digestions by endo-N (Angata and Fukuda, 2003; Petridis *et al.*, 2004; Angata *et al.*, 2004) and PI-PLC (He *et al.*, 1986; Saffell *et al.*, 1995). C6 neural cells are embryonic brain cells, therefore the polysialic acid moiety of NCAM is high (Chap. 1; Sec.1.2.3.1).

Endo-neuraminidase specifically cleaves α-2,8-linked sialic acid residues attached to NCAM, whereas PI-PLC attacks the glucosyl-phosphatidylinositol (GPI) membrane anchor of NCAM-120 kDa (Saffell *et al.*, 1995). The NCAM profile of C6 neural cells has not been characterised. Removal of the NCAM-120 isoform was however, shown to be sufficient for inhibition of the F-actin accumulation at the cell-

cell interface. Figure 4.8d shows little accumulation of F-actin at the cell-cell contact interface. Intensity measurements (Fig. 4.7) showed an 8-fold decrease in the amount of F-actin at the cell-cell interface of cells exposed to ultrasound for 30 min, in comparison to a control sample (cells suspended in NSM alone), where an intensity value of 28×10^3 μm^2, consistent with earlier measurements (Fig. 4.6) was obtained. Glycolytic digestion of NCAM also had a marked effect on the ability of cells to spread over each other. Cells appeared as perfect spheres with clear resolution of the individual cell boundaries, as it has been the case for cells suspended in NSM in the presence of anti-NCAM (Fig. 4.9b). An important point is thus raised. In the presence of NCAM, membrane spreading of neighbouring cells is pronounced; in contrast, inactivation of NCAM either by antibody blockage or glycolytic digestion abolishes membrane spreading. This suggests the importance of NCAM in the process of membrane spreading, demonstrating that cadherin molecules are not solely responsible for membrane spreading, even in the presence of standard concentrations of free Ca^{2+}. Furthermore, the non-invasive role of the acoustic forces as means that concentrate and hold cells locally, as in tissue, without modifying the *in vitro* expression of surface receptor interactions, is further supported by the absence of actin cytoskeleton remodelling following digestion of the GPI bond.

The role of NCAM in the process of membrane spreading has been addressed by several investigators. Sandig et al. (1997) reported that mouse Sertoli TM4 cells exhibited epitheloid characteristics and formed overlapping NCAM-rich lamella at regions of cell-cell contact. Inhibition of cellular spreading on NCAM-coated substrata by anti-NCAM antibodies has been reported in many cell systems (Murray and Jensen, 1992), whereas its role as a stabiliser of cell-cell contacts render it a

tumour marker, as expression of NCAM has been shown to reduce migration (Zhang *et al.*, 2004) and invasion of glioma cells (Prag *et al.*, 2002).

Two conclusions can thus be drawn: a) NCAM interactions are important for stabilisation of the cell-cell contacts and the process of membrane spreading and b) at low calcium concentrations (2.3 pM) cadherins are still able to attach to each other and cause redistribution of the F-actin cytoskeleton once stable cell-cell contacts have been formed. The neural system thus illustrates the cooperative involvement of different molecular mechanisms in cell adhesion.

4.5 Preliminary conclusions

It has been shown in this study that the interactions at the plasma membranes of cells in close proximity in the ultrasound trap transduce signals that consequently have major impacts on the cell shape and on the organisation of F-actin at the cell interface, across the membrane.

Spreading of membrane occurred between the aggregated cells; the rate of spreading of the tangentially developing intercellular contact area was 0.19 μm/min. As a result, the form of the suspended aggregate changed from one of a hexagonal arrangement of cells to one of a cell-monolayer-like continuous sheet of mostly quadrilateral and pentagonal cells as in cell monolayer on a solid substratum. Investigation of the reorganisation of F-actin at the cell-cell interface showed that F-actin progressively accumulated at the spreading cell-cell interfaces within 30 min of levitation in the trap.

Further analysis of the influence of Ca^{2+} concentration on the reorganisation of the neural cell actin cytoskeleton showed that, in contrast to the published literature, at Ca^{2+}concentrations of 2.3 pM accumulation of F-actin at the cell-cell contact interface

was still possible. The role of NCAM in membrane spreading and as a stabiliser of cell-cell contacts emerged through use of a NCAM-blocking antibody and glycolytic digestion of the GPI bond.

In general, neural cells progressed from physical aggregation, through molecular adhesion, to displaying the intracellular consequences of receptor interactions. The extent to which cells in a levitated monolayer in the ultrasound trap are able to, in addition to adhere, also communicate with each other will be introduced in the following Chapter 5.

Chapter 5

Cytoskeletal development and gap junctional intercellular communication in articular cartilage cells suspended in an ultrasound trap

5.1 Introduction

One of the earliest morphological event in the differentiation of the limb skeleton is the condensation of mesenchymal cells in areas of prospective cartilage and bone formation (Coleman and Tuan, 2003). Cellular condensations form as a result of altered mitotic activity and failure of cells to move apart, as reviewed by Hall and Miyake (2000). As a result, an increase in the mesenchymal cell-packing density, *i.e.* an increase in cells/unit area or volume without an increase in cell proliferation is observed (DeLise and Tuan, 2002). Cellular condensation is associated with an increase in cell-cell contacts through cell adhesion interactions involving neural cadherin (N-cadherin) and neural cell adhesion molecule (NCAM) (Tavella *et al.*, 1994). Perturbation of the function of these molecules reduces chondrogenesis both *in vivo* and *in vitro* (Oberlender and Tuan, 1994; DeLise and Tuan, 2002; Kosteskii *et al.*, 2005). As the condensations mature, N-cadherin and NCAM expression decreases and these molecules are not found in differentiated cartilage in chondrocytes (Widelitz *et al.*, 1992; Oberlender and Tuan, 1994).

Gap junctions are also important for the condensation process; they facilitate intercellular communication and the transfer of small molecules between cells (Hall and Miyake, 2000; DeLise and Tuan, 2002). Gap junctions in mesenchymal

condensations influence cellular communication in limb buds in terms of both establishment of pattern and differentiation (Zimmermman, 1984; Coelho and Kosher, 1991; Levin *et al*, 2001). Within the limb, transcripts of the gap junction gene, *connexin* 43 (Cx43), are strongly expressed in the mesenchyme condensations forming cartilage (Coleman and Tuan, 2003). Connexins are also expressed in mature cartilage. For example, it has been shown that some cells within the surface zone of adult articular cartilage occur in pairs and thus are able to communicate *in vivo* (Chi *et al.*, 2004). Additionally, chondrocytes re-express Cx43 in cell clusters (chondrones) that are characteristic in osteoarthritis (Hellio Le Graverand *et al.*, 2001).

Gap junctional intercellular communication (GJIC) in cartilage has been demonstrated *in vivo* in whole tissue sections (*i.e.* without differentiating between zones) of mouse and rat knee joints (Schwab *et al.*, 1998), femoral condyles of mature rabbits (Chi *et al.*, 2004), chondrocytes in the suture regions of calvaria of young rats (Jones *et al.*, 1993) and young cartilage of mouse embryos (Zimmermann *et al.*, 1982). *In vitro*, monolayer and micromass cultures have shown widespread occurrence of gap junctions (Donahue *et al.*, 1995; D'Andrea and Vittur, 1996; Zhang *et al.*, 2002).

Chondrocytes in 3D micromass cultures retain their differentiation status (Schulze-Tanzil *et al.*, 2002) but lose it when cultured on a monolayer that lacks the requisite characteristic micro-environment together with a loss of rounded cell configuration (Schulze-Tanzil *et al.*, 2002).

Within articular cartilage, the chondrocyte cytoskeleton comprises a dynamic three dimensional network consisting principally of the proteins actin, vimentin and tubulin that are organised into microfilaments, intermediate filaments and microtubules respectively (Trickey *et al.*, 2004). The cytoskeleton plays an important role in the physical interactions between the chondrocyte and its extracellular matrix

and is involved in the process of mechanical signal transduction in articular cartilage (Langelier *et al.*, 2000), as well as in the control of the chondrocyte phenotype (Vinhall *et al.*, 2002). It is also believed to contribute to the biomechanical properties of the chondrocyte, which also influence the interactions between the cell and its pericellular and extracellular matrices (Guilak and Mow, 2000).

Little attention appears to have been paid to the development of the chondrocyte F-actin cytoskeleton in interacting cells in micromass cultures. Chondrocytes in micromass cultures form a mass within one hour, in the sense that 60 min was the period 'allowed for adhesion to occur' prior to initiating studies of micromass properties (Coelho and Kosher, 1991). Data on GJIC or actin cytoskeleton development are usually extracted after at least 1 day in culture (Coelho and Kosher, 1991; Woods *et al.*, 2005). While chondrocytes can come into contact in free suspension, there have been no reports of formation of functional communication in such conditions. This idea will be explored in this Chapter using surface zone chondrocytes. Surface zone chondrocytes were selected for study for practical reason they are the preferred cells in investigations of approaches to articular cartilage repair. Additionally, from a 'biology of adhesion' perspective, surface zone chondrocytes *in vivo* are least in contact with each other compared to middle and deep zone chondrocytes. They therefore offer a model system to explore cell-cell interactions in *vitro* in a system where cell-matrix interactions dominate *in vivo*.

The distributions of F-actin and Cx43 over the first 60 min of ultrasound exposure were monitored. It was shown that the distribution of these molecules significantly changed with time. These differences were quantified using the integral intensity approach described in Chapter 4 (Sec. 4.2.6).

The chapter also describes assays in order to examine the functionality of gap junctions. These included simple dye transfer assays in the presence or absence of a

gap junctional blocker. Counts of fluorescently labelled cells over time provided evidence in support of functional gap junctions.

Experiments were also carried out in the presence of the protein synthesis inhibitor cycloheximide to investigate the distribution of F-actin and Cx43 upon stimulation of cell-cell contact in the ultrasound trap when synthesis of total cellular proteins has been inhibited. Integral intensity measurements were again used to assess the effect of cycloheximide.

Finally, the role of calcium on the formation of gap junctions is addressed. The findings point towards a common response of cells in low calcium conditions in agreement with the observations presented in Chapter 4 (Sec. 4.3.6) for neural cells.

5.2 Material and Methods

5.2.1 Ultrasound trap, optical system and experimental procedure

The acoustic trap employed here for chondrocyte aggregation and molecular adhesion, as well as its drive have already been described in Chapter 4 (Sec. 4.2.1). Formation of aggregates took place according to the protocol described in Chapter 3 (Sec. 3.3.1), *i.e.* cells were initially exposed to ultrasound at a pressure amplitude of 0.54 MPa for 30 s, at 0.27 MPa for 5 min and finally at the levitation pressure amplitude threshold of 0.06 MPa for the remaining 55 min of exposure.

Aggregate growth and morphology were monitored with an Olympus BX41M reflection epi-fluorescent microscope employing a CCD F-view camera as described in Chapter 4 (Section 4.2.1), whereas immunofluorescent specimen analysis was performed with an Olympus BX61 epi-fluorescent microscope (Appendix B) (1× TV adapter, U-CMAD-3) also employing a CCD F-view camera. Samples were introduced into the trap at room temperature with a 2 ml sterile syringe (Plastipak,

Becton Dickinson, UK). Ultrasound exposure was then immediately initiated. Images were captured and processed using the analySIS 3.1 software.

5.2.2 Chondrocyte Isolation and Preparation

Chondrocytes were isolated from the surface zone (SZ) of 7–day bovine metacarpal phalangeal joints by fine dissection (Fig. 5.1). Cartilage shavings were placed in a 50 ml pre-weighted tube, containing 20 ml of Dulbecco's Modified Eagle Medium/Ham's F-12 (DMEM without sodium pyruvate, with 4.5 mg/ml glucose with pyridoxine; GIBCO BRL, Life Technologies Ltd., UK) and Ham's F-12 medium (Ham's F-12; GIBCO BRL, Life Technologies Ltd., UK) at a 1:1 ratio). 5% foetal calf serum (FCS; GIBCO BRL, Life Technologies Ltd., UK), 100 mg/ml ascorbic acid (Sigma, UK) and 50 mg/ml gentamycin (GIBCO BRL, Life Technologies Ltd., UK) were also added to DMEM/Ham's F-12 medium (in the total medium volume of 500 ml) *(Isolation step)*. Chondrocytes were released from the surrounding matrix by sequential digestion, using 3.17 units/ml pronase (made up in 20 ml of DMEM/Ham's F-12 medium) (from *Streptomyces griseus*; Boehnringer Mannheim). The cell suspension was incubated for 3 h at 37°C on a roller. Pronase was removed by decanting and cartilage shavings were incubated in 0.12 units/ml of collagenase (made up in 20 ml of DMEM/Ham's F-12 medium) (Type II Collagenase, prepared from *Clostridium histolyticum*; GIBCO BRL, Life Technologies Ltd., UK) overnight at 37°C on a roller *(Extracellular matrix release step)*. Following collagenase digestion, the cell suspension and the remaining tissue debris were filtered through a 40 μm Nitex cell strainer (FALCON) into a sterile 50 ml centrifuge tube. The cells were pelleted by centrifugation at 260 g for 5 min.

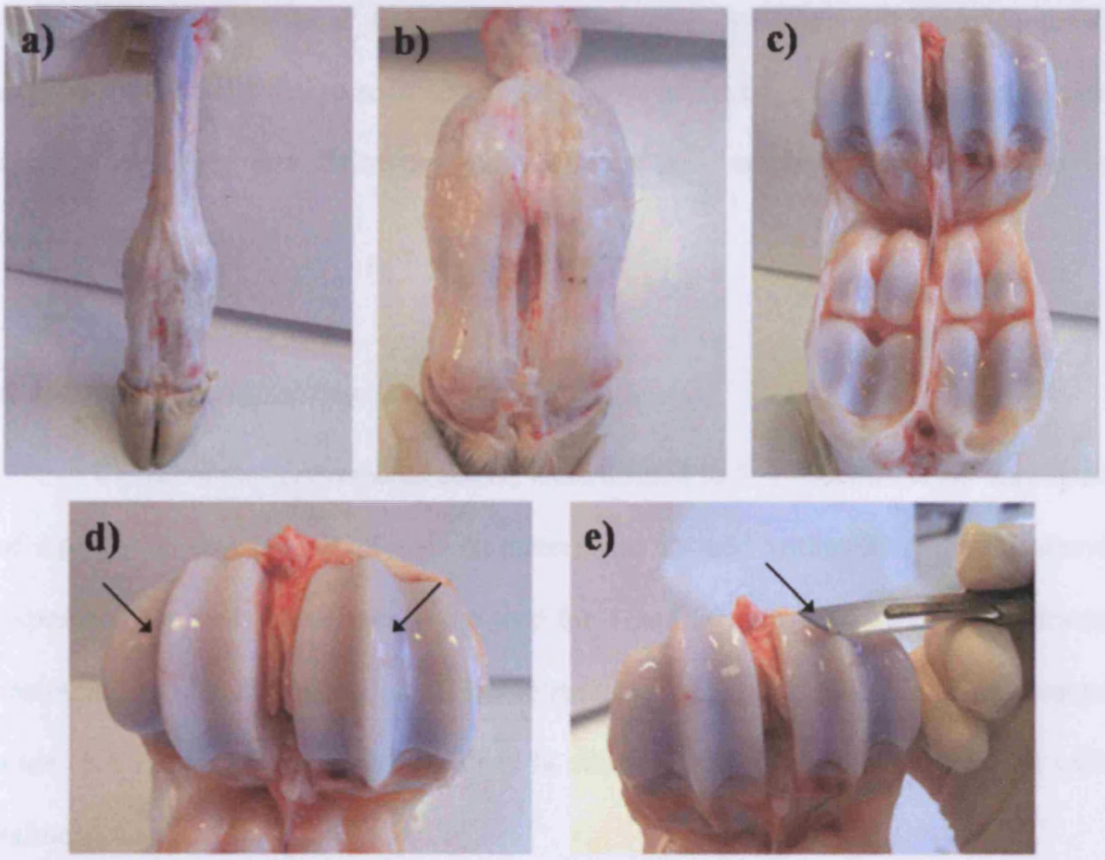

Figure 5.1: Chondrocyte isolation: a) cow foot, b) close-up of metacarpal phalangeal joint, c) open joint d) close-up of condyles (arrows) and e) removal of surface zone slivers shown with arrows.

Aspiration of the supernatant was followed by resuspension of the cell pellet in a known volume of serum-free DMEM/Ham's F-12. Cells were centrifuged for a second time at 260 g for 5 min. Cells were counted on a Bright-line haemocytometer (Reichert, USA) and finally diluted to the desired concentration in serum-free DMEM/Ham's F-12 medium *(Preparation step)*.

5.2.3 Assaying the mechanical strength of the aggregates

Chondrocytes were prepared as described above, suspended in serum-free DMEM/Ham's F-12 medium and diluted to 10^5 cells/ml. Cell suspensions were

levitated in the trap for 1 min and 1 h. Sonication was then terminated and the aggregates were allowed to sediment to the bottom of the trap. The extent of aggregate dispersion during and following sedimentation was microscopically observed in duplicate experiments.

5.2.4 Immunolabelling

Chondrocytes prepared as above, were diluted to 5×10^6 cells/ml. An aggregate of significant size (*i.e. ca.* 1 mm diameter) was formed within 30 s of ultrasound exposure. The cells were held in the trap for 1 and 60 min. They were then slowly removed from the trap using a 2 ml sterile syringe, placed on a HistoBond microscope slide (RA Lamb, UK) and fixed with 90% ethanol. The slides were then rinsed with saline.

Cells were dual-labelled for F-actin and Cx43. Samples were blocked at room temperature with goat serum (DAKO, UK) at 1:20 dilution in PBS and incubated with the primary antibody (monoclonal anti-connexin 43, 5 μg/ml, Chemicon, UK) overnight at 4°C (Beyer *et al.*, 1987). After washing in PBS, samples were incubated with Alexa 594 conjugated anti-mouse IgG (5 μg/ml, Molecular Probes, Inc. Eugene, OR, USA) for 1 h. After further washing (×3), F-actin actin was labelled by adding 2U/ml of Phalloidin-Alexa 488 conjugate (Molecular Probes, Inc. Eugene, OR, USA). The slides were incubated at room temperature in the dark, rinsed and mounted in Vectashield (Vector, UK) prior to microscopic examination. Dual-labeled slides were observed (Olympus BX61 epi-fluorescent microscope) with different filters, as appropriate for each stain. Each resulting pair of images was merged using the analysis 3.1 software.

Immunolabelling of non-sonicated chondrocytes was performed on cells (10^6 cells/ml) retained for 1 h in suspension in serum-free DMEM/Ham's F12 medium. A 100 µl cell suspension aliquot was placed on a Histobond slide, fixed and separately stained for Cx43 and F-actin.

5.2.5 Isolation of articular cartilage explants

Slivers of surface and deep zone cartilage were surgically removed from three metacarpal phalangeal joints of three different 7–day immature bovine calves. Slivers were washed in DMEM medium (Sec. 5.2.2) and snap frozen in *n*-hexane (Sigma, UK) contained in a dry ice/ethanol bath. Slivers were stored at -80°C prior to the RNA extraction step.

5.2.6 In vivo Cx43 mRNA expression

5.2.6.1 Sample preparation

Pooled slivers of frozen cartilage (surface and deep zone) from the same joint were homogenised in the presence of 1 ml TRI Reagent™ (Sigma, UK) using a Mikro-Dismembrator (B. Braun Biotech International, Melsunger, Germany). TRI Reagent™ is a mixture of guanidine thiocyanate and phenol in a mono-phase solution that quickly and effectively dissolves DNA, RNA and protein on homogenisation of tissue sample. Samples were allowed to stand for 5 min at room temperature for complete dissociation of nucleoprotein complexes. 200 µl of chloroform (Sigma. UK) were then added to the samples. Samples were mixed vigorously for 15 s and allowed to stand for 10 min at room temperature. A centrifugation step of the resulting mixture at 12,000 g for 15 min at 4°C followed. Centrifugation separated the mixture into 3

phases: a red organic phase containing the protein, an interphase that contained the DNA and a colorless upper aqueous phase that contained the RNA.

5.2.6.2 RNA extraction

The RNA-containing phase of each sample was transferred to a fresh tube, while the interphase and organic phases were discarded. 500 µl of isopropanol (Sigma, UK) were then added to the samples. The samples were allowed to stand at room temperature for 10 min prior to a centrifugation step at 12,000 g for 15 min at 4°C. The RNA precipitate of each sample formed a pellet on the bottom of each tube. The supernatant was removed and the RNA pellets were washed by adding 1 ml of 75 % ethanol. Samples were then mixed briefly and centrifuged at 7,500 g for 5 min at 4°C. The supernatant was extracted and the RNA pellets were air dried for 10 min. Finally, pellets were resuspended in 50 µl of diethylpyrocarbonate (DEPC)-treated dH_2O.

5.2.6.3 UV spectrophotometry

A DNA digestion step was performed in order to remove any DNA contamination of the RNA samples. A mixture of 10×RQ1 buffer, RNasin (4 U/µl), DNase I RQI (1 U/µl, 5 Units) (Promega Ltd.) and DEPC double distilled (dd) H_2O was added to each RNA sample. Samples were mixed by gentle pipetting and incubated for 30 min at 37°C. The RQ1 enzyme was heat denatured at 65°C for 30 min. The RNA concentration of the extraction was measured by light absorbance at 260 and 280 nm. The concentration of RNA in the extract was calculated using the equation:

$$[RNA] = A_{260} \times D \times 40\ \mu g/ml \qquad (5.1)$$

where A_{260} is the absorbance of the solution at 260 nm and D is the final dilution factor. The absorbance of 40 μg of RNA at 260 nm is 1.0. A total RNA amount of 200 ng was extracted and was sufficient to study all the mRNA transcribed within the cells.

5.2.6.4 Reverse Transcription of total RNA(cDNA synthesis)

cDNA was transcribed from 200 ng of RNA from surface and deep zone chondrocytes samples using a reverse transcription polymerase chain reaction (RT-PCR). The reaction mixture is shown in Table 5.1. All reagents were purchased form Promega Ltd. The reaction mixture was gently mixed and further incubated at 25°C

Table 5.1: Reagents used for cDNA synthesis

Product	***Volume (μl)***
RNA (200 ng/ml)	10
5× Moloney's Murine Leukaemia Virus reverse Transcriptase (MMLV RT) buffer	10
MMLV Reverse Transcriptase (200 U/μl)	0.5
Deoxynucleotide Triphosphate (dNTPs; dATP, dCTP, dGTP and dTTP) (25 mM each)	1
Random hexamers (10 ng/μl)	1
RNasin (1U/μl)	1.25
DEPC H_2O	26.25
Total	**50**

for 10 min, followed by 48°C for 60 min and 95°C for 10 min to denature the reverse transcriptase enzyme. All cDNA was synthesised using a Perkin Elmer cDNA thermal cycler. The cDNA products were used immediately in PCR or stored at - 20°C.

5.2.6.5 Real-Time Polymerase Chain Reaction (PCR)

PCR primers were designed using Oligo 4.0 Software (National Biosciences) and synthesized by Invitrogen (Paisley, UK). Primers used in this study were based on sequences for bovine gluceraldehyde-3-phosphate dehydrogenase (GAPDH), serving as the house-keeping gene and bovine connexin 43 (Cx43). All primers were dissolved in 10 mM Tris HCl, 1 mM EDTA, pH 8.0 (TE buffer) at stock concentrations of 50 μM. Table 5.2 lists the primers' nucleotide sequences used in the present study. The PCR reaction mixture is listed in Table 5.3. All reagents were purchased from Promega Ltd. The PCR reaction, performed on a GeneAMP PCR system (PE Applied Biosystems), was cycled at 94°C for 30 s, 53°C for 30 s and 72°C for 30 s for 35 cycles with each primer pair.

Table 5.2: Oligonucleotide primers used to generate PCR products

Target Template	*Forward Primer*	*Reverse Primer*	*Optimal Annealing Temperature (°C)*	*Product Size (bp)*
GAPDH	ATT CTG GCA AGT GGA CAT CG	GGG CCA TCC ACA GTC TTC TG	58	327
Cx43	TGA TTT CCC AGA CGA CCA CCA	TCC CTC TCC ACT CGC CTA TCC	57	501

5.2.6.6 Gel electrophoresis

PCR products were separated by 1% (w/v) agarose gel electrophoresis run in Tris-Borate-EDTA (TBE) buffer. The gel was stained with 0.1 μg/ml ethidium bromide (Sigma, UK) for 20 min and excess ethidium bromide was removed by immersion in water. Loading dye (×6, 8 μl; Promega Ltd.) was added to each 50 μl sample. 0.5 μg of φX174 DNA/Hae III marker dye (Promega Ltd.) was also added to the gel. The gel was run at 60 V for 45 min. The bands were visualised on an ultraviolet light box and the gel documented using a GelDoc 2000 and the Quantity One™ software (BioRads Labs, Hertfordshire, UK).

Table 5.3: Reagents used for PCR analysis

Product	***Volume (μl)***
Forward Primer (50 μM)	1
Reverse Primer (50 μM)	1
cDNA	2
dNTPs (25 mM each)	0.5
Taq DNA Polymerase in Storage buffer B (5U/μl)	0.25
10× Promega buffer	5
$MgCl_2$ (1.5 mM)	3
dH_2O	37.25
Total	**50**

5.2.7 Gene sequencing

PCR products were purified from contaminating primer dimer products using spin column purification, according to the QIAquick® Spin hand book protocol provided by Qiagen. Purified PCR products were then sequenced according to the ABI PRISM dRhodamine Terminator Cycle Sequencing Ready Reaction Kit provided by Applied Biosystems. Briefly, 0.5 μg of PCR (5 μl) product was placed in a tube containing 4 μl of Terminator Ready Reaction Mix, 3.2 pmol of forward Cx43 primer (1 μl) in a total volume of 20 ml, set by addition of dH_2O. The samples were subjected to the following cycles (performed on a GeneAMP PCR system (PE Applied Biosystems): 96°C for 10 s, 50°C for 5 s and 60°C for 4 min for 25 cycles. The products were purified by ethanol precipitation and the resulting pellets were air-dried for 10 min. Sequence homology of the purified products was compared against published cDNA sequences.

5.2.8 Gap junctions function

Chondrocytes were prepared as described in Section 5.2.2 and diluted to 10^6 cells/ml. The sample was then aliquoted into two tubes each containing 1 ml. One sample was stained with Green CMFDA Cell Tracker Probe according to the manufacturers' instructions (20 μM; Molecular Probes, Inc. Eugene, OR, USA), whereas the other population remained unstained. (Gap junctions are permeable to the reaction product of Green CMFDA Cell Tracker Probe (Barhoumi *et al.*, 1993)). The two cell populations were then mixed at a ratio of 1:1 by volume. A sample was then introduced to the resonator and the aggregates formed at the pressure node were retained there for 60 min. Gap junction functionality was assessed by continuous video fluorescence microscopy. In separate experiments, to demonstrate that cell to cell dye

transfer occurs via gap junctions, the gap junctional blocker 1-octanol (4 μM, Sigma, UK) was included in the mixture of the two cell populations (Chi *et al.*, 2004).

An aggregate was formed in the trap and the microscope (objective magnification ×50) was focussed on a randomly selected field of view containing approximately 200 cells (the total number of cells in an aggregate is approximately 10,000). Fields of view where a low number of fluorescent cells were present initially were selected to highlight dye transfer. The chosen set of cells was monitored over a period of 1 h. The experiment was performed twice and the number of fluorescent cells after 60 min of ultrasound exposure was compared to the initial number of fluorescent cells in the same field of view (*i.e.* at 5 min following activation of the trap).

5.2.9 Protein synthesis inhibition

Chondrocytes (5×10^6 cells/ml) were suspended in serum-free DMEM/Ham's F12 containing 10 μg/ml cycloheximide (CHX) (Musil *et al.*, 2000) (Sigma, UK) and incubated for 1 h at 37°C/5% CO_2. Cells were then washed in fresh serum-free DMEM/Ham's F12 prior to introduction to the resonator. Aggregates were removed from the trap after 1 or 60 min of ultrasound levitation and double labeled for F-actin and Cx43. The integral intensity of F-actin and Cx43 at the cell-cell contact interface was measured at the above times for 10 randomly selected pairs of cells from each of two replicate experiments.

5.2.10 Addition of EDTA

Chondrocytes (5×10^6 cells/ml) were suspended in DMEM/Ham's F-12 medium containing 10 mM EDTA. The free [Ca^{2+}] in the medium, calculated as

described in Chapter 4 (Sec. 4.2.6.1), was 2.3 pM. Aggregates were removed from the trap after 1 and 60 min of ultrasound exposure and double stained for F-actin and Cx43.

5.3 Results

5.3.1 Formation and morphology of cell monolayers

Surface zone chondrocytes moved into the optically focussed nodal plane of the ultrasound trap within 1 s of initiation of sonication. Single cells and some small clusters moved towards the central aggregation area after 10 s of initiation of ultrasound (Fig. 5.2a). Some small clumps (consisting of approximately 20 cells) were formed outside the field of view and moved towards the central axis (20 s) (Fig. 5.2b). A small aggregate had formed by 30 s (Fig. 5.2c). Incoming single cells and 2-D closely-packed small clusters rolled along the periphery of the growing aggregate and rearranged to give a closely-packed structure within 1 min of sonication (Fig. 5.2d). Aggregate growth (Fig. 5.2e-h) continued with the incorporation of further clusters over the following 4 min. The aggregate growth was complete within 5 min of initiation of ultrasound, as characterised by the absence of free single cells from the field of view. The aggregate morphology was a hexagonally ordered closely-packed one with only a few voids (Fig. 5.2h). The void index ($A_v \backslash A_p$) of a typical chondrocyte cell aggregate was 0.03, resembling a control (0 mM $CaCl_2$) particle aggregate (Chap. 2, Sec. 2.3.2.3). Cells were levitated in the trap for an overall period of 1 h. The morphology of cells progressed from a circular to a pentagonal one within 1 h of exposure as shown later in Figures 5.5b, e.

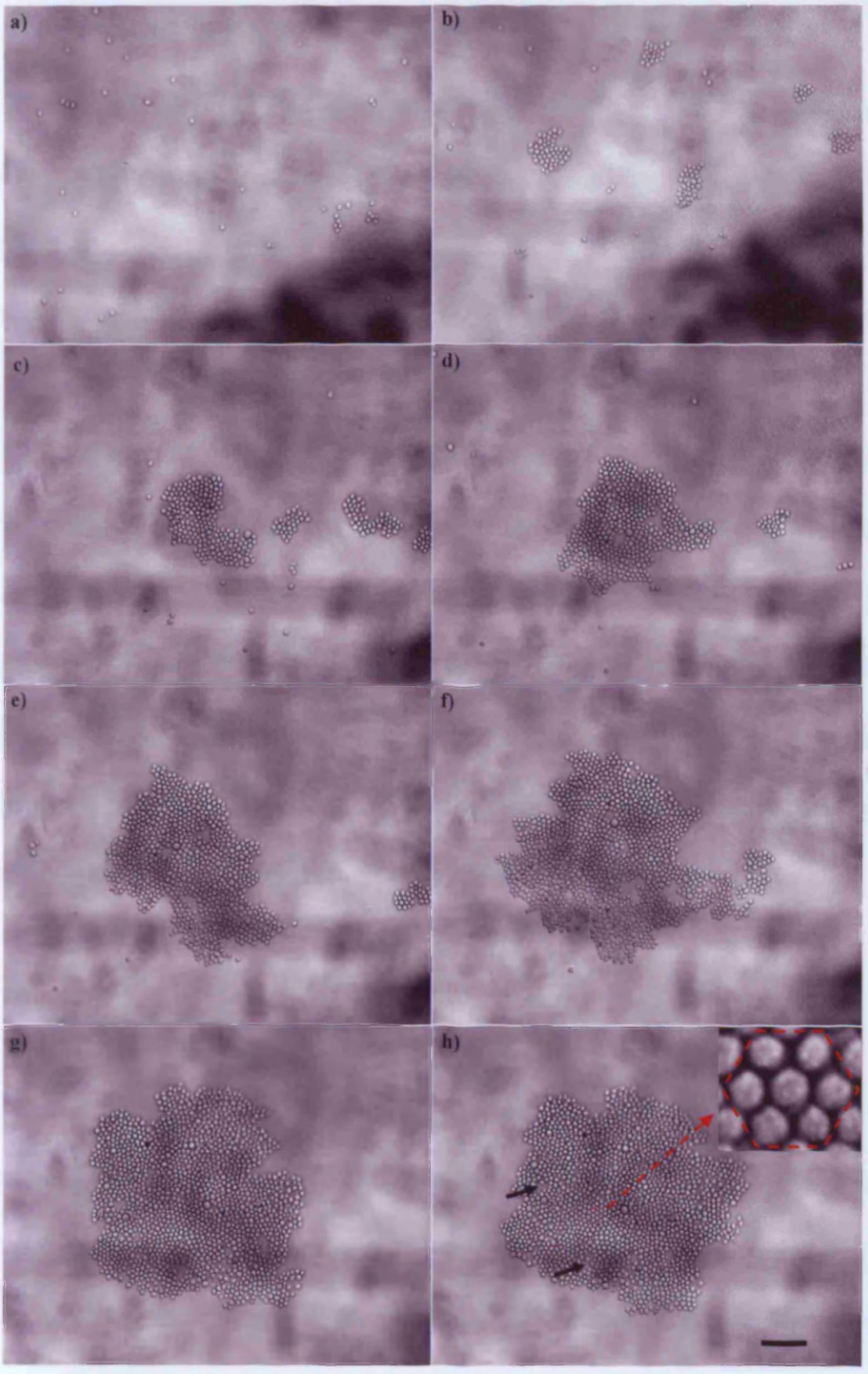

Figure 5.2: Development of a 2-D chondrocyte aggregate: (a) 10 s, (b) 20 s, (c) 30 s, (d) 1 min, (e) 2 min, (f) 3 min, (g) 4 min and (h) 5 min after ultrasound initiation. Scale bar is 100 μm. The few voids of the aggregate are shown with arrows in (h), while the hexagonal order of the aggregate is depicted in the zoom-in image shown on the top right-hand part of **(h)**.

5.3.2 Mechanical strength of aggregates

The dependence of the mechanical strength of aggregates on duration of sonication was investigated by termination of sonication at different stages of aggregate growth. Aggregates (10^5 cells/ml) that were allowed to form for 1 min before termination of sonication exhibited a high degree of dissociation with many openings within the aggregate (Fig. 5.3a).

The number of cells that had retained contact with neighbouring cells was small. In contrast, the 1 h aggregate remained fully intact on sedimentation (Fig. 5.3b). The results are consistent with increasing mechanical strength of an aggregate with time. Aggregates responded similarly upon their recovery from the ultrasound trap and deposition on a glass slide for immunofluorescent processing. Aggregates after 1 min of ultrasound exposure showed significant degree of dissociation upon deposition on a glass slide, whereas 1 h aggregates remained at their majority intact.

5.3.3 Actin localisation and Cx43 distribution

Initially, non-sonicated (control) cells were assayed. Cx43 in control (non-sonicated) cells was concentrated in finely granulated discrete regions, located mainly in the cytoplasm as shown as shown in Figure 5.4a (arrows). While, in general, control cells were distributed as single cells, Figure 5.4a, illustrating intracellular Cx43, was selected, despite having some cells in contact, to show the dominant occurrence of cytoplasmic staining in most cells. The actin cytoskeleton on the other hand, consisted of an intricate network throughout the cell (Fig. 5.4b, arrows).

Sonicated samples were then assayed. After 1 min of levitation Cx43 was located diffusely mainly at the periphery of the cells in the form of foci (Fig. 5.5a,

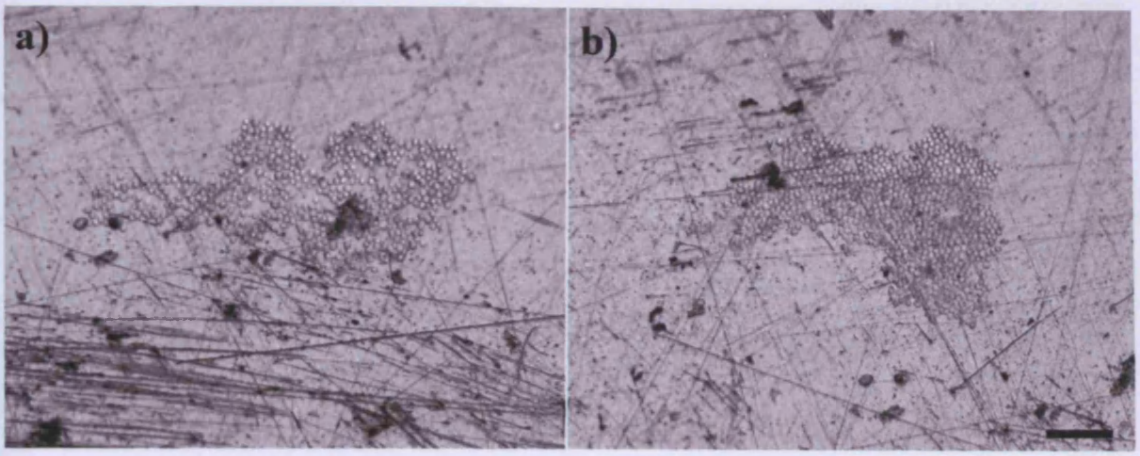

Figure 5.3: Sedimentation of chondrocyte aggregates upon ultrasound termination after 1 min (a) and 1 h (b). Aggregates levitated in the trap for 1 min (a) largely dispersed upon sedimentation at the bottom of the trap, while those levitated in the trap for 1 h (b) reached the bottom of the trap intact. Scale bar is 100 μm.

arrows). However, 1 h later Cx43 has clearly accumulated at the cell-cell contact interface as a nearly continuous line (Fig. 5.5d, arrows).

F-actin was distributed in a ring-type pattern at the cell surface following 1 min of ultrasound exposure. Some internal actin organization and a short cell-cell interface were also observed (Fig. 5.5b, arrows). After 1 h, F-actin had clearly accumulated at the long cell-cell contact interface (Fig. 5.5e, arrows). Comparison of the superimposed images (Figs. 5.5c and 5.5f) shows that the strong co-localisation of F-actin and Cx43 observed at 60 min had not yet been established at 1 min (Fig. 5.5c). Integral intensity measurements of the phalloidin-Alexa 488 and Alexa 594 labelling of 20 randomly selected cell-cell interfaces from two slides of each of three replicate experiments showed that the amount of F-actin and Cx43 at the cell-cell contact region had increased over 60 min (Fig. 5.6).

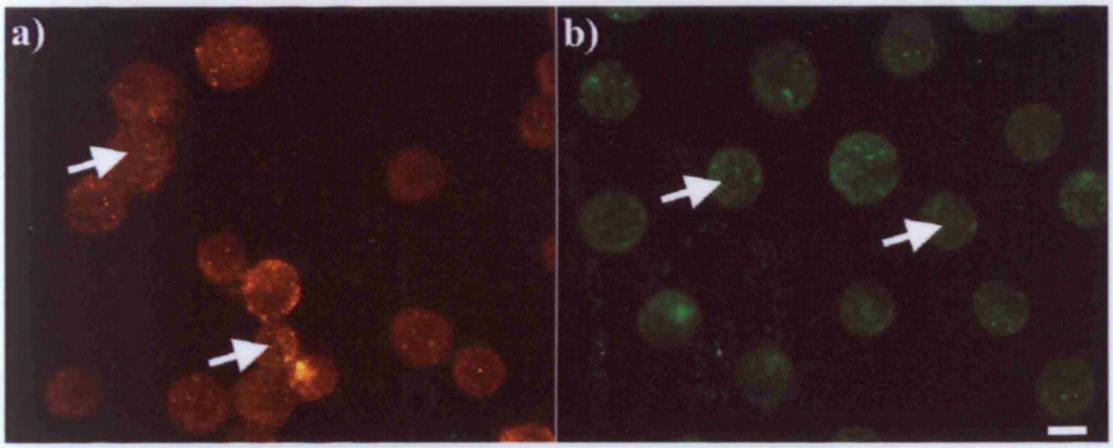

Figure 5.4: Distribution of (a) Cx43 and (b) F-actin in non-sonicated chondrocytes 1 h after their preparation. Cx43 (a) appeared highly granulated at the cytoplasm of the cells (arrows), while F-actin (b) consisted of an intricate network (arrows). Scale bar is 10 μm.

5.3.4 Reverse transcriptase-PCR

Reverse transcriptase-PCR was used to detect whether Cx43 mRNA present in RNA isolated from slivers of surface and deep zone chondrocytes is transcribed. A fragment of 327 bp was detected in agarose gel electrophoresis suggestive of the presence of Cx43 mRNA product (Fig. 5.7). The presence of Cx43 was confirmed by gene sequencing.

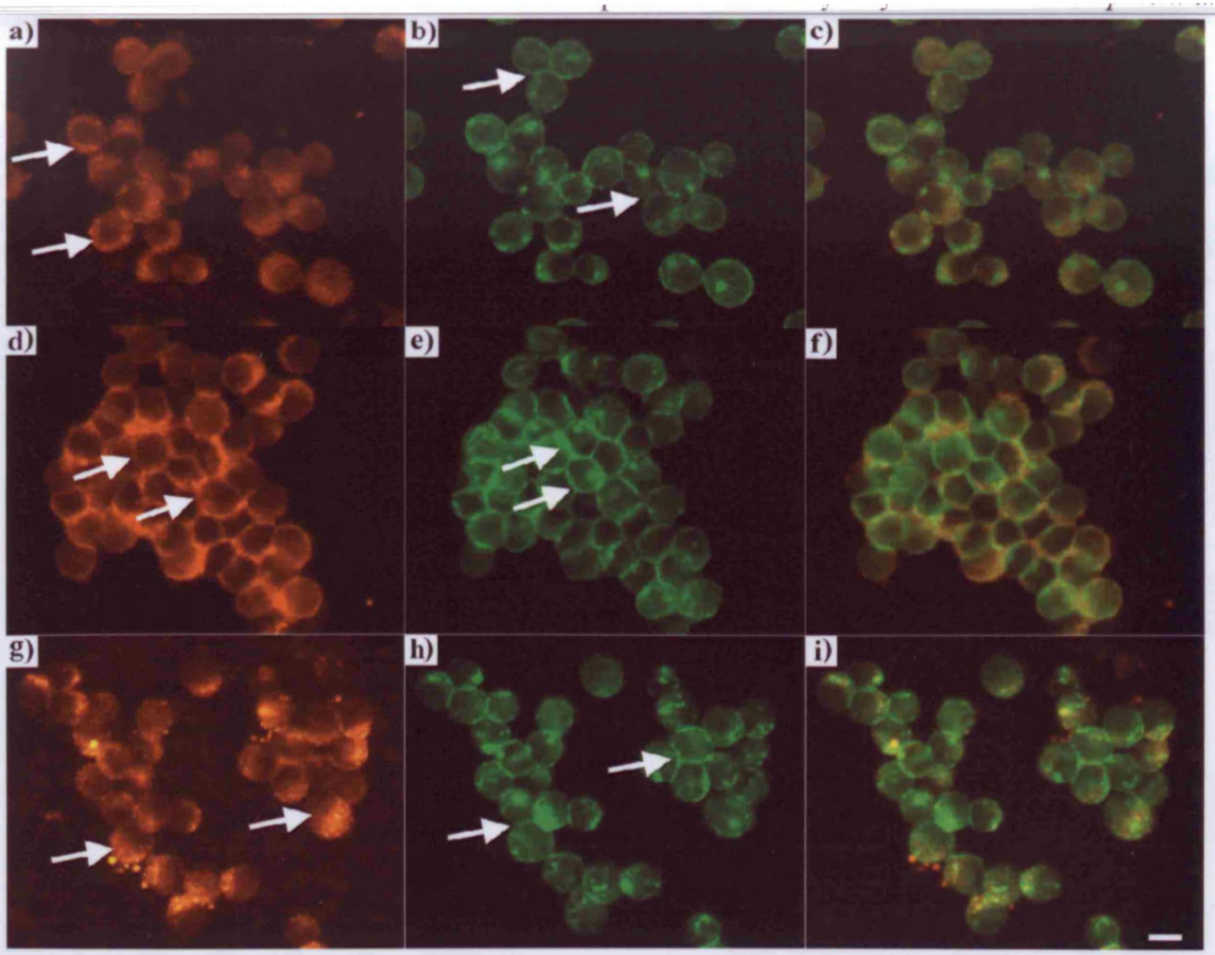

Figure 5.5: Distribution of peripheral (a, arrows) and interfacial (d, arrows) Cx43, and short (b, arrows) and long (e, arrows) interfacial F-actin in aggregates isolated from the trap after 1 (a, b) and 60 (d, e) min of ultrasound exposure respectively: (c, f) superimposed images. (g, h) distribution of Cx43 (intense cytoplasmic Cx43 pool, g, arrows) and F-actin (accumulation at the cell-cell interface, h, arrows) respectively in chondrocytes pre-incubated with 10 µg/ml CHX and levitated for 1 h in the trap. The superimposed image of g, h is shown in i. Scale bar is 10 µm.

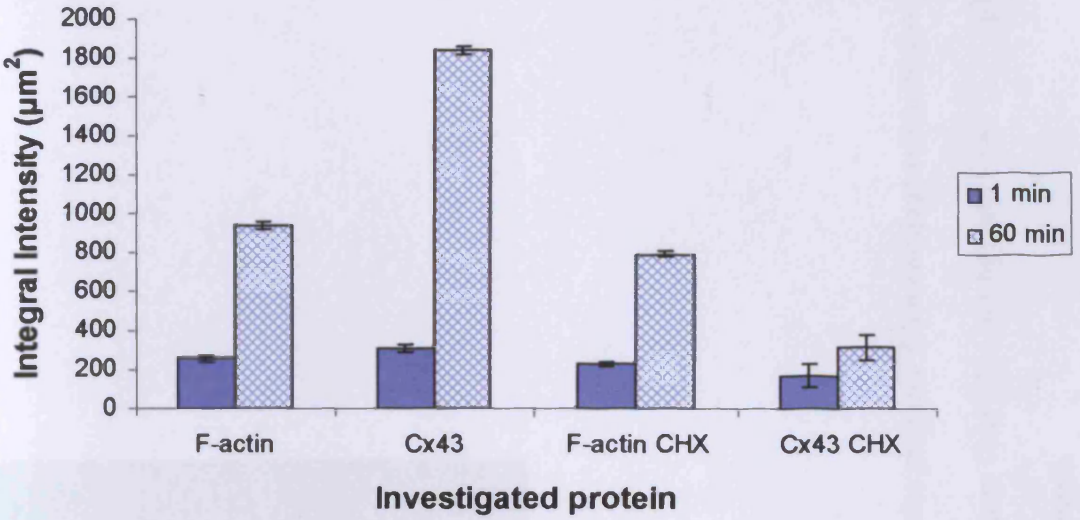

Figure 5.6: Measurements of the integral intensity of F-actin and Cx43 in control and cycloheximide (10 µg/ml CHX) -pretreated cells, at the cell-cell interface of 20 randomly selected pairs of cells (10 randomly selected pairs of cells from each of two replicate experiments.) The error bars represent one standard error of the means from the two replicates.

5.3.5 Functional gap junction activity

The results (Table 5.4) showed that, for cases where there were 31 and 35 CMFDA stained cells, at time 5 min, in single fields of view from repeated experiments, all (183 and 192 respectively) cells in those fields were stained after 60 min of exposure showing that there was intercellular dye transfer (Table 5.4).

On the other hand, in the presence of the gap junctional blocker 1–octanol, the increase in the number of fluorescently-labeled cells over a time period of 60 min was small. In particular, after 5 min of sonication the number of labeled cells was 40 and 48 (from total cells per field of 197 and 214 respectively), whereas 55 min later that number had increased to 52 and 57 respectively so that most (145 and 157 respectively) of the cells were unstained (Table 5.4).

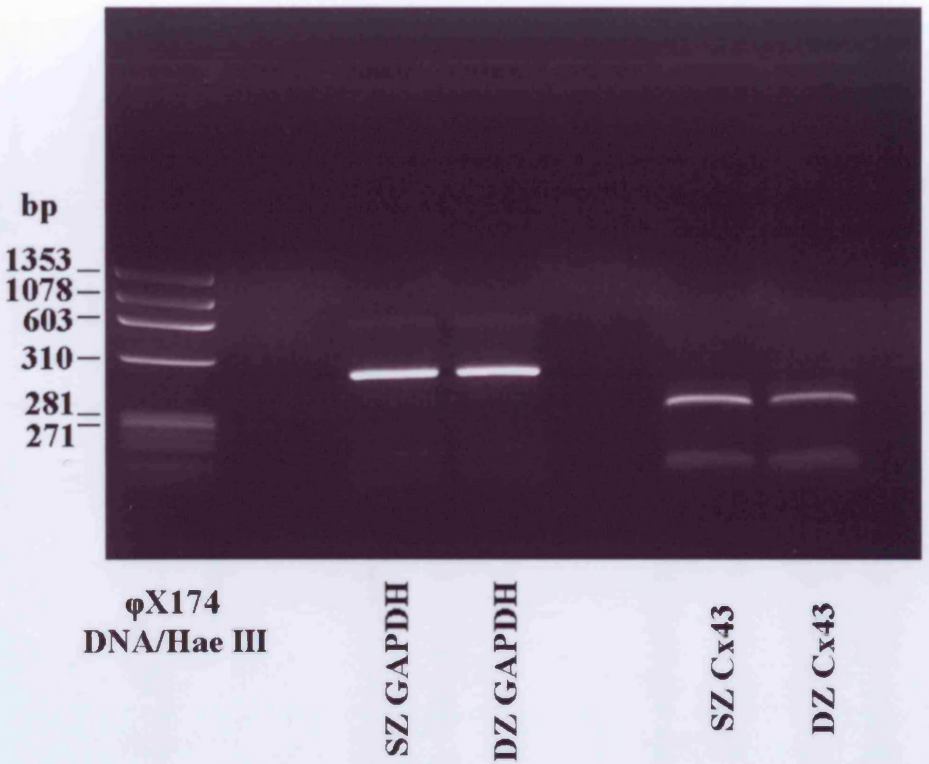

Figure 5.7: RT-PCR analysis of Cx43 gene expression in immature bovine articular cartilage. cDNA was prepared from cartilage removed from the surface and deep zones of the joint and subjected to PCR using primers specific for housekeeping gene GAPDH (501 bp) and Cx43 (327 bp). The results are representative amplifications from experiments using explants taken from 3 different donors.

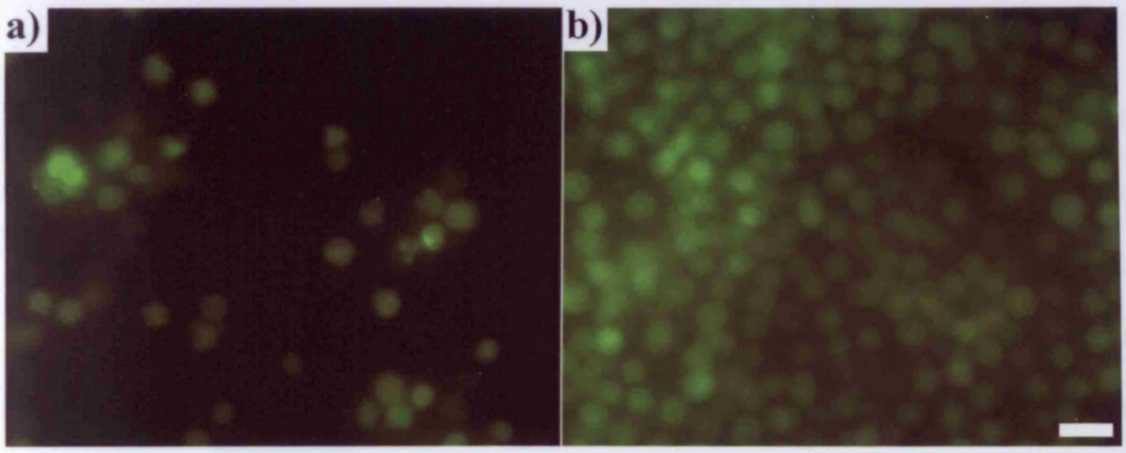

Figure 5.8: Green CMFDA Cell Tracker Probe dye transfer assays: (a) 35 cells in the field showed initial strong labeling (1 min in the trap), whereas 60 min later (b) 192 cells in the same field of view have been. A field of view where a low initial number of cells was stained (a) has been chosen to highlight the investigated phenomenon. Scale bar is 30 μm.

Table 5.4: Counts of labeled cells present in a randomly selected field of view in the presence and absence of the gap junctional blocker 1-octanol over time.

	Control		***1-Octanol***	
Time (min)	***Set 1***	***Set 2***	***Set 1***	***Set 2***
5	31	35	40	48
60	183	192	52	57
Total number of cells in the examined field of view	183	192	197	214

5.3.6 Protein synthesis inhibition

Chondrocytes were exposed to the protein synthesis inhibitor cycloheximide (10 μg/ml) to examine the distribution of F-actin and Cx43 upon stimulation of cell-cell contact in the ultrasound trap when synthesis of total cellular proteins has been inhibited. The qualitative microscopic patterns showing little accumulation of Cx43 at the cell-cell interface in aggregates recovered from the trap after 1 h of ultrasound exposure (Fig. 5.5g) and an intense cytoplasmic Cx43 pool (Fig. 5.5g; arrows) were quantitatively confirmed by intensity measurements of Alexa 594 staining (Fig. 5.6). The mean intensities of Cx43 and F-actin were derived from measurements of 10 randomly selected pairs of cells from each of two replicate experiments. The variances of the intensity distributions of the sets of measurements were not significantly different. The mean intensity was therefore calculated from the combined set of 20 measurements). After 1 h of levitation in the trap F-actin had accumulated at the cell-cell contact interface (Fig. 5.5 h). Figure 5.5i emphasises the co-localisation of F-actin and Cx43. The integral intensity data (Fig. 5.6) show that the amount of F-actin in 1 h samples was reduced by only 1.2-fold in cycloheximide pre-treated cells compared to control non-cycloheximide pretreated cells.

5.3.7 Role of EDTA

Microscopic observations showed that, in the presence of 10 mM EDTA(*i.e.* the free [Ca^{2+}] in the medium was 2.3 pM (Chap. 4; Sec. 4.2.6.1)), after 1 min of ultrasound exposure F-actin was localised around the surface of the cells, whereas Cx43 was distributed in a punctate pattern on the surface of the cells. However, 1 h later both F-actin and Cx43 had strongly accumulated at the cell-cell interface (Fig. 5.9), consistent with the observations presented for chondrocytes suspended in serum-

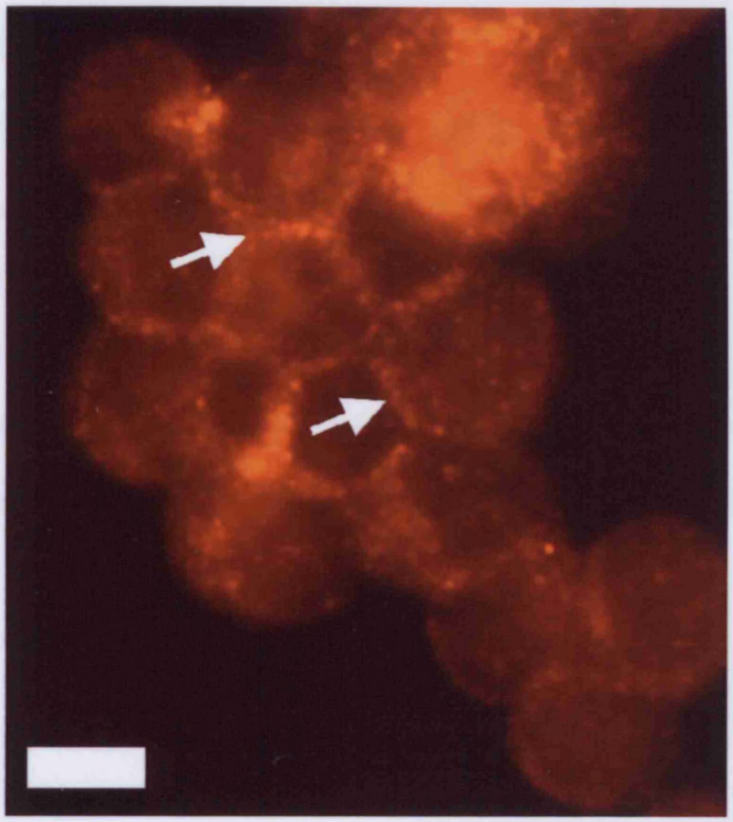

Figure 5.9: Accumulation of Cx43 at the cell-cell interface (arrows) of chondrocytes that had been suspended in DMEM/Ham's F-12 containing 10 mM EDTA. The aggregate was allowed to form for 1 h in the sound field, recovered from the trap and immunoassayed for Cx43. Scale bar is 10 μm.

free DMEM/Ham's F-12 medium alone (Fig. 5.5d). Integral intensity measurements of the phalloidin-Alexa 488 and Alexa 594 labelling of 20 randomly selected cell-cell interfaces cells from two slides of each of duplicate experiments showed that the amounts of F-actin and Cx43 at the cell-cell contact region were comparable to control (*i.e.* chondrocytes suspended in serum-free DMEM/Ham's F-12) values (Fig. 5.6). Additionally, bright field microscopic observations showed that the chondrocyte morphology progressively changed from a circular to a pentagonal one.

5.4 Discussion

5.4.1 Morphology of chondrocyte aggregates formed in a USWT

Upon ultrasound initiation, chondrocytes came into contact in the sound field and formed closely-packed hexagonally ordered structures of circular-profile cells (Fig. 5.2h). The aggregate form gradually changed to become a continuous sheet of quadrilateral and pentagonal cells typical of confluent monolayers on glass, thus reflecting a freedom to reorganise form rapidly within the unconstrained suspended monolayer as already described for neural cells (Chap. 4; Sec. 4.4.2). These morphological changes were accompanied by changes in the distribution of F-actin and Cx43.

5.4.2 F-actin redistribution

F-actin, after 1 min in the trap was distributed in a ring pattern at the cell surface with some evidence of internal organization (Fig. 5.5b) similar to that observed in non-sonicated samples (Fig. 5.4b). A thin and short interface at the cell- cell contact region was also observed. After 1 h, F-actin had clearly accumulated at the cell-cell contact interface (Fig. 5.5e) in a way that was consistent with the finding that the mechanical strength of the aggregates increased with time (Sec. 5.3.2). Aggregates that were allowed to form for 1 min, dispersed upon termination of sonication (Fig. 5.3a), while aggregates that were allowed to form for 1 h, sedimented at the bottom of the trap intact (Fig. 5.3b).

The overall cytoskeleton remodelling and mechanical strength increase correlation is in line with the recent report of Chu et al. (2004). These authors showed that (i) after 30 min F-actin had strongly accumulated at the linear interface of doublets of Sarcoma 180 (S180) cells formed in suspension and (ii) that the force

required to separate cells in a doublet formed by bringing cells, each supported by a micropipette, into contact for a period of 60 min increased rapidly over the first 30 min and more slowly thereafter to the 60 min value.

The chondrocyte cytoskeleton plays an important role in the physical interactions between the chondrocyte and its extracellular matrix and is intimately involved in the process of mechanical signal transduction in articular cartilage (Langelier *et al.*, 2000), as well as in the control of the chondrocyte phenotype (Vinhall *et al.*, 2002). The organisation of actin in chondrocytes affects differentiation. *In vivo*, they have a diffuse cortical actin distribution, with no prominent fibrous structures (Durrant *et al.*, 1999). If plated into conventional monolayer culture, chondrocytes flatten and phenotypically modulate, developing prominent actin stress fibres at the same time. If the stress fibres are disassembled by cytochalasin treatment, cells re-express the chondrogenic phenotype (Benya *et al.*, 1988; Mallein-Gerin *et al.*, 1991). The F-actin cytoskeleton was in both cases analysed after 1 day in culture (Woods *et al.*, 2005). Previous studies on chondrocyte cytoskeleton in agarose cultures reported remodelling of the cytoskeleton between 3 and 14 days in culture (Trickey *et al.*, 2004; Idowu *et al.*, 2000). Such a temporal delay does not occur in the USWT. Temporal data on the distribution of F-actin in a neural cell monolayer levitated in suspension in an ultrasound trap have already been given in Chapter 4 (Sec. 4.3.5). Redistribution of the neural F-actin cytoskeleton occurred within 30 min of cell-cell contact initiation in the ultrasound trap (Sec. 4.3.5). However, there has been no critical study reporting rapid (within 1 h) and synchronous remodelling of the cytoskeleton of interacting chondrocytes in suspension.

It is interesting to note that chondrocytes cultured in monolayer do not exhibit cytoskeletal variability (Knight *et al.*, 2001), as is the case for chondrocytes suspended

It is interesting to note that chondrocytes cultured in monolayer do not exhibit cytoskeletal variability (Knight *et al.*, 2001), as is the case for chondrocytes suspended in agarose cultures (Knight *et al.*, 2001). In contrast, chondrocytes in suspension in the ultrasound trap do not exhibit such cytoskeletal variability.

It is known that low intensity pulsed ultrasound promotes fracture healing and articular cartilage repair *in vivo* (Zhang *et al.*, 2003) by mechanisms that remain unclear (Iwabuchi *et al.*, 2005). Studies of these processes have included assays of chondrocyte properties following exposure to ultrasound. The time scales at which responses were monitored were typically days after ultrasound administration rather than the 1 h upper limit of the present work. For example, daily ultrasound exposures of mesenchymal stem cells in pellet culture increased aggrecan deposition and transforming growth factor beta (TGF-β)- induction of cell differentiation to chondrocytes (Ebisawa *et al.*, 2004). Also, chondrocytes in alginate beads exposed to ultrasound showed inhibition of collagen type X expression after 7 days (Zhang *et al.*, 2003). Since temporal changes in the F-actin distributions, similar to those reported here for chondrocytes and to those summarised above where cell contact occurs in non-ultrasound systems, have been found also in USWT neural cell adhesion (Chap. 4) and in prostate epithelial cells (Chap. 6), it is concluded that the observed effects on F-actin and Cx43 distribution reported above follow from engagement of receptors rather than from any currently unknown ultrasound mechanism.

5.4.3 Cx43 redistribution and formation of gap junctions

Figures 5.4a, 5.5a and 5.5d show a clear progression of Cx43 from an intracellular location (cytoplasmic pool) (Fig. 5.4a; non-sonicated cells), to the plasma membrane (Fig. 5.5a; 1 min in the trap) to finally concentrate at the cell-cell contact

interface (Fig. 5.5d; 1 h in the trap). The concentration of Cx43 at the cell-cell interface of chondrocytes (Fig. 5.5d) and the octanol blockade (Sec. 5.3.5) provide strong evidence in support of the presence of functional gap junctions (Contreras *et al.*, 2002; Hunter *et al.*, 2003).

Connexin oligomerisation into connexons is a sequential process commencing in the endoplasmic reticulum continued in the endoplasmic-Golgi-intermediate compartment (ERGIC) and is completed following arrival at the Golgi (Evans and Martin, 2002). The final destination of the connexons, via tubulovesicular networks, is the gap junctions present at the cell membrane (Bruzzone *et al.*, 1996; George *et al.*, 1999; Windoffer *et al.*, 2000; Theiss and Meller, 2002). The data on Cx43 distribution presented in this study as determined by immunofluorescence are in agreement with reports for Cx43 trafficking.

The temporal progression of gap junction formation in various cell systems has been addressed by several investigators. George et al. (1999) using a Cx43-Aeq chimera model in COS-7 cells cultured on coverslips reported that transportation of Cx43 to the plasma membrane occurs within 10 min, whereas Lauf et al. (2002) reported that transportation of Cx43-GFP from the Golgi compartment to the plasma membrane occurs within 90 s. The same authors also reported that a gap junction 1 μm^2 in size that consists of ~10,000 channels could be assembled within 2 h in HeLa cells in confluent monolayer. Musil et al. (2000) showed that mouse sarcoma cells, at confluent density in monolayer cultures, establish functional gap junctional channels within 30 min of *de novo* cell-cell contacts formation, whereas in a donor-acceptor cell model of human gingival fibroblasts (HGFs) presented by Ko et al. (2000) distinct gap junctional complexes were evident by 3 h. The time scale data on Cx43 distribution in chondrocytes are consistent with those reported above for other cell systems, whereas

in chondrocytes functional gap junctions have been reported to form *within* 24 h from the onset of the micromass culture (Coelho and Kosher, 1991; Langille, 1994) and 3-6 days from the initiation of monolayer cultures (D'Andrea and Vittur, 1996; Schwab *et al.*, 1998; Loty *et al.*, 2000).

5.4.4 Cx43 protein expression

It is interesting that Cx43 mRNA (Fig. 5.7) was still expressed after chondrocyte differentiation, as chondrocytes within mature articular cartilage exist as individual cells not in physical contact with one another (Donahue *et al.*, 1995; Loty *et al.*, 2000; Elfervig *et al.*, 2001). However, recent data (Chi *et al.*, 2004) have revealed that at least some chondrocytes of the surface zone of adult human articular cartilage in the knee and ankle occur in pairs (Schumacher *et al.*, 2002), possibly due to an incomplete division of the chondron microenvironment during development (Chi *et al.* 2002) or due to the chondrocytes' ability to organize themselves into pairs or groups by recapitulating the events of development (Morrison *et al.*, 2000).

Blocking the production of new connexin molecules with the protein synthesis inhibitor cycloheximide resulted in a major reduction of Cx43 at the cell-cell interface as shown Figure 5.5g. The six-fold reduction in measured Cx43 fluorescence intensity of at the cell-cell interface of cycloheximide-preincubated cells supports the immunofluorescent data (Fig. 5.6). It has been known for a long time that gap junctions are subject to rapid turnover given the short half life of their molecular subunits (Musil *et al.* 2000). For Cx43 a half life of <1.5 h has been reported in the adult rat heart *in vivo* and cultured cardiac myocytes (Beardslee *et al.*, 1998), whereas longer half times have been reported for mouse sarcoma (Musil *et al.* 2000) and NRK cell monolayers (Musil and Goodenough, 1991). In contrast to the Cx43 data,

equilibrium with monomeric G-actin (Upadhya and Strasberg, 1999) (Chap. 1; Sec. 1.2.1.1) and has been reported to have a half life of ~4.5 h (Sympson and Geoghegan, 1990). It was therefore shown that cycloheximide affects the production of new Cx43 protein as it has a very short half life but it has a small effect on the redistribution of the longer half-life F-actin.

5.4.5 Role of Ca^{2+}

It was shown that at a concentration of 2.3 pM free [Ca^{2+}] in the medium, redistribution of the actin cytoskeleton from a circular-type of distribution around the surface of the cells, towards an accumulation at the cell-cell contact interface occurred within 1 h of ultrasound exposure (data not shown) in agreement with the observations for the case where cells were suspended in serum-free DMEM/Ham's F-12 containing 1 mM free [Ca^{2+}] (Fig. 5.5e). Additionally, the morphology of the cells progressed from a circular to a quadrilateral or pentagonal one. Integral intensity measurements performed at the cell-cell interface of 20 randomly selected pairs of cells further support these observations. After 1 h of ultrasound exposure the phalloidin-Alexa 488 integral intensity was 950 μm^2, in accord with the measurements obtained for the control suspension (Fig. 5.6). Likewise, 2.3 pM of free [Ca^{2+}] in the extracellular phase had no effect on the redistribution of Cx43 molecules from intracellular locations towards the cell surface. As shown in Figure 5.9, Cx43 has accumulated at the cell-cell interphase, while the intensity measurements of Cx43 at the cell-cell interphase showed similar values (*i.e.* 1790 μm^2) to the control suspension (Fig. 5.6).

It was therefore shown that depleting Ca^{2+} from the culture medium does not affect the ability of chondrocytes to redistribute their F-actin cytoskeleton or form gap junctions upon stimulation of cell-cell contact in the ultrasound field.

It was therefore shown that depleting Ca^{2+} from the culture medium does not affect the ability of chondrocytes to redistribute their F-actin cytoskeleton or form gap junctions upon stimulation of cell-cell contact in the ultrasound field.

The extent to which cadherins in low calcium conditions participate in the reorganisation of the F-actin cytoskeleton of neural cells has been already discussed in Chapter 4 (Sec. 4.4.4). The cooperativity of two different adhesion mechanisms (NCAM and N-cadherin) was shown to be important for an organised outcome.

Strong association between members of the cadherin-catenin complex and gap junctions has also been reported, as cadherin-mediated cell-cell adhesion has been reported to be a prerequisite for formation of gap junctions (Zuppinger *et al.*, 2000; Giepmans, 2004) as already described in Chapter 1 (Sec. 1.6.4). Chondrocytes express NCAM and N-cadherin during pre-chondrogenic condensation (DeLise *et al.*, 2000); however as condensations mature, N-cadherin and NCAM expression decreases, whereas these molecules are no longer found in differentiated cartilage (*i.e.* in chondrocytes) (Widelitz et al. 1992; Oberlender and Tuan 1994) (Sec. 5.1). Yet, as reported by Tavella et al. (1994) re-expression of NCAM and N-cadherin in aggregated chondrocytes had occurred within 12 h of their transfer from anchorage-dependent (culture flask) to anchorage-independent (agarose culture-suspension culture) conditions. It is therefore reasonable to consider that initiation of chondrocyte cell-cell contact in the sound field may result in a rapid expression of NCAM and N-cadherin molecules that to an extent cooperate in a mutual way as has been described for neural cells (Chap. 4; Sec. 4.4.4). Nevertheless, further work needs to be done to clarify this hypothesis.

Interactions between gap junctions and the cytoskeleton are becoming increasingly evident as disruption of the actin cytoskeleton by cytochalasin B exposure

intercellular communication in cultured astrocytes (Theiss and Meller, 2002) and cultured lens epithelial cells (Giessmann *et al.*, 2003). Interaction between actin and connexins has been further confirmed by co-immunoprecipitation and immuno-co-localisation (Butkevich *et al.*, 2004; Liu *et al.*, 2005). Figure 5.5f shows complete co-localisation of F-actin with Cx43, indicating that these molecules are activated together and thus a strong association between these molecules exists.

5.5 Preliminary Conclusions

In conclusion, the results presented in this Chapter showed that Cx43 gene expression is retained in isolated chondrocytes in suspension. The development of the chondrocyte F-actin cytoskeleton occurred within 60 min of initiation of cell-cell contact in the ultrasound field. This time scale is consistent with reports on F-actin redistribution in other cell systems, such as in neural cells (Chap. 4; Sec. 4.3.5) and keratinocytes (Braga, 2002). In contrast, data on functional gap junction formation in chondrocytes has not been explored in times less than 24 h. This Chapter presented the first detection of gap junction formation in chondrocytes within 1 h of cell contact.

It also emerges from this work that the interactions at the plasma membranes of cells in close proximity in the ultrasound trap transduce signals to the cytoplasm that set in train the reorganisation of F-actin at the cell interfaces, changes in cell and the development of functional gap junctions. The passive physical trap facilitation of cell contact led to accumulation of Cx43 in cells released from protein synthesis inhibition, showing that the biological consequences of the contact proceeded, as in the *in vivo* situation, to influencing protein expression. The potential of the ultrasound trap as a technique sensitive enough to aid in the identification of the adhesive properties of cancer cells is introduced in the last experimental Chapter 6 of this thesis.

released from protein synthesis inhibition, showing that the biological consequences of the contact proceeded, as in the *in vivo* situation, to influencing protein expression. The potential of the ultrasound trap as a technique sensitive enough to aid in the identification of the adhesive properties of cancer cells is introduced in the last experimental Chapter 6 of this thesis.

Chapter 6

Comparison of the adhesive properties of epithelial and cancer prostate cell lines using the ultrasound trap

6.1 Introduction

Prostate cancer is the second leading cause of cancer deaths in men and the leading male cancer in Western countries (Mason *et al.*, 2002), while it is not invariably lethal. It is a heterogeneous disease ranging from asymptomatic to a rapidly fatal systemic malignancy (Hughes *et al.*, 2005). For patients with prostatic carcinoma, tumour invasion and metastasis are life-threatening events and the patients frequently have poor prognosis as a result of local or distant metastasis (Mason *et al.*, 2002). The frequency of prostate cancer is so high that it can be considered a normal age-related phenomenon. In recent years, there have been large increases in the five year survival rates for prostate cancer, with a five year relative age standardized survival rate of 65% in England and Wales for the years 1996-1999 (Hughes *et al.*, 2005). This was the third highest survival rate of all cancers over this time period. Unfortunately, this improvement does not reflect better prognosis or treatment for prostate cancer (Hughes *et al.*, 2005).

During tumour progression, loss of epithelial characteristics (cuboidal morphology, apical and basolateral membrane domains, tight cell-cell adhesion) results in de-differentiation, a process involving not only morphological alterations (cell-cell adhesion and cytoskeletal networks), but also changes in attachment to

substratum, motility rate and gene expression profile (*i.e.* epithelial-specific genes are switched off). In other words, de-differentiation marks the epithelial-mesenchymal transition occurring during tumour progression (Lozano *et al.*, 2003). With the disruption of junctions (*e.g.* adherens junctions) between neighbouring cells, increased motility, facilitated by the degradation of matrix proteins, is observed. Cells are thus able to infiltrate the neighbouring tissues, gain access to blood vessels and colonise distant sites (metastasis) (Lozano *et al.*, 2003; Crnic and Christofori, 2004).

The fact that cancer cells commonly show decreased intercellular adhesiveness as well as that most cancers are of epithelial origin has led to increased interest in studying the E-cadherin/catenin complex. A role for E-cadherin in limiting invasion of tumour cells and acting as a suppressor of invasion has been accepted by many investigators (Wheelock *et al.*, 2001, Bremmes *et al.*, 2002). Compared with normal tissues, malignant tumours generally show less expression or more heterogeneous expression of E-cadherin and catenin proteins.

The expression of E-cadherin is reduced in prostate cancer cells compared to normal prostate tissue (Graff *et al.*, 1995; Davies *et al.*, 2000; Lu *et al.*, 2005). Furthermore, the expression of both α- and β- catenins in prostate cancer is also altered (Graff *et al.*, 1995; Yang *et al.*, 2005). It follows that the E-cadherin/catenin complex in association with the actin cytoskeleton can serve as a prognostic and predictive tumour marker for identifying the cellular origin of the tumour and for denoting changes in the normal cell phenotype (Lozano *et al.*, 2003). Early cancer prognosis offers the possibility of early supporting therapy.

In the present chapter the ultrasound trap is used to establish and compare the temporal distribution of the cadherin/catenin complex and F-actin upon facilitation of cell-cell contact of epithelial prostate cells (PZ-HPV-7) and prostate cancer cells

(DU-145). The distributions of F-actin, E-cadherin, α-, β- and γ-catenins were monitored over the first 60 min of ultrasound exposure. It was shown that the distribution of these molecules was significantly different in the two cell lines. Changes in the amounts of F-actin, α-, β- and γ-catenins over time were quantified using the integral intensity approach described in Chapter 4 (Sec. 4.2.6), whereas a simple 'scoring' approach was used to quantify the transcellular distributions of E-cadherin, α-, β- and γ-catenins. The heterogeneity of each cell line was also assessed. The ability of cells to spread over neighbouring cells was in addition quantified.

6.2 Materials and Methods

6.2.1 Ultrasound trap, optical system and experimental procedure

The acoustic trap and optical system used here as well as the experimental procedures have already been described in Chapter 4 (Sec. 4.2.1). Formation of aggregates took place according to the protocol described in Chapter 3 (Sec. 3.3.1), *i.e.* cells were initially exposed to ultrasound at a pressure amplitude of 0.54 MPa for 30 s, at 0.27 MPa for 5 min and finally at the levitation pressure amplitude threshold of 0.06 MPa for the remaining 55 min of exposure. Microscopic observation was performed as described in Chapter 4 (Sec. 4.2.1).

6.2.2 Culture of PZ-HPV-7 and DU-145 cells

The human epithelial prostate cell line PZ-HPV-7 and the human epithelial cancer prostate cell line DU-145 were obtained from the American Type Culture Collection (ATCC) (Rockville, Md). Cell lines were maintained, as replicative cultures at 37°C under an atmosphere of 95% air and 5% CO_2, in Ham's F-12 medium

supplemented with 10% foetal calf serum (PAA Laboratories, Austria) and 100 μg/ml penicillin-streptomycin solution (Sigma, UK). The medium was changed every third day.

Routine sub-culturing procedure was performed according to the protocol provided by ATCC. Cells at the confluence phase were rinsed with 2 ml of 5 mM EDTA (Sigma, UK) and then treated with 1-2 ml of trypsin/EDTA (trypsin 0.01% (w/v) (Sigma, UK) and EDTA 0.05% (w/v)). Cells were then incubated for 5 min at 37°C to allow for cell detachment. Once cells had detached from the surface of the flask, the effect of trypsin was neutralised by the addition of 5 ml of Ham's F-12 medium (supplemented with 10 % foetal calf serum and 100 μg/ml penicillin-streptomycin solution). Cells were counted on a Bright-line haemocytometer (Reichert, USA) and finally seeded into culture flasks at a cell density of 10^6 cells/ml.

The protocol followed for experimental work was based on that described by Jiang et al. (1995). Cells at the confluence phase were rinsed with 3 ml of N-2-hydroxyethylpiperazine-N'-2-ethanesulfonic acid (HEPES) Ca^{2+} and Mg^{2+}-free buffered saline (HCMF) and then treated with 3 ml of Accutase (Innovative Cell Technologies Inc), a solution that contains mild collagenolytic and proteolytic enzymes (the names and concentrations of these enzymes are the company's proprietary information) for 15 min to release cells from the culture flask surface. Cells were filtered through a 40 μm Nitex cell strainer (FALCON) to ensure a single cell suspension. Cells were then centrifuged at 600 g for 5 min, resuspended in HCMF/5 mM $CaCl_2$, counted and finally diluted to the desired concentration.

6.2.3 Immunolabelling

Non-sonicated (control) cells were initially assayed. Cells were prepared as described in Section 6.2.2 (experimental work protocol), and incubated as suspension cultures for 1 h at 37°C/ 5% CO_2. A 100 µl aliquot from each cell line was placed on a HistoBond slide after 1 h of incubation. Samples were then fixed and stained for E-cadherin (monoclonal anti-human; 5 µg/ml; R and D Systems, Oxford, UK), α-, β- and γ-catenins (monoclonal anti-human; 5 µg/ml; BD Transduction Laboratories, UK), and F-actin (Chap. 4; Sec. 4.2.5) as described in Chapter 4 (Sec. 4.2.5).

Sonicated samples were then assayed. Both cell lines were prepared as described above (Sec. 6.2.2; experimental work protocol) and diluted to a concentration of 3×10^6 cells/ml. Cells were then immediately placed in the ultrasound trap. Aggregates of significant size (*i.e. ca.* 1 mm diameter) were formed within 30 s of ultrasound exposure and were held in the trap for 1 min and 1 h. They were then slowly removed, fixed and double-stained for E-cadherin and F-actin according to the procedure described in Chapter 5 (Sec. 5.2.4) and for α-, β- and γ- catenins as described in Chapter 4 (Sec. 4.2.5).

The integral intensity of the phalloidin labelling at the cell-cell interface was quantified as detailed in Chapter 4 (Sec. 4.2.5) and it was used here as i) an indicator of change in the amount of the labeled molecule and ii) an index of the effectiveness of the cadherin/catenin complex. A second index, an estimate of the angle θ subtended by the F-actin staining region at the centres of a pair of interacting cells, was used to quantify the extent of membrane-membrane contact over different times. The angle was calculated as follows:

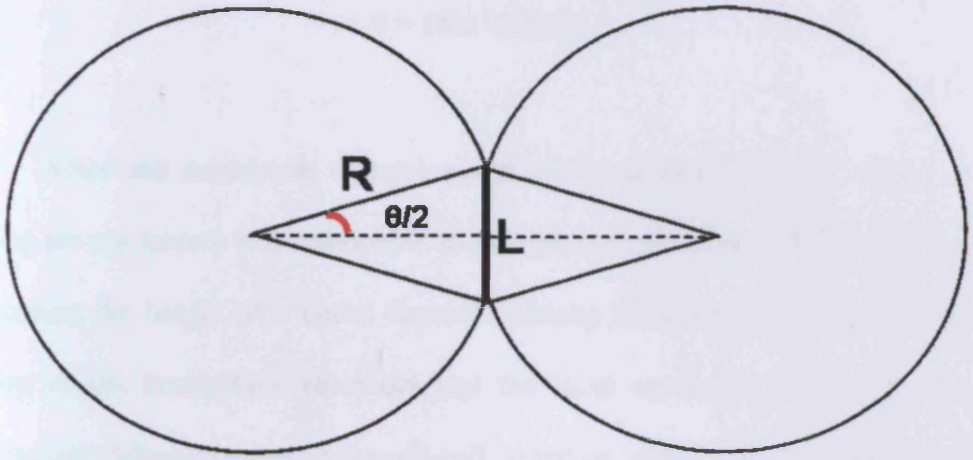

Figure 6.1: Schematic diagram of an interacting cell doublet; L is the length of the F-actin staining region or 'chord' (drawn here as a straight line), R is the radius of the cells and θ is the angle subtended by the chord at the centre of the cell.

The contact region was treated as a shared chord of 'overlapping' circles. It is appreciated that the cell perimeters are longer than those for perfect circles as cells have surface area in excess of that required to contain a spherical cell volume (a property necessary so that when a cell divides the two resulting smaller volumes are each continuously covered by membrane). No allowance can be made for the consequent departure from circular profiles as membrane spreading continues. Within that limitation it will be taken that for a cell-cell contact chord' L and cell radius R (Fig. 6.1) then Sin (θ/2), where θ is the angle subtended by the chord at the centre of the cell, is given by

$$\text{Sin}\,(\theta/2) = (L/2)/R = L/2R \qquad (6.1)$$

so that

$$\theta/2 = \text{Sin}^{-1}(L/2R) \qquad (6.2)$$

and

$$\theta = 2\mathrm{Sin}^{-1}(L/2R) \qquad (6.3)$$

While the membrane dynamics and micromechanics at the end of contact regions are not known it is reasonable to assume that, for cells, the ability to continue to increase the length of a chord depends, among other things, on both the surface density of the homophilic receptors and the local resistance of the membrane to deformation. Measurements of the cell-cell interface 'chord' were performed using the analySIS 3.1 software.

6.2.4 Scoring the incidence of different categories of distribution of cadherin/catenin-complex molecules in PZ-HPV-7 and DU-145 cells

Five randomly selected immunofluorescent images (Sec. 6.2.3) (1 image from each of three experiments and 2 images from a fourth) were examined in order to identify the distribution of E-cadherin and α-, β- and γ-catenins in both cell lines. A dominant distribution of a particular molecule, for example E-cadherin, was identified for PZ-HPV-7 cells and coded as $PZ_{E\text{-}cadDom.}$ Its incidence for the five randomly selected fields of view was scored and summed (X_{PZDom}). The dominant distribution of E-cadherin in DU-145 ($DU_{E\text{-}cadDom}$) was then identified, counted and summed as Y_{DUDom}. It emerged that almost all (*ca.* 98%) of the cells in the five fields of view for each cell line fell into either one or other category. Table 6.1 is an exemplar 2×2 contingency Table for data obtained as above.

Table 6.1: Exemplar 2×2 contingency table constructed for the identification and scoring of the distribution of E-cadherin (as well as α-, β- and γ-catenins) in both cell lines.

	$PZ_{E\text{-}cadDom}$	$DU_{E\text{-}cadDom}$
PZ-HPV-7	X_{PZDom}	Y_{DUDom}
DU-145	Y_{DUDom}	X_{PZDom}

The different molecular distributions were scored for the two cell lines for two time points: 1 min and 1 h. The total number of cells in the five images ranged from 98 to 277 for the different experiments. χ^2-test was performed for each time point to establish whether there was a significant difference between the frequencies of the selected molecular distributions in the two cell lines. The information for each molecule at each time is presented in the Results Section 6.3, in Tables containing the description of the dominant distribution form, the number of cells scored, the percentage of cells scored that had the dominant distribution for each cell line and the χ^2-parameter for each contingency Table as above. This presentation is intended to focus on the important points and yet allow the original count data to be deduced should a reader consider it necessary.

6.3 Results

6.3.1 Aggregate morphologies

Cells of both cell lines suspended in HCMF/$CaCl_2$ moved into the optically focussed nodal plane of the USWT within 1 s of initiation of sonication. A small

aggregate had formed 20 s later at the central region of the nodal plane. Incoming single cells and dendritic small clusters formed strong contact instantly with the peripheral of the growing aggregate, *i.e.* they did not roll along the periphery. However, the short dendritic clusters rotated, without internal reorganisation, about their first contact point with the main aggregate so that it developed a more closely packed form, (with little evidence of hexagonal order over an extended area) as was the case for neural cells (Chap. 4; Sec. 4.3.1). The void indices ($A_v \backslash A_p$) of typical PZ-HPV-7 and DU-145 cell aggregates were 0.06 and 0.05 respectively, resembling particle aggregates suspended in 2-4 mM $CaCl_2$ (Chap. 2, Sec. 2.3.2.3). An aggregate was fully formed within 5 min of ultrasound exposure, as characterised by the absence of free single cells from the field of view (Fig. 6.2). Cells were exposed to ultrasound for an overall period of 1 h.

6.3.2 Membrane spreading

Spreading of the membranes of cells in contact in the trap occurred, for both cell lines to a smaller extent from that described for neural cells (Chap. 4; Sec. 4.3.2). Some reduction in the resolution of the individual cell boundaries occurred within 60 min of ultrasound exposure, resulting in a cell morphology change from a circular (1 min of exposure) to a pentagonal one (60 min of exposure) and to some compaction of the aggregate (Fig. 6.7b, d). The ability of cells to spread was quantified by measuring the angle θ of the cell-cell interface 'chord' (Fig. 6.3). The angle θ of PZ-HPV-7 cells increased from 43° ± 1.3 to 91° ± 2.4 (*i.e.* it increased by a factor of 2.1), whereas that of DU-145 cells increased by a factor of 1.5 (from 42°± 0.92 to 65° ± 1.37) (Fig. 6.3).

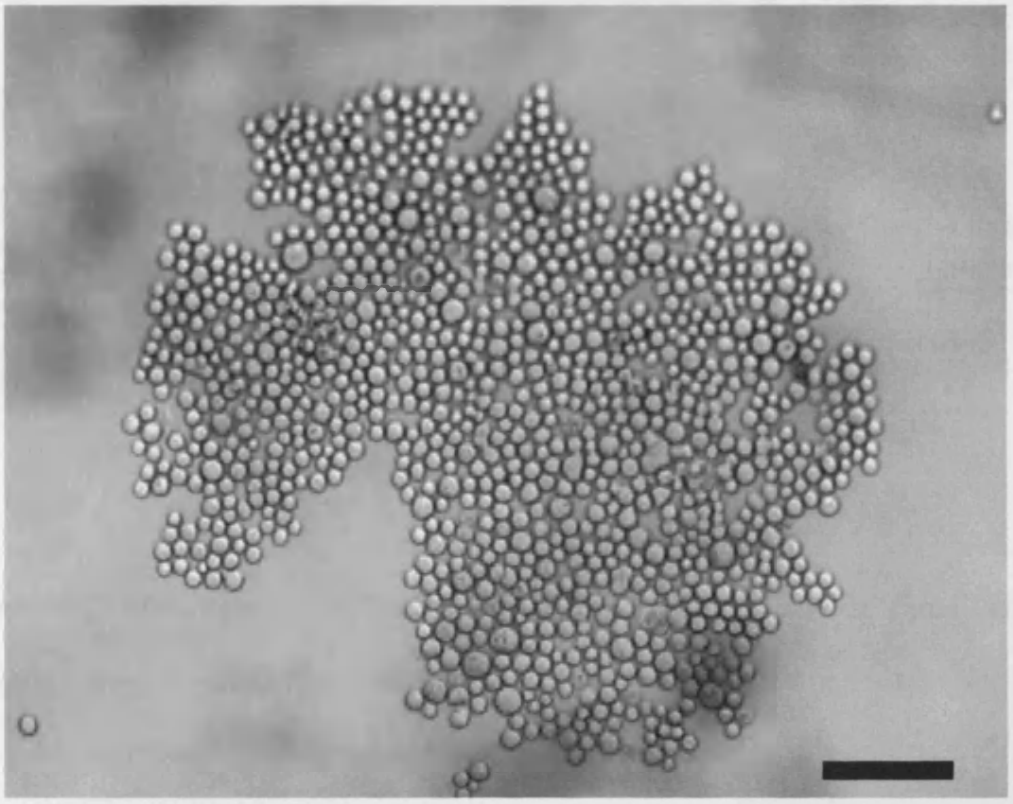

Figure 6.2: PZ-HPV-7 cells suspended in the trap for 5 min; pressure, 0.27 MPa. Scale bar is 100 μm. Cell aggregate morphology was closely packed with little evidence of hexagonal order.

Statistical analysis performed with Student's two-tailed t-test showed that there was no significant difference between the 1 min mean values of the angle θ of the cell-cell interface 'chord' of both cell lines ($P > 0.05$), whereas a P value of less than 0.05 was obtained for the 1 h mean values.

6.3.3 Immunofluorescence of non-sonicated samples (Control)

6.3.3.1 E-cadherin

E-cadherin in PZ-HPV-7 cells was concentrated mainly at the cell surface in the form of a homogeneous ring-type pattern (Figs. 6.4a, 6.5a) after 1 h in suspension culture. A low level of diffuse cytoplasmic staining was also observed.

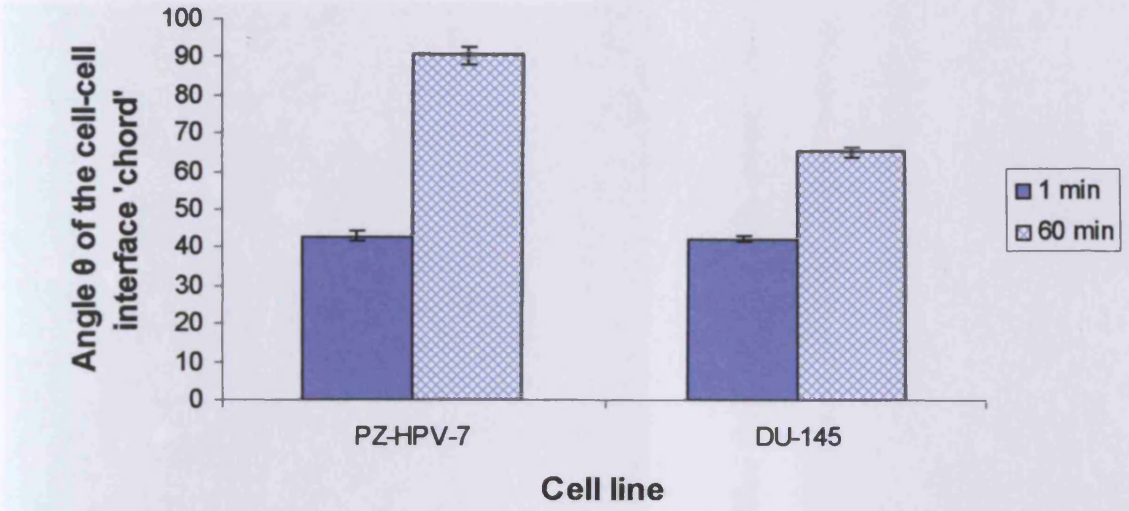

Figure 6.3: Measurements of the angle θ of the 'cell-cell interface chord' for 20 randomly selected pairs of cells after 1 and 60 min of levitation in the trap, for both cell lines (error bars represent one standard error of the mean).

In DU-145 cells, E-cadherin staining appeared quite diffuse throughout the cells, while the ring-type pattern at the cell surface was granulated and less prominent than in PZ-HPV-7 cells (Figs. 6.4f, 6.5f). Both fields of view were selected as they contained a high number of cells. Observations for all molecules (E-cadherin, F-actin, α-, β- and γ-catenins) were based on separate experiments performed twice.

6.3.3.2 F-actin

The F-actin cytoskeleton of PZ-HPV-7 cells was concentrated near the nuclear region of the cells (Figs. 6.4b; arrows and 6.5b), whereas in DU-145 cells strong cortical F-actin signal was observed (Figs. 6.4g; arrows and 6.5g).

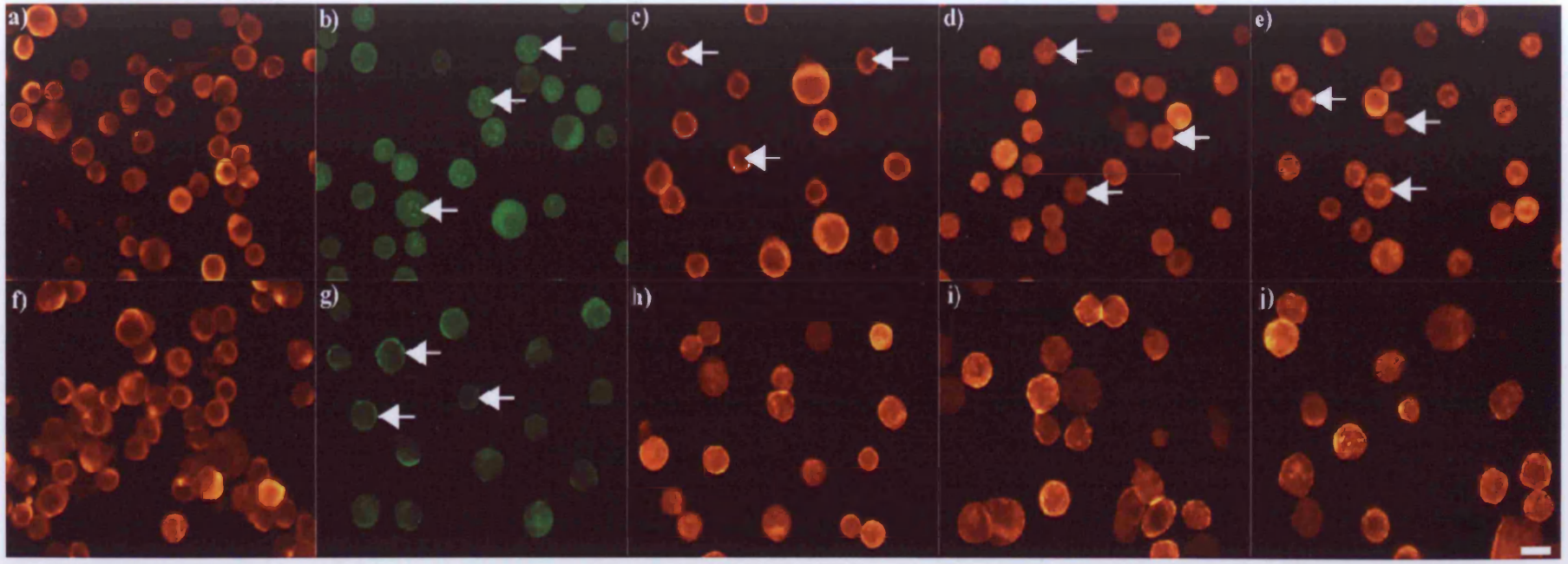

Figure 6.4: Representative micrographs of the distribution of E-cadherin (a, pericellular staining; f, diffuse staining), F-actin (b, nuclear staining (arrows); g, cortical F-actin (arrows)), α- (c, perinuclear halo (arrows); h, diffuse staining), β- (d, discrete intracellular staining (arrows); i, diffuse staining) and γ- (e, discrete intracellular staining (arrows); j, diffuse staining) catenins in PZ-HPV-7 (a-e) and DU-145 (f-j) non-sonicated (control) cells after 1 h in suspension culture. Scale bar is 20 μm.

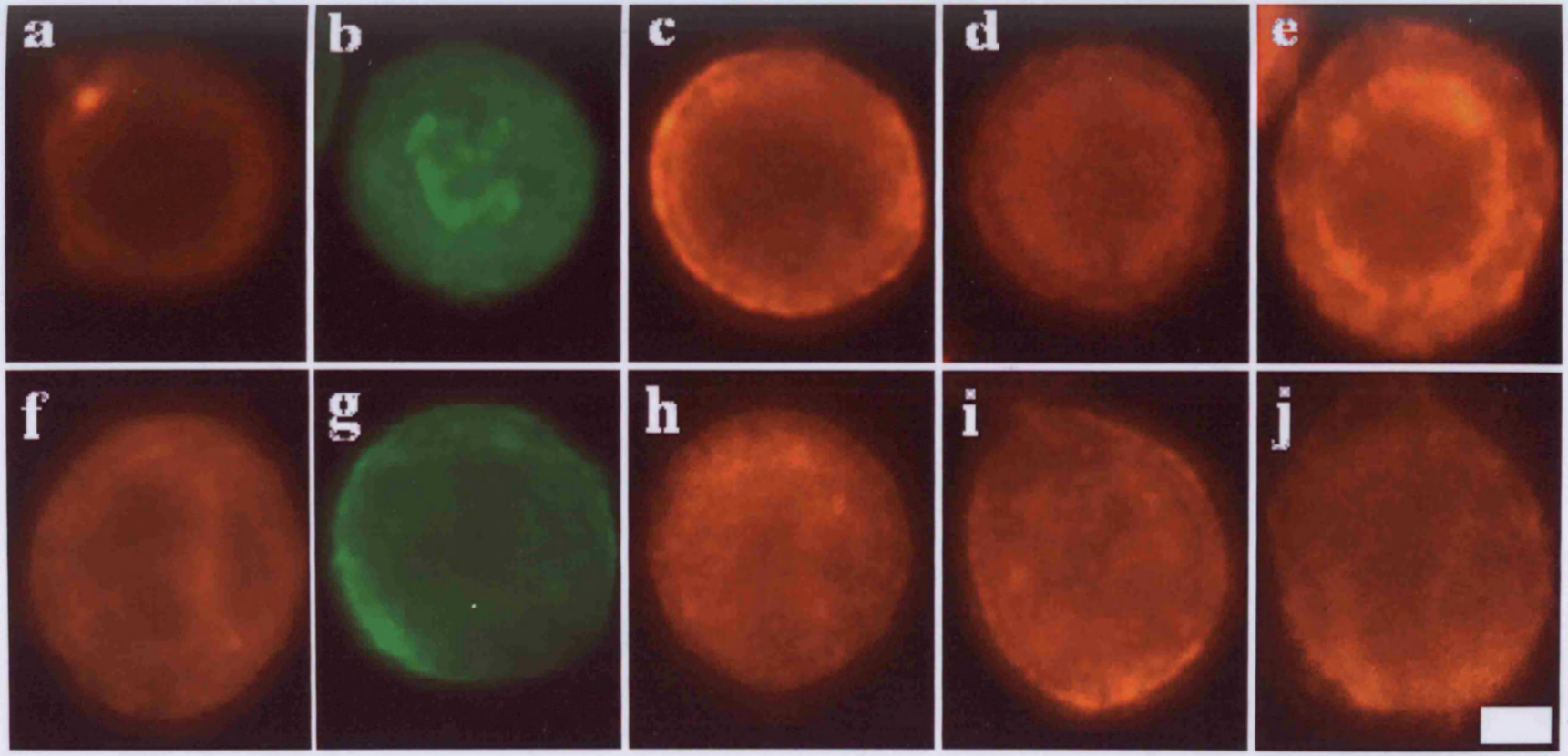

Figure 6.5: Typical distribution of E-cadherin (a, pericellular staining; f, diffuse staining), F-actin (b, intense nuclear staining; g, cortical F-actin), α- (c, perinuclear halo; h, diffuse staining), β- (d, discrete intracellular staining; i, diffuse staining) and γ- (e, discrete intracellular staining; j, diffuse staining) catenins in PZ-HPV-7 (a-e) and DU-145 (f-j) single non-sonicated (control) cells after 1 h in suspension culture. Scale bar is 5 μm.

6.3.3.3 α-, β- and γ- catenins

α-catenin in PZ-HPV-7 cells was distributed around the rim of the cells, resulting in what Mitchell et al. (2000) had described as a perinuclear halo, while less staining of the cytoplasm was observed (Figs. 6.4c; arrows and 6.5c). β- and γ-catenins were distributed in small discrete intracellular regions 1-2 μm from the cell surface, in a pattern that led to the formation of an intracellular ring (Figs. 6.4d, e; arrows and 6.5d, e). On the other hand, in DU-145 cells, α-, β- and γ- catenins appeared quite diffuse throughout the cells with little particular concentration (Figs. 6.4h-j and 6.5h-j).

6.3.4 Immunolabelling of sonicated samples

Immunolabelling of sonicated samples was performed as described in Section 6.2.3. Observations were based on separate experiments performed four times

6.3.4.1 E-cadherin

After 1 min of levitation in the trap, E-cadherin in PZ-HPV-7 cells exhibited a clear homogeneous ring-type distribution around the surface of the cells with little cytoplasmic staining (Fig. 6.6a), while in DU-145 cells, E-cadherin exhibited a granulated ring-type distribution at the surface of the cells with clear cytoplasmic staining (Fig. 6.6d), as for non sonicated PZ-HPV-7 and DU-145 cells (Fig. 6.5a, f).

After 1 h, E-cadherin in PZ-HPV-7 cells had accumulated at the cell-cell interface in a grainy pattern (Fig. 6.7a). This pattern was similar to that highlighted in Chapter 4, zoom-in image of Fig. 4.5f, which was suggestive of adherens junctions formation.

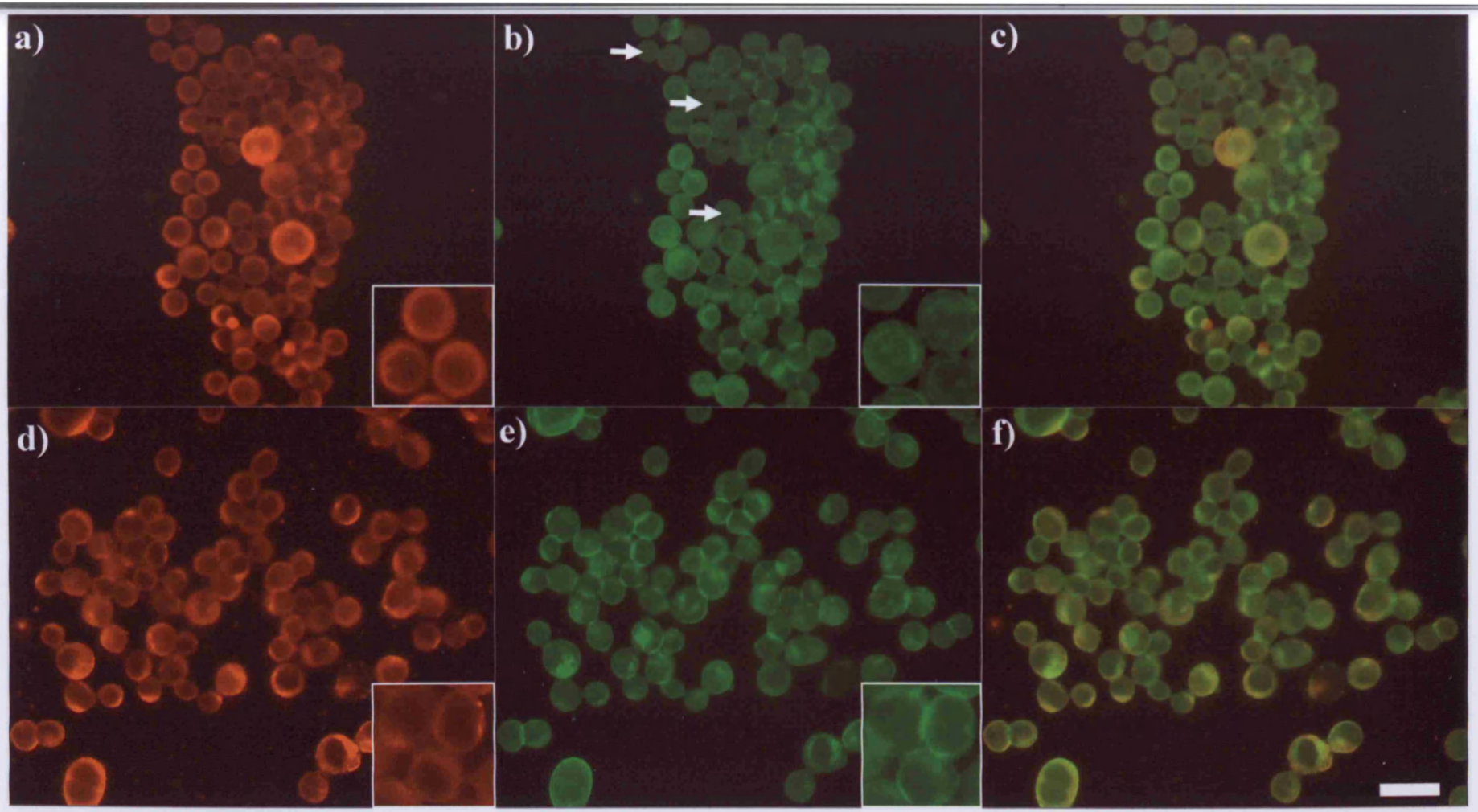

Figure 6.6: Distribution of E-cadherin and F-actin in PZ-HPV-7 (a and b respectively) and DU-145 (d, e) cells exposed to ultrasound for 1 min. PZ-HPV-7 cells showed internal regions of high phalloidin stain (b, arrows). The superimposed images are shown in c, f respectively. Zoom-in images of parts of the aggregates are shown on the bottom right hand side of each image, to highlight the distribution pattern. Scale bar is 50 μm.

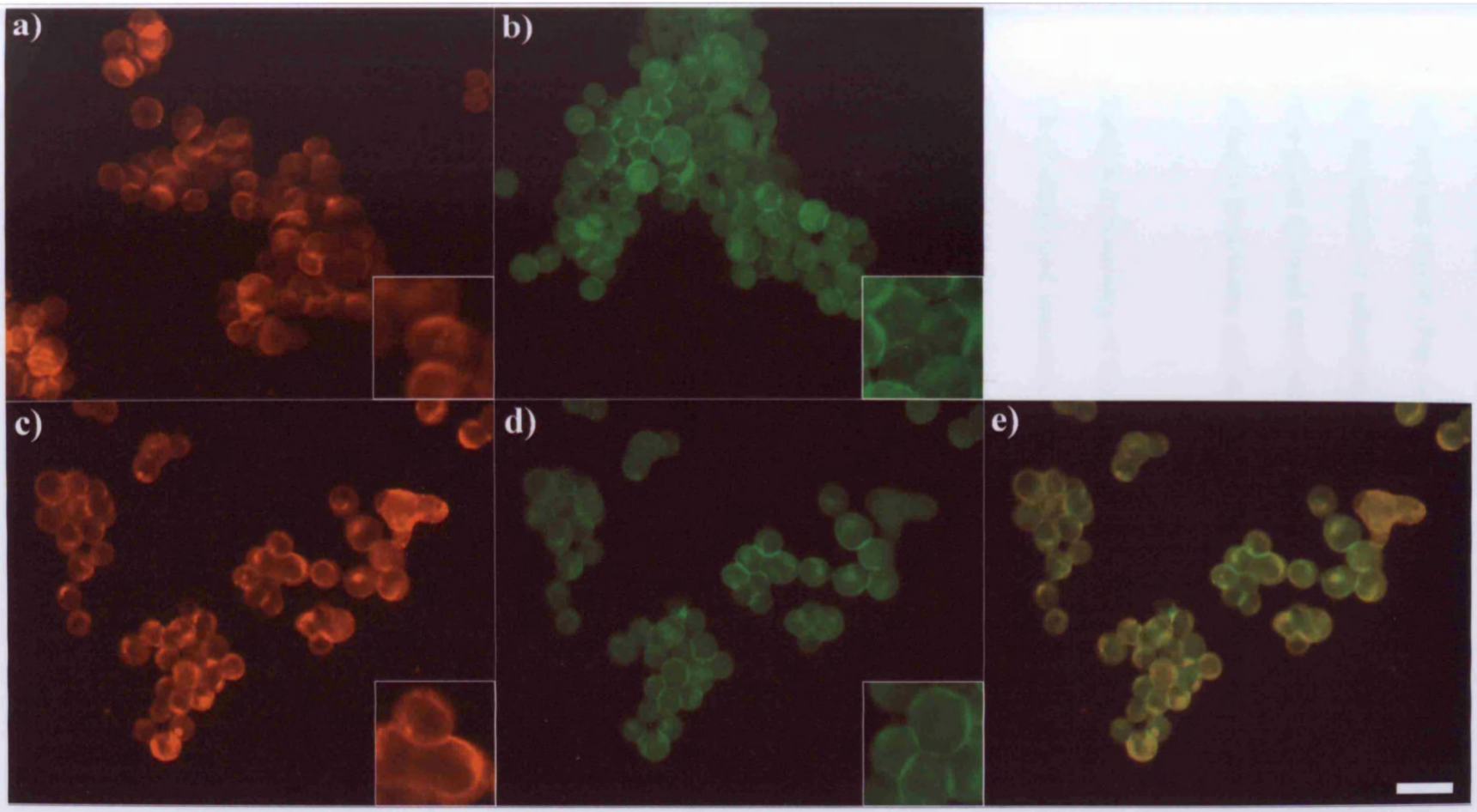

Figure 6.7: Distribution of E-cadherin and F-actin in PZ-HPV-7 (a and b respectively) and DU-145 (d, e) cells exposed to ultrasound for 1 h. PZ-HPV-7 cells showed internal regions of high phalloidin stain (b, arrows). Zoom-in images of parts of the aggregates are shown on the bottom right hand side of each image, to highlight the distribution pattern. The superimposed image for the DU-145 cell line is shown in e. Scale bar is 50 μm.

In contrast, in DU-145 cells E-cadherin had retained the ring- type pattern at the periphery of the cells, while a more intense staining was often not confined to a cell-cell contact region (Fig. 6.7c); no indication (*i.e.* observation of grainy interface) of the formation of adherens junctions was observed in DU-145 cells. χ^2- test for each time point showed that there was significant difference between the frequencies of the different E-cadherin distributions in the two cell lines (Table 6.2).

Table 6.2: Summary of the distribution of E-cadherin in both cell lines after 1 min and 1 h of ultrasound initiation. The percentages of the E-cadherin distribution pattern that was dominant for each cell line is given together with the overall number of cells examined (n) and the χ^2 value for the contingency Tables at each time (Sec. 6.2.4; Table 6.1).

	E-cadherin	
	1 min	***1 h***
PZ-HPV-7	At the cell surface in a homogeneous ring pattern 94 % (n = 245)	At the cell-cell interface in a granulated pattern 96 % (n = 164)
DU-145	At the cell surface in a granulated ring pattern 97 % (n = 277)	At the cell surface in a granulated ring pattern 94 % (n = 154)
χ^2	426* (P << 10^{-3})	260* (P << 10^{-3})

*P = 0.001 when χ^2 = 12, consequently P is negligible when χ^2 reaches these values

6.3.4.2 F-actin

After 1 min in the trap, F-actin in both cell types had concentrated in a thin and short region at the cell-cell contact region (Fig. 6.6b). Diffuse cytoplasmic staining was observed for both cell types. However, PZ-HPV-7 cells exhibited some internal regions of high phalloidin stain, as was the case for control non-sonicated cells (Figs. 6.4b and 6.5b). No difference was observed between non-sonicated cells and cells levitated in the trap for 1 min for both cell lines. The superimposed images of E-cadherin and F-actin are shown in Figures 6.6c and f respectively.

Following 1 h in the trap, F-actin in both cell types had clearly accumulated at the cell-cell interface, while the internal F-actin staining regions remained in PZ-HPV-7 cells (Fig. 6.7b). The superimposed image of E-cadherin and F-actin of the DU-145 cell line is shown in Figure 6.7e. The E-cadherin and F-actin Figures alone are shown for the PZ-HPV-7 cell line as these highlighted the localisation of the respective molecules with a clarity that was not resolvable in the co-localisation image. The F-actin integral intensity at the cell-cell interface of PZ-HPV-7 cells increased by a factor of 2.7, whereas that of DU-145 increased by a factor of 1.7 (the increases at the two time points were significantly different ($P < 0.05$)) (Fig. 6.8).

6.3.4.3 α-, β- and γ-catenins

After 1 min of ultrasound exposure α-catenin in both cell types exhibited a diffuse distribution throughout the cells with some accumulation at the cell-cell interface (Fig. 6.9a, c).

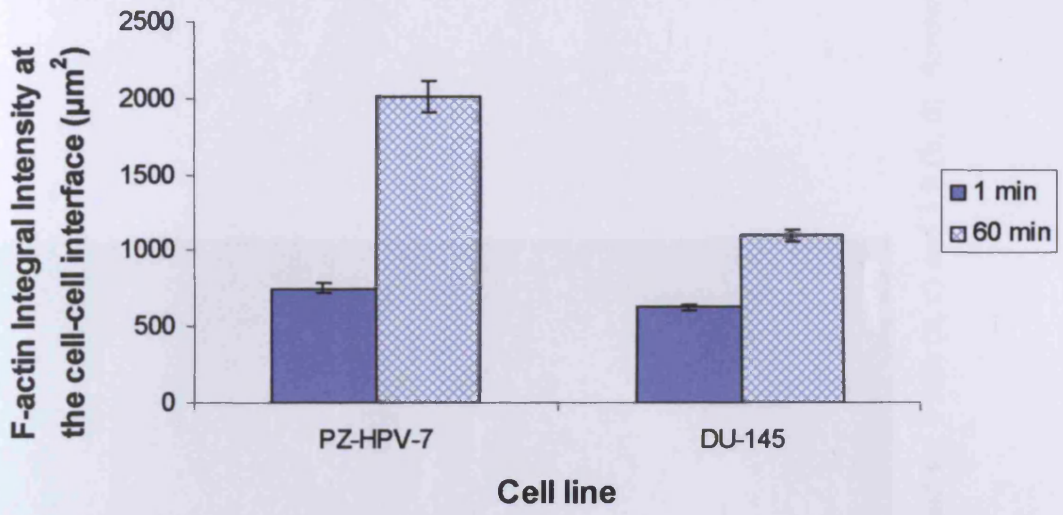

Figure 6.8: Integral intensity measurements of F-actin at the cell-cell interface of 20 randomly selected pairs of cells after 1 and 60 min of levitation in the trap, for both cell lines (error bars represent one standard error of the mean).

After 1 h, α-catenin in both cell types had accumulated at the cell-cell interface, while an α-catenin-free nuclear region was clearly defined (Fig. 6.9b, d; arrows), as was the case for control non-sonicated PZ-HPV-7 (Figs. 6.4c and 6.5c) but not for control DU-145 cells (Figs. 6.4h and 6.5h). χ^2- test for both time points showed that there was no significant difference between the frequencies of the α-catenin distribution patterns in the two cell lines (Table 6.3).

On the other hand, the amount of α-catenin recruited at the cell-cell interface over 1 h of ultrasound exposure, as quantified by the integral intensity index, was higher for the PZ-HPV-7 than the DU-145 cell line. α-catenin in PZ-HPV-7 cells increased from 1550 to 3960 μm^2 within 1 h of levitation in the trap (*i.e.* by a factor of 2.3), while in DU-145 cells it increased from 900 to 1440 μm^2 within 1 h of levitation in the trap (*i.e.* a 1.6 factor increase) (both time point cell samples were significantly different ($P < 0.05$)) (Fig. 6.10).

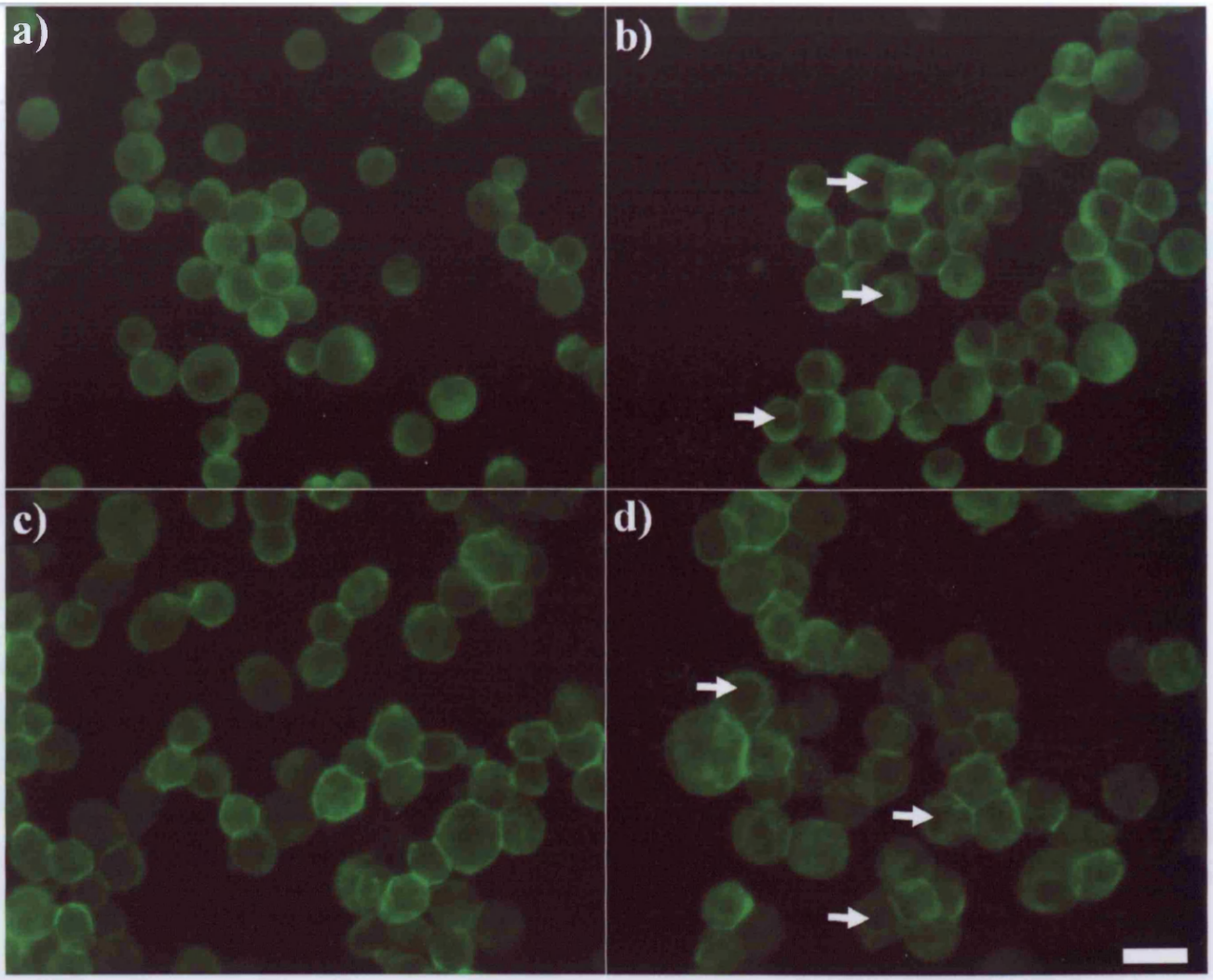

Figure 6.9: Distribution of α-catenin in PZ-HPV-7 (a, b) and DU-145 (c, d) cells exposed to ultrasound for 1 min (a, c) and 1 h (b, d). Arrows show the cytoplasmic/nuclear α-catenin-free region. Scale bar is 50 μm.

Table 6.3: Summary of the distribution of α-catenin in both cell lines after 1 min and 1 h of ultrasound initiation. The percentages of the dominant α-catenin distribution pattern are given together with the overall number of cells examined (n) and the χ^2 values.

	α -catenin	
	1 min	***1 h***
PZ-HPV-7	Diffuse throughout the cells 90 % (n = 134)	Nuclear/cytoplasmic α-catenin-free region 77 % (n = 109)
DU-145	As for PZ-HPV-7 87 % (n = 135)	As for PZ-HPV-7 73 % (n = 101)
χ^2	0.91 (P > 0.05)	0.475 (P > 0.05)

β- and γ-catenins in PZ-HPV-7 cells exposed to ultrasound for 1 min were distributed around the rim of the cells, while the intracellular ring observed in non-sonicated samples remained (Figs. 6.4d, e and 6.5d, e). A clear β-/γ-catenin-free nuclear/cytoplasmic region was observed (Figs. 6.11a and 6.13a; arrows). After 1 h, β- and γ-catenins had accumulated at the cell-cell interface with little cytoplasmic staining; the intracellular ring was still present (Figs. 6.11b and 6.13b). In contrast, in DU-145 cells a diffuse cytoplasmic staining of β- and γ-catenins was observed after 1 min and 1 h of exposure (Figs 6.11c and 6.13d). Accumulation of labels at the cell-cell interface was also observed for both time points (Figs. 6.11c and 6.13d). χ^2- tests for both time points showed that there was significant difference between the frequencies of the different β- and γ-catenins distributions in the two cell lines (Table 6.4).

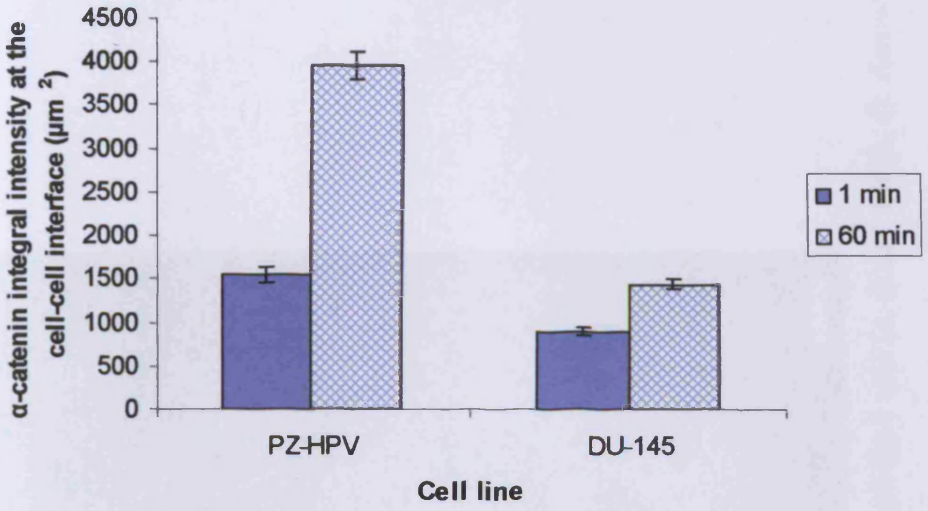

Figure 6.10: Integral intensity measurements of α-catenin at the cell-cell interface of 20 randomly selected pairs of cells after 1 and 60 min of levitation in the trap, for both cell lines (error bars represent one standard error of the mean).

The temporal progression of β- and γ-catenin redistribution was quantified by measuring the integral intensity of these molecules at the cell-cell interface for both cell lines (Figs. 6.12 and 6.14). The β-catenin integral intensity of PZ-HPV-7 cells increased from 1830 to 4200 μm^2, *i.e.* by a factor of 2.3, whereas that of DU-145 increased from 780 to 2600 μm^2, *i.e.* by a factor of 3.3 (both time point cell samples were significantly different ($P < 0.05$)) (Figs. 6.12 and 6.14). Additionally, the γ-catenin integral intensity of PZ-HPV-7 cells increased from 1470 to 6600 μm^2, *i.e.* by a factor of 4.5, whereas that of DU-145 increased from 1280 to 3300 μm^2, *i.e.* by a factor of 2.6 (both time point cell samples were significantly different ($P < 0.05$)) (Figs. 6.12 and 6.14).

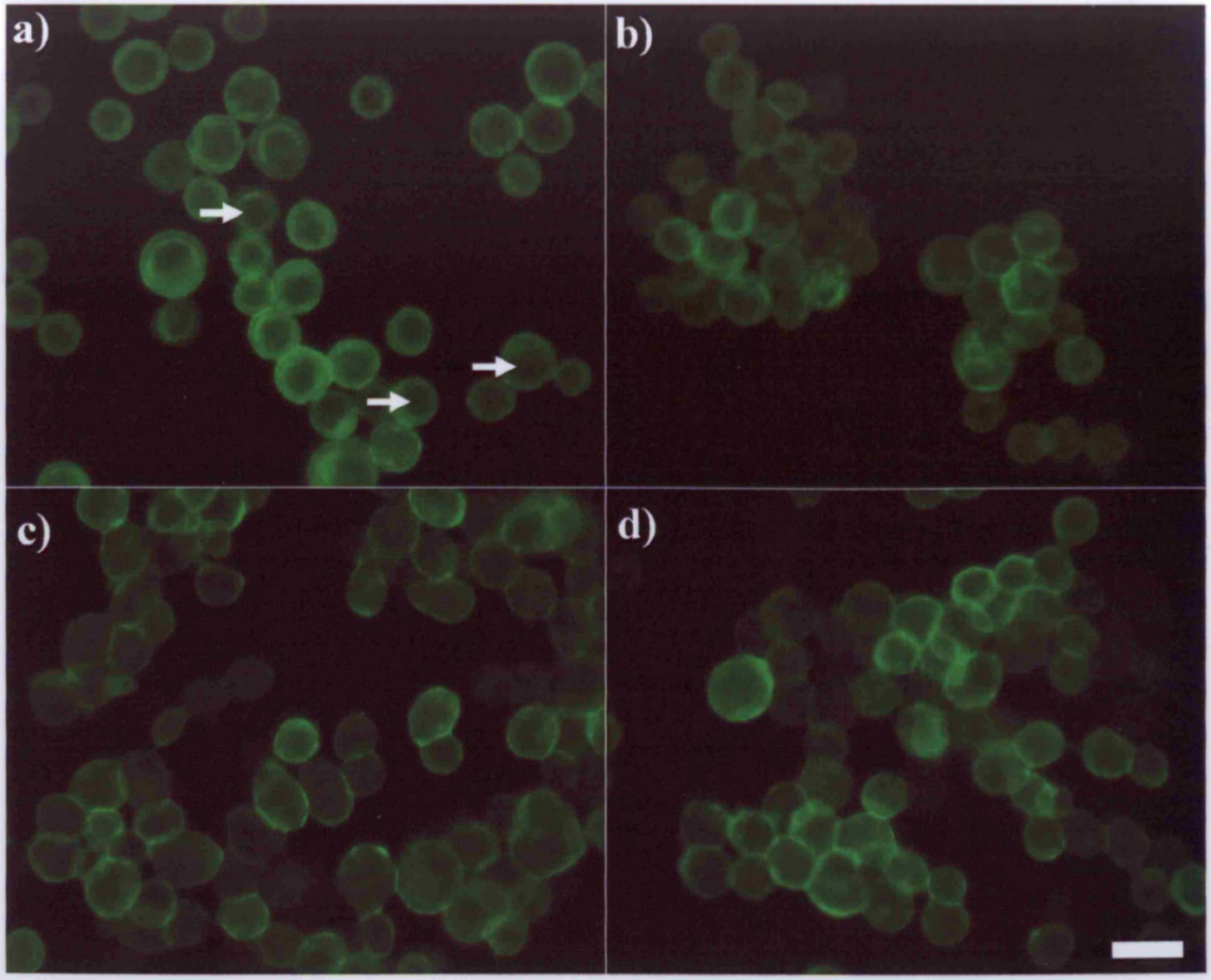

Figure 6.11: Distribution of β-catenin in PZ-HPV-7 (a, b) and DU-145 (c, d) cells exposed to ultrasound for 1 min (a, c) and 1 h (b, d). Arrows show the cytoplasmic/nuclear β-catenin-free region. Scale bar is 50 μm.

Table 6.4: Summary of the distribution of β- and γ-catenins in both cell lines after 1 min and 1 h of ultrasound initiation. The percentages of the dominant β- and γ-catenins distribution patterns together with the overall number of cells examined (*n*) and the χ^2 value are given.

	β-catenin		**γ-catenin**	
	1 min	***1 h***	***1 min***	***1 h***
PZ-HPV-7	Intracellular ring 79 % (n = 146)	Little cytoplasmic staining 76 % (n = 98)	As for β-catenin 82 % (n = 125)	As for β-catenin 70 % (n = 115)
DU-145	Diffuse staining throughout the cells 86 % (n = 154)	Diffuse staining throughout the cells 79 % (n = 201)	As for β-catenin 78 % (n = 127)	As for β-catenin 80 % (n = 150)
χ^2	120 ($P << 10^{-3}$)	61 ($P << 10^{-3}$)	90 ($P << 10^{-3}$)	68 ($P << 10^{-3}$)

6.3.5 Contrasting the heterogeneity of the cell lines

The immunolabelling results presented in Section 6.3.3 showed that the staining intensity of E-cadherin and α-, β- and γ-catenins varied among cells of the same DU-145 cell population. Cells of high staining intensity (integral intensity values between 2,500 and 3,500 μm^2) were found adjacent to cells of medium (1,500 to 2,500 μm^2) or low (350 to 1,500 μm^2) staining intensity; consequently, the DU-145 cell line was characterised as heterogeneous. In contrast, PZ-HPV-7 cells exhibited a homogeneous staining intensity for all molecules under investigation. The χ^2-test for cells exposed to ultrasound for 1 h showed that there was significant difference

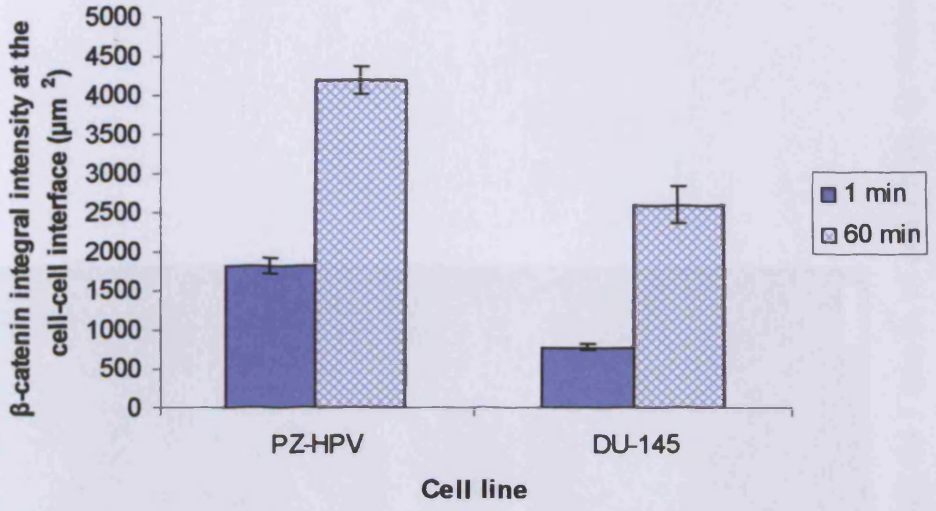

Figure 6.12: Integral intensity measurements of β-catenin at the cell-cell interface of 20 randomly selected pairs of cells after 1 and 60 min of levitation in the trap, for both cell lines (error bars represent one standard error of the mean).

between the frequencies of different staining intensities (high, medium and low staining intensities as defined above, *n* ranging from 125 to 245) in the two cell lines.

6.4 Discussion

6.4.1 Aggregate morphology

Microscopic observations of aggregate growth showed no detectable difference in the production of closely-packed aggregates without long-range hexagonal order (Sec. 6.3.1; Fig. 6.2) for both cell lines, upon stimulation of cell-cell contact in the trap. Such behaviour is consistent with the fact that both cell types express E-cadherin (Sec. 6.3.3); therefore, there is homophilic interaction between E-cadherin receptors on apposing cells upon stimulation of cell-cell contact in the trap.

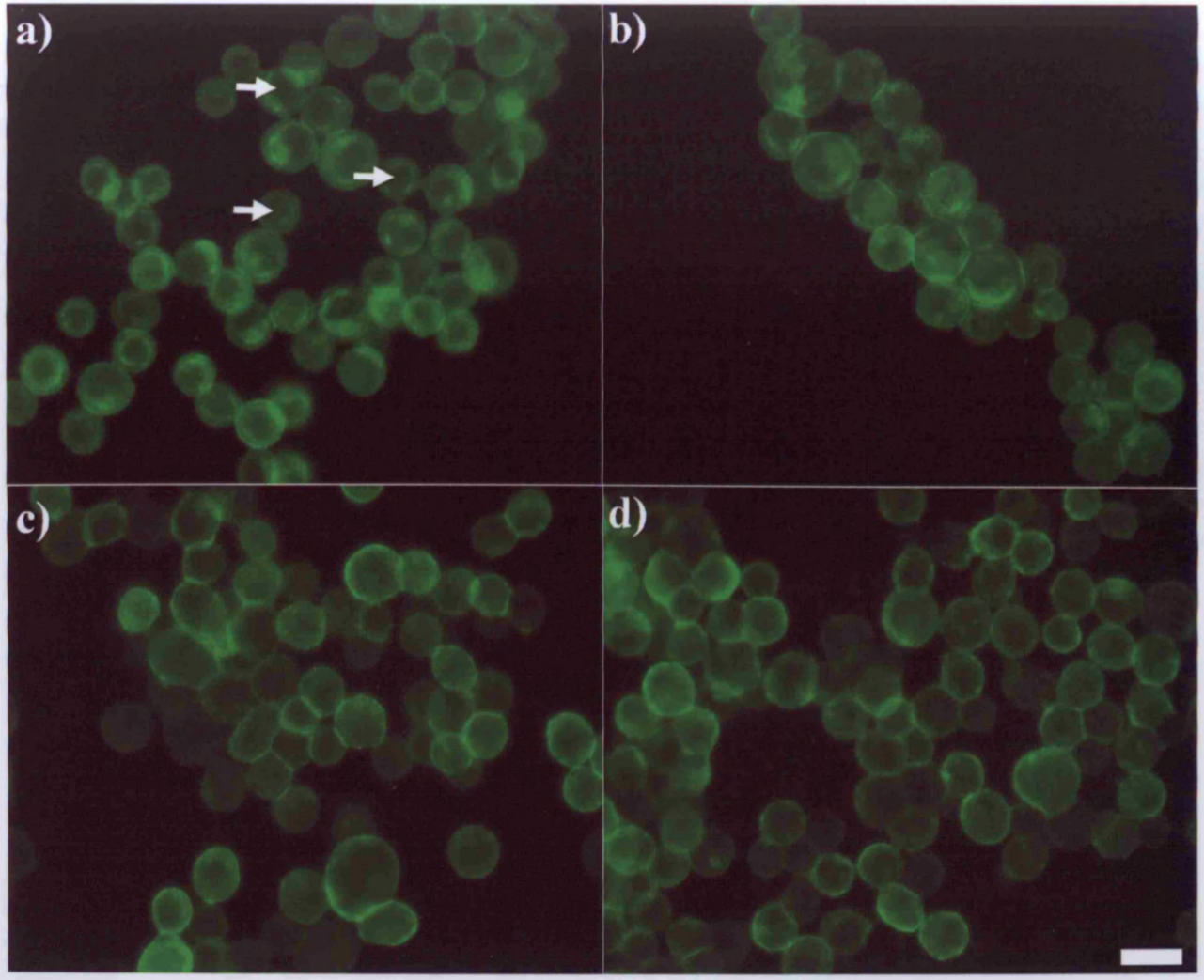

Figure 6.13: Distribution of γ-catenin in PZ-HPV-7 (a, b) and DU-145 (c, d) cells exposed to ultrasound for 1 min (a, c) and 1 h (b, d). Arrows show the cytoplasmic/nuclear γ-catenin-free region. Scale bar is 50 μm.

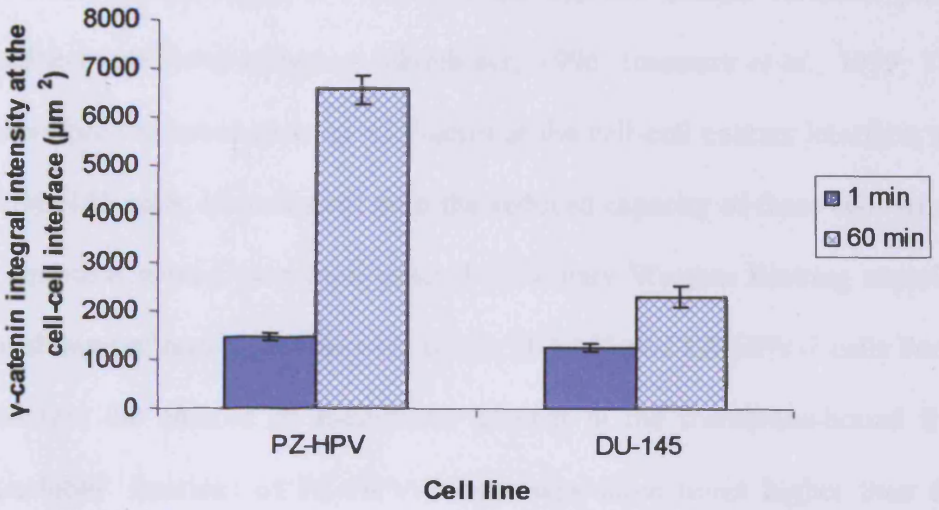

Figure 6.14: Integral intensity measurements of γ-catenin at the cell-cell interface of 20 randomly selected pairs of cells after 1 and 60 min of levitation in the trap, for both cell lines (error bars represent one standard error of the mean).

6.4.2 Immunolabelling

Differences in the ability of the two cell types to spread over neighbouring cells were observed and quantified. These differences were also associated with changes in the amount of F-actin at the cell-cell interface. The angle θ of the cell-cell 'chord' of PZ-HPV-7 cells increased over 1 h in the trap by a factor of 2.1, whereas that of DU-145 cells increased by a factor of 1.5 (Fig. 6.3). As well, the F-actin integral intensity of PZ-HPV-7 cells increased over 1 h in the trap by a factor of 2.7, whereas that of DU-145 increased by a factor of 1.7 (Fig. 6.8).

Both cell lines showed progressive accumulation of F-actin at the cell-cell interface within 1 h of levitation in the trap; however, PZ-HPV-7 cells exhibited strong intracellular F-actin aggregates (as for control, non-sonicated cells), possibly associated with the perinuclear region (Ñeco *et al.*, 2003).

Increased recruitment of F-actin to the cell-cell contact interface promotes strong cadherin-mediated adhesion (Gumbiner, 1996; Imamura *et al.*, 1999; Tepass, 2002), therefore the lower amount of F-actin at the cell-cell contact interface, shown here for DU-145 cells, is consistent with the reduced capacity of these cells to adhere strongly and thus spread over each other. Preliminary Western Blotting experiments (data not shown) of non-sonicated cells of the DU-145 and PZ-HPV-7 cells lines also suggested that the amount of E-cadherin present at the membrane-bound fraction ('Triton-soluble' fraction) of PZ-HPV-7 cells was three times higher than that of DU-145 cells, further supporting the evidence that PZ-HPV-7 cells have a greater ability to attach and spread over neighbouring cells than the malignant DU-145 cells.

A lower amount of F-actin in malignant cells compared to normal has also been reported by Gück et al. (2005). These authors employing an optical stretcher combined with microfluidic delivery, showed that the optical deformability (elasticity) of single human breast cancer cells was significantly increased compared to their normal counterparts. Such deformability was also accompanied by a 30% reduction in the F-actin content of the cells. The equilibrium between G and F-actin (Chap. 1; Sec. 1.4.1.1) is a marker of cell transformation and tumourigenesis. Increased G- to F-actin ratio has been reported in malignant human keratinocytes (Katsantonis *et al.*, 1994), human uroepithelial cells (Rao *et al.*, 1997; Rao, 2002), mouse H-Ras transformed fibroblasts (Moustakas and Stournaras, 1999), as well as in tissue sections of malignant prostate glands (Hemstreet *et al.*, 2000).

The overall cytoskeleton and cell shape remodelling results presented here for both cell lines are in line with the recent report of Chu et al. (2004). These authors showed that (i) after 30 min F-actin had strongly accumulated at the linear interface of doublets of Sarcoma 180 (S180) cells formed in suspension and (ii) that the force

required to separate cells in a doublet formed by bringing cells, each supported by a micropipette, into contact for a period of 60 min increased rapidly over the first 30 min and more slowly thereafter. This force was primarily determined by the amount of E-cadherin expressed at the cell surface. A calculation, by the present author, of the angle θ of the cell-cell 'chord' of E-cadherin expressing cells was on average 91° (n = 3), in agreement with the value reported here for the high E-cadherin expressing PZ-HPV-7 cells.

It has therefore been shown here, that malignant DU-145 cells have a reduced capacity to recruit F-actin at the cell-cell interface and that their rate of membrane spreading is lower than that of PZ-HPV-7 cells.

The distributions of the individual components of the cadherin/catenin complex are discussed in the following Sections.

6.4.2.1 E-cadherin

PZ-HPV-7 cells exhibited homogeneous membranous E-cadherin staining within 1 h of ultrasound exposure (Figs. 6.6a and 6.7a; Table 6.1), possibly associated with the formation of adherens junctions, while diffuse E-cadherin cytoplasmic staining and less membranous staining were observed for DU-145 cells (Figs. 6.6d and 6.7c; Table 6.1). In addition, Western Blotting analysis of DU-145 cells levitated in the ultrasound trap for 1 h (data not shown) showed that the amount of E-cadherin present in the cytoplasm ('Triton-insoluble' fraction) was higher than that present on the cell membrane ('Triton-soluble' fraction).

The results reported here on E-cadherin distribution after 1 h of levitation in the trap, are in agreement with earlier studies in various tumour tissue sections and cell lines, where an increased diffuse cytoplasmic and reduced membranous distribution of

E-cadherin, as shown here for the DU-145 cell line, is associated with tumour progression. These previously reported studies are listed in Table 6.5.

In prostate cancer in particular, E-cadherin is rarely permanently lost (Chesire and Isaacs, 2003). Davies et al. (2000) found that DU-145 cells at the confluence phase presented E-cadherin at the cell-cell interface similarly to their normal counterparts (*i.e.* PZ-HPV-7 cells; as shown here in Figs. 6.7a, d; Table 6.2), whereas Mitchell et al. (2000) reported both intense cytoplasmic and membranous expression of E-cadherin in cells of the DU-145 cell line, in line with the results presented here (Fig. 6.7c).

It has therefore been shown that during tumour progression, E-cadherin does not always show absent or reduced expression but that there is redistribution from the cell membrane to the cytoplasm.

6.4.2.2 α-catenin

Both cell lines, PZ-HPV-7 and DU-145, showed diffuse α-catenin cytoplasmic staining (1 min; Fig. 6.9a, c; Table 6.2), with staining exclusion from the nuclear and cytoplasmic region occurring within 1 h of ultrasound exposure (Fig. 6.9b, d; Table 6.2). It is noted that α-catenin in control, non-sonicated PZ-HPV-7 cells (Figs. 6.4c and 6.5c) exhibited a similar distribution as in cells levitated in the trap for 1 h (Fig. 6.9b) but not with cells levitated in the trap for 1 min (Fig. 6.9a). A reason for this may be that sonicated samples were introduced into the trap immediately after their preparation, whereas non-sonicated cells were kept in suspension culture for 1 h prior to immunofluorescent studies. On the other hand, no difference was observed between non-sonicated DU-145 cells (Figs. 6.4h and 6.5h) and 1 min samples (Fig. 6.9c). It is also noted that such differences between non-sonicated and sonicated cells have been

observed only for α-catenin. However, further work is required for elucidation of the above differences.

As is the case for E-cadherin, reduced membranous and increased cytoplasmic staining of α-catenin have been reported in tissue sections of breast (Nakopoulou *et al.*, 2002), colorectal (Tucker *et al.*, 2003; Wijnhoven *et al.*, 2004; Buda and Pignatelli, 2004), lung (Al Moustafa *et al.*, 2002), renal (Aaltomaa *et al.*, 2004) and oesophageal tumours cancers (Khare *et al.*, 1999), as well as in a range of colorectal (El-Bahrawy *et al.*, 2000; 2002), ovarian carcinoma (Bullions *et al.*, 1997) and metastatic thyroid follicular carcinoma (Huang *et al.*, 1998) cell lines.

In prostate cancer, cytoplasmic staining of α-catenin has been reported in cells of the DU-145 cell line (Mitchell *et al.*, 2000), whereas Davies et al. (2000) reported loss of α-catenin from DU-145 cells in relation to PZ-HPV-7 cells. However, in the present study no significant difference was observed or quantified by the χ^2- test between the α-catenin staining of both cell lines (Fig. 6.9; Table 6.2).

Nevertheless, a number of variables, such as differences in the E-cadherin antibody and staining techniques (Wheelock *et al.*, 2001) used might explain the difference observed between the results presented here and by Mitchell et al. (2000) and that reported by Davies et al. (2000).

On the other hand the amount of α-catenin recruited to the cell membrane after 1 h in the trap was for the PZ-HPV-7 cells 2.7 times higher than that of DU-145 cells (Fig. 6.10), further indicating that DU-145 cells possess a less adherent cadherin/catenin complex than PZ-HPV-7 cells.

Table 6.5: Published reports on reduced membranous and increased cytoplasmic distribution of E-cadherin in cancer tissue sections and cell lines.

	Tissue Sections		
	Tumour description	***Reference***	
Reduced membranous and increased cytoplasmic distribution of E-cadherin	Neoplastic mammary glands	Torres *et al.*, 2005	
	Breast	Sarrio *et al.*, 2004	
	Distal oesophagus	Khare *et al.*, 1999; Winjhoven *et al.*, 2004	
	Basal cell carcinoma	Kooy *et al.*, 1999	
	Gastric cardia	Winjhoven *et al.*, 2004	
	Oral epithelial dysplasia	Williams *et al.*, 1998	
	Squamous cell carcinoma	Williams *et al.*, 1998	
	Gastric cancer	Ohene-Abuakwa *et al.*, 2000; Tucker *et al.*, 2003	
	Colorectal carcinoma	Buda and Pignatelli, 2004; Rosivatz *et al.*, 2004	
	Cell lines		
	Cell line description	***Designation***	***Reference***
	Colorectal carcinoma	HT29, HCT116, HSC-39	El-Bahrawy *et al.*, 2000
	Gastric cancer	Caco-2	Kawanishi *et al.*, 1995
	Mesothelioma	HMC-1-5	Orecchia *et al.*, 2004
	Bladder cancer	TCCSUP	Kyker *et al.*, 2003

6.4.2.3 β- and γ-catenin

Figures 6.11 and 613 show the distributions of β- and γ-catenins in cells of the PZ-HPV-7 and DU-145 cell lines suspended in the trap for 1 min and 1 h. Both molecules show almost complete co-localisation, an expected observation as β- and γ-catenins share the greatest structural and functional homology among the catenins and bind to the cytoplasmic tail of E-cadherin in a mutually exclusive manner (Schlosshauer *et al.*, 2000; Bremnes *et al.*, 2002; Breault *et al.*, 2005) (Chap. 1; Sec. 1.3.2.2).

β- and γ-catenin expression in the majority of normal cell types is confined to the cell membrane, while accumulation of β- and γ-catenin in the cytoplasm and nucleus, found here in DU-145 cells (Figs 6.11c, d and 6.13c, d; Table 6.3), is consistent with similar observations reported in various malignant cells such as melanoma (Kageshita *et al.*, 2001), gastric cancer (Ohene-Abuakwa *et al.*, 2000), oral epithelial dysplacia and squamous cell carcinoma (Williams *et al.*, 1998), colorectal carcinoma (El-Bahrawy *et al.*, 2000), renal cell carcinoma (Aaltomaa *et al.*, 2004), adenocarcinomas of the gastro-oesophageal junction (Winjhoven *et al.*, 2004), medulloblastomas (Misaki *et al.*, 2005), thyroid and lung cancers (Shiina *et al.*, 2005).

In cells of the prostate cancer cell line DU-145, cytoplasmic and membranous expression of β- and γ-catenin has been reported (Mitchell *et al.*, 2000), whereas studies where the presence of the two molecules was confirmed by immunofluorescence and RT-PCR have also been reported (Bussemakers *et al.*, 2000; Shiina *et al.*, 2005). The amounts of β- and γ-catenins at the cell-cell interface of PZ-HPV-7 cells (Figs. 6.12 and 6.14) were 1.6 and 2.8 times higher than those of DU-145 cells. Similar observations were made by Davies et al. (2000), also based on

the staining intensity of immunofluorescence of β- and γ-catenins in confluent monolayers of PZ-HPV-7 and DU-145 cells.

The β-catenin protein found usually in the lateral cell membrane, as shown here for PZ-HPV-7 cells, partially reflects the function of cell adhesion, whereas that found in the cytoplasm and nucleus, as shown for DU-145 cells, functions as a mediator of wnt signal transduction (Shiina *et al.*, 2005). Similarly, cytoplasmic and nuclear γ-catenin can, as described in Chapter 1 (Sec. 1.3.2.3), also interact with the same transcriptional factors as β-catenin (Gooding *et al.*, 2004; Shiina *et al.*, 2005) and overexpression of γ-catenin could drive part of the endogenous β-catenin into the nucleus, most probably by displacing it from cadherin (Ohene-Abuakwa *et al.*, 2000), resulting in the nuclear accumulation of β-catenin that in turn may activate other genes to act as oncogenes (Chap. 1; Sec. 1.3.2.3) (Bremmes *et al.*, 2002).

6.4.3 Heterogeneity of cell lines

The immunolabelling results presented here for the cadherin/catenin complex (Sec. 6.4.2) showed that the distribution of these molecules in PZ-HPV-7 cells is homogeneous, whereas DU-145 cells showed heterogeneous expression of all proteins. Cells of high protein expression were found adjacent to cell with lower protein expression. Statistical analysis performed with the χ^2- test for cells exposed to ultrasound for 1 h showed that there is significant difference between the frequencies of different staining intensities in the two cell lines.

These results are consistent with earlier studies where the human DU-145 cell line was characterised as heterogeneous (Mitchell *et al.*, 2000; Chunthapong *et al.*, 2004), as well as with the currently accepted view that prostate cancer is heterogeneous and multiclonal in nature; features that are closely linked to genetic

instability (Chunthapong *et al.*, 2004). However, Mitchell et al. (2000) and Chunthapong et al. (2004) comment on the heterogeneity of the DU-145 cell line only in respect to E-cadherin expression. Heterogeneity in respect to α- , β- and γ-catenins has not been previously reported.

6.5 Preliminary conclusions

Initial investigation of the ability of the different cell types to spread over neighbouring cells, as quantified by measuring the cell-cell interface 'chord', showed that the epithelial PZ-HPV-7 prostate cells spread more than the epithelial DU-145 prostate cancer cells.

Differences in the amounts of the cadherin/catenin complex were also observed and quantified for both cell lines. PZ-HV-7 cells recruited more α-, β- and γ-catenins as well as F-actin in relation to DU-145 cells over 60 min of levitation in the trap. The overall conclusion that DU-145 cells are less adhesive than PZ-HPV-7 cells is thus drawn. The results presented here were consisted with previously published reports were a reduced cell-cell adhesion ability was observed for various types of tumour cells.

The ultrasound trap allowed the identification of differences in the amounts and distributions of molecules of the cadherin/catenin complex in the two cell types even at samples removed from the trap after 1 min.

Chapter 7

General Discussion

7.1 General

The work described in this thesis has further developed (Chap. 3) an ultrasound standing wave trap capable of creating 2-dimensional microparticle aggregates (Chap. 2) and applied it (Chaps. 3-6) to form cell aggregates in suspension, away from the influence of solid surfaces. Validation of the non-intrusive influence of the physical environment of the trap on cell wellbeing was carried out in Chapter 3, while, the cell-cell adhesion and cytoskeletal development events of different cell systems as well as the cell-cell communication process were examined in the subsequent chapters (Chaps. 4-6). These different components of the thesis are integrated in the following.

7.2 The acoustic trap

In the first experimental chapter (Chap. 2) the ultrasound trap was used as an approach to examine growth and formation of 2-dimensional microparticle aggregates at a range of different electrolyte ($CaCl_2$) concentrations. Particle aggregates were formed in the bulk phase (Spengler and Coakley, 2003) rather than at an air-water interface (Hidalgo-Álvarez *et al.*, 1996), removing in this way the constraint of particle location at an interface and the resulting requirement (Hidalgo-Álvarez *et al.*, 1996) of modification of particle interaction terms (van der Waals, electrostatic and structural forces) for that situation. The change in the magnitude of the repulsive

electrostatic particle-particle interaction terms in the suspending phase resulted in a gradual transition in the aggregate morphology from a hexagonally ordered towards a dendritic disordered one with increasing electrolyte concentration. These results provided guidance on the interpretation of the temporal development of the morphology of cell aggregates described in the succeeding chapters (Chaps. 3-6). A range of different indices was introduced to characterise morphology (Fractal dimension), order (Fast Fourier Transform) and degree of 'openness' (Void analysis) of the 2-D aggregate structures.

Since an aqueous bulk phase environment, as that provided by the acoustic trap, is an absolute requirement for animal cell aggregation *in vitro*, the above method introduced a new technique to obtain, for animal cells, the kinetic, dynamic and morphological information (Coakley *et al.*, 2004) discussed for particles in Chapter 2, as well as study the molecular consequences of cell-cell interactions away from the influence of solid surfaces (Chaps. 4-6). Additionally, the void index, was subsequently chosen and used as appropriate index for quantifying cell-cell interactions, as these were reflected in the overall aggregate morphology (Chap. 4).

As discussed in Chapter 3, a controlled physical environment is essential for the wellbeing of cells. It was therefore important, as with all physical cell traps, to examine the suitability of the trap for the accommodation of animal cells and the study of the biology of cell-cell interactions. It is noted that a similar comprehensive study has not been performed for either optical or dielectrophoretic traps.

Several physical parameters including, temperature increase, acoustic streaming, cavitation and intercellular forces that might influence the function of cells in the trap were quantified. It was shown that the temperature increase in the trap was $<<0.5$ K over the examined 30 min. Acoustic streaming velocities about the aggregate

exposed the cells to less stress than the gentle centrifugation processes employed during cell suspension preparation. No acoustic emissions, that are the signature of cavitation activity, were detected during the exposures. The van der Waals force dominated any ultrasonic contribution at the low separations at which homophilic surface receptors engage. Finally, cell viability assays further validated the non-intrusive nature of the ultrasound trap.

The suitability of the trap arises because:

(i) The 300:1 ratio of the major to minor semi-axes of the 2-D acoustic potential well makes 2-D aggregation insights, valued in particle aggregation studies, available in the biological domain (Coakley *et al.*, 2004). The cell systems examined in the present study acquired, within 30-60 min, an epithelial-like morphology (Chaps. 4-6), allowing direct comparison with conventional studies of established cell monolayers in culture flasks.

(ii) The single-cell thickness of the 2-D aggregate provides an excellent optical system to apply immunofluorescent techniques to monitor progression of the adhesion process, while *in-situ* as well as post-ultrasound exposure.

(iii) Significant numbers of cell-cell interactions can synchronously take place, as a 2-D aggregate with a diameter of 1 mm contains approximately 10,000 cells. Such high cell numbers have proved to be particularly useful in obtaining sufficient examples of the process under investigation. Statistically well defined measures could then be extracted, allowing the process under investigation (for example, the progression of the length of cell-cell contact in monolayers or the

distribution of F-actin (Chaps. 3-6) and catenins (Chap. 6)) to be designated as 'typical'. Furthermore, the numbers of cells in an aggregate have proved to be sufficient to carry out molecular techniques, such as Western Blotting (Chap. 6), on cells essentially stimulated synchronously by initiation of cell-cell contact in the aggregate.

7.3 Cell-cell adhesion

Chapters 4-6 described the process of cell-cell adhesion in neural (Chap. 4), chondrocyte (Chap. 5) and prostate epithelial and cancer cells (Chap. 6), with particular attention to the ability of cells to (i) increase the area of cell-cell contact and (ii) redistribute F-actin from intracellular locations to the cell-cell contact interface upon stimulation of cell-cell contact in the sound field. Additionally, (iii) the void index A_v/A_p was used as an indicator of the openness of the cell aggregates that reflects to an extent the strength of the initial cell-cell adhesion. Finally, (iv) parallels have been drawn between the different cell aggregate morphologies and the equivalent particle aggregates formed in different [$CaCl_2$] solutions. Factor (i) was quantified by measuring the angle θ of the cell-cell interface 'chord' (Sec. 6.2.3). It is noted that after 1 h in the trap cells are no longer circular but mostly quadrilateral or pentagonal, therefore there has been an assumption in the calculation of the angle θ, as the diameter $2R$ of the cells was considered as a constant from earlier measurements of the same sample. Factor (ii) was quantified using the integral intensity approach described in Chapter 4, Section 4.2.5. Factor (iii) was quantified according to the procedure detailed in Chapter 2, Section 2.2.6.2, while factor (iv) derived was based on comparison of cell aggregates and particle aggregates formed in different [$CaCl_2$]

solutions. Table 7.1 summarises the differences in factors (i-iv) described above, quantified for the cell systems used in the present study after 1 h of initiation of cell-cell contact in the sound field.

Table 7.1: Differences in the angle θ (± standard error of the mean) made by the cell-cell interface 'chord', F-actin integral intensity (μm^2) of Phalloidin-Alexa Fluor 488 (± standard error of the mean) and void index of the various systems used in the course of this thesis after 1h* in the trap. The [$CaCl_2$] for equivalent latex aggregate morphology is also shown.

	Particles	*DU-145*	*Chondrocytes*	*PZ-HPV-7*	*Neural cells*
Angle θ of the cell-cell interface 'chord'	0	65° ± 1.4	72° ± 0.6	90° ± 2.4	114° ± 3.5
F-actin integral intensity (μm^2)	NA	1094 ± 35	940 ± 37	2008 ± 102	27846 ± 2225
Void index A_v/A_p at 5 min**	Chapter 2 Section 2.3.2.3	0.05	0.03	0.06	0.21
[$CaCl_2$] for equivalent particle aggregate morphology	Chapter 2 Section 2.3.2.1	2-4 mM	0 mM	2-4 mM	8-10 mM

* Measurements for the neural cells were performed within 30 min of ultrasound exposure
** The void index data have been derived from measurements on a single aggregate for each case

The neural and DU-145 cell contact seams spread most and least extensively respectively. Similarly, F-actin staining intensity at the cell-cell interface was highest for neural cells and least for DU-145 cells and chondrocytes. The difference in the

integral intensities of the latter two systems is small but statistically significant different (a two-tailed two sample t-test gave a P value of less than 0.005). These results will now be discussed in the context of their membrane receptor profiles. (It is noted that while the void index, the angle θ and the equivalent $CaCl_2$ concentrations changed by a factor of not more than 4, the F-actin staining was more than 10-fold greater for neural than for any other. Consequently, care has been taken to confirm this observation).

In tissues, neural and PZ-HPV-7 cells express cell-cell mediated adhesion systems and, as shown in Chapters 4 and 6, *in vitro* they exhibit strong staining for N- (Sec. 4.3.3) and E-cadherin (Sec. 6.3.2.1) at the cell-cell contact interface within 30 and 60 min respectively of cell-cell contact in the trap. The staining patterns were consistent with formation of adherens junctions. Increased localisation of cadherin receptors at the cell-cell contact interface promotes strong cell-cell adhesion (Gumbiner, 1996; Imamura *et al.*, 1999; Tepass, 2002), resulting in increased localisation of the F-actin cytoskeleton at the sites of cell-cell contact bringing about cell movements and morphological interactions that underlie normal cell shape, *i.e.* cell spreading (Zicha *et al.*, 2003). In addition, the void index for neural cells was 0.21, corresponding to a [$CaCl_2$] for equivalent particle aggregate morphology of 8-10 mM, while for PZ-HPV-7 cells, the void index was 0.06, much less than that of neural cells and corresponding to a [$CaCl_2$] for equivalent particle aggregate morphology of 2-4 mM.

The indices in Table 7.1 consistently show that neural and PZ-HPV-7 cells were more adhesive than the other cell systems examined in the present thesis. However, the above indices were lower for PZ-HPV-7 cells than neural cells (Table 7.1) even though both mediate cell-cell interactions *in vivo*. One possible explanation

might be the fact that neural cells have shown (Chap. 4; Sec. 4.3.5) strong expression of NCAM, the role of which was crucial in the process of cell spreading (Chap. 4; Sec 4.4.3). In contrast, the author has found no association of NCAM with PZ-HPV-7 cells in the published literature. Thus, the possible absence of NCAM from the PZ-HPV-7 cells might account for the observed reduced spreading and adhesive capacities of PZ-HPV-7 cells in relation to that of neural cells.

On the other hand, chondrocytes contain a high level of the cell-matrix integrin receptors that mediate cell-matrix interactions *in vivo* (cell-matrix adhesion), (Svoboda, 1998). Chondrocytes display cell-cell interactions only during pre-chondrogenic condensations (Coleman and Tuan, 2003), while after cartilage formation cell-matrix interactions prevail (Chi *et al.*, 2004). In the present study fully differentiated chondrocytes were challenged for cell-cell rather than cell-matrix adhesion expression. It may be for this reason that their adhesive and spreading capacities, as well as the low void index (0.03, equivalent to control (0 mM [$CaCl_2$]) particle aggregates), are lower than those reported for the neural and PZ-HPV-7 cells (Table 7.1). However, accumulation of F-actin at the cell-cell interface was clearly observed, indicating that cell-cell receptor interactions at the cell membrane have taken place. As discussed in Section 6.1, pre-chondrogenic condensations are mediated by NCAM and N-cadherin (DeLise and Tuan, 2002) whereas these molecules are not found in differentiated cartilage (*i.e.* in chondrocytes). On the other hand, Tavella et al. (1994) reported that both of these molecules are reexpressed by chondrocytes within 12 and 24 h respectively of initiation of suspension cultures. It could then well be that initiation of chondrocyte-chondrocyte contact in the sound field, causes rapid expression and translocation of NCAM and N-cadherin at the cell surface, at least to the extent where association with the F-actin cytoskeleton and

redistribution of the latter was clearly identified by immunofluorescent studies (Sec. 5.3.3).

DU-145 cells on the other hand, are malignant cells, with increased cytoplasmic and less E-cadherin staining at the cell-cell contact interface (Chap. 6; Sec. 6.3.4.1), in line with the published literature, where increased cytoplasmic E-cadherin staining is associated with tumour progression (Mitchell *et al.*, 2000; Winjhoven *et al.*, 2004; Buda and Pignatelli, 2004). Malignant cells are characterised by reduced cell-cell adhesion and increased cell motility (Lozano *et al.*, 2003), therefore reasonably their adhesive and spreading capacities (Table 7.1), quantified in the present study, are lower than those reported for the other cell systems examined. It must be noted however, that DU-145 cells also exhibited reduced membranous expression of α-, β- and γ-catenins (Sec. 6.3.4.3), indicating that the cadherin/catenin complex mediating cell-cell adhesion and associated spreading are less effective in their non-cancerous counterparts, PZ-HPV-7 cells, as well as that of neural cells (Table 7.1). It is also noted that the void index of DU-145 cells is 0.05 (equivalent to 2-4 mM [$CaCl_2$]), similar to that of PZ-HPV-7 cells, despite the fact that their measured adhesive and spreading capacities are lower that those of PZ-HPV-7 cells. This could be explained by the fact that DU-145 cells expressed E-cadherin at the cell surface (Chap. 6, Sec. 6.3.4.1), therefore there is some level of E-cadherin receptor interactions taking place on apposing cells, giving rise to a little disordered cell aggregated morphology.

Finally, colloidal interactions are simpler than cell-cell interactions as they are the result of the electrostatic repulsion and van der Waals attraction (Chap. 2). Classification of a particle aggregate as weakly adhesive is based on observations of its morphology. A particle aggregate is less adhesive the more closely-packed its

morphology is, as the electrical double layer is thick (Chap. 2; Sec. 2.1.1.1), while screening of the negative charge by addition of $CaCl_2$ (*i.e.* reducing the thickness of the double layer), delivers strongly adhesive dendritic structures.

7.4 The media

A complete list of the cell culture media used in the present study can be found in Appendix A. A common property was that all cell systems were, for the cell adhesion studies in the ultrasound field, suspended in serum-free media. Neural cells were suspended in serum-free NSM, chondrocytes in serum-free DMEM/Ham's F-12 and prostate epithelial and cancer cells in serum-free HCMF/$CaCl_2$.

The major advantage of serum-free media is that it has a 'control over growth' characteristic as it is chemically-defined and selective for a particular cell type. The possibility of overgrowth of fibroblasts is thus effectively tackled (Freshney, 2000). Serum-free media were particularly important, for the maintenance and sub-culturing procedure of C6 neural cells, as this is a unique conditionally-immortalized clonal cell line, of limited availability, able to replicate as a homogeneous population of progenitor cells, as described in Chapter 4 (Sec. 4.1). It was therefore important to maintain the purity of this cell line and to ensure optimum cell function in the sound field. On the other hand, prostate epithelial and cancer cells were maintained, according to the protocol provided by ATCC, in Ham's F-12 containing 10% foetal calf serum, as in accordance with the situation for many tumour cell lines, minimal stromal overgrowth is generally observed. Serum-free media were therefore most appropriate for suspension of chondrocytes, prostate epithelial and cancer cells for adhesion studies.

The absence of serum in DMEM/Ham's F-12 and HCMF/$CaCl_2$ had no detectable effect on the wellbeing of chondrocytes, as assessed by various viability assays (Chap. 3; Sec. 3.3.5), or of prostate epithelial and cancer cells, as assessed by microscopic observations of the bright field images, while in the trap.

The choice of media might also have influenced the different extents of membrane spreading of neural and PZ-HPV-7 cells. Both neural and PZ-HPV-7 were in serum-free media in the ultrasound trap. However, while the neural cells were also cultured in NSM, the PZ-HPV-7 cells were cultured in the less defined, serum containing, Ham's F-12 medium (supplemented with 10% foetal calf serum and 100 μg/ml penicillin-streptomycin solution). It was though beyond the scope of this study to examine and assess the effects/impacts of various cell culture media on the adhesive and spreading abilities of the cell systems examined in this thesis.

7.5 Trafficking of molecules

Monitoring the trafficking of cell receptor or gap junctions molecules provided valuable insight for the establishment of temporal changes in cell-cell adhesion and cell-cell communication processes. In this study, temporal changes of localisation of the following molecules was examined: NCAM and N-cadherin in neural cells (Chap. 4), Cx43 in chondrocytes (Chap. 5), E-cadherin, α-, β-, γ- catenins in prostate epithelial and cancer cells (Chap. 6) and F-actin in all cell systems. As noted in Chapter 4 (Sec. 4.3.5) samples were removed from the trap after 1, 8, 30 or 60 min but the respective immunofluorescent images correspond to the 'real' times of 2.5, 9.5 31.5 and 61.5 min due to the time gap from termination of ultrasound (1, 8, 30 and 60 min) to specimen fixation.

Intracellular responses, *i.e.* localisation of molecules at the short cell-cell contact regions, were quite clear, from a range of 2 to 4 duplicate experiments, for all of the above molecules. Accumulation of the above molecules at the long cell-cell contact interface, accompanied by formation of gap junctions and, apparently, adherens junctions, occurred within 30 and 60 min of initiation of contact in the sound field. It follows then, that the intervening 29 min period to confluent-culture-like F-actin patterns and 59 min to functional gap junctions offer significant opportunities to monitor the kinetics of adhesion complex components as they approach their equilibrium distributions. However, the localisation of these molecules at intermediate time points was not examined, with the exception of NCAM, N-cadherin and F-actin in neural cells (time point of 8 min). Still, the possibility that equilibrium distributions may have already been reached in significantly faster times than those reported in this thesis cannot be ruled out.

The potential of the ultrasound trap for detection of rapid molecular processes following cell-cell contact will now be set in the context of the various methods and techniques used for the study of cell-cell adhesion and communication.

Approaches to fluorescence microscopy studies of the time course of the molecular development of the cell cytoskeleton in a cell monolayer following receptor mediated cell-cell interactions include the 'calcium-switch' approach, and cell overlay systems (Chap. 1; Sec.1.8.1). Undoubtedly, the 'calcium switch' approach has contributed significantly to the extraction of temporal information on cell-cell adhesion, as cells are rapidly and synchronously stimulated to initiate cell-cell contact upon transfer from low calcium (0.02-0.1 mM) to complete growth medium (1.2-1.8 mM calcium); however, limitations of this method include: (i) a small number of cells is examined (each patch contained 4-8 cells (Braga, 2002)), (ii) growth of cells in low

calcium medium usually takes 3-10 days, (iii) the adhesion process of mixtures of different cell types seeded, for co-culture purposes, in a monolayer cannot be examined, due to the random growth of the different cell types (iv) cells are grown on coverslips, thus cell-cell interactions are not free of the effects of the underlying solid substratum.

The overlay method has been particularly useful in the study of cell-cell communication, as the time required for passage of a dye from the loaded to the unloaded population reflects the formation of functional gap junctions and the extent of coupling. This is a rapid and easy method to perform, where synchrony of cell-cell interactions is ensured but also mixtures of cell populations can be examined; however, the effect of the solid substratum on cell interactions is overcome, for only one of the partner cells (Ko *et al.*, 2000; Becker and Green, 2002)

Micromass culture approaches on the other hand are limited by: (i) reduced nutrient availability in the middle of the cultures, (ii) microscopic observations the 3-D environment moderates microscopic observations (Fish, 2005), (iii) the outer layer of the cultures is in contact with a substratum and (iv) a 1 h delay to the beginning of observations (Coelho and Kosher, 1991). Taking into account that intracellular responses have been shown to occur within 60 s of initiation of cell-cell contact in the trap, micromass and pellet cultures possibly provide information on the already established equilibrium distributions of adhesion and communication molecules.

Recently, the use of a dual micropipette assay (Chu *et al.*, 2004) allows cell-cell interactions to be studied synchronously and rapidly in suspension, as well as mixtures of cells to be examined. The main disadvantage of this technique, however, is that only two cells can be supported each time by the micropipettes; therefore the

extrapolation of statistically 'safe' data requires several doublets to be assayed, something that can be quite time consuming.

As discussed in Chapter 6, significant attention has been focussed on the distribution of the cadherin/catenin complex in normal and cancer tissues, directly taken form donor patients (Winjhoven *et al.*, 2004; Tucker *et al.*, 2003). However, in this case, the temporal changes of localisation of adhesion and communication molecules cannot be continuously monitored.

The ultrasound technique can thus simply, rapidly and with some precision produce data on molecular changes during development of adhesion or cell communication away from the influence of solid substrata.

7.6 The role of Ca^{2+}

A large number of published reports stress the role and importance of Ca^{2+} in the formation of cadherin-based cell-cell contacts, with particular emphasis to the disruption of cell-cell contacts in a low Ca^{2+} environment (Braga *et al.*, 2002). The role of Ca^{2+} in the ability of cells to redistribute their F-actin cytoskeleton at sites of cell-cell contact was examined here in neural cells (Sec. 4.3.6.1) and chondrocytes (5.3.7), by depleting it from the culture medium using the chelator EDTA. Both types of cells showed clear accumulation of F-actin at the cell-cell contact interface even at extracellular Ca^{2+} concentrations of 2.3 pM.

As discussed in Chapter 4 (Sec. 4.4.2) neural cells express NCAM and N-cadherin; at low Ca^{2+} concentrations, the role of the former may have been the formation and maintenance of the primary cell-cell contacts at close enough separation distances, for the N-cadherin molecules to interact and associate with the F-actin cytoskeleton. Expression of NCAM and N-cadherin has been shown to occur in

chondrocytes within 12 and 24 h in suspension cultures (Tavella *et al.*, 1994); it may therefore also be the case in chondrocytes in suspension that at a low Ca^{2+} concentrations, the Ca^{2+}-independent NCAM keeps the cells in sufficiently close distance for N-cadherin interactions in apposing cells to occur and finally result in the redistribution of the F-actin cytoskeleton at sites of cell-cell contact. These results raise the following interesting point.

In contrast to the situations observed in confluent monolayers on solid substrata, where at a low Ca^{2+} concentration, cells retract form each other (Frixione *et al.*, 2003) and thus receptor molecules are far from each other, the ultrasound trap provides the gentle constraint that keeps cells in close contact so that NCAM-NCAM binding can occur and allow for the partially inactivated or fully functional cadherins to attach to each other and cause accumulation of actin at the cell-cell interface. As suggested by Frixione et al. (2003) perhaps confluent cells do not passively dissociate primarily because Ca^{2+} levels are too low for the *trans*-interactions of neighbouring cadherin molecules to occur, but disruption of the intercellular junctions becomes facilitated and perhaps even forced because in the first place internally generated mechanical tension pulls the borders of contiguous cells, held on a substratum, away from each other.

Chapter 8

Final Conclusions

Individual conclusions for each of the five topics, investigated here, *i.e.* particle aggregation, the suitability of the ultrasound trap for manipulation of mammalian cells, cell-cell adhesion and communication of normal and cancer cells in an ultrasound trap, have already been drawn at the end of the corresponding Chapters 2, 3, 4, 5 and 6. Final conclusions from the results discussed shall be drawn in the following.

This thesis has overall demonstrated and established the temporal progression of cell-cell interactions from the early stages of receptor engagement to cytoskeletal organisation in a range of cell systems, using a 2-D ultrasound standing wave trap capable of levitating cells in suspension, free of the substratum effects that are known to influence cell properties.

The framework for the establishment of the particle-particle interaction parameters defining aggregate morphology was set in Chapter 2. It has been demonstrated that acoustic interaction forces between particles (and cells) are small compared with van der Waals interactions. Consequently the function of the trap is to hold cells close together so that the likelihood of cell receptor interaction is increased very significantly over the 'encounter in suspension' situation (Chap. 3). The structure of the aggregate, the outcome of cell-cell interactions in a suspended aggregate and

their consequences for cell behaviour were shown not to be compromised by or dependent on the physical environment of the 2-D ultrasound trap (Chap. 3).

The underlying molecular consequences of cell-cell interactions in the trap were established in Chapters 4-6. It was demonstrated that the synchronous adhering cells, following membrane receptor interactions, underwent the intracellular F-actin, catenin and connexin responses on rapid time scales. Neural C6 cells aggregated, spread their cell-cell contact interface and developed confluent-culture-like F-actin patterns over the period of 1-30 min in the trap (Chap. 4), while aggregated differentiated calf chondrocytes showed clear F-actin and Cx43 distribution that was consistent with measured gap junction functionality over the period of 1-60 min in the trap (Chap. 5).

The potential of the ultrasound trap in the area of cancer biology was recognised in Chapter 6. It was shown that the ultrasound trap was a technique sensitive enough to aid in the identification of the adhesive properties of cancer cells. Cancer cells expressed proteins of the cadherin/catenin complex to a lesser extent than their non-cancerous counterparts and as a result they were classified as less adhesive.

An integrated view of the development of a cell monolayer in the ultrasound trap can be seen as a non biological concentration of cells under millimetre range acoustic forces, a non-intrusive effect of the micron scale acoustic particle interaction force that is small compared to the van der Waals interaction, acoustic-independent cell receptor interactions that modify the short range interactions leading to adhesion and then acoustic-independent progression of intracellular processes to form the adhesively strong and communicating monolayer.

Some aspects of the work presented in this thesis might initiate future activities. A selection of the most promising directions will be presented in the last Chapter 9 of this thesis.

Chapter 9

Future work

9.1 General

In this Chapter, a number of future research paths, stimulated by the results presented in this thesis, for further studies on cell-cell interactions in the ultrasound trap will be reviewed.

9.2 Use of green fluorescent protein (GFP)

Transfecting a population of cells with green fluorescent protein (GFP) for E-cadherin, for example, would provide an approach to monitoring in real-time the trafficking/distribution of this molecule in a large number of cells simultaneously triggered to make contact in a high-resolution, real-time fluorescence imaging or confocal microscopy field. GFP is used particularly as a fusion tag to monitor protein localisation within living cells and is attracting tremendous attention, as it is a strong visible fluorescent reporter molecule which is species-independent and does not require any cofactors or substrates (Herman, 1998).

An even more challenging approach that could find practical applications is based on the availability of several different coloured mutants of GFP, opening up in this way the attractive possibility of multiparameter imaging in living cells. Through the use of enhanced blue fluorescent protein (EBFP), cyan fluorescent protein (CFP),

enhanced green fluorescent protein (EGFP) and enhanced yellow fluorescent protein (EYFP) as well as careful selection of appropriate excitation, dichroic and emission interference filters, it is possible to examine four distinct tagged cellular constituents in the same cell. Some putative molecule combinations are listed in the following table (Table 9.1). Sets 1-3 are focused on adherens and gap junctions, while set 4 investigates the whole intercellular junctional complex (Chap. 1; Sec. 1.1). It is noted that combinations of only two or three molecules is also possible.

Table 9.1: Investigation of protein complexes using GFP variants

Set 1	*Set 2*	*Set 3*	*Set 4*
N-cadherin	E-/N-cadherin	E-/N-cadherin	Claudins
NCAM	α-catenin	α-catenin	E-cadherin
Cx43	β-catenin	β- /γ-catenin	Cx43
F-actin	γ-catenin	F-actin	DSG or DSC

9.3 Investigation of the behaviour of heterogeneous cell populations

The experiments presented in Chapters 4, 5 and 6 were carried out with a single homogeneous cell population. However, the ultrasound approach, with its ability to monitor developing adhesive, partitioning and invasive behaviours of cell *consortia* free of the constraining influence of solid substrata, can facilitate quantitative measures of the cell consortium order or 'cellular sociology' (Adam *et al.*, 2001), that reflect the influence of cell surface receptors on tumour invasiveness (Chap. 6) and on condensation processes in development (Chap. 5). Study of the adhesion of cells in a consortium in suspension provides a significant advance on the

'calcium switch' approach, described in Chap. 1 (Sec. 1.8.1), that is limited to attached monolayers of homogeneous cells.

9.4 Moving into a 3-D system

In vivo, adhesion events occur 3-dimensionally, where cells attach to surrounding 3-D mesh-like fibres rather than 2-D coated surfaces. The ultrasound trap employed here could be a powerful tool for studies of cell-ECM interactions. Solutions of ECM, *e.g.* fibronectin or collagen can be injected into the trap, without disturbing the stably levitated aggregate. Cells free in suspension will then be input to the trap and will surround the ECM coated 2-D aggregate. The 3-D aggregate can then be taken from the chamber after a range of incubation times, and stained for different receptor or cytoskeletal molecules.

In cancer research, tumour-stromal interactions are considered important in tumour progression (Cukierman *et al.*, 2002), as transient loss of basement membrane in pre-malignant epithelium is an early event associated with tumour progression (Yang *et al.*, 2002). This loss facilitates interactions between epithelial cells and stroma. In fact, the majority of tumour-derived myoepithelial cells are deficient in their ability to impart polarity because of aberrant synthesis and matrix deposition (Gudjonsson *et al.*, 2002). These complex alterations in tumour-stromal interactions in cancer progression may be excellent candidates for study using 3-D matrix systems developed in an USW system.

9.5 Applications in tissue engineering

Tissue engineering seeks to repair or replace a damaged or diseased tissue with ideally, a structure developed from the recipient's cells (De Bank *et al.*, 2005).

Designing functional 3-D tissues from monodispersed expanded cell cultures is an ongoing challenge in tissue engineering (Martin *et al.*, 2004). Scaffolds on which tissue cells can grow and differentiate while retaining biological and mechanical functions such as a native ECM, are central to the repair of tissue defects (Kim *et al.*, 1998; Quirk *et al.*, 2004). Scaffold-free approaches on the other hand include: a) cultivation in gyratory flasks or shakers, b) centrifugation-based compression, c) maintenance in cell-culture inserts and d) gravity-enforced assembly of microspheres in hanging drops (Kelm and Fussenegger, 2004). The ultrasound trap may provide an alternative strategy that assembles cells in a scaffold-free and tissue-mimicking way, thus extending options for scaffold-free tissue engineering. The significant short time (of the order of 10s of seconds; Chap.1, Fig. 1. 7a, iii) over which a cell aggregate is formed as well as the established wellbeing of the cells in the trap (Chap. 3) might offer advantages over the current scaffold-free approaches described above. Alternatively, as has been shown by Wang et al. (2004), acoustically driven polymer meshes can by used for the retention of mammalian cells from flowing suspensions. This approach might be applicable to tissue engineering were the mesh to be replaced by a scaffold arrangement. Wang et al. (2004) used an acoustic chamber of an internal volume of 13 ml, operating at 1.12 MHz. The chamber was filled with a polyester mesh having a pore size 2 orders of magnitude larger than the cells (approximately 1250 μm). Cell densities of over 1.5×10^8 cells/ml have been retained over a 5 h period of ultrasound exposure with a $-29 \pm 8.5\%$ change in cell viability.

These suggestions will hopefully stimulate continuing interest in future research on USW cell manipulation as well as new application fields.

Bibliography

Aaltomaa, S., Lipponen, P., Karja, V., Lundstedt, S., Lappi, J. and Kosma, V. M. (2004) The expression and prognostic value of alpha-, beta- and gamma-catenins in renal cell carcinoma. *Anticancer Research* **24** (4): 2407-2413

Adam, L., Mazumdar, A., Sharma, T., Jones, T. R. and Kumar, R. (2001) A three-dimensional and temporo-spatial model to study invasiveness of cancer cells by heregulin and prostaglandin E-2. *Cancer Research* **61** (1): 81-87

Adams, C. L., Chen, Y. Y., Smith, S. J. and Nelson, W. J. (1998) Mechanisms of epithelial cell-cell adhesion and cell compaction revealed by high-resolution tracking of E-cadherin-green fluorescent protein. *Journal of Cell Biology* **142** (4): 1105-1119

Adams, C. L., Nelson, W. J. and Smith, S. J. (1996) Quantitative analysis of cadherin-catenin-actin reorganisation during development of cell-cell adhesion. *Journal of Cell Biology* **135**: 1899-1911

Ahrens, P. B., Solursh, M. and Reiter, R. S. (1977) Stage-related capacity for limb chondrogenesis in cell-culture. *Developmental Biology* **60** (1): 69-82

Alberts, B., Johnson, A., Lewis, J., Raff, M., Roberts, K. and Walter, P. (2003) *Molecular Biology of the Cell*. New York: Garland Publishing, Inc

Al-Moustafa, A. E., Yen, L., Benlimame, N. and Alaoui-Jamali, M. A. (2002) Regulation of E-cadherin/catenin complex patterns by epidermal growth factor receptor modulation in human lung cancer cells. *Lung Cancer* **37** (1): 49-56

Amos, L. A. and Baker, T. S. (1979) 3-dimensional image of tubulin in zinc-induced sheets, reconstructed from electron-micrographs. *International Journal of Biological Macromolecules* **1** (4): 146-156

Anastasiadis, P. Z. and Reynolds, A. B. (2000) The p120 catenin family: complex roles in adhesion, signalling and cancer. *Journal of Cell Science* **113** (8): 1319-1334

Angata, K. and Fukuda, M. (2003) Polysialytransferases: major players in polysialic acid synthesis on the neural cell adhesion molecule. *Biochimie* **85** (1-2): 195-206

Angata, K., Long, J. M., Bukalo, O., Lee, W., Dityatev, A., Wynshaw-Boris, A., Schachner, M., Fukuda, M. and Marth, J. D. (2004) Sialyltransferases ST8Sia-II assembles a subset of polysialic acid that directs hippocampal axonal targeting and promotes fear behaviour. *Journal of Biological Chemistry* **279** (31): 32603-32613

Angst, B. D., Marcozzi, C. and Magee, A. I. (2001) The cadherin superfamily: diversity in form and function. *Journal of Cell Science* **114**: 629-641

Aplin, A. E. and Juliano, R. L. (2001) Regulation of nucleocytoplasmic trafficking by cell adhesion receptors and the cytoskeleton. *Journal of Cell Biology* **155** (2): 187-191

Ashmawi, W. M. and Zirky, M. A. (2003) Single void morphological and grain-boundary effects on overall failure in F. C. C polycrystalline systems. *Materials Science and Engineering* **A343**: 126-142

Asnaghi, D., Carpineti, M., Giglio, M. and Vailati, A. (1995) Light scattering studies of aggregation phenomena. *Physica A* **213**: 148-158

Asnaghi, D., Carpinetti, M., Giglio, M. and Sozzi, M. (1992) Coagulation kinetics and aggregate morphology in the intermediate regimes between diffusion-limited and reaction-limited cluster aggregation. *Physical Review A* **45** (2): 1018-1023

Balto, H. A. (2004) Attachment and morphological behaviour of human periodontal ligament fibroblasts to mineral trioxide aggregate: a scanning electron microscopy study. *Journal of Endodontics* **30**: 25-29

Barger, J. E. (1964) "Thresholds of acoustic cavitation". Tech Memo No 57 Acoustic Reseach Laboratory, Harvard University, Cambridge, MA

Barhoumi, R., Bowen, J. A., Stein, L. S., Echols, J. and Burghardt, R. C. (1993) Concurrent analysis of intracellular glutathione content and gap junctional intercellular communication. *Cytometry* **14**: 747-756

Barmatz, M. and Collas, P. (1985) Acoustic radiation potential on a sphere in plane, cylindrical and spherical standing wave fields. *Journal of the Acoustic Society of America* 77 (3): 928-945

Baumgartner, W., Hinterdorfer, P., Ness, W., Raab, A., Vestweber, D., Schindler, H. and Drenckhahn, D. (2000) Cadherin interaction probed by atomic force microscopy. *Proceeding of the National Academy of Sciences of the USA* **97** (8): 4005-4010

Beardslee, M. A., Laing, J. G, Beyer, E. C. and Saffitz, J. E. (1998) Rapid turnover of connexin43 in the adult rat heart. *Circulation Research* **83**: 629-635

Becker, D. and Green, C. (2002) Gap junction-mediated interactions between cells. In: Fleming, T. P. ed. *Cell-cell interactions*, Oxford: University Press, pp.47-70

Benes, E., Gröschl, M., Nowotny, H., Trampler, F., Keijzer, T., Böhm, H., Radel, S., Gherardini, L., Hawkes, J.J., König, R., and Delouvroy, C. (2001). Ultrasonic separation of suspended particles. In: *IEEE Ultrasonics Symposium Proceedings* 1-2. Atlanta, Georgia: pp. 649-659

Benya, P. D., Brown, P. and Padilla, S. R. (1988) Microfilament modification by dihydrocytochalasin B causes retinoic acid-modulated chondrocytes to re-express the differentiated collagen phenotype without a change in shape. *Journal of Cell Biology* **106**: 161-170

Bergoffen, J., Scherer, S. S., Wang, S., Oronzi Scott, M., Bone, L. J., Paul, D. L., Chen, K., Lensch, M. W., Chance, P. F. and Fischbeck, K. H. (1993) Connexin mutations in X-linked Charcot-Marie-Tooth disease. *Science* **262**: 2039-2042

Berthoud, V. M., Beyer, E. C., Kurata, W. E., Lau, A. F. and Lampe, P. D. (1997) The gap junction protein connexin 56 is phosphorylated in the intracellular loop and the carboxy-terminal region. *European Journal of Biochemistry* **244**: 89-97

Beyer, E. C., Paul, D. L. and Goodenough, D. A. (1987) Connexin43- a protein from the rat heart homologous to a gap junction protein from liver. *Journal of Cell Biology* **105**: 2621-2629

Bhaskar, S., Banavaliker, J. N., Bhardwaj, K. and Upadhyay, P. (2002) A novel ultrasound-enhanced latex agglutination test for the detection of antibodies against *Mycobacterium tuberculosis* in serum. *Journal of Immunological Methods* **262** (1-2): 181-186

Blaschuk, O. W., Sullivan, R., David, S. and Pouliot, Y. (1990) Identification of a cadherin cell-adhesion recognition sequence. *Developmental Biology* **139** (1): 227-229

Bottenstein, J .E. and Sato, G. H. (1979) Growth of a rat neuroblastoma cell line in a serum-free supplemented medium. *Proceedings of the National Academy of Sciences of the USA* **76**: 514-517

Bourdeau, N. J. and Jones, P. L. (1999) Extracellular matrix and signalling: the shape of things to come. *Biochemical Journal* **339**: 481-488

Brady-Kalnay, S. M., Rimm, D. L. and Tonks, N. K. (1995) Receptor protein-tyrosine-phosphatase PTP-mu associates with cadherins and catenins in vivo. *Journal of Cell Biology* **130** (4): 977-986

Braga, V. (2000) Epithelial cell shape: cadherins and small GTPases. *Experimental Cell Research* **261**: 83-90

Braga, V. (2002) Cadherin adhesion regulation in keratinocytes. In: ed. Fleming. T. P. *Cell-cell interactions*. Oxford: Oxford University Press; pp. 1-36

Braga, V. M. M. (2002) Cell-cell adhesion and signalling. *Current Opinion in Cell Biology* **14**: 546-556

Braga, V. M. M., Del Maschio, A., Machesky, L. and Dejana, E. (1999) Regulation of cadherin function by Rho and Rac: Modulation by junction maturation and cellular context. *Molecular Biology of the Cell* **10** (1): 9-22

Braga, V. M. M., Machesky, L. M., Hall, A. and Hotchin, N. A. (1997) The small GTPases Rho and Rac are required for the establishment of cadherin-dependent cell-cell contacts. *Journal of Cell Biology* **137** (6): 1421-1431

Breault, J. E., Shiina, H., Igawa, M., Ribeiro, L. A., Deguchi, M., Enokida, H., Urakami, S., Terashima, M., Nakagawa, M., Kane, C. J., Caroll, P. R. and Dahiya, R. (2005) Methylation of the gamma-catenin gene is associated with poor prognosis of renal cell carcinoma. *Clinical Cancer Research* **11** (2): 557-564

Bremnes, R. M., Veve, R., Hirch, F. R. and Franklin, W. A. (2002) The E-cadherin cell-cell adhesion complex and lung cancer invasion, metastasis and prognosis. *Lung cancer* **36**: 115-124

Brieher, W. M., Yap, A. S. and Gumbiner, B. M. (1996) Lateral dimerisation is required for the homophilic binding activity of C-cadherin. *Journal of Cell Biology* **135** (2): 487-496

Brummendorf, T. and Rathjen, F. G. (1995) Cell-adhesion molecules. 1. Immunoglobulin superfamily-introduction. *Protein Profile* **1** (9): 951-1058

Brusés, J. L. and Rutishauser, U. (2001) Roles, regulation, and mechanism of polysialic acid function during neural development. *Biochimie* **83**: 635-643

Bruzzone, R., White, T. W. and Paul, D. L. (1996) Connections with connexins: the molecular basis of direct intercellular signalling. *European Journal of Biochemistry* **238**: 1-27

Buda, A. and Pignatelli, M. (2004) Cytoskeletal network in colon cancer: form genes to clinical application. *International Journal of Biochemistry and Cell Biology* **36**: 759-765

Bullions, L. C., Notterman, D. A., Chung, L. S. and Levine, A. J. (1997) Expression of wild-type alpha-catenin protein in cells with a mutant alpha-catenin gene restores both growth regulation and tumour suppressor activities. *Molecular and Cellular Biology* **17** (8): 4501-4508

Burridge, K., Fath, K. Kelly, T., Nuckolls, G. and Turner, C. (1998) Focal adhesions: transmembrane junctions between the extracellular matrix and the cytoskeleton. *Annual Reviews in Cell Biology* **4**: 487-525

Bushell, G. C., Yan, Y. D., Woodfield, D., Raper, J. and Amal, R. (2002) On techniques for the measurement of mass fractal dimension of aggregates. *Advances in Colloid and Interface Science* **95**: 1-50

Bussemakers, M. J. G., van Bokhoven, A., Tomita, K., Jansen, C. F. J. and Schalken, J. A. (2000) Complex cadherin expression in human prostate cancer cells. *International Journal of Cancer* **85** (3): 446-450

Butkevich, E., Hulsmann, S., Wenzel, D., Shirao, T., Duden, R. and Majoul, I. (2004) Drebrin is a novel connexin-43 binding partner that links gap junctions to the submembrane cytoskeleton. *Current Biology* **14** (8): 650-658

Büttner, B., Kannicht, C., Reutter, W. and Horstkorte, R. (2003) The neural cell adhesion molecule is associated with major components of the cytoskeleton. *Biochemical and Biophysical Research Communications* **310**: 967-971

Cagnet, M., Francon, M. and Thrierr, J. C. (1962) Atlas of optical phenomena. New York: Spinger-Verlag

Caplan, M. R., Moore, P. N., Zhang, S., Kamm, R. D. and Lauffenburger, D. A. (2000) Self-assembly of a β-sheet protein governed by relief of electrostatic repulsion relative to van der Waals attraction. *Biomacromolecules* **1**: 672-631

Carlier, M. F. (1998) Control of actin dynamics. *Current Opinion in Cell Biology* **10**: 45-51

Carlier, M. F. and Pantaloni, D. (1997) Control of actin dynamics in cell motility. *Journal of Molecular Biology* **269**: 459-467

Chang, L. and Goldman, R. D. (2004) Intermediate filaments mediate cytoskeletal crosstalk. *Nature Molecular Cell Biology* **5**: 601:613

Chappuis-Flament, S., Wong, E., Hicks, L. D., Kay, C. M. and Gumbiner, B. M. (2001) Multiple cadherin extracellular repeats mediate homophilic binding and adhesion. *Journal of Cell Biology* **154** (1): 231-243

Chen, X. Y., Kojima, S., Borisy, G. G. and Green, K. G. (2003) p120 catenin associates with kinesin and facilitates the transport of cadherin-catenin complexes to intercellular junctions. *Journal of Cell Biology* **163** (3): 547-557

Chesire, D. R. and Isaacs, W. B. (2003) β-catenin signalling in prostate cancer: an early perspective. *Endocrine-Related Cancer* **10**: 537-560

Chi, S. S., Rattner, J. B. and Matyas, J. R. (2004) Communication between paired chondrocytes in the superficial zone of articular cartilage. *Journal of Anatomy* **205**: 363-370

Chitaev, N. A. and Troyanovsky, S. M. (1998) Adhesive but not lateral E-cadherin complexes require calcium and catenins for their formation. *Journal of Cell Biology* **142** (3): 837-846

Chu, Y. S., Thomas, W. A., Eder, O., Pincet, F., Rerez, E., Thiery, J. P. and Dufour, S. (2004) Force measurements in E-cadherin-mediated cell doublet reveal rapid adhesion strengthened by actin cytoskeleton remodelling through Rac and Cdc42. *Journal of Cell Biology* **167** (6): 1183-1194

Chunthapong, J., Seftor, E. A., Khalkhali-Ellis, Z., Seftor, R. E. B. and Amir, S., Lubaroff, D. M., Heidger, P. M. and Hendrix, M. J. C. (2004) Dual roles of E-cadherin in prostate cancer invasion. *Journal of Cellular Biochemistry* **91** (4): 649-661

Coakley W. T., Bardsley, D. W. and Grundy, M.A. (1989) Cell manipulation in ultrasonic standing wave fields. *Journal of Chemical Technology and Biotechnology* **44**: 43-62

Coakley, W. T., Bazou, D., Morgan, J., Foster, G. A., Archer, C. W., Powell, K., Borthwick, K. A. J., Twomey, C. and Bishop, J. (2004). Cell-cell contact and membrane spreading in an ultrasound trap. *Colloids and Surfaces B: Biointerfaces* **34**: 221-230

Coakley, W. T., Whitworth, G., Grundy, M. A., Gould, R. K. and Allman, R. (1993) Ultrasonic manipulation of particles and cells. *Bioseparations* **4**: 73-83

Coelho, C. N. D. and Kosher, R. A. (1991) Gap junctional communication during limb cartilage differentiation. *Developmental Biology* **144**: 47-53

Cohen, M. B., Griebling, T. L., Ahagotou, C. A., Rokhlin, O. W. and Ross, J. S. (1997) Cellular adhesion molecules in urologic malignancies. *American Journal of Clinical Pathology* **107** (1): 56-63

Coleman, C. M. and Tuan, R. S. (2003) Functional role of growth/differentiation factor 5 in chondrogenesis of limb mesenchymal cells. *Mechanisms of Development* **120**: 823-836

Contreras, J. E., Sanchez, H. A., Eugenin, E. A., Speidel, D., Theis, M., Willecke, K., Bukauskas, F. F., Bennett, M. V. L. and Saez, J. C. (2002) Metabolic inhibition induces opening of unapposed connexin 43 gap junction hemichannels and reduces gap junctional communication in cortical astrocytes in culture. *Proceedings of the National Academy of Sciences of the USA* **99** (1): 495-500

Cousins, C. M., Melin, J. R., Venables, W. A. and Coakley, W. T. (2001) Investigation of enhancement of two processes, sedimentation and conjugation, when bacteria are concentrated in ultrasonic standing waves. *Bioseparation* **9**: 343-349

Cox, B., Hadjantonakis, A. K., Collins, J. E. and Magee, A. I. (2000) Cloning and expression throughout mouse development of mfat 1, a homologue of the Drosophila tumour suppressor gene fat. *Developmental dynamics* **217** (3): 233-240

Cramer, L. P., Mitchison, T. J. and Theriot, J. A. (1994) Actin-dependent motile forces and cell motility. *Current Opinion in Cell Biology* **6**: 82-86

Critchley, D. R. (2000) Focal adhesions-cytoskeletal connection. *Current Opinion in Cell Biology* **12**: 133-139

Crnic, I. and Christofori, G. (2004) Novel technologies and recent advances in metastasis research. *International Journal of Developmental Biology* **48** (5-6): 573-581, Sp. Issue SI

Cukierman, E., Pankov, R. and Yamada, K. M. (2002) Cell interactions with three-dimensional matrices. *Current Opinion in Cell Biology* **14** (5): 633-639

D'Andrea, P. and Vittur, F. (1996) Gap junctions mediate intercellular calcium signaling in cultured articular chondrocytes. *Cell Calcium* **20**: 389-397

Dalseg, A. M., Gaardsvoll, H. and Bock, E. (1994) Molecular biology of cadherins in the nervous system. *Molecular Neurobiology* 7 (3-4): 207-228

Dantec Dynamics. (2000) FlowManager software and introduction to PIV instrumentation. Software User's Guide, Slovlunde, Denmark

Davies, G., Jiang, W. G. and Mason, M. D. (2000) Cell-cell adhesion molecules and signalling intermediates and their role in the invasive potential of prostate cancer cells. *Journal of Urology* **163**: 985-992

Darnell, J., Lodish, H. and Baltimore, D. (1986) *Molecular Cell Biology*. Baltimore: Scientific American, Inc.

Davis, M. A., Ireton, R. C. and Reynolds, A. B. (2003) A core function for p120-catenin in cadherin turnover. *Journal of Cell biology* **163** (3): 525-534

De Bank, P. A., Kellam, B., Kendall, D. A. and Shakesheff, K. M. (2005) Altered cellular response to adsorbed matrix protein by chemoselective ligation of small molecules. *Journal of Materials Chemistry* **15**: 2047-2055

Delhon, G. A., Gonzalez, M. J. and Murcia, P. R. (2002) Susceptibility of sensory neurons to apoptosis following infection by bovine herpes virus type 1. *Journal of General Virology* **83**: 2257-2267

DeLise, A. M. and Tuan, R. S. (2002) Alterations in the spatiotemporal expression pattern and function of N-cadherin inhibit cellular condensation and chondrogenesis of limb mesenchymal cells *in vitro*. *Journal of Cellular Biochemistry* **87**: 342-359

DeLise, A. M., Fischer, L. and Tuan, R. S. (2000) Cellular interactions and signaling in cartilage development. *Osteoarthritis and Cartilage* **8**: 309-334

Denker, B. M. and Nigam, S. K. (1998) Molecular structure and assembly of the tight junction. *American Journal of Physiology-Renal Physiology* **274** (1): F1-F9

DePianto, D. and Coulombe, P. A. (2004) Intermediate filaments and tissue repair. *Experimental Cell Research* **301**: 68-76

Di Biasio, A., Bolle, G., Cametti, C., Codastefano, P., Sciortino, F. and Tartaglia, P. (1994) Crossover region in the aggregation of colloids. *Physical Review E* **50** (2): 1649-1652

Dihne, M., Bernreuter, C., Sibbe, M., Paulus, W. and Schnachner, M. (2003). A new role for the cell adhesion molecule L1 in neural precursor cell proliferation,

differentiation, and transmitter-specific subtype generation. *Journal of Neuroscience* **23**: 6638-6650

Doblhoffdier, O., Gaida, T., Katinger, H., Burger, W., Groschl, M. and Benes, E. (1994) A novel ultrasonic resonance field device for the retention of animal cells. *Biotechnology Progress* **10**: 428-432

Dohner, K., Nagel, C. H. and Sodeik, B. (2005) Viral stop-and-go along microtubules: taking a ride with dynein and kinesins. *Trends in Microbiology* **13** (7): 320-327

Doinikov, A. A. (1994) Acoustic radiation pressure on a compressible sphere in a viscous-fluid. *Journal of Fluid Mechanics* **267**: 1-21

Doinikov, A. A. and Zavtrak, S. T. (1997) Radiation forces between two bubbles in a compressible liquid. *Journal of the Acoustical Society of America* **102** (3): 1424-1431

Donahue, H. J., Guilak, F., Vander Molen, M. A., McLeod, K. J., Rubin, C. T., Grande, D. A. and Brink, P. R. (1995). Chondrocytes isolated from mature articular cartilage retain the capacity to form functional gap junctions. *Journal of Bone and Mineral Research* **10**:1359-1364

Durrant, L. A., Archer, C. W., Benjamin, M. and Ralphs, J. R. (1999) Articular chondrocytes reorganize their cytoskeleton in response to changing mechanical conditions in organ culture. *Journal of Anatomy* **194**: 343-354

Durrschmid, M. P., Landauer, K., Simic, G., Klug, H., Keijzer, T., Trampler, F., Oudshoorn, A., Groschl, M., Muller, D. and Doblhoff-Dier, O. (2003) Comparison of fluidized bed and ultrasonic cell-retention systems for high cell density mammalian cell culture. *Biotechnology Progress* **19** (3): 1045-1048

Dwir, O., Kansas, G. S. and Alon, R. (2001) Cytoplasmic anchorage of L-selectin controls leukocyte capture and rolling by increasing the mechanical stability of the selectin tether. *Journal of Cell Biology* **155** (1): 145-156

Dyson, M., Woodward, B. and Pond, J. B. (1971) Flow of red blood cells stopped by ultrasound. *Nature* **232**: 572-573

Ebert, M. P. A., Yu, J., Hoffmann, J., Rocco, A., Rocken, C., Kahmann, S., Muller, O., Korc, M., Sung, J. J. and Malfertheiner, P. (2003) Loss of beta-catenin expression in metastatic gastric cancer. *Journal of Clinical Oncology* **21** (9): 1708-1714

Ebisawa, K., Hata, K. I., Okada, K., Ueda, M., Torii, S. and Watanabe, H. (2004) Ultrasound enhances transforming growth factor-beta mediated chondrocyte dedifferentiation of human mesenchymal stem cells. *Tissue Engineering* **10**: 921-929

Eckart, C. (1948) Vortices and streams caused by sound waves. *Physical Review* **73** (1): 68-76

Ehrhardt, C., Kneuer, C. and Bakowsky, U. (2004) Selectins- an emerging target for drug delivery. *Advanced Drug Delivery Reviews* **56**: 527-549

Elfervig, M. K., Graff, R. D., Lee, G. M., Kelley, S. S., Sood, A. and Banes, A. J. (2001) ATP induces Ca^{+2} signalling in human chondrons in three-dimensional agarose films. *Osteoarthritis and Cartilage* **9**: 518-526

Elimelech, M., Gregory, J., Jia, X. and Williams, R. A. (1995) *Particle deposition and aggregation*. Woburn: Butterworth-Heinemann

Ellis, R. W. and Sobanski, M. A. (2000) Diagnostic particle agglutination using ultrasound: a new technology to rejuvenate old microbiological methods. *Journal of Medical Microbiology* **49**: 1-7

Engelman, E. H. and Orlova, A. (1995) New insights into actin filament dynamics. *Current Opinion in Structural Biology* **5**: 172-180

Etienne-Manneville, S. (2004) Actin and microtubules in cell motility: which one is in control? *Traffic* **5**: 470-477

Evans, W. H. and Martin, P. E. M. (2002) Gap junctions: Structure and function. *Molecular Membrane Biology* **19**: 121-136

Ewart, J. L., Cohen, M. F., Meyer, R. A., Huang, G. Y., Wessels, A., Gourdie, R. G., Chin, A. J., Park, S. M. J., Lazatin, B. O., Villabon, S. and Lo, C. W. (1997) Heart and neural tube defects in transgenic mice overexpressing the Cx43 gap junction gene. *Development* **124**: 1281-1292

Fath, K. R., Edgell, C. S. and Burridge, K. (1989) The distribution of distinct integrins in focal contacts is determined by the substratum composition. *Journal of Cell Science* **92**: 67-75

Fey, P., Stephens, S., Titus, M. A. and Chisholm, R. L. (2002) SadA, a novel adhesion receptor in Dictyostelium. *Journal of Cell Biology* **159**: 1109-1119

Fish, R. S. (2005) 'Cell-cell interactions and matrix deposition in tendon development in citro and in vivo'. Doctoral Dissertation, Cardiff University

Freshney, R. I. (2000). *Culture of animal cells: A manual of basic technique*. Chichester: Wiley-Liss Inc

Friedl, P. and Brocker, E. B. (2000) The biology of cell locomotion within three-dimensional extracellular matrix. *Cellular and Molecular Life Sciences* **57** (1): 41-64

Friedl, P. and Brocker, E-B (2002). TCR triggering on the move: diversity of T-cell interactions with antigen-presenting cells. *Immunological Reviews* **186**: 83-89.

Frixione, E., Lagunes, R., Ruiz, L., Urbán, M. and Porter, R. M. (2003) Mechanical responses of single non-confluent epithelial cells to low extracellular calcium. *Journal of Muscle Research and Cell Motility* **24**: 477-485

Fujimoto, I., Bruses, J. L. and Rutishauser, U. (2001) Regulation of cell adhesion by polysialic acid. *Journal of Biological Chemistry* **276** (34): 31745-31751

Fujimoto, K., Nagafuchi, A., Tsukita, S., Kuraoka, A., Ohokuma, A. and Shibata, Y. (1997) Dynamics of connexins, E-cadherin and α-catenin on cell membranes during gap junction formation. *Journal of Cell Science* **110**: 311-322

Furukawa, R. and Fechheimer, M. (1997) The structure, function and assembly of actin filament bundles. *International Review of Cytology-A Survey of Cell Biology* **175**: 29-90

Harburn, G., Taylor, C.A. and Welberry, T. A. (1983) *Atlas of Optical Transforms*. London: Bell and Hyman Ltd

Gaida, T., Doblhoff-Dier, O., Strutzenberger, K., Katinger, H., Burger, W., Gröschl, M., Handl, B. and Benes, E. (1996) Selective retention of viable cells in ultrasonic resonance field devices. *Biotechnological Progress* **12**: 73-76

Gardner, K. H., Theis, T. L. and Young, T. C. (1998) Colloid aggregation: numerical solution and measurements. *Colloids and Surfaces A: Physicochemical and Engineering Aspects* **141**: 237-252

Garner, D. L., Thomas, C. A., Joerg, H. W., DeJarnette, J. M. and Marshall, C. E. (1997) Fluorometric assessments of mitochondrial function and viability in cryopreserved bovine spermatozoa. *Biology of Reproduction* **57**: 1401-1406

Garrod, R., Merritt, A. J. and Nie, Z. (2002) Desmosomal cadherins. *Current Opinion in Cell Biology* **14**: 537-545

George, C. H., Kendall, J. M. and Evans, W. H. (1999) Intracellular trafficking pathways in the assembly of connexins into gap junctions. *Journal of Biological Chemistry* **274**: 8678-8685

Ghezzi, F., Earnshaw, J. C., Finnis, M. and McCluney, M. (2001) Pattern formation in colloidal monolayers at the air-water interface. *Journal of Colloid and Interface Science* **238**: 433-446

Giepmans, B. N. G. (2004) Gap junctions and connexin-interacting proteins. *Cardiovascular Research* **62** (2): 233-245

Giessmann, D., Theiss, C., Breipohl, W. and Meller, K. (2003) Microinjection of actin antibodies impaired gap junctional intercellular communication in lens epithelial cells in vitro. *Current Eye Research* **27** (3): 157-164

Goldberg, G. S., Moreno, A. P. and Lampe, P. D. (2002) Gap junctions between cells expressing connexin 43 or 32 show inverse permselectivity to adenosine and ATP. *Journal of Biological Chemistry* **277** (39): 36725-36730

Gonzalez-Amaro, R. and Sanchez-Madrid, F. (1999) Cell adhesion molecules: Selectins and integrins. *Critical reviews in immunology* **19** (5-6): 389-429

Gooding, J. M., Yap, K. L. and Ikura, M. (2004) The cadherin-catenin complex as a focal point of cell adhesion and signalling: new insights from three-dimensional structures. *BioEssays* **26**: 497-511

Gor'kov, L. P. (1962) On the forces acting on a small particle in an acoustical field in an ideal fluid. *Soviet Physics* **6** (9): 773-775

Gorenflo, V. M., Smith, L., Dedinsky, B., Persson, B. and Piret, J. M. (2002) Scale-up and optimisation of an acoustic filter for 200 L/ day perfusion of a CHO cell culture. *Biotechnology and Bioengineering* **80** (4): 438-444

Gould, R. K. and Coakley, W. T. (1974) The effects of acoustic forces on small particles in suspension. In: Bjorn, L. ed. *Proceeding of the 1973 Symposium, Finite Amplitude Wave Effects in Fluids*. Guilford: pp. 252-257

Govindarajan, R., Zhao, S., Song, X. H., Guo, R. J., Wheelock, M., Johnson, K. R. and Mehta, P. P. (2002) Impaired trafficking of connexins in androgen-independent human prostate cancer cell lines and its migration by alpha-catenin. *Journal of Biological Chemistry* **277** (51): 50087-50087

Graff, J. R., Herman, J. G., Lapidus, R. G., Chopra, H., Xu, R., Jarrard, D. F., Isaacs, W. B., Pitha, P. M., Davidson, N. E. and Baylin, S. B. (1995) E-cadherin expression is silenced by DNA hypermethylation in human breast and prostate carcinomas. *Cancer Research* **55** (22): 5195-5199

Gray, S. J., Sobanski, M. A., Kaczmarski, E. B., Guiver, M., Marsh, W. J., Borrow, R., Barnes, R. A. and Coakley, W. T. (1999) Ultrasound-enhanced latex immunoagglutination and PCR as complementary methods for non-culture-based confirmation of meningococcal disease. *Journal of Clinical Microbiology* **37** (6): 1797-1801

Green, K. J. and Gaudry, C. A. (2000) Are desmosomes more than tethers for intermediate filaments? *Nature Molecular Cell Biology* **1** (3): 208-216

Gregory, J. (2004) Monitoring floc formation and breakage. *Water Science and Technology* **50** (12): 163-170

Grier, D. G. (2003) A revolution in optical manipulation. *Nature* **424**: 810-816

Gross, S. P. (2004) Hither and yon: a review of bi-directional microtubule-based transport. *Physical Biology* **1** (1-2): R1-R11

Grundy, M. A. (1994) 'Ultrasonic concentration and manipulation of small particles and biological cells'. Doctoral Dissertation, Cardiff University

Grundy, M. A., Bolek, W. E., Coakley, W. T. and Benes, E. (1993) Rapid agglutination testing in an ultrasonic standing-wave. *Journal of Immunological Methods* **165** (1): 47-57

Gück, J., Schinkinger, S., Lincoln, B., Wottawah, F., Ebert, S., Romeyke, M., Lenz, D., Erickson, H. M., Ananthakrishnan, R., Mitchell, D., Kas, J., Ulvick, S. and Bilby, C. (2005) Optical deformability as an inherent cell marker for testing malignant transformation and metastatic competence. *Biophysical Journal* **88** (5): 3689-3698

Gudjonsson, T., Ronnov-Jessen, L., Villadsen, R., Rank, F., Bissell, M. J. and Petersen, O. W. (2002) Normal and tumour-derived myoepithelial cells differ in their ability to interact with luminal breast epithelial cells for polarity and basement membrane deposition. *Journal of Cell Science* **115** (1): 39-50

Guilak, F. and Mow, V. C. (2000) The mechanical environment of the chondrocyte: a biphasic finite element model of cell-matrix interactions in articular cartilage. *Journal of Biochemistry* **33**: 1663-1673

Gumbiner, B. (1996) Cell adhesion: the molecular basis of tissue architecture and morphogenesis. *Cell* **84**: 345-357

Gumbiner, B. (2005) Regulation of cadherin-mediated adhesion in morphogenesis. *Nature Molecular Cell Biology* **6**: 622-634

Gupta, S. and Feke, D. L. (1998) Filtration of particulate suspensions in acoustically driven porous media. *AICHE Journal* **44** (5): 1005-1014

Hall, B. K. and Miyake, T. (2000) All for one and one for all: condensations and the initiation of skeletal development. *BioEssays* **22**: 138-147

Harris, N., Hill, M., Shen, Y., Townsend, R. J., Beeby, S. and White, N. (2004) A dual frequency, ultrasonic, microengineered particle manipulator. *Ultrasonics* **42** (1-9): 139-144

Harvey, E. N. and Loomis, A. L. (1928) High frequency sound waves of small intensity and their biological effects. *Nature* **121**: 622-624

Häussinger, D., Ahrens, T., Sass, H. J., Pertz, O., Engel, J. and Grzesiek, S. (2002) Calcium-dependent homoassociation of E-cadherin by NMR spectroscopy: changes in mobility, conformation and mapping of contact regions. *Journal of Molecular Biology* **324**: 823-839

Hawkes, J. J. and Coakley, W. T. (1996) A continuous flow ultrasonic cell filtering method. *Journal of Enzyme and Microbial Technology* **19**: 57-62

Hawkes, J. J., Barrow, D. and Coakley, W. T. (1998a) Microparticle manipulation in millimetre scale ultrasonic standing wave chambers. *Ultrasonics* **36**: 925-931

Hawkes, J. J., Cefai, J. J., Coakley, W. T. and Briarty, L. G. (1998b) Ultrasonic manipulation of particles in microgravity. *Journal of Physics D-Applied Physics* **31** (14): 1673-1680

Hawkes, J. J. and Coakley, W. T. (2001) Force field particle filter, combining ultrasound standing waves and laminar flow. *Sensors and Actuators B* **75**: 213-222

Hawkes, J. J., Barber, R. W., Emerson, D. R. and Coakley, W. T. (2004) Continuous cell washing and mixing driven by an ultrasound standing wave within a microfluidic channel. *Lab on a Chip* **4** (5): 446-452

He, H. T., Barbet, J., Chaix, J. C. and Goridis, C. (1986) Phosphatidylinositol is involved in the membrane attachment of NCAM-120, the smallest component of the neural cell-adhesion molecule. *EMBO Journal* **5** (10): 2489-2494

Heida, T., Rutten, W. L. C. and Marani, E. (2002). Understanding dielectrophoretic trapping of neuronal cells: modelling electric field, electrode-liquid interface and liquid flow. *Journal of Physics D-Applied Physics* **35**: 1592-1602

Hellio Le Graverand, M. P., Sciore, P., Eggerer, J., Rattner, J. P., Vignon, E., Barclay, L., Hart, D. A. and Rattner, J. B. (2001) Formation and phenotype of cell clusters in osteoarthritic meniscus. *Arthritis and Rheumatism* **44**: 1808-1818

Hemstreet, G. F., Bonner, R. A., Hurst, R. E., Bell, D. and Bane, B. L. (2000) Abnormal G-actin content in single prostate cells as a biomarker of prostate cancer. *Cancer Detection and Prevention* **24** (5): 464-472

Hennings, H. and Holbrook, K. A. (1983) Calcium regulation of cell-cell contact and differentiation of epidermal cells in culture. *Experimental Cell Research* **143**: 127-142

Herman, B. (1998) *Fluorescence microscopy*. New York: Springer-Verlag

Hernandez-Blasquez, F. J., Joazeiro, P. P., Omori, Y. and Yamasaki, H. (2001) Control of intracellular movement of connexins by E-cadherin in murine skin papilloma cells. *Experimental Cell Research* **270** (2): 235-247

Hidalgo-Álvarez, R., Martín, A., Fernández, A., Bastos, D., Martínez, F. and de las Nieves F. J. (1996) Electrokinetic properties, colloidal stability and aggregation kinetics of polymer colloids. *Advances in Colloid and Interface Science* **67**: 1-118

Hiemenz, P. C. (1986) *Principles of colloid and surface chemistry*. New York: Marcel Decker

Higashitani, K., Fukushima, M. and Matsuno, Y. (1981) Migration of suspended particles in plane stationary ultrasonic field. *Chemical Engineering Science* **36** (12): 1877-1882

Hill, G. and Holman, J. (1995) *Chemistry in context*. Surrey: Thomas Nelson and Sons Ltd

Huang, S. H., Wu, J. C., Chang, K. J., Liaw, K. Y. and Wang, S. M. (1998) Distribution of the cadherin-catenin complex in normal human thyroid epithelium and a thyroid carcinoma cell line. *Journal of Cellular Biochemistry* **70** (3): 330-337

Huetter, T. F. and Bolt, R. H. (1955). Piezoelectric transducers. In: Huetter, T. F. and Bolt, R. H. ed. *Sonics*. New York: John Wiley & Sons, Inc; pp. 86-162

Hughes, C., Murphy, A., Martin, C., Sheils, O. and O'Leary, J. (2005) Molecular pathology of prostate cancer. *Journal of Clinical Pathology* **58** (7): 673-684

Hunter, A. W., Jourdan. J. and Gourdie, R. G. (2003) Fusion of GFP to the carboxy terminus of connexin 43 increases gap junction size in HeLa cells. *Cell Communication and Adhesion* **10** (4-6): 211-214

Hurd, A. J. and Schaefer, D. W. (1985) Diffusion-limited aggregation in two dimensions. *Physical Review Letters* **54** (10): 1043-1046

Hwang, S. H. and Koo, Y. M. (2003) Design of acoustic cell settler for filtering and recycling microbial cells. *Biotechnology Letters* **25** (4): 345-348

Hynes R. O. (1996) Targeted mutations in cell adhesion genes: what have we learned from them? *Developmental Biology* **180**: 402-412

Hynes, R. O. (1992) Integrins: versatility, modulation and signalling in cell adhesion. *Cell* **137**: 11-25

Idowu, B. D., Knight, M. M., Bader, D. L. and Lee, D. A. (2000) Confocal analysis of cytoskeletal organization within isolated chondrocyte sub-populations cultured in agarose. *Histochemical Journal* **32**: 165-174

Ikeguchi, R., Kakinoki, R., Okamoto, T., Matsumoto, T., Hyon, S. H. and Nakamura, T. (2003) Successful storage of peripheral nerve before transplantation using green tea polyphenol: asn experimental study in rats. *Experimental Neurology* **184**: 688-696

Imamura, Y., Itoh, M., Maeno, Y., Tsukita, S. and Nagafuchi, A. (1999) Functional domains of alpha-catenin required for the strong state of cadherin-based cell adhesion. *Journal of Cell Biology* **144** (6): 1311-1322

Ireton, R. C., Davis, M. A., van Hengel, J., Mariner, D. J., Barnes, K., Thoreson, M. A., Anastasiadis, P. Z., Matrisian, L., Bundy, L. M., Sealy, L., Gilbert, B., van Roy, F. and Reynolds, A. B. (2002) A novel role for p120 catenin in E-cadherin function. *Journal of Cell Biology* **159** (3): 465-476

Issa, M. A., Islam, Md. S. and Chudnovsky, A. (2003) Fractal dimension- a measure of fracture roughness and toughness of concrete. *Engineering Fracture Mechanics* **70**: 125-137

Iwabuchi, S., Ito, M., Hata, J., Chikanishi, T., Azuma, Y. and Haro, H. (2005) *In vitro* evaluation of low-intensity pulsed ultrasound in herniated disc resorption. *Biomaterials* **26**:7104-7114

Jamora, C. and Fuchs, E. (2002) Intercellular adhesion, signalling and the cytoskeleton. *Nature Cell Biology* **4**: 101-108

Jenkins, P., Barnes, R. A. and Coakley, W. T. (1997) Detection of meningitis antigens in buffer and body fluids by ultrasound-enhanced particle agglutination. *Journal of Immunological Methods* **205**: 191-200

Jiang, W. G., Hiscox, S., Hallett, M. B., Horrobin, D. F., Mansel, R. E. and Puntis, M. C. A. (1995) Regulation of the expression of E-cadherin on human cancer cells by gamma-linoleic acid. *Cancer Research* **55**: 5043-5048

Jin, H. and Varner, J. (2004) Integrins: roles in cancer development and as treatment targets. *British Journal of Cancer* **90**:561-565

Job, D., Valiron, O. and Oakley, B. (2003) Microtubule nucleation. *Current Opinion in Cell Biology* **15** (1): 111-117

Johnson, C. P., Fujimoto, I., Perrin-Tricaud, C., Rutishauser, U. and Leckband, D. (2004) Mechanism of homophilic adhesion by the neural cell adhesion molecule: use of multiple domains and flexibility. *Proceedings of the National Academy of Sciences of the USA* **101** (18): 6963-6968

Johnson, C. P., Fujimoto, I., Rutishauser, U. and Leckband, D. E. (2005) Direct evidence that neural cell adhesion molecule (NCAM) polysialylation increases intermembrane repulsion and abrogates adhesion. *Journal of Biological Chemistry* **280** (1): 137-145

Johnson, R. G., Meyer, R. A., Li, X. R., Preus, D. M., Tan, L., Grunenwald, H., Paulson, A. F., Laird, D. W. and Sheridan, J. D. (2002) Gap junctions assemble in the presence of cytoskeletal inhibitors, but enhanced assembly requires microtubules. *Experimental Cell Research* **275** (1): 67-80

Jones, M. N. (1975). *Biological Interfaces*. Amsterdam: Elsevier Scientific Publishing Company

Jones, S. J., Gray, C., Sakamaki, H., Boyde, A., Gourdie, R. and Green, C. (1993) The incidence and size of gap junctions between the bone cells in rat calvaria. *Anatomy and Embryology* **187**: 343-352

Jørgensen, O. S. and Bock, E. (1974) Brain specific synaptosomal membrane proteins demonstrated by crossed immunoelectrophoresis. *Journal of Neurochemistry* **23**: 879-880

Juliano, R. L. (2002) Signal transduction by cell adhesion receptors and the cytoskeleton: functions of integrins, cadherins, selectins and immunoglobulin-superfamily members. *Annual Reviews in Pharmacology and Toxicology* **42**: 283-323

Kaibuchi, K., Kuroda, S., Fukata, M. and Nakagawa, M. (1999) Regulation of cadherin-mediated cell-cell adhesion by the Rho family GTPases. *Current Opinion in Cell Biology* **11**: 591-596

Kageshita, T., Hamby, C. V., Ishihara, T., Matsumoto, K., Saida, T. and Oto, T. (2001) Loss of β-catenin expression associated with disease progression in malignant melanoma. *British Journal of Dermatology* **145** (2): 210-216

Katsantonis, J., Tosca, A., Koukouritaki, S. B., Theodoropoulos, P. A., Gravanis, A. and Stournaras, C. (1994) Differences in the G/total actin ratio and microfilament

stability between normal and malignant human keratinocytes. *Cell Biochemistry and Function* **12** (4): 267-274

Kawanishi, J., Kato, J., Sasaki, K., Fujii, S., Watanabe, N. and Niitsu, Y. (1995) Loss of E-cadherin-dependent cell-cell adhesion due to mutation of the β-catenin gene in a human cancer cell line, HSC-39. *Molecular and Cellular Biology* **15** (3): 1175-1181

Kelm, J. M. and Fussenegger, M. (2004) Microscale tissue engineering using gravity-enforced cell assembly. *Trends in Biotechnology* **22**: 195-202

Khanna, S., Amso, N. N., Paynter, S. J. and Coakley, W. T. (2003) Contrast agent bubble and erythrocyte behaviour in a 1.5 MHz standing ultrasound wave. *Ultrasound in Medicine and Biology* **29**: 1463-1470

Khare, L., Sabourin, C. L. K., De Young, B. R., Jamasbi, R. J. and Stoner, G. D. (1999) Altered localization of E-cadherin and alpha-catenin in rat esophageal tumours. *International Journal of Oncology* **14** (1): 33-40

Kim, A. Y. and Berg, J. C. (2000) Fractal aggregation: scaling of fractal dimension with stability ratio. *Langmuir* **16**: 2101-2104

Kim, B. S., Putnam, A. J., Kulik, T. J. and Mooney, D. J. (1998) Optimising seeding and culture methods to engineer smooth muscle tissue on biodegradable polymer matrices. *Biotechnology and Bioengineering* **57** (1): 46-54

King, L. V. (1934) On the acoustic radiation pressure on spheres. *Proceedings of the Royal Society* **147**: 212-240

Kiselyov, V. V., Soroka, V., Berezin, V. and Bock, E. (2005) Structural biology of NCAM homophilic binding and activation of FGFR. *Journal of Neurochemistry* **94**: 1169-1179

Klimkovsky, M. W. and Parr, B. (1995) The body language of cells: the intimate connection between cell adhesion and behaviour. *Cell* **83**: 5-8

Knight, M. M., Idowu, B. D., Lee, D. A. and Bader, D. L. (2001) Temporal changes in cytoskeletal organisation within isolated chondrocytes quantified using a novel image analysis technique. *Medical and Biological Engineering and Computing* **39** (3): 397-404

Ko, K., Arora, P., Lee, W., McCulloch, C. (2000) Biochemical and functional characterization of intercellular adhesion and gap junctions in fibroblasts. *American Journal of Physiology-Cell Physiology* **271**: C147-C157

Kobeliak, A. and Fuchs, E. (2004) α-catenin: at the junction of intercellular adhesion and actin dynamics. *Nature Molecular Cell Biology* **5**: 614-625

Koch, A. W., Pokutta, S., Lustig, A. and Engel, J. (1997) Calcium binding and homoassociation of E-cadherin domains. *Biochemistry* **36** (25): 7697-7705

Koch, A. W., Boric, D., Pertz, O. and Engel, J. (1999) Homophilic adhesion of cadherins. *Current Opinion in Structural Biology* **9**: 275-281

Koch, A. W., Manzur, K. L. and Shan,W. (2004) Structure-based models of cadherin-mediated cell adhesion: the evolution continues. *Cellular and Molecular Life Sciences* **61**: 1884-1895

Kooy, A. J. W., Tank, B., de Jong, A. A. W., Vuzevski, V. D., van der Kwast, T. H. and van Joost, T. (1999) Expression of E-cadherin, alpha- and beta-catenin, and CD44V(6) and the subcellular localization of E-cadherin and CD44V(6) in normal epidermis and basal cell carcinoma. *Human Pathology* **30** (11): 1328-1335

Kosteskii, I., Li, J. F., Xiong, Y. M., Zhou, R., Ferrari, V. A., Patel, V. V., Molkentin, J. D. and Radice, G. L. (2005) Induced deletion of N-cadherin gene in the heart leads to dissociation of the intercalated disc structure. *Circulation Research* **96**: 346-354

Kühl, N. K., Kunz, J. and Rensing, L. (2000) Heat shock-induced arrests in different cell cycle phases of rat C6-glioma cells are attenuated in heat shock-primed thermotolerant cells. *Cell Proliferation* **33**: 147-166

Kumai, M., Nishii, K., Nakamura, K., Takeda, N., Suzuki, M. and Shibata, Y. (2000) Loss of connexin 45 causes a cushion defect in early cardiogenesis. *Development* **127** (16): 3501-3512

Kumar, N. M. and Gilula, N. B. (1996) The gap junction communication channel. *Cell* **84**: 381-388

Kundt, A. and Lehmann, O. (1874) Ueber longitudinale schwingungen und klangfiguren in cylindrischen flussigkeitssaulen. *Annals Physik Chemie (Poggendoff)* **153**: 1-11

Kürner, J., Medalia, Linaroudis, A. A. and Baumeister, W. (2004) New insights into the structural organisation of eukaryotic and prokaryotic cytoskeletons using cryo-electron tomography. *Experimental Cell Research* **301**: 38-42

Kuznetsova, L. A. and Coakley, W. T. (2004) Microparticle concentration in short pathlength ultrasonic resonators: roles of radiation pressure and acoustic streaming. *Journal of the Acoustic Society of America* **116** (4): 1956-1966

Kyker, K. D., Culkin, D. J. and Hurst, R. E. (2003) A model for 3-dimensional growth of bladder cancers to investigate cell-matrix interactions. *Urologic oncology-seminars and original investigations* **21** (4): 255-261

Laird, D. W., Fistouris, P., Batist, G., Alpert, L., Huynh, H. T., Carystinos, G. D. and Alaoui-Jamali, M. A. (1999) Deficiency of connexin 43 gap junctions is an independent marker for breast tumours. *Cancer Research* **59** (16): 4104-4110

Lambrechts, A., van Troys, M. and Ampe, C. (2004) The actin cytoskeleton in normal and pathological cell motility. *International Journal of Biochemistry and Cell Biology* **36**: 1890-1909

Langelier, E., Suetterlin, R., Hoemann, C. D., Aebi, U. and Buschmann, M. D. (2000) The chondrocyte cytoskeleton in mature articular cartilage: structure and distribution of actin, tubulin and vimentin filaments. *Journal of Histochemistry and Cytochemistry* **48**: 1307-1320

Langer, R. and Vacanti, J. P. (1993) Tissue engineering. *Science* **260** (5110): 920-926
Langille, R. M. (1994) Chondrogenic differentiation in cultures of embryonic rat mesenchyme. *Microscopy Research and Technique* **28**: 455-469

Lauf, U., Giepmans, B. N. G., Lopez, P., Braconnot, S., Chen, S. C. and Falk, M. M. (2002) Dynamic trafficking and delivery of connexons to the plasma membrane and accretion to gap junctions in living cells. *Proceedings of the National Academy of Sciences of the USA* **99**: 10446-10451

Le, T. L., Yap, A. S. and Stow, J. L. (1999) Recycling of E-cadherin: a potential mechanism for regulating cadherin dynamics. *Journal of Cell Biology* **146**: 219-232

Lee, Y. H. and Peng, C. A. (2005) Enhanced retroviral gene delivery in ultrasonic standing wave field. *Gene Therapy* **12** (7): 625-633

Levin, M. (2001) Isolation and Community: a review of the role of gap-junctional communication in embryonic patterning. *Journal of Membrane Biology* **185**: 177-192

Limaye, M. S. and Coakley, W. T. (1998) Clarification of small volume microbial suspensions in an ultrasonic standing wave. *Journal of Applied Microbiology* **84** (6): 1035-1042

Lin, M. Y., Lindsay, H. M., Weitz, D. A., Ball, R. C., Klein, R. and Meakin, P. (1989) Universality in colloid aggregation. *Nature* **339**: 360-362

Liu, Y., Tan, Z. P., Pan, Q., He, L. Q., Cai, F., Wu, L. Q., Liang, D. S., Xia, K., Xia, J. H. and Zhang, Z. H. (2005) Screening, identification and functional research of the human gap junction connexin 31 interaction proteins. *Progress in Biochemistry and Biophysics* **32** (1): 18-24

Loty, S., Foll, C., Forest, N. and Sautier, J. M. (2000) Association of enhanced expression of gap junctions with *in vitro* chondrogenic differentiation of rat nasal septal cartilage-released cells following their dedifferentiation and redifferentiation. *Archives of Oral Biology* **45**: 843-856

Lozano, E., Betson, M. and Braga, V. M. M. (2003) Tumour progression: small GTPases and loss of cell-cell adhesion. *BioEssays* **25**: 452-463

Lu, Q., Dobbs, L. J., Gregory, C. W., Lanford, G. W., Revelo, M. P., Shappell, S. and Chen, Y. H. (2005) Increased expression of delta-catenin/neural plakophillin-related armadillo protein is associated with the down-regulation and redistribution of E-cadherin and p120(ctn) in human prostate cancer. *Human Pathology* **36** (10): 1037-1048

Mallein-Gerin, F., Garrone, R. and van der Rest, M. (1991) Proteoglycan and collagen synthesis are correlated with actin organisation in dedifferentiating chondrocytes. *European Journal of Cell Biology* **56**: 364-373

Manabe, R., Kovalenko, M., Webb, D. J. and Horwitz, A. R. (2002) GIT1 functions on a motile, multi-molecular signalling complex that regulates protrusive activity and cell migration. *Journal of Cell Science* **115**: 1497-1510

Manaresi, N., Romani, A., Medoro, G., Altomare, L., Leonardi, A., Tartagni, M. and Guerrieri, R. (2003). A CMOS chip for individual cell manipulation and detection. *IEEE Journal of Solid-State Circuits* **38** (12): 2297-2305

Mandelbrot, B. B. (1982) The Fractal geometry of nature. San Francisco: Freeman

Mandralis, Z. I. and Feke, D. L. (1993) Fractionation of suspensions using synchronized ultrasonic and flow-fields. *AICHE Journal* **39** (2): 197-206

Mareel, M. and Leroy, A. (2003) Clinical, cellular, and molecular aspects of cancer invasion. *Physiological Reviews* **83**: 337-376

Martin, I., Wendt, D. and Heberer, M. (2004) The role of bioreactors in tissue engineering. *Trends in Biotechnology* **22**: 80-86

Martin, S. J., Reutelingsperger, C. P. M., McGahon, A. J., Rader, J. A., van Schie, R. C. A. A., LaFace, D. M. and Green, D. R. (1995) Early redistribution of plasma membrane phosphatidylserine is a general feature of apoptosis regardless of the initiating stimulus: Inhibition by overexpression of Bcl-2 and Abl. *Journal of Experimental Medicine* **182**: 1545-1556

Martin, S. P., Townsend, R. J., Kuznetsova, L. A., Borthwick, K. A. J., Hill, M., McDonnell, M. B. and Coakley, W. T. (2005) Spore and micro-particle capture on an immunosensor surface in an ultrasound standing wave system. *Biosensors and Bioelectronics* **21**: 758-767

Mary, S., Charrasse, S., Meriane, M., Comunale, F., Travo, P., Blangy, A. and Gauthier-Rouvière, C. (2002) Biogenesis of N-cadherin-dependent cell-cell contacts in living fibroblasts is a microtubule-dependent kinesin-driven mechanism. *Molecular Biology of the Cell* **13**: 285-301

Mason, M. D., Davies, G. and Jiang, W. G. (2002) Cell adhesion molecules and adhesion abnormalities in prostate cancer. *Critical Reviews in Oncology Hematology* **41** (1): 11-28

Mauro, L. and Surmacz, E. (2004) IGF-I receptor, cell-cell adhesion, tumour development and progression. *Journal of Molecular Histology* **35** (3): 247-253

Mauro, L., Salerno, M., Morelli, C., Boterberg, T., Bracke, M. E. and Surmacz, E. (2003) Role of the IGF-I receptor in the regulation of cell-cell adhesion: implications in cancer development and progression. *Journal of Cellular Physiology* **194** (2): 108-116

McEver, R. P. (1997) Selectin-carbohydrate interactions during inflammation and metastasis. *Glycoconjugate journal* **14** (5): 585-591

McEver, R. P. (2002) Selectins: lectins that initiate cell adhesion under flow. *Current Opinion in Cell Biology* **14**: 581-586

Meakin, P. (1988) Fractal Aggregates. *Advances in Colloid and Interface Science* **28**: 249-331

Mercola, M. (1999) Embryological basis for cardiac left-right asymmetry. *Seminars in Cell and Developmental Biology* **10**: 109-116

Meyer, R. A., Laird, D. W., Revel, J. P. and Johnson, R. G. (1992) Inhibition of gap junction and adherens junction assembly by connexin and A-CAM antibodies. *Journal of Cell Biology* **119** (1): 179-189

Miller, D. L. (1976) Instrument for microscopical observation of the biophysical effects of ultrasound. *Journal of the Acoustical Society of America* **60**: 1203-1212

Mio, C., Gong, T., Terray, A. and Marr, D. W. M. (2001) Morphological control of mesoscale colloidal models. *Fluid Phase Equilibria* **185** (1-2): 157-163

Misaki, K., Marukawa, K., Hayashi, Y., Fukusato, T., Minamoto, T., Hasegawa, M., Yamashita, J. and Fujisawa, H. (2005) Correlation of gamma-catenin expression with good prognosis in medulloblastomas. *Journal of Neurosurgery* **102** (2): 197-206 Suppl. S.

Mitchell, S., Abel, P., Ware, M., Stamp, G. and Lalani, E. N. (2000) Phenotypic and genotypic characterisation of commonly used human prostatic cell lines. *British Journal of Urology International* **85** (7): 932-944

Moncho-Jordá, A., Martínez-López, F. and Hidalgo-Álvarez, R. (2002) The effect of the salt concentration and counterion valence on the aggregation of latex particles at the air/water interface. *Journal of Colloid and Interface Science* **249**: 405-411

Monier-Gavalle, F. and Duband, J. L. (1997) Cross talk between adhesion molecules: control of N-cadherin activity by intracellular signals elicited by β_1 and β_3 integrins in migrating neural crest cells. *Journal of Cell Biology* **137**: 1663-1681

Morrison, S. L., Campbell, C. K. and Wright, G. M. (2000) Chondrogenesis of the branchial skeleton in embryonic sea lamprey, Petromyzon marinus. *Anatomical Record* **260**: 252-267

Moustakas, A. and Stournaras, C. (1999) Regulation of actin organisation by TGF-beta in H-ras-transformed fibroblasts. *Journal of Cell Science* **112** (8): 1169-1179

Muller, T., Gradl, G., Howitz, S., Shirley, S., Schnelle, T. and Fuhr, G. (1999) A 3-D microelectrode system for handling and caging single cells and particles. *Biosensors and Bioelectronics* **14**: 247-256

Murray, B. A. and Jensen, J. J. (1992) Evidence for heterophilic adhesion of embryonic retinal cells and neuroblastoma cells to substratum adsorbed NCAM. *Journal of Cell Biology* **116** (6): 1311-1320

Musil, L. S. and Goodenough, D. A. (1991) Biochemical analysis of connexin 43 intracellular transport, phosphorylation and assembly into gap junctional plaques. *Journal of Cell Biology* **115** (5): 1357-1374

Musil, L. S., Le, A. C. N., Van Slyke, J. K. and Roberts, L. M. (2000) Regulation of connexin degradation as a mechanism to increase gap junction assembly and function. *Journal of Biological Chemistry* **275**: 25207-25215

Nagafuchi, A. (2001) Molecular architecture of adherens junctions. *Current opinion in Cell Biology* **13**: 600-603

Nagar, B., Overduin, M., Ikura, M. and Rini, J. M. (1996) Structural basis of calcium-induced E-cadherin rigidification and dimerisation. *Nature* **380** (6572): 360-364

Nakopoulou, L., Gakiopoulou-Givalou, H., Karayiannakis, A. J., Giannopoulou, I., Keramopoulos, A, Davaris, P. and Pignatelli, M. (2002) Abnormal α-catenin expression in invasive breast cancer correlates with poor patient survival. *Histopathology* **40**: 536-546

Nasmyth, K. (2005) How do so few control so many? *Cell* **120** (6): 739-746

Ñeco, P., Giner, D., Frances, M. D., Viniegra, S. and Gutierrez, L. M. (2003) Differential participation of actin- and tubulin-based vesicle transport systems during secretion in bovine chromaffin cells. *European Journal of Neuroscience* **18** (4): 733-742

Noble, M., Groves, A. K., Ataliotis, P. and Jat, P. S. (1992) From choice to choice in the generation of neural cell lines. *Brain Pathology* **2**: 39-46

Nollet, F., Kools, P. and van Roy, F. (2000) Phylogenetic analysis of the cadherin superfamily allows identification of six major subfamilies besides several solitary members. *Journal of Molecular Biology* **299** (3): 551-572

Nose, A., Tsuji, K. and Takeichi, M. (1990) Localisation of specificity determining sites in cadherin cell adhesion molecules. *Cell* **61**: 147-155

Nyborg, W. L. (1978) Physical Principles of ultrasound. In: Fry, F. J. ed. *Ultrasound: Its applications in Medicine and Biology, part 1.* Amsterdam: Elsevier Scientific Publishing Company; pp. 1-75.

Nyborg, W. L. (2001) Biological effects of ultrasound: development of safety guidelines. Part II: general review. *Ultrasound in Medicine and Biology* **27**: 301-333

Oberlender, S. A. and Tuan, R. S. (1994) Expression and functional involvement of N-cadherin in embryonic limb chondrogenesis. *Development* **120**: 177-187

Ohene-Abuakwa, Y., Noda, M., Perenyi, M., Kobayashi, N., Kashima, K., Hattori, T. and Pignatelli, M. (2000) Expression of the E-cadherin/catenin (α-, β- and γ-) complex correlates with the macroscopic appearance of early gastric cancer. *Journal of Pathology* **192**: 433-439

Orecchia, S., Schillaci, F., Salvio, M., Libener, R., Betta, P. G. (2004) Aberrant E-cadherin and gamma-catenin expression in malignant mesothelioma and its diagnostic and biological relevance. *Lung Cancer* **45**: S37-S43, Suppl. 1

Orlova, A., Shvetsov, A., Galkin, V. E., Kudryashov, D. S., Rubenstein, P. A., Egelman, E. H. and Reisler, E. (2004) Actin-destabilising factors disrupt filaments by means of a time reversal of polymerisation. *Proceedings of the National Academy of Sciences of the USA* **101** (51): 17664-17668

Pal, J. D., Liu, X., Mackay, D., Shiels, A., Berthoud, V. M., Beyer, E. C. and Ebihara, L. (2000) Connexin 46 mutations linked to congenital cataract show loss of gap junction channel function. *American Journal of Physiology-Cell Physiology* **279**: C596-602

Pantaloni, D., Le Clainche, C. and Carlier, M. F. (2001) Mechanisms of actin-based motility. *Science* **292**: 1502-1506

Patel, S. D., Chen, C. P., Bahna, F., Honig, B. and Shapiro, L. (2003) Cadherin-mediated cell-cell adhesion: sticking together as a family. *Current Opinion in Structural Biology* **13**: 690-698

Pearson, R. G., Molino, Y., Williams, P. M. Tendler, S. J. B., Davies, M. C., Roberts, C. J. and Shakesheff, K. M. (2003) Spatial confinement of neurite regrowth from dorsal root ganglia within nonporous microconduits. *Tissue Engineering* **9** (2): 210-208

Peiper, M. and Yap, A. S. (2003) Traffic control: p120-catenin acts as a gatekeeper to control the fate of classical cadherins in mammalian cells. *Journal of Cell Biology* **163** (10): 437-440

Perego, C., Vanoni, C., Massari, S., Raimondi, A., Pola, S., Cattaneo, M. G., Francolini, M., Vicentini, L. M. and Petrini, G. (2002) Invasive behaviour of glioblastoma cell lines is associated with altered organisation of the cadherin-catenin adhesion system. *Journal of Cell Science* **115**: 3331-3340

Perez-Moreno, M., Jamora, C. and Fuchs, E. (2003) Sticky business: orchestrating cellular signals at adherens junctions. *Cell* **112** (4): 535-548

Perret, E., Leung, A., Feracci, H. and Evans, E. (2004) Trans-bonded pairs of E-cadherin exhibit a remarkable hierarchy on mechanical strengths. *Proceedings of the National Academy of Sciences of the USA* **101**: 16472-16477

Pertz, O., Bozic, D., Koch, A. W., Fauser, C., Brancaccio, A. and Engel, J. (1999) A new crystal structure, Ca^{2+} dependence and mutational analysis reveal molecular details of E-cadherin homoassociation. *EMBO Journal* **18** (7): 1738-1747

Peterson, S., Perkins, G. and Baker, C. (1986) Development of an ultrasonic blood cell separator. *IEEE/Eighth Annual Conference of the Engineering in Medicine and Biology Society*, pp. 154-156

Petridis, A. K., El Maarouf, A. and Rutishauser, U. (2004) Polysialic acid regulates cell contact-dependent neuronal differentiation of projenitor cells from the subventricular zone. *Developmental Dynamics* **230** (4):675-684

Pokutta, S. and Weis, W. I. (2002) The cytoplasmic face of cell contact sites. *Current Opinion in Structural Biology* **12**: 255-262

Pollard, T. D., Blanchoin, L. and Mullins, R. D. (2000) Molecular mechanisms controlling actin filament dynamics in nonmuscle cells. *Annual Reviews in Biophysical and Biomolecular Structures* **29**: 545-576

Porritt, R. J., Mercer, J. L. and Munro, R. (2003) Ultrasound-enhanced latex immunoagglutination test (USELAT) for detection of capsular polysaccharide antigen of *Neisseria meningitis* from CSF and plasma. *Pathology* **35** (1): 61-64

Povlsen, G. K., Ditlevsen, D. K., Berezin, V. and Bock, E. (2003) Intracellular signalling by the neural cell adhesion molecule. *Neurochemical Research* **28** (1): 127-141

Prag, S., Lepekhin, E. A., Kolkova, K., Hartmann-Petersen, R., Kawa, A., Walmod, P. S., Belman, V., Gallagher, H. C., Berezin, V., Bock, E. and Pedersen, N. (2002) NCAM regulates cell motility. *Journal of Cell Science* **115** (2): 283-292

Puertas, A. M., Fernández-Barbero, A. and de las Nieves, F. J. (2001) Colloidal aggregation induced by attractive interactions. *Journal of Chemical Physics* **115** (12): 5662-5668

Quirk, R. A., France, R. M., Shakesheff, K. M. and Howdle, S. M. (2004) Supercritical fluid technologies and tissue engineering scaffolds. *Current Opinion in Solid State and Materials Science* **8**: 313-321

Rafell, M., Seelhorst, U. and Willert, C. (1998) Vortical flow structures at a helicopter rotor model measured by LDV and PIV. *Aeronautical Journal* **102** (1014): 221-227

Rao, J. Y., Bonner, R. B., Hurst, R. E., Liang, Y. Y., Reznikoff, C. A. and Hemstreet, G. P. (1997) Quantitative changes in cytoskeletal and nuclear actins during cellular transformation. *International Journal of Cancer* **70** (4): 423-429

Rao, J. Y. (2002) Targeting actin remodeling profiles for the detection and management of urothelial cancers-A perspective for bladder cancer research. *Frontiers in Bioscience* **7**: E1-E8

Rauscher, K., Voigt, J., Wilke, I. and Wilke, K. Th. (1982) *Chemische Tabellen und Rechentafeln fuer die analytische Chemie*. Deutsch: Verlag Harri

Rayleigh, J. W. S. (1945) *The theory of sound*, volume 2. Dover Publications New York (reprint)

Redey, S. A., Nardin, M., Bernache-Assolant, D., Rey, C., Delannoy, P., Sedel, K. and Marie, P. J. (2000). Behaviour of human osteoblastic cells on stoichiometric hydroxyapatite and type A carbonate apatite: Role of surface energy. *Journal of Biomedical Materials Research* **50**: 353-364

Revenu, C., Athman, R., Robine, S. and Louvard, D. (2004) The co-workers of actin filaments: from cell structures to signals. *Nature Molecular Cell Biology* **5**: 1-12

Richard, G. (2003) Connexin gene pathology. *Clinical and Experimental Dermatology* **28**: 397-409

Robinson, D. J. and Earnshaw, J. C. (1992) Experimental study of colloidal aggregation in two dimensions. III. Structural dynamics. *Physical Review A* **46** (4): 2065-2071

Roigas, J., Wallen, E. S., Loening, S. A. and Moseley, P. L. (2002) Estramustine phosphate enhances the effects of hyperthermia and induces the small heat shock protein HSP27 in the human prostate carcinoma cell line PC-3. *Urological Research* **30** (2): 130-135

Rosivatz, E., Becker, I., Bamba, M., Schott, C., Diebold, J., Mayr, D., Hofler, H. and Becker, K. F. (2004) Neoexpression of N-cadherin in E-cadherin positive colon cancers. *International Journal of Cancer* **111** (5): 711-719

Rüdiger, M. (1998) Vinculin and α-catenin: shared and unique functions in adherens junctions. *BioEssays* **20**: 733-740

Russ, J. C. (1998). *The image Processing Tool Kit 3.0*. Boca Raton USA: CRC Press

Rutishauser, U. (1998) Polysialic acid at the cell surface: Biophysics in service of cell interactions and tissue plasticity. *Journal of cellular biochemistry* **70** (3): 304-312

Sáez, J. C., Berthoud, M., Brañes, M. C., Martínez, A. D. and Beyer, E. C. (2003) Plasma membrane channels formed by connexins: their regulation and functions. *Physiological Reviews* **83**: 1359-1400

Saffell, J. L., Doherty, P., Tiveron, M. C., Morris, R. J. and Walsh, F. S. (1995) NCAM regulates a cytoplasmic domain to function as a neurite outgrowth-promoting neuronal receptor. *Molecular and Cellular Neuroscience* **6** (6): 521-531

Sandig, M., Kalnins, V. I. and Siu, C. H. (1997) Role of NCAM, cadherins, and microfilaments in cell-cell contact formation in TM4 immature mouse Sertoli cells. *Cell Motility and the Cytoskeleton* **36** (2): 149-163

Sano, K., Tanihara, H., Heimark, R. L., Obata, S., Davidson, M., StJohn, T., Taketani, S. and Suzuki, S. (1993) Protocadherins- a large family of cadherin-related molecules in central – nervous- system. *EMBO Journal* **12** (6): 2249-2256

Sarrio, D., Perez-Mies, B., Hardisson, D., Moreno-Bueno, G., Suarez, A., Cano, A., Martinez-Perez, J., Gamallo, C. and Palacios, J. (2004) Cytoplasmic localization of p120ctn and E-cadherin loss characterize lobular breast carcinoma from preinvasive to metastatic lesions. *Oncogene* **23** (19): 3272-3283

Scemes, E., Duval, N. and Meda, P. (2003) Reduced expression of $P2Y_1$ receptors in connexin43-null mice alters calcium signalling and migration of neural progenitor cells. *Journal of Neuroscience* **23**: 11444-11452

Schaller, M. D. and Schaefer, E. M. (2001) Multiple stimuli induce tyrosine phosphorylation of the Crk-binding sites of paxillin. *Biochemical Journal* **360** (1): 57-66

Schlichting, H. (1932) Berechnung ebener periodischer Grenzschicht Strömungen. *Physikalische Zeitschrift* **33** (8): 327

Schlosshauer, P. W., Brown, S. A., Eisinger, K., Yan, Q. Y., Guglielminetti, E. R., Parsons, R., Ellenson, L. H. and Kitajewski, J. (2000) APC truncation and increased beta-catenin levels in a human breast cancer cell line. *Carcinogenesis* **21** (7): 1453-1456

Schneeberger, E. E. and Lynch, R. D. (2004) The tight junction: a multifunctional complex. *American Journal of Cell Physiology* **286**: C1213-C1228

Schulze-Tanzil, G., de Souza, P., Villejas Castrejon, H., John, T., Merker, H.-J., Scheid, A. and Shakibaei, M. (2002) Redifferentiation of dedifferentiated human chondrocytes in high-density cultures. *Cell and Tissue Research* **308**: 371-379

Schumacher, B., Su, J. L., Lindley, K. M., Kuettner, K. E. and Cole, A. A. (2002) Horizontally oriented clusters of multiple chondrons in the superficial zone of ankle, but not knee articular cartilage. *Anatomical Record* **266**: 241-248

Schwab, W., Hofer, A. and Kasper, M. (1998) Immunohistochemical distribution of connexin 43 in the cartilage of rats and mice. *Histochemical Journal* **30**: 413-419

Shan, W. S., Tanaka, H., Phillips, G. R., Arndt, K., Yoshida, M., Colman, D. R. and Shapiro, L. (2000) Functional cis-heterodimers of N- and R-cadherins. *Journal of Cell Biology* **148** (3): 579-590

Shapiro, L., Fannon, A. M., Kwong, P. D., Thompson, A., Lehmann, M. S., Grubel, G., Legrand, J. F., Als-Nielsen, J., Colman, D. R. and Hendrickson, W. A. (1995) Structural basis of cell-cell adhesion by cadherins. *Nature* **374**: 327-337

Shiiina, H., Breault, J. E., Basset, W. W., Enokida, H., Urakami, S., Li, L. C., Okino, S. T., Deguchi, M., Kaneuchi, M., Terashima, M., Yoneda, T., Shigeno, K., Carroll, P. R., Igawa, M. and Dahiya, R. (2005) Functional loss of the γ-catenin gene through epigenetic and genetic pathways in human prostate cancer. *Cancer Research* **65** (6): 2130-2138

Shirgaonkar, I. Z., Lanthier, S. and Kamen, A. (2004) Acoustic cell filter: a proven cell retention technology for perfusion of animal cell cultures. *Biotechnology Advances* **22** (6): 433-444

Simon, A. M., Goodenough D. A. and Paul, D. L. (1998) Mice lacking connexin40 have cardiac conduction abnormalities characteristic of atrioventricular block and bundle branch block. *Current Biology* **8**: 295-298

Sivasankar, S., Brieher, W., Lavrik, N., Gumbiner, B. and Leckband, D. (1999) Direct molecular force measurements of multiple adhesive interactions between cadherin ectodomains. *Proceedings of the National Academy of Sciences of the USA* **96** (21): 11820-11824

Sivasankar, S., Gumbiner, B. and Leckband, D. (2001) Direct measurements of multiple adhesive alignments and unbinding trajectories between cadherin extracellular domains. *Biophysical Journal* **80**: 1758-1768

Skjeltorp, A. T. (1987) Visualisation and characterisation of colloidal growth from ramified to faceted structures. *Physical Review Letters* **58** (14): 1444-1447

Soft Imaging System GmbH, *analySIS 3.1 user's guide*. (1999) Soft Imaging System GmbH Munster, Germany

Söllner, K. and Bondy, C. (1937) Mechanisms of coagulation by ultrasonic waves. *Transactions of the Faraday Society* **32**: 612-623

Spengler, J. F., Coakley, W. T. and Christensen, K. T. (2003) Microstreaming effects on particle concentration in an ultrasonic standing wave. *AICHE Journal* **49**: 2773-2782.

Spengler, J. and Jekel, M. (2000) Ultrasound conditioning of suspensions-studies of streaming influence on particle aggregation on a lab- and pilot-plant scale. *Ultrasonics* **38**: 624-628

Spengler, J. F. (2002) 'Application of ultrasonic standing waves for suspended particle manipulation in the water industry'. Doctoral Dissertation, Technische Universität Berlin

Spengler, J. F. and Coakley, W. T. (2003). Ultrasonic trap to monitor morphology and stability of developing microparticle aggregates. *Langmuir* **19**: 3635-3642

Spengler, J. F., Jekel, M., Christensen, K. T., Andrian, R. J., Hawkes, J. J. and Coakley, W. T. (2001) Observation of yeast cell movement and aggregation in small scale MHz-ultrasonic standing wave field. *Bioseparation* **9**: 329-341

Spinardi, L., Rietdorf, J., Nitch, L., Bono, M., Tacchetti, C., Way, M. and Marchisio, P. C. (2004) A dynamic podosome-like structure of epithelial cells. *Experimental Cell Research* **295**: 360-374

Steel, K. P. and Kros, C. J. (2001) A genetic approach to understanding auditory function. *Nature Genetics* **27** (2): 143-149

Strelkov, S. V., Herrmann, H. and Aebi, U. (2003) Molecular architecture of intermediate filaments. *BioEssays* **25**: 243-251

Stringer, B. M. J., Verhofstad, A. A. J. and Foster, G. A. (1994) Raphé neural cells immortalised with a temperature-sensitive oncogene: differentiation under basal conditions down a APUD cell lineage. *Developmental Brain Research* **79**: 267-274

Stuhlmann, D., Ale-Agha, N., Reinehr, R., Steinbrenner, H., Ramos, M. C., Sies, H. and Brenneiser, P. (2003) Modulation of homologous gap junctional intercellular communication of human dermal fibroblasts via a paracrine factor(s) generated by squamous tumour cells. *Carcinogenesis* **24** (11): 1737-1748

Svoboda, K. K. H. (1998) Chondrocyte-matrix attachment complexes mediate survival and differentiation. *Microscopy Research and technique* **43** (2): 111-122

Sympson, C. J. and Geoghegan, T. E. (1990) Actin gene expression in murine erythroleukemia cells treated with cytochalasin D. *Experimental Cell Research* **189**: 28-32

Takaishi, K., Sasaki, T., Kotani, H., Nishioka, H. and Takai, Y. (1997) Regulation of cell-cell adhesion by Rac and Rho small G proteins in MDCK cells. *Journal of Cell Biology* **139** (4): 1047-1059

Takeda, H., Shimoyama, Y., Nagafuchi, A. and Hirohashi, S. (1999) E-cadherin functions as a cis-dimer at the cell-cell adhesive interface in vivo. *Nature Structural Biology* **6** (4): 310-312

Takeichi, M. (1991)Cadherin cell adhesion receptors as a morphogenetic regulator. *Science* **251**: 1451-1455

Tamura, K., Shan, W. S., Hendrickson, W. A., Colman, D. R. and Shapiro, L. (1998) Structure-function analysis of cell adhesion by neural (N-) cadherin. *Neuron* **20** (6): 1153-1163

Tavella, S., Raffo, P., Tacchetti, C., Cancedda, R. and Castagnola, P. (1994) N-CAM and N-cadherin expression during *in vitro* chondrogenesis. *Experimental Cell Research* **215**: 354-362

Tepass, U. (2002) Adherens junctions: new insight into assembly, modulation and function. *BioEssays* **24**: 690-695

Tepass, U., Truong, K., Godt, D., Ikura, M. and Peifer, M. (2000) Cadherins in embryonic and neural morphogenesis. *Nature Molecular Cell Biology* **1**: 91-100

ter Haar, G. and Wyard, S. J. (1978) Blood cell banding in ultrasonic standing wave fields: A physical analysis. *Ultrasound in Medicine and Biology* **4**: 111-123

Tezel, A., Sens, A. and Mitragori, S. (2002) Investigations of the role of cavitation in low-frequency sonophoresis using acoustic spectroscopy. *Journal of Pharmaceutical Sciences* **91** (2): 444-453

Theiss, C. and Meller, K. (2002) Microinjected anti-actin antibodies decrease gap junctional intercellular communication in cultured astrocytes. *Experimental Cell Research* **281**: 197-204

Thiery, J. P., Brackenbury, R., Rutishauser, U. and Edelman, G. M. (1977) Adhesion among neural cells of the chick embryo. II. Purification and characterisation of a cell adhesion molecule from neural retina. *Journal of Biological Chemistry* **252**: 6841-6845

Thill, A., Moustier, S., Aziz, J., Wiesner, M. R. and Bottero, J. Y. (2001) Flocs restructuring during aggregation: experimental evidence and numerical simulation. *Journal of Colloid and Interface Science* **243**: 171-182

Thomas, N. E., Sobanski, M. A. and Coakley, W. T. (1999) Ultrasonic enhancement of coated particle agglutination immunoassays: influence of particle density and compressibility. *Ultrasound in Medicine and Biology* **4**: 111-123

Thomas, T., Jordan, K. and Laird, D. W. (2001) Role of cytoskeletal elements in the recruitment of Cx43-GFP and Cx26-YFP into gap junctions. *Cell Communication and Adhesion* **8** (4-6): 231-236

Thoreson, M. A., Anastasiadis, P. Z., Daniel, J. M., Ireton, R. C., Wheelock, M. J., Johnson, K. R., Hummingbird, D. K. and Reynolds, A. B. (2000) *Journal of Cell Biology* **148** (1): 189-201

Toikka, J., Aalto, J., Häyrinen, J., Pelliniemi, L. J. and Finne, J. (1998) The polysialic acid units of the neural cell adhesion molecules NCAM form filament bundle networks. *Journal of Biological Chemistry* **273** (44): 28557-28559

Tomschy, A., Fauser, C., Landwehr, R. and Engel, J. (1996) Homophilic adhesion of E-cadherin occurs by a co-operative two-step interaction of N-terminal domains. *EMBO Journal* **15** (14): 3507-3514

Torres, L. N., Matera, J. M., Vascocellos, C. H., Avanzo, J. L., Hernandez-Blasquez, F. J. and Dagli, M. L. Z. (2005) Expression of connexins 26 and 43 in canine hyperplastic and neoplastic mammary glands. *Veterinary Pathology* **42** (5): 633-641

Trickey, W. R., Vail, T. P. and Guilak, F. (2004) The role of the cytoskeleton in the viscoelastic properties of human articular chondrocytes. *Journal of Orthopeadic Research* **22**: 131-139

Tucker, E., Buda, A., Jangha, N., Baker, J., Coad, J., Moorghan, M., Havler, M., Dettmar, O. and Pignatelli, M. (2003) Abnormalities of the cadherin-catenin complex in chemically-induced colorectal carcinogenesis. *Proceedings of the Nutrition Society* **62** (1): 229-236

Tuziuti, T., Kozuka, T. and Mitome, H. (1999) Measurement of distribution of acoustic radiation force perpendicular to sound beam axis. *Japanese Journal of Applied Physics* **38** (5B, Pt.1): 3297-3301

Upadhya, G. A. and Strasberg, S. M. (1999) Evidence that actin disassembly is a requirement for matrix metalloproteinase secretion by sinusoidal endothelial cells during cold preservation in the rat. *Hepatology* **30**: 169-176

Usui, T., Shima, Y., Shimada, Y., Hirano, S., Burgess, R. W., Schwarz, T. L., Takeichi, M. and Uemura, T. (1999) Flamingo, a seven-pass transmembrane cadherin, regulates planar cell polarity under the control of frizzled. *Cell* **98** (5): 585-595

Vidulescu, C., Clejan, S. and O'Connor, K. C. (2004) Vesicle traffic through intercellular bridges in DU 145 human prostate cancer cells. *Journal of Cellular and Molecular Medicine* **8** (3): 388-396

Vine, A. L. and Bertram, J .S. (2002) Cancer chemoprevention by connexins. *Cancer and Metastasis Reviews* **21**: 199-216

Vinhall, R. L., Hao Lo, S. and Reddi, A. H. (2002) Regulation of articular chondrocyte phenotype by morphogenetic protein 7, interleukin 1, and cellular context is dependent on the cytoskeleton. *Experimental Cell Research* **272**: 32-44

von Smoluchowski, M. (1918) Versuch einer mathematischen theore der Koagulation-skinetik kolloider Lösungen. *Zeitschrift Physikalische Chemie* **92**, 129-168

Voura, E. B., Sandig, M., Kalnins, V. I., Siu, C. H. (1998) Cell shape changes and cytoskeleton reorganisation during transendothelial migration of human melanoma cells. *Cell and Tissue Research* **293**: 375-387

Wahl, J. K. 3rd, Kim, Y. J., Cullen, J. M., Johnson, K. R. and Wheelock, M. J. (2003) N-cadherin-catenin complexes for prior to cleavage of the proregion and transport to the plasma membrane. *Journal of Biological Chemistry* **278** (19): 17269-17276

Walmod, P. S., Kolkova, K., Berezin, V. and Bock, E. (2004) Zippers make signals: NCAM-mediated molecular interactions and signal transduction. *Neurochemical Research* **29** (11): 2015-2035

Wang, Y. J. and Rose, B. (1995) Clustering of Cx43 cell-to-cell channels into gap junction plaques-regulation by cAMP and microfilaments. *Journal of Cell Science* **108** (11): 3501-3508

Wang, Z. W., Grabenstetter, P., Feke, D. L. and Belovich, J. M. (2004) Retention and viability characteristics of mammalian cells in an acoustically driven polymer mesh. *Biotechnology Progress* **20** (1): 384-387

Watanabe, T., Noritake, J. and Kaibuchi, K. (2005) Regulation of microtubules in cell migration. *Trends in Cell Biology* **15** (2): 76-83

Watt, F. M., Mattey, D. L. and Garrod, D. R. (1984) Calcium induced reorganisation of desmosomal components in cultured human keratinocytes. *Journal of Cell Biology* **99**: 2211-2215

Wei, C. J., Xu, X. and Lo, C. W. (2004) Connexins and cell signalling in development and disease. *Annual Reviews in Cell and Developmental Biology* **20**: 811-838

Weiser, M. A. H., Apfel, R. E. and Neppiras, E. A. (1984) Interparticle forces on red cells in standing wave field. *Acustica* **56**: 114-119

Wetts, R. and Vaughn, J. E. (2000) Manipulation of intracellular calcium has no effect on rate of migration of rat autonomic motor neurons in organotypic slice cultures. *Neuroscience* **98**: 369-376

Wheeler, A. P. and Ridley, A. J. (2004) Why three Rho proteins? Rho A, Rho B, Rho C, and cell motility. *Experimental Cell Research* **301**: 43-49

Wheelock, M. J. and Johnson, K. R. (2003) Cadherins as modulators of cellular phenotype. *Annual Reviews in Cell and Developmental Biology* **19**: 207-235

Wheelock, M. J., Soler, A. P. and Knudsen, K. A. (2001) Cadherin junctions in mammary tumours. *Journal of Mammary Gland Biology and Neoplasia* **6** (3): 275-285

Whitworth, G. and Coakley, W. T. (1992) Particle column formation in a stationary ultrasonic field. *Journal of the Acoustical Society of America* **91** (1): 79-85

Whitworth, G., Grundy, M. A. and Coakley, W. T. (1991) Transport and harvesting of suspended particles using modulated ultrasound. *Ultrasonics* **29**: 439-444

Widelitz, R. B., Jiang, T. X., Murray, B. A. and Chuong, C. M. (1993) Adhesion molecules in skeletogenesis: II. Neural cell adhesion molecules mediate precartilaginous mesenchymal condensations and enhance chondrogenesis. *Journal of Cell Physiology* **156**: 399-411

Wiklund, M., Toivonen, J., Tirri, M., Hänninen, P. and Hertz, H. M. (2004) Ultrasonic enrichment of microspheres for ultrasensitive biomedical analysis in confocal laser-scanning fluorescence detection. *Journal of Applied Physics* **96** (2): 1242-1248

Willecke, K., Eiberger, J., Degen, J., Eckardt, S (2002) Structural and functional diversity of connexin genes in the mouse and human genome. *Biological Chemistry* **383**: 725-737

Williams, A. F. and Barclay, A. N. (1988) The immunoglobulin superfamily-domains for cell surface recognition. *Annual Reviews in Immunology* **6**: 381-405

Williams, H. K., Sanders, D. S. A., Jankowski, J. A. Z., Landini, G. and Brown, A. M. S. (1998) Expression of cadherins and catenins in oral epithelial dysplasia and squamous cell carcinoma. *Journal of Oral Pathology and Medicine* **27** (7): 308-317

Windoffer, R., Beile, B., Leibold, A., Thomas, S., Wilhelm, U. and Leube, R. E. (2000) Visualization of gap junction motility in living cells. *Cell and Tissue Research* **299**: 347-362

Winjhoven, B. P. L., Tucker, E. T., Dinjens, W. N. M., Tilanus, H. W. and Pignatelli, M. (2004) Biochemical analysis and subcellular distribution of E-cadherin-catenin in adenocarcinomas of the gastro-oesophageal junction. *Anticancer Research* **24**: 1369-1376

Woods, A., Wang, G. and Beier, F. (2005) RhoA/ROCK signaling regulates Sox9 expression and actin organization during chondrogenesis. *Journal of Biological Chemistry* **280**: 11626-11634

Woodside, S. M., Bowen, B. D. and Piret, J. M. (1997) Measurement of ultrasonic forces for particle-liquid separations. *AICHE Journal* **43** (7): 1727-1736
Wu, J. R. (1991) Acoustical tweezers. *Journal of the Acoustical Society of America* **89**: 2140-2143

Wu, W. and Maniatis, T. (1999) A striking organisation of a large family of human neural cadherin-like cell adhesion genes. *Cell* **97**: 779-790

Yagi, T. and Takeichi, M. (2000) Cadherin superfamily genes: functions, genomic organisation and neurologic diversity. *Genes and Development* **14**: 1169-1180

Yamada, K. M. and Kemler, R. (2002) Cell-to-cell contact and extracellular matrix. *Current Opinion in Cell Biology* **14**: 527-530

Yamaji, S., Suzuki, A., Sugiyama, Y., Koide, Y., Yoshida, M., Kanamori, H., Mohri, H., Ohno, S. and Ishigatsubo, Y. (2001) A novel integrin-linked kinase-binding protein, affixin, is involved in the early stage of cell-substrate interaction. *Journal of Cell Biology* **153**: 1251-1264

Yang, D. H., Smith, E. R., Cohen, C., Wu, H., Patriotis, C., Godwin, A., Hamilton, T. and Xu, X. X. (2002) Molecular events associated with dysplastic morphologic transformation and initiation of ovarian tumorigenicity. *Cancer* **94**: 2380-2392

Yang, X. Z., Chen, M. W., Terry, S., Vacherot, F., Chopin, D. K., Bemis, D. L., Kitajewski, J., Benson, N. C., Guo, Y. L. and Buttyan, R. (2005) A human- and male-specific protocadherins that acts through the Wnt signalling pathway to induce neuroendocrine transdifferentiation of prostate cancer cells. *Cancer Research* **65** (12): 5263-5271

Yap, A. S. and Kovacs, E. M. (2003) Direct cadherin-activated signalling: a view from the plasma membrane. *Journal of Cell Biology* **160** (1): 11-16

Yap, A. S., Brieher, W. M. and Gumbiner, B. M. (1997) Molecular and functional analysis of cadherin-based adherens junctions. *Annual Reviews in Cell and Developmental Biology* **13**: 119-146

Yap, A. S., Niessen, C. M. and Gumbiner, B. M. (1998) The juxtamembrane region of the cadherin cytoplasmic tail supports lateral clustering, adhesive strengthening and interaction with p129 (ctn). *Journal of Cell Biology* **141** (3): 779-789

Yasuda, K. (1999) Measurement of microscopic spatial distribution of acoustic force using microspheres and electrostatic force. *Japanese Journal of Applied Physics* **38** (1, 5B): 3316-3319

Yin, T. and Green, K. J. (2004) Regulation of desmosome assembly and adhesion. *Seminars in Cell and Developmental Biology* **15**: 665-677

Yonemura, S., Itoh, M., Ngafuchi, A. and Tsukita, S. (1995) Cell-to-cell adherens junction formation and actin filament organisation: similarities and differences between non-polarised fibroblasts and polarised epithelial cells. *Journal of Cell Science* **108**: 127-142

Zarembo, L. K. (1971). Acoustic Streaming. In: Rozenberg, L. D. ed. *High-intensity ultrasonic fields*. New York: Plenum Press; pp. 137-197

Zhang, H., Vutskits, L., Calaora, V., Durbec, P. and Kiss, J. Z. (2004) A role for the polysialic acid-neural cell adhesion molecule in PDGF-induced chemotaxis of oligodendrocyte precursor cells. *Journal of Cell Science* **117** (1): 93-103

Zhang, W., Green, C. and Scott, N. S. (2002) Bone morphogenetic protein-2 modulation of chondrogenic differentiation *in vitro* involves gap junction-mediated intercellular communication. *Journal of Cell Physiology* **193**: 233-243

Zhang, Z-J., Huckle, J., Francomano, C. A. and Spencer, G. S. (2003) The effects of pulsed low-intensity ultrasound on chondrocyte viability, proliferation, gene expression and matrix production. *Ultrasound in Medicine and Biology* **29**:1645-1651

Zhou, C. H., Pivarnik, P., Rand, A. G. and Letcher, S. V. (1998) Acoustic standing-wave enhancement of a fiber-optic Salmonella biosensor. *Biosensors and Bioelectronics* **13** (5): 495-500

Zhurinsky, J., Shtutman, M. and Ben-Ze'ev, A. (2000) Plakoglobin and β-catenin: protein interactions, regulation and biological roles. *Journal of Cell Science* **113**: 3127-3139

Zicha, D., Dobbie, I. M., Holt, M. R., Monypenny, J., Soong, D. Y. H., Gray, C. and Dunn, G. A. (2003) Rapid actin transport during cell protrusion. *Science* **300**: 142-145

Zimmermann, B. (1984). Assembly and disassembly of gap junctions during mesenchymal cell condensation and early chondrogenesis in limb buds of mouse embryo. *Journal of Anatomy* **132**: 351-363

Zimmermann, B., Scharlach, E. and Kaatz, R. (1992) Cell contact and surface coat alterations of limb-bud mesenchymal cells during differentiation. *Journal of Embryology and Experimental Morphology* **72**: 1-18

Zuppinger, C., Schaub, M. C. and Eppenberger, H. M. (2000) Dynamics of early contact formation in cultured adult rat cardiomyocytes studied by N-cadherin fused to green fluorescent protein. *Journal of Molecular and Cellular Cardiology* **32**: 539-555

List of Figures

List of Tables

List of Equations

-Appendices-

Appendix A

Culture media

The conditionally immortalised 921202-6 (C6) neural cell line was maintained in a defined medium based on that described by Bottenstein and Sato (1979). All chemicals for the preparation of this medium have been purchased from Sigma-Aldrich, unless otherwise stated. Human epithelial and cancer prostate cells, as well as freshly isolated chondrocytes were maintained in Ham's F-12 and DMEM/Ham's F-12 respectively; these media are commercially available from various companies such as Sigma-Aldrich, UK and Gibco; BRL, Life Technologies Ltd., UK. However, as described in Chap. 6 (Section 6.2.2), human epithelial and cancer prostate cells were, for the experiments described in the ultrasound trap, suspended in HCMF/5 mM $CaCl_2$; the formulation of the HCMF medium is given in the following. The chemicals were in this case purchased from Fisher Scientific, UK unless otherwise stated.

A.1 Neuronal supplemented medium (NSM)

I. Preparation of Neuronal supplemented stock (NSS)

1) Dissolve 20 mg corticosterone in 10 ml ethanol in a glass container

2) Dissolve 3.1 mg progesterone in 25 ml ethanol in a glass container

3) Dissolve 10 mg 3, 3', 5-triiodo-L-thyronine in 50 ml 10 mM NaOH

4) Dissolve 100 mg of BSA in 10 ml DPBS

5) Dissolve 2 g apo-transferrin in 20 ml DPBS

6) Dissolve 320 mg putrescine in 4 ml H_2O

7) Dissolve 10.4 mg sodium selenite in 10 ml H_2O

8) Dilute 100 µl sodium selenite solution in 4.9 ml DPBS

9) Add 49 ml DPBS to a sterile 500 ml beaker containing a sterile stirring bar

10) Stir the DPBS slowly while adding the following:

- 10 ml BSA (point 4)
- 20 ml apo-transferrin (point 5)
- 4 ml putrescine (point 6)
- 5 ml sodium selenite (point 8)
- 1 ml 3, 3', 5-triiodo-L-thyronine (point 3)
- 117 ml DPBS
- 1 ml progesterone (point 2)
- 200 µl corticosterone (point 1)

11) Pour the prepared stock supplement into a cup of a 250 ml filter bottle unit (22 µm filter membrane) in a tissue culture cabinet and vacuum filter

12) Aliquot 8 ml into each of 25, 25 ml universal containers

13) Store at – 20°C for up to 6 months

II. Preparation of insulin stock

1) Add 7.8 ml of sterile (filtered) 20 mM HCl to 100 mg insulin in its original container

2) Gently pipette the solution up and down to insure all the insulin is dissolved

3) Aliquot 300 µl of the solution to each of 26, 2 ml cryovials

4) Store at – 20°C for up to one year

III. Preparation of NSM

1) Pour 200 ml Ham's F-12 and 200 ml DMEM into a cup of a sterile 500 ml bottle filter unit ((22 μm filter membrane)
2) Add 8 ml NSS and add 4 ml of penicillin: streptomycin solution, filter using a vacuum pump
3) Add 300 μl of insulin to the bottle of medium after filtration
4) Store at 4°C for up to 1 month

A.2 HEPES Ca^{2+} and Mg^{2+} -free buffered saline (HCMF)

1) NaCl	4.0 g
2) KCl	0.2 g
3) $Na_2HPO.2H_2O$	0.045 g
4) D-glucose	0.5 g
5) HEPES	1.19 g

The above components are added in a volume of 500 ml of distilled H_2O. The pH is finally adjusted to 7.4 using 1M NaOH.

A.3 DMEM/Ham's F-12 media

Table A.1: List of the amino acids contained in DMEM/Ham's F-12 together with their molarities (Sigma, UK)

Amino Acids	*Molarity (mM)*
Glycine	0.250
L-Alanine	0.0500
L-Arginine hydrochloride	0.699
L-Asparagine-H_2O	0.0500
L-Aspartic acid	0.0500
L-Cysteine hydrochloride-H_2O	0.0998
L-Cysteine-$2H_2O$	0.1000
L-Glutamic acid	0.0500
L-Histidine hydrochloride-H_2O	0.150
L-Isoleucine	0.416
L-Leucine	0.451
L-Lysine hydrochloride	0.499
L-Methionine	0.116
L-Phenylalanine	0.215
L-Proline	0.150
L-Serine	0.250
L-Threonine	0.449
L-Tryptophan	0.0442
L-Tyrosine disodium salt dihydrate	0.214
L-Valine	0.452

Table A.2: List of the vitamins contained in DMEM/Ham's F-12 together with their molarities (Sigma, UK)

Vitamins	***Molarity (mM)***
Ascorbic acid	0.00863
Biotin	0.0000143
Choline chloride	0.0641
D-Calcium pantothenate	0.00470
Folic acid	0.00601
i-Inositol	0.0700
Niacinamide	0.0166
Pyridoxine hydrochloride	0.00971
Riboflavin	0.000582
Thiamine hydrochloride	0.00644
Vitamin B-12	0.000502

Table A.3: List of the trace elements and reducing agents contained in DMEM/Ham's F-12 together with their molarities (Sigma, UK)

Trace Elements	***Molarity (mM)***
Ammonium metavanadate	0.0000026
Manganous chloride	0.0000003
Sodium selenite	0.0000286
Reducing Agents	***Molarity (mM)***
Glutathionine, monosodium	0.00326

Table A.4: List of the inorganic salts contained in DMEM/Ham's F-12 together with their molarities (Sigma, UK)

Inorganic Salts	***Molarity (mM)***
Calcium chloride ($CaCl_2$)	1.05
Cupric sulphate ($CuSO_4$-$5H_2O$)	0.0000052
Ferric nitrate (Fe(NO3)3''$9H_2O$)	0.000124
Ferric sulphate ($FeSO_4$-$7H_2O$)	0.00150
Magnesium chloride ($MgCl_2$)	0.301
Magnesium sulphate ($MgSO_4$)	0.407
Potassium chloride (KCl)	4.16
Sodium bicarbonate ($NaHCO_3$)	29.02
Sodium chloride (NaCl)	120.61
Sodium phosphate dibasic (NaH_2PO_4)	0.500
Sodium phosphate monobasic (NaH_2PO_4-H_2O)	0.453
Zinc sulphate ($ZnSO_4$-$7H_2O$)	0.00300

Table A.5: List of other components contained in DMEM/Ham's F-12 together with their molarities (Sigma, UK)

Other Components	***Molarity (mM)***
D-Glucose (Dextrose)	17.51
Ethanolamine	0.0195
Hypoxanthine	0.0150
Linoleic acid	0.000150
Lipoic acid	0.000510
Phenol red	0.0215
Putrescine- 2HCl	0.000503
Sodium pyruvate	1.000
Thymidine	0.00151

Appendix B

Microscope

The optical set-up for epi- or reflected light microscope is shown in Figure B.1. The light from a suitable source is guided through the optical system so that the specimen is illuminated from above. The light scattered by the sample is collected by the microscope optics and can be viewed through the binocular eye-pieces or the TV/Photograph-port (illumination ratio of 100% in both cases). Various filter cubes essential for fluorescence microscopy as well as a brightfield cube for normal brightfield microscopy, are integrated in the microscope's cube turret.

The light source used in this work was a mercury light arc burner attached to an Olympus BX40, BX41M and BX61 epi-microscopes. The BX40 model was employed for the investigation of particle aggregate growth and acoustic microstreaming, as it is connected to a video camera enabling continuous recording of the process under investigation (Chaps. 2 and 3; Secs. 2.2.3 and 3.2.2). The BX41M model was largely used for fluorescence microscopy, as it employs an F-view digital fluorescent camera (Chap. 4; Sec. 4.2.1), while the BX61 model was chosen for analysis of the Cx43-related specimens (Chap. 5; Sec. 5.2.1) as it employs an F-view digital fluorescent camera together with a ×100 oil immersion lens.

Fluorescence microscopy is based on the ability of some substances to absorb light of a particular wavelength and after a brief interval, termed the fluorescence

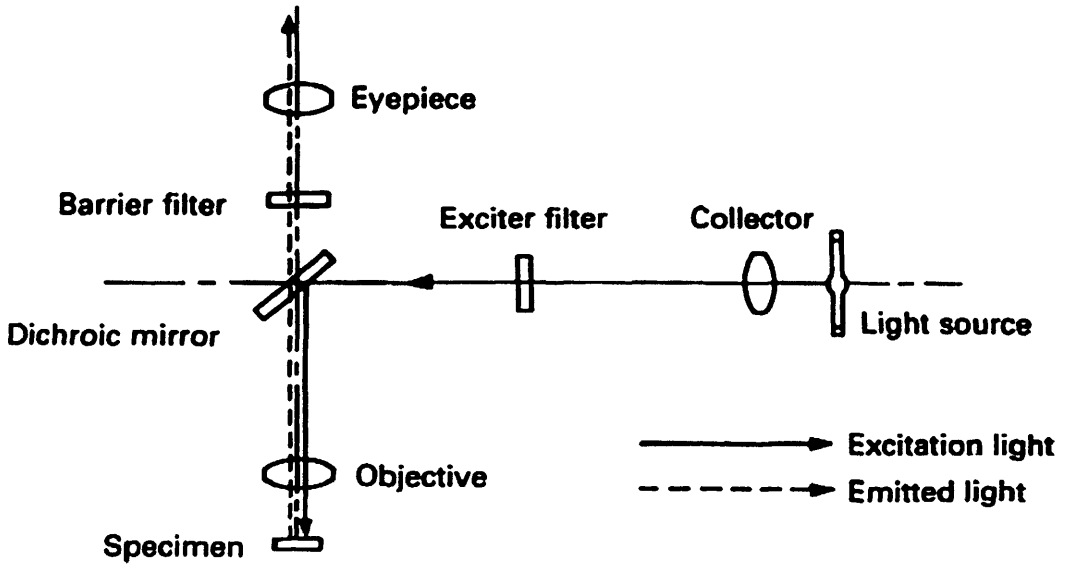

Figure B.1: Optical set-up for epi- or reflected light microscope

lifetime, to re-emit light at longer wavelengths, as during this process there is some energy loss during energy conversion (Herman, 1998). In doing so, the excitation light illuminates the specimen but only the emitted light is detected resulting in a high contrast image. Excitation and barrier filters are employed for this purpose. The former transmit only wavelengths of light required for excitation of a specific fluorophore, whereas the latter transmit the emitted fluorescence and block out any unwanted wavelengths, thus providing a black background. Additionally, a dichroic mirror directs the excitation light through the objective, to the area of the specimen, thus providing efficient illumination.

Figure B.2 illustrates the characteristic transmission curves for excitation filter (BP), barrier filter (BA) and dichroic mirror (DM) of the filter cubes employed in the present study. A table (Table B.1) of the characteristic excitation and detected colours of Olympus fluorescence filter cubes follows, while Table B.2 lists the excitation and emission spectra of the fluorophores used in the present thesis.

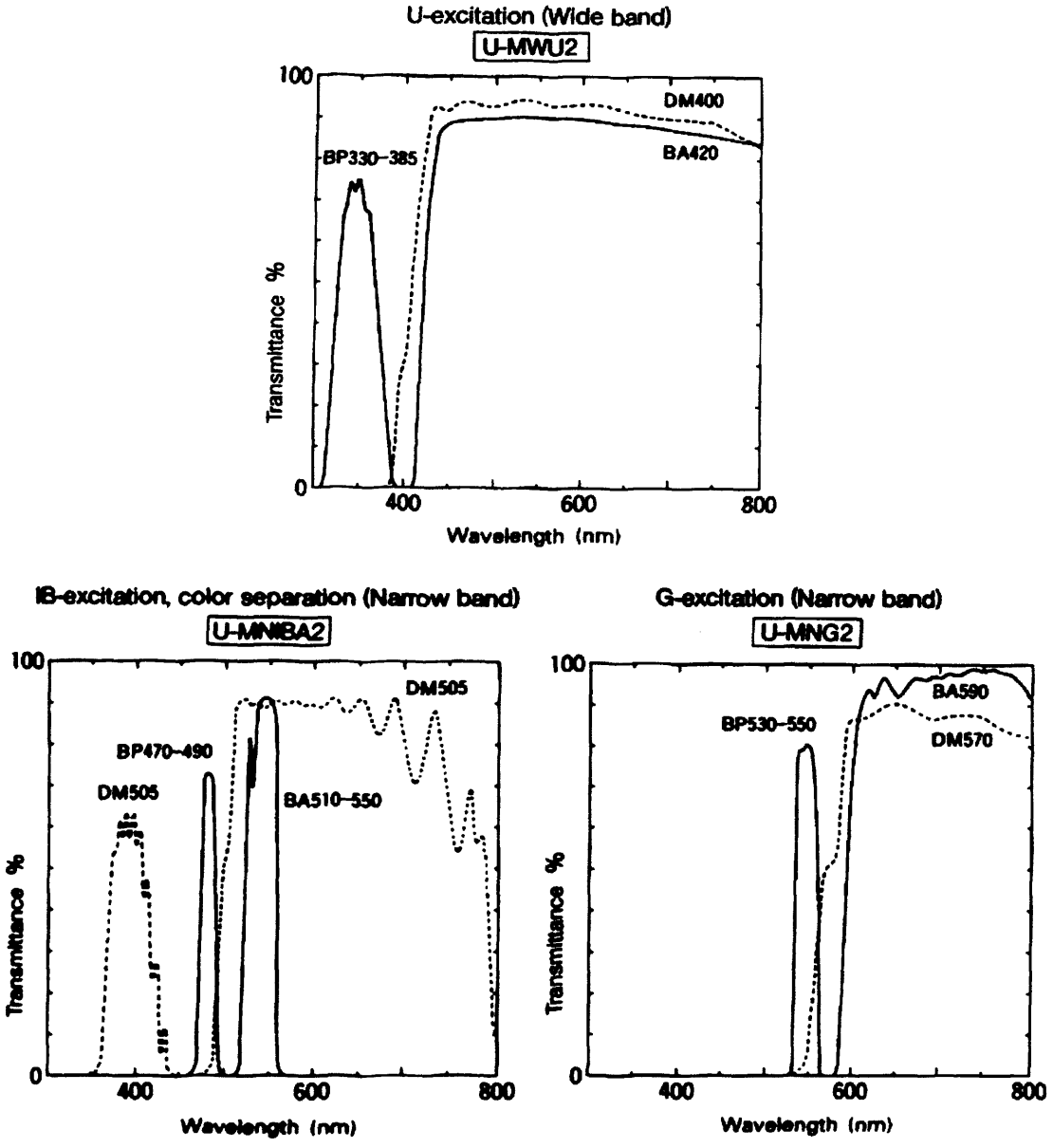

Figure B.2: Optical characteristics of Olympus fluorescence filter cubes

Finally, Tables B.3, B.4 list the optical characteristics of the objectives used with the three different microscope set-ups.

Table B.1: Summary of the spectral emission and detection colours of Olympus fluorescence filter cubes

Fluorescent filter cube	U-MNIBA	U-MNG	U-MWU
Excitation	Blue	Green	UV
Detection	Yellow/Green-Red	Orange-Red	Blue-Red

Table B.2: Summary of the emission and detection spectra of the fluorophores used in the present study (Molecular Probes Inc. Eugene, OR, USA and Sigma, UK catalogues)

Fluorophore	***Excitation (nm)***	***Emission (nm)***	***Filter Cube***
Calcein AM	490	515	U-MNIBA
Ethidium Homodimer-1 (EthD-1)	528	617	U-MNG
Propidium Iodide	535	617	U-MNG
ApoAlert Annexin V-FITC	495	518	U-MNIBA
Green MiTo Tracker FM	490	516	U-MNIBA
Phalloidin-FITC	495	520	U-MNIBA
Phalloidin Alexa Fluor-488	495	518	U-MNIBA
Alexa Fluor-594	580	609	U-MNG

Table B.3: Characteristics of the OLYMPUS BX40, BX41M objectives (Data adapted from Olympus BX40, BX41M-FLA Reflected light fluorescence Attachment User's guide)

Objectives	*Magnification*	*Numerical Aperture NA*	*Working Distance (mm)*	*Resolution (μm)*	*Field of view (mm^2)*
UMPlanF1	×5	0.15	20.0	2.24	0.96×1.28
	×10	0.30	10.1	1.12	0.48×0.64
	×20	0.46	3.1	0.73	0.24×0.32
LMPlanF1	×50	0.80	0.66	0.42	0.096×0.128

Table B.4: Characteristics of the OLYMPUS BX61 objectives (Data adapted from Olympus BX61-FLA Reflected light fluorescence Attachment User's guide)

Objectives	*Magnification*	*Numerical Aperture NA*	*Working Distance (mm)*	*Resolution (μm)*	*Field of view (mm^2)*
UMPlanFI-P	×4	0.13	17.0	2.58	1.2×1.6
	×10	0.30	10.0	1.12	0.48×0.64
	×40	0.75	0.51	0.45	0.12×0.16
UPlan Apo	×100	0.60-1.30	0.10	0.26	0.048×0.064

Appendix C

Abbreviations

APC	Adenomatous polyposis coli
CHX	Cycloheximide
Cx43	Connexin 43
DLCA	Diffusion limited colloidal aggregation
DLVO	Derjaguin-Landau-Verwey-Overbeek theory
DMEM	Dulbecco's modified Eagle's medium
DRF	Direct radiation force
DSC	Desmocollin
DSG	Desmoglein
DZ	Deep zone
EC	Extracellular cadherin domain
ECM	Extracellular matrix
EDTA	Ethylenediaminetetraacetic acid
EGF	Epidermal growth factor
EthD-1	Ethidium Homodimer 1
F-actin	Filamentous actin
FGF	Fibroblast growth factor

FITC	Fluorescein-5-isothiocyanate
G-actin	Globular actin
GFP	Green fluorescent protein
GJIC	Gap junctional intercellular communication
GPI	Glycosyl-phosphatidylinositol
HCMF	HEPES Ca^{2+} and Mg^{2+}-free buffered saline
IgCAM	Immunoglobulin cell adhesion molecules
IgSF	Immunoglobulin superfamily
LEF	Lymphocyte enhancing factor
MDCK	Madin Darby Canine Kidney
NCAM	Neural cell adhesion molecule
NSM	Neuronal supplemented medium
PBS	Phosphate buffered saline
PCR	Polymerase chain reaction
PI-PLC	Phosphatidyl inositol phospholipase C
PIV	Particle image velocimetry
PSA	Polysialic acid
RLCA	Reaction limited colloidal aggregation
SZ	Surface zone
TCF	T cell factor
USW	Ultrasonic standing wave
USWT	Ultrasonic standing wave trap
ZO	Zonula occludens

Appendix D

Publications

The work presented in this thesis has so far been published as follows (state December 2005)

A. Referred Journals

Bazou, D., Foster, G. A., Ralphs, J. R. and Coakley, W. T. (2005) Molecular adhesion development in a neural cell monolayer forming in an ultrasound trap. *Molecular Membrane Biology* **22**: 229-240

Bazou, D., Kuznetsova, L. A. and Coakley, W. T. (2005) Physical environment of 2-D animal cell aggregates formed in a short pathlength ultrasound standing wave trap. *Ultrasound in Medicine and Biology* **31**: 423-430

Bazou, D., Coakley, W. T., Meek, K. M., Yang, M. and Pham, D. T. (2004) Characterisation of the morphology of 2-D particle aggregates in different electrolyte concentrations in an ultrasound trap. *Colloids and Surfaces A: Physicochemical and Engineering Aspects* **143**: 97-104

Coakley, W. T., Bazou, D., Morgan, J., Foster, G. A., Archer, C. W., Powell, K., Borthwick, K. A, Twomey, C. and Bishop, J. (2004) Cell-cell contact and membrane spreading in an ultrasound trap. *Colloids and Surfaces B: Biointerfaces* **34**: 221-230

Bazou, D., Dowthwaite, G. P., Khan, I. M., Archer, C. W., Ralphs, J. R. and Coakley, W. T. Gap junctional intercellular communication and cytoskeletal organisation in chondrocytes in suspension in an ultrasound trap. *Submitted in Molecular Membrane Biology.*

B. Review Chapter

Coakley, W. T. and Bazou, D. Particle and cell manipulation by radiation force in ultrasound standing waves. In: Pandalai, S. G. ed. *Bubble and particle dynamics in acoustic fields: Modern trends and applications.* Research signpost: Transworld research network. *In press.*

C. Conference Proceedings

Coakley, W. T., Bazou, D. and Kuznetsova L. A. (2004) Cell and particle manipulation in an ultrasound standing wave trap. In: *Proceedings of the 18th international congress on acoustics.* April 8-11. Kyoto. V3713-3716.

Bazou, D., Foster, G. A. and Coakley, W. T. (2003) Cell adhesion processes in an ultrasound standing wave trap. In: *Proceedings on the world congress on ultrasonics.* September 7-10. Paris. 1241-1244

Coakley, W. T., Bazou, D. and Spengler J. F. (2003) Particle aggregate growth in an ultrasound standing wave trap. In: *Proceedings on the world congress on ultrasonics.* September 7-10. Paris. 1237-1240

Bazou, D., Bishop, J. C., Archer, C. W., Foster, G. A. and Coakley, W.T. (2003) Cell-cell interactions in a 2-D ultrasound trap. *European Cells and Materials Journal* **6**; Suppl.2: 28.

D. Papers in preparation

Bazou, D., Foster, G. A and Coakley, W. T. Temporal progression of cell adhesion and cytoskeletal development in NCAM modified neural cells.

Bazou, D., Foster, G. A. and Coakley, W. T. Adhesion of neural cells in an ultrasound trap in the presence of low calcium concentrations.

Bazou, D., Davies, G., Jiang, W. G. and Coakley, W. T. Comparison of the adhesion properties of epithelial and cancer prostate cells.